NASA CR-72744
MTI 70TR44

DEVELOPMENT OF LONG LIFE JET ENGINE THRUST BEARINGS

By

L. W. Winn

R. H. Badgley

MECHANICAL TECHNOLOGY INCORPORATED

Prepared for

NATIONAL AERONAUTICS AND SPACE ADMINISTRATION

NASA—Lewis Research Center

Contract NAS3-11163

W. J. Anderson
Chief, Bearings Branch

D. P. Townsend - Project Manager
Bearings Branch

NOTICE

This report was prepared as an account of Government-sponsored work. Neither the United States, nor the National Aeronautics and Space Administration (NASA), nor any person acting on behalf of NASA:

A.) Makes any warranty or representation, expressed or implied, with respect to the accuracy, completeness, or usefulness of the information contained in this report, or that the use of any information, apparatus, method or process disclosed in this report may not infringe privately-owned rights; or

B.) Assumes any liabilities with respect to the use of, or for damages resulting from the use of, any information, apparatus, method or process disclosed in this report.

As used above, "person acting on behalf of NASA" includes any employee or contractor of NASA, or employee of such contractor, to the extent that such employee or contractor of NASA or employee of such contractor prepares, disseminates, or provides access to any information pursuant to this employment or contract with NASA, or his employment with such contractor.

NASA CR-72744
MTI 70TR44

FINAL REPORT

DEVELOPMENT OF LONG LIFE JET ENGINE THRUST BEARINGS

By

L. W. Winn
R. H. Badgley

MECHANICAL TECHNOLOGY INCORPORATED
968 Albany-Shaker Road
Latham, New York 12110

Prepared For

NATIONAL AERONAUTICS AND SPACE ADMINISTRATION

NASA-Lewis Research Center
Cleveland, Ohio

Contract NAS3-11163

W. J. Anderson
Chief, Bearings Branch

D. P. Townsend
Project Manager
Bearings Branch

June 1970

FOREWORD

The work described herein was performed under NASA Contract No. NAS3-11163 with Mr. D. P. Townsend as Project Manager. The authors wish to acknowledge their thanks for the critical comments and valuable suggestions made by Mr. W. J. Anderson, Chief, Bearings Branch of NASA and Dr. D. F. Wilcock, Director, Technology Development at MTI, during the course of this work.

ABSTRACT

This report describes the analyses, design and testing of a Hybrid Boost Bearing. The hybrid boost bearing makes use of the inherent advantages of both the fluid film and rolling contact element bearings, at the same time minimizing their disadvantages and limitations. The net result is a bearing with extended life and low wear characteristics. The life extention is mainly achieved via a load sharing process.

TABLE OF CONTENTS

TABLE OF CONTENTS (continued)

TABLE OF CONTENTS (continued)

LIST OF FIGURES

LIST OF FIGURES (continued)

LIST OF FIGURES (continued)

LIST OF FIGURES (continued)

LIST OF FIGURES (continued)

LIST OF FIGURES (continued)

LIST OF FIGURES (continued)

LIST OF TABLES

1.0 SUMMARY

This report contains the results of the first stage of development of the hybrid boost bearing concept for jet engine thrust bearing applications performed under NASA Contract No. NAS3-11163. Under this contract two hybrid boost bearings were optimized and designed. One of the bearings contained a fluid film bearing with a planar surface and the other a fluid film bearing with a conical surface. The ball bearing component of the hybrid boost bearing assembly consisted in both cases of a 120 mm bore M-50 tool steel bearing supplied by NASA. The fluid film bearings were analyzed through the use of computer programs available at MTI. The bearing surface geometry was that of a Rayleigh shrouded pad. Four pads were used per bearing. The ball bearings were analyzed using the A. B. Jones Rolling Element Bearing Computer Program, also available at MTI. Upon completion of the analysis and design, the conical bearing was selected for testing and evaluation.

Tests of the hybrid boost bearing containing the conical fluid film bearing component were performed over a wide range of speeds and temperatures. The maximum DN value to which the bearings were subjected was 1.2 million. The maximum oil temperature was 300 F (149 C) and the maximum externally applied thrust loading was 3,000 pounds (13,350 n). In general, the hybrid boost bearing operated successfully over the test range of speeds, loads, and oil temperatures.

Analyzing the results, some shortcomings have been noted with regard to the applicability, of the particular hybrid boost bearing tested, to jet engines. The power loss and flow requirements of the fluid film bearing were high for an airborne gas turbine engine application. Furthermore, whereas the calculated and tested load carrying capacity of the fluid film bearing component were in good agreement at relatively low fluid film shear stresses, the load carrying capacity at high shear stresses fell considerably below the predicted value. These discrepancies appear to be due to non-isothermal behavior of the oil film and inadequately accurate analytical treatment of the transition region between laminar and turbulent flow.

The results of the testing indicate that in order to improve the applicability potential of the hybrid boost bearing to airborne jet engines, further work

must be done on the fluid film bearing to (a) reduce its power loss, (b) reduce its flow requirements, and (c) improve its load carrying capability at high shear stresses. Specific recommendations with regard to the required improvements are made in this report.

2.0 INTRODUCTION

Modern jet engines require highly reliable systems for rotor supports. Continuous increases in operating speeds, loads and temperatures impose severe limitations on the bearing reliability and life. One of the most critically stressed components particularly subject to life limitation is the main thrust bearing. The bore size of this bearing is usually determined by rotor stiffness requirements. In order to accommodate the required thrust loads rolling elements of appreciable size are employed. This is an acceptable solution as long as the speeds remain low. At high speeds a point is reached in the bearing size beyond which the centrifugal forces due to the orbiting motion of the balls become the major factors limiting life. To avoid increase in bearing size, two or more bearings are often used in tandem. To assure adequate load sharing in tandem arrangements requires extremely fine tolerances; even under the most favorable circumstances one bearing normally carries the bulk of the load and thus becomes a limiting item. These problems and limitations are increased by the effects of modern lubricants on bearing life (particularly when the lubricant is exposed to gradual decomposition or major changes in its properties), by exposure of the bearing materials to high temperature during operation and by the effects of manufacturing finishes and tolerances.

The search for solutions to the problems mentioned above has been conducted for years. New ideas have been generated most of which center around improved cleaner steels, and the reduction in Hertzian stresses through closer conformity and/or compliance and through the use of hollow rolling elements. The reduction of these ideas to practice requires the formation of a new base of empirical knowledge. Such a process in turn calls for many years of lengthy, meticulous and costly investigations.

In contrast to the above mentioned approaches, the bearing concept discussed in this report utilizes the existing state-of-the-art in ball bearing technology. This concept, hereafter referred to as the Hybrid Boost Bearing, reduces Hertzian stresses, occurring in the rolling element bearing during operation, through the sharing of the bearing load between a fluid film bearing and a

ball bearing. Reductions in Hertz stress, in turn, substantially increase the ball bearing fatigue life. This is an established fact requiring no further confirmation.

The employment of a rolling element bearing in parallel with a fluid film bearing results also in the elimination of contact between the stationary and rotating surfaces of the fluid film bearing at start and stopping conditions. This greatly reduces the possibility of wear and may if properly designed lead to the elimination of fluid film bearing material compatibility requirements.

The hybrid boost bearing, as discussed in this report, thus makes use of the inherent advantages of both the fluid film and rolling element bearings, at the same time minimizing their disadvantages and limitations. The net result is a bearing with a greatly extended life and low wear characteristics. Because of the bearings' dual nature (fluid film and ball bearing in one assembly) the engineering information gained during this developmental stage can be easily applied to the extension of fluid film bearing as well as ball bearing design technology.

The work performed within the scope of the NAS3-11163 contract was initially composed of three tasks, i.e.,

Task I - Bearing and Test Rig Design

The task consisted primarily of the analytical evaluation and design of two hybrid boost bearing concepts — of planar, and conical face types. Analyses were performed over the full range of test conditions specified by NASA for the individual fluid film and ball bearing components. The results were then combined to produce the hybrid boost bearing performance curves. This task included also the design of the test head, instrumentation, and spindle required for the general test set up, thermal maps and calculations of thermo-elastic and mechanical deformations of the critical bearing parts.

Task II - Fabrication of Bearing and Test Rig

The selection of one bearing design (the conical type) was performed on

the basis of comparison of the available design data, and the bearing design was fabricated for test and evaluation. This task also included the procurement and calibration of the required instrumentation as well as the fabrication of the spindle.

Task III - Testing

The hybrid boost bearing was assembled and tested over a wide range of operating conditions (speed 4,000 to 10,000 rpm, load 500 to 3,000 lbs., and oil temperature 100 to 300 F). Test data was accumulated also on the performance of the ball bearing and fluid film bearing components over the full, specified range of conditions. The data was then reduced and analyzed.

An additional task (Task IV) was included in this work as a result of extension of the analytical scope of this program, brought about by the need for a better definition of the fluid film bearing behavior in the transition region between laminar and turbulent flow. The work in this task was performed by Dr. V. N. Constantinescu (visiting scientist - Institute of Fluid Mechanics of the Romanian Academy, Bucharest, Romania), Dr. C.H.T. Pan (MTI) and Mr. F. Hsing (MTI). The results are described in Appendix A to this report. A detailed description and discussion of the work performed within the scope of this program is given in the following sections.

3.0 HYBRID BOOST BEARING DESIGN

3.1 Analysis of Bearing

The design of a hybrid boost bearing involves a number of interrelated tasks. First, the fluid film bearing must be designed and optimized, and its load-deflection characteristics determined. Next, the load-deflection characteristics of the selected rolling contact bearing must be established and possibly altered to improve its interaction with the fluid film bearing. Finally, these two bearings must be combined into an overall hybrid boost design which achieves proper thrust load distribution between the two bearings and which contains adequate fail-safe provisions. This design sequence is described in more detail in the following sections.

The design point for hybrid boost bearing optimization was chosen to be representative of the cruise condition of a hypothetical medium size jet engine. The following conditions were assumed to be prevalent at cruise:

Speed - 10,000 rpm
Oil Temperature - 300°F (149°C)
Oil Supply Pressure - 50 psig (34.3×10^4 Newtons/m^2)
Thrust Load - 3000 lbs. (13,400 Newtons)
Shaft Size - 4.724 inch (120 mm)
Lubricant - MIL-L-7808 Oil

The ball bearing was supplied by NASA. This bearing also served as a guide in the selection of the overall fluid film bearing dimensions. The criterion employed here was that the total volume occupied by the hybrid boost bearing should not exceed the volume occupied by two tandem mounted ball bearings each similar in size to the selected ball bearing.

3.1.1 Fluid Film Bearing Component

In a jet engine application, where reasonably high shaft rotational speeds prevail, the oil supply system can be counted upon to deliver about 50 psig (39.3×10^4 Newtons/m^2) at the entrance to the fluid film bearing under normal engine operating conditions. In such a case,

the bearing type to be employed should take advantage, not only of the hydrostatic, but also of the hydrodynamic means available for producing load support capability. Hence, the fluid film bearing should be of the hybrid type.

There are several different fluid film thrust bearing types which can be considered for this hybrid role. The tilting-pad design, well suited for stable high speed operation and very commonly used in fluid film thrust bearings, must be ruled out because of the space required for the pivot and leveling mechanisms and the difficulty of transferring the inlet pressure across the pivot to obtain hybrid operation.

The fixed, tapered land design is more suitable than the pivoted-pad configuration, but it is not easily adapted to hybrid operation. A shrouded-step design, to be described in more detail in the following paragraphs, appears to offer the necessary combination of good hydrodynamic action combined with hydrostatic load support capability.

A representative section of the shrouded step thrust bearing is shown in Fig. 1. An number of pads of the general shape shown are arranged to form an annular thrust bearing surface. The step area, of length E and width L, is depressed (an amount $h_2 - h_1$) below the otherwise uniformly flat top surface of the bearing. Lubricant is admitted under pressure at the lubricant supply groove at the entrance to the step pocket. A drain may be provided as shown between each pad, although this is not essential for proper operation of the bearing. During operation, the motion of the runner drags fluid from the inlet groove across the depressed step pocket area toward the termination of the pocket at the step. The termination requires the fluid to rise over the step when it reaches the end of the pocket. This restriction causes fluid film pressure to increase along the pocket, such that it reaches a maximum at the step and decreases over the end land. The side lands (of width b) serve to limit side flow from the bearing thereby increasing its pressure generating capability. There is, of course, an optimum width

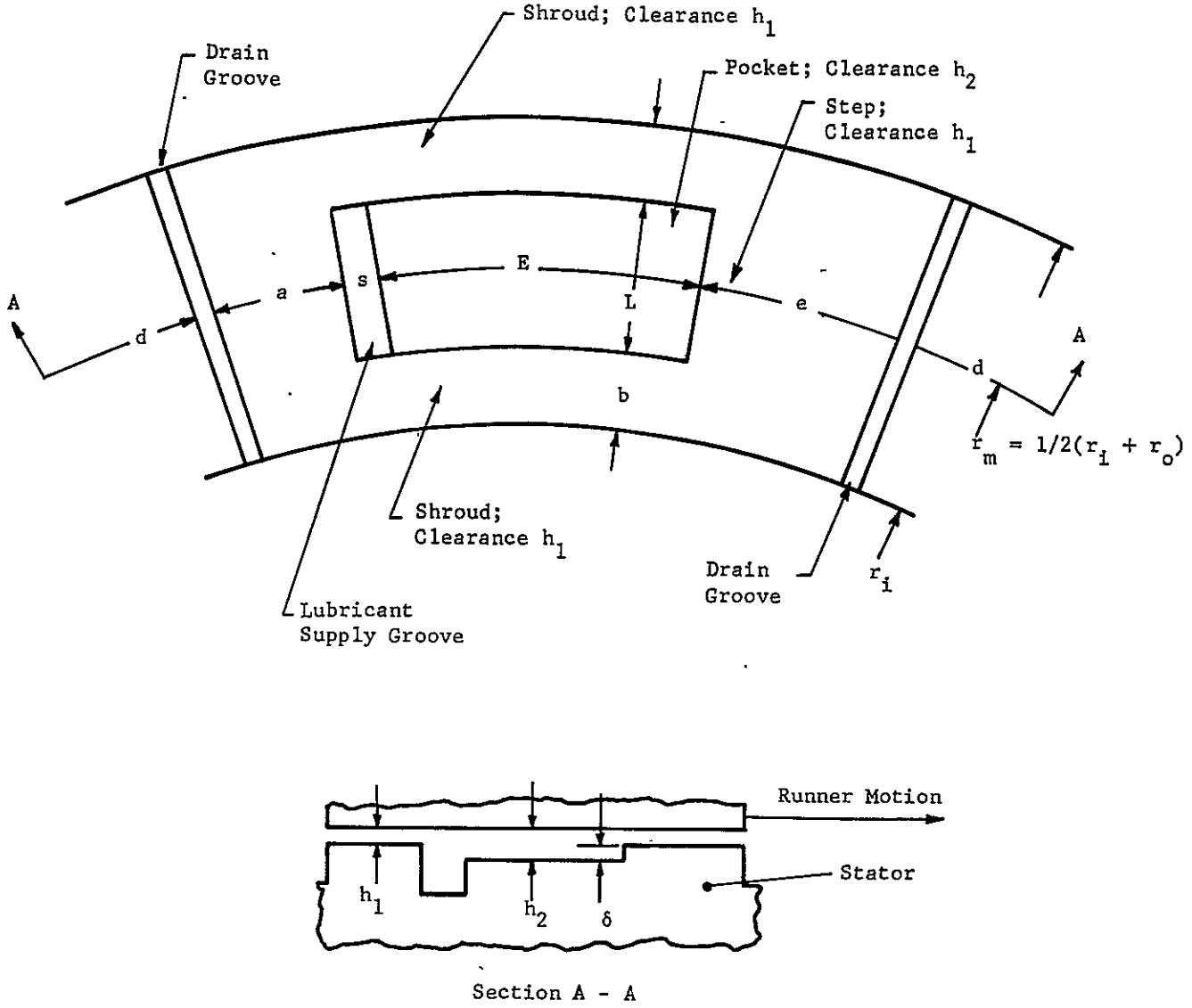

Fig. 1 Schematic of Fixed, Shrouded Step Bearing Pad. Clockwise Runner Rotation.

for the side lands, normally about 1/6 of the total bearing width (Ref. 1).

The computer program used in the following calculations, described in detail in Ref. 1, is based on an isothermal one dimensional flow analysis. Flow is assumed to be laminar between Reynolds numbers of 0 to 2000. Fully turbulent flow is assumed to develop at Reynolds numbers of 4000 and above. Between R_e of 2000 - 4000 a straight line was drawn on the G_x vs R_e curve. This was a strictly arbitrary attempt to compensate for the fluid film bearing behavior in the transition region. All analytical data presented in this report are calculated on that basis. In order to shed more light upon the bearing performance in the transition region a detailed study leading up to the development of a method for evaluation of the operational bearing characteristics in the transition region was performed. The details of this work are described in Appendix A. The developed methods for treatment of the transition region will be incorporated in fluid film bearing programs to be employed in future work.

Two shrouded step bearing configurations were given detailed consideration throughout the design phase - one planar and one of conical shape. The conical bearing was selected for fabrication and test.

3.1.1.1 Optimization of Pocket Geometry - Planar Configuration

The following procedure was followed to arrive at thrust bearing dimensions which would yield maximum load capacity.

1) Identification of Dimensions

The dimensions to be selected are identified in Fig. 1: d - drain groove width at mean radius r_m; a - front land width at mean radius r_m; s - inlet groove width at mean radius r_m; E - pocket length at mean radius r_m; e - back land width at mean radius r_m; b - side land width (both side lands); L - pocket width.

In addition, the pocket depth and operating film thickness, shown in Fig. 1, were to be selected where: h_1 - film thickness above lands; h_2 - film thickness above pockets; δ - pocket depth ($h_2 - h_1$).

2) Initial Selection of Bearing Dimensions for Optimization

Test ball bearing dimensions led to selection of the following

initial constraints on diameters: D_o = 7.00 in. (178.5 mm); D_i = 5.25 in. (133.5 mm); thus D_m = 6.125 in.(155.2mm).

From previous similar optimization studies, (Ref. 1), high load capacity at reasonably low flow rates (high W/Q ratio) is attained when $\frac{b}{L + 2b}$ = .167. To establish the required size of b and L,

R_o = 3.5 in. (89 mm)
R_i = 2.625 in. (67.3 mm)
ΔR = 2b + L = .875 in. (22.3 mm)

hence,

b = .875 (.167) = .146 in. (3.7 mm)

and

L = .583 in. (14.9 mm)

Similarly, good load capacity may be achieved when the ratio of $\frac{e}{E + e}$ is maintained at about 0.2. Considering further the need for restricting land "a" and the inlet oil groove width "s", the following dimensions were arbitrarily arrived at:

a = 0.280 (7.1 mm)
s = 0.200 (5.1 mm)
E = 3.400 (86.5 mm)
e = 0.805 (20.5 mm)

When all of the dimensions are accounted for within the specified bearing size, a 0.5 inch (12.7 mm) width remains which can then be used to provide four radial grooves of 0.125 in. (3.18 mm) width each (dimension "d").

The bearing dimensions thus established were employed in the optimization procedure of other bearing parameters (see following sections) which produced the final bearing dimensions employed in the design.

3) Pocket Depth (δ) Optimization

The operating land film thickness was assumed to be 0.002 in. (0.051 mm). The value of δ was varied between 0.002 (0.051 mm) and 0.025 in. (0.635 mm) with all other dimensions fixed, and for speed equal to 10,000 rpm, inlet pressure of 50 psig (34.3×10^4 Newtons/m^2), and lubricant temperature of 300°F (149°C) whereby $\mu = 0.21 \times 10^{-6}$ reyn = 1.44 cp). The resulting variation in total bearing thrust load (four similar pads) is shown in Fig. 2. Maximum load capacity was attained with pocket depth δ equal to 0.018 in. (0.417 mm). This value was selected for the design and is used in subsequent optimizations. Thus, $h_2/h_1 = (h_1 + \delta)h_1 = 10$ for optimum load support capability. (It should be noted here that a different value of this ratio will very likely result should the optimization be based upon stiffness.)

4) Pocket Location (Dimensions a and e) Optimization

In this study, the following bearing dimensions were used:

b = 0.146 in. (3.7 mm)
L = 0.583 in. (14.9 mm)
s = 0.200 in. (5.1 mm)
E = 3.400 in. (86.5 mm)
d = 0.125 in. (3.2 mm)
h_1 = 0.002 in. (0.051 mm)
δ = 0.018 in. (0.45 mm)

In addition,

N = 10,000 rpm
p_i = 50 psig (34.3×10^4 Newtons/m^2)
μ = 0.21×10^{-6} reyn (1.44 cp)
(MIL-L-7808 Oil at 300°F (149°C)).

Bearing Dimensions

D_o - Outer diameter = 7.0 in. (178.5 mm)
D_i - Inner diameter = 5.25 in. (133.5 mm)
E - Pocket length = 3.40 in. (86.5 mm)
L - Pocket width = 0.583 in. (14.9 mm)
a - Front land width = 0.28 in. (2.54 mm)
b - Outer and inner lands = 0.146 in. (3.7 mm)
e - Back land width = 0.8105 in. (25 mm)
s - Oil groove width = 0.20 in. (5.08 mm)
d - Drain groove width = 0.125 in. (3.18 mm)

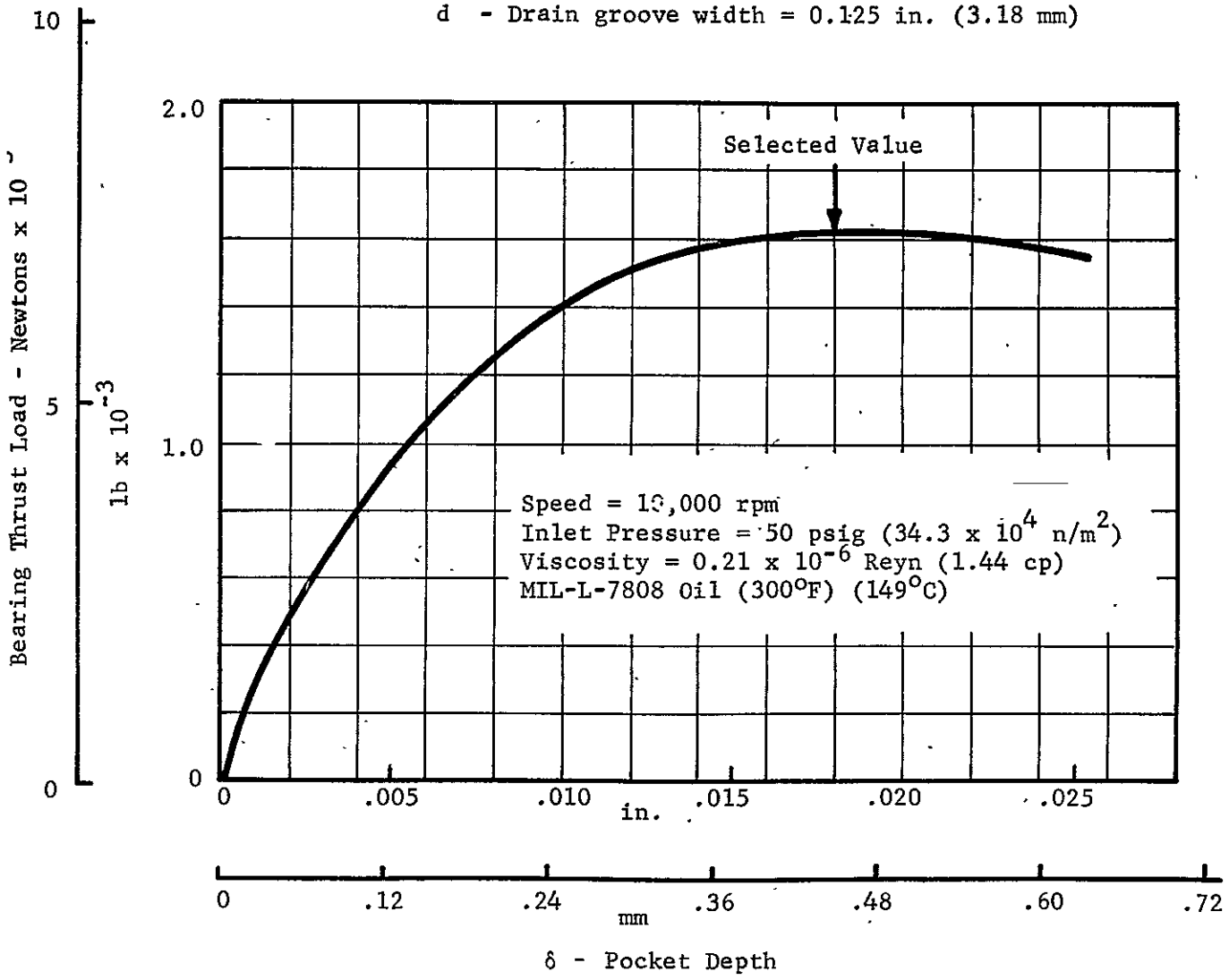

Fig. 2 Bearing Thrust Load vs. Pocket Depth for Planar Shrouded-Step Thrust Bearing

Dimensions a and e were varied such that their sum was held constant: a + e = 1.085 in. (27.5 mm). Thus, the location of a constant-length pocket was varied within the pad sector. Values of dimension "a" between 0.1 in. (2.54 mm) and 1.3 in. (33 mm) were considered, and the resulting variations in load are plotted in Fig. 3 vs. dimension "a". A value of 0.1 in. (2.54 mm) was selected for "a" in order to have as great a load capacity as possible. Although the load curve is still increasing with decrease in "a" at a = 0.1 in. (2.54 mm), it was felt that excessive flow backward over the front land might result if "a" was decreased below 0.1 in. (2.54 mm).

Thus,

$a = 0.10$ in. (2.54 mm)
$e = 0.985$ in. (25 mm))

5) Pocket Length (E) Optimization

In this study, the following bearing dimensions were specified:

$b = 0.146$ in. (3.7 mm)
$L = 0.583$ in. (14.9 mm)
$d = 0.125$ in. (3.18 mm)
$a = 0.100$ in. (2.54 mm)
$s = 0.200$ in. (5.08 mm)
$h_1 = 0.002$ in. (0.051 mm)
$\delta = 0.018$ in. (0.417 mm)

Further,

$N = 10{,}000$ rpm
$P_i = 50$ psig (34.3×10^4 Newtons/m^2)
$\mu = 0.21 \times 10^{-6}$ reyn (1.44 cp)

Dimensions E and e were varied such that their sum was held constant: E + e = 4.385 in. (111.5 mm). Thus, the length of

Bearing Dimensions

D_o - Outer diameter = 7.0 in. (178.5 mm)
D_i - Inner diameter = 5.25 in. (133.5 mm)
E - Pocket length = 3.40 in. (86.5 mm)
L - Pocket width = 0.583 in. (14.9 mm)
b - Outer and inner lands = 0.146 in. (3.7 mm)
e - Back land width = 0.985 in. (25 mm)
s - Oil groove width = 0.200 in. (5.08 mm)
d - Drain groove width = 0.125 in. (3.18 mm)
δ - Pocket depth = 0.018 in. (0.417 mm)

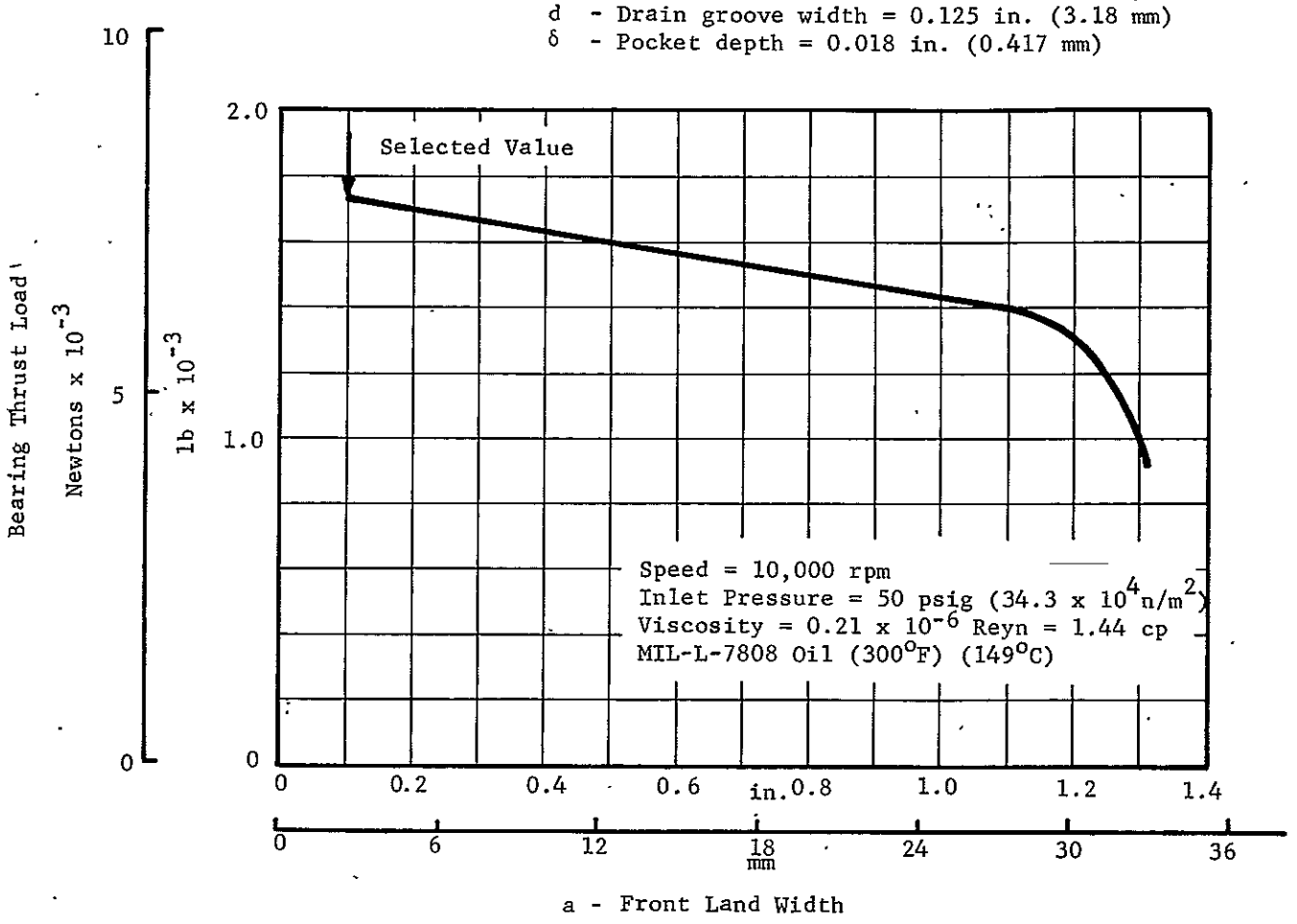

Fig. 3 Bearing Thrust Load vs. Front Land Width for Planar Shrouded-Step Thrust Bearing

a pocket with fixed inlet position was varied. Values of "E" between 2.5 in. (63.5 mm) and 4.0 in. (101.6 mm) were considered and the resulting variations in load are plotted in Fig. 4 vs. dimension "E". A value of 3.4 in. (86.5 mm) was selected for "E", and "e" was thus 0.985 in. (25 mm).

6) Modification of Outer Diameter to Obtain Greater Load Capacity

Variations in outer diameter were considered in order to increase the thrust load capacity to 2500 lbs (11000 Newtons). Values were taken from 7.0 in. (178.5 mm) to 7.5 in (191.2 mm) by 0.05 in. (1.27 mm). Dimensions δ, d, a, S, and E were held constant, with the slight increases in mean circumference being added to dimension e. Dimensions b and L were scaled upward, maintaining the same proportions previously selected. The resulting load variations are plotted vs. D_o in Fig. 5. The selected value of D_o is 7.4 in. (187.96 mm). The resulting dimensions for the final design are as follows:

d = 0.125 in. (3.175 mm)
a = 0.100 in. (2.54 mm)
s = 0.200 in. (5.08 mm)
E = 3.400 in. (8.636 mm)
e = 1.135 in. (28.829 mm)
b = 0.179 in. (4.547 mm)
L = 0.714 in. (18.136 mm)
h_1 = 0.002 in. (.051 mm)
δ = 0.018 in. (.457 mm)

Subsequent calculations indicated that the oil inlet groove width (dimension "s") should be at least 0.30 in. (7.62 mm) to limit the lubricant pressure drop to about 5 psi (3.43×10^4 Newtons/m^2) across the orifice. Thus, s = 0.30 in. (7.62 mm) and E = 3.30 in. (83.82 mm).

Resulting Dimensions

D_o - Outer diameter = 7.0 in. (178.5 mm))
D_i - Inner diameter = 5.25 in. (133.5 mm)
L - Pocket width = 0.583 in. (14.9 mm)
a - Front land width = 0.1 in. (2.54 mm)
b - Outer and inner land = 0.146 in. (3.7 mm)
e - Back land width = 0.985 in. (25 mm)
s - Oil groove width = 0.20 in. (5.08 mm)
d - Drain groove width = 0.125 in. (3.18 mm)
δ - Pocket depth = 0.018 in. (0.417 mm)

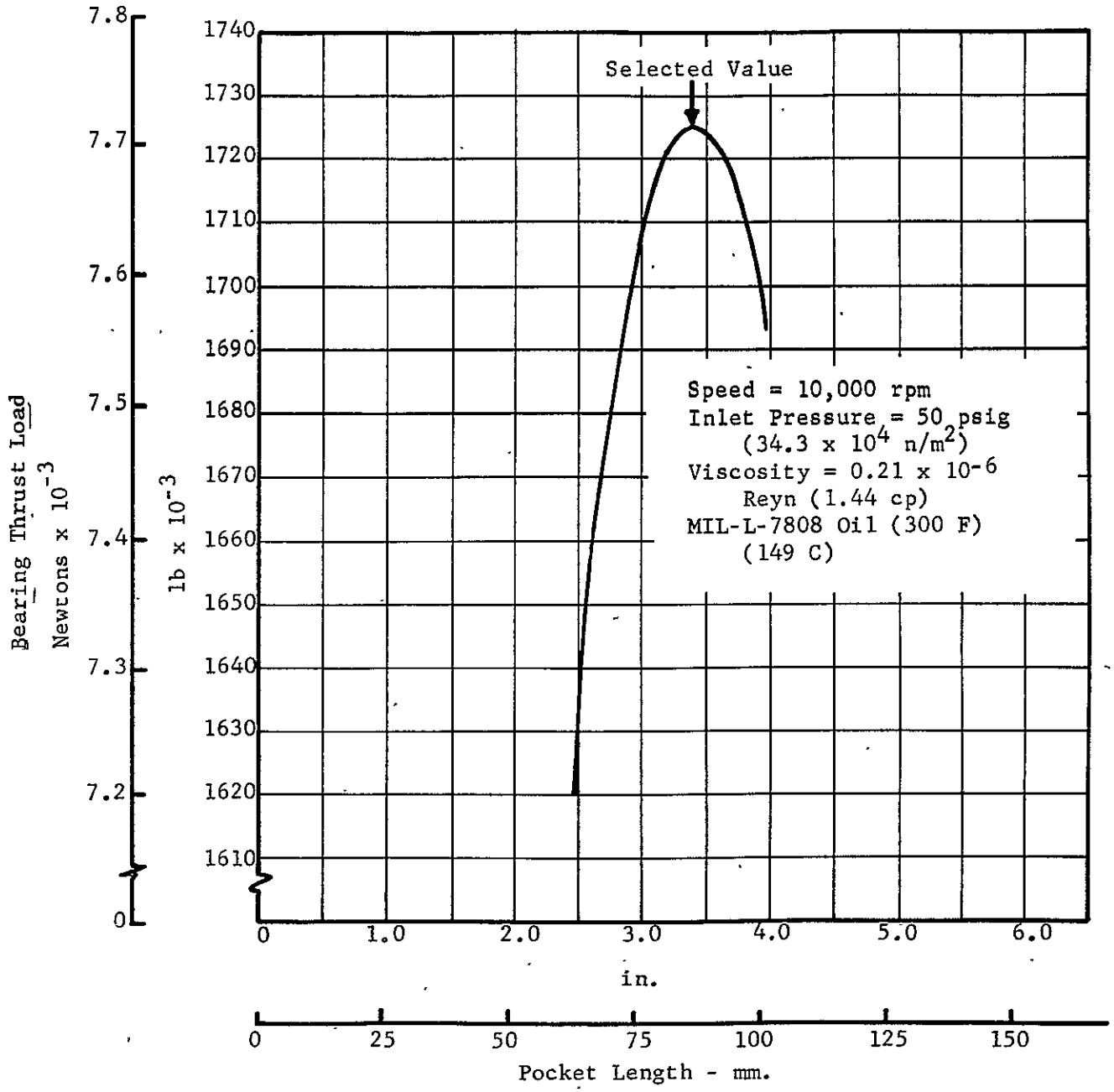

Fig. 4 Optimization of Pocket Length for Planar Thrust Bearing

Bearing Dimensions

(All dimensions based on a D_o of 7.4 inches)

D_i - Inner diameter = 5.25 in. (133.5 mm)
E - Pocket length = 3.40 in. (86.5 mm)
L - Pocket width = 0.714 in. (18.15 mm)
a - Front land width = 0.11 in. (2.79 mm)
b - Outer and inner lands = 0.179 in. (4.55 mm)
e - Back land width = 1.135 in. (28.8 mm)
s - Oil groove width = 0.20 in. (5.08 mm)
d - Drain groove width = 0.018 in. (3.18 mm)
δ - Pocket depth = 0.018 in. (0.417 mm)

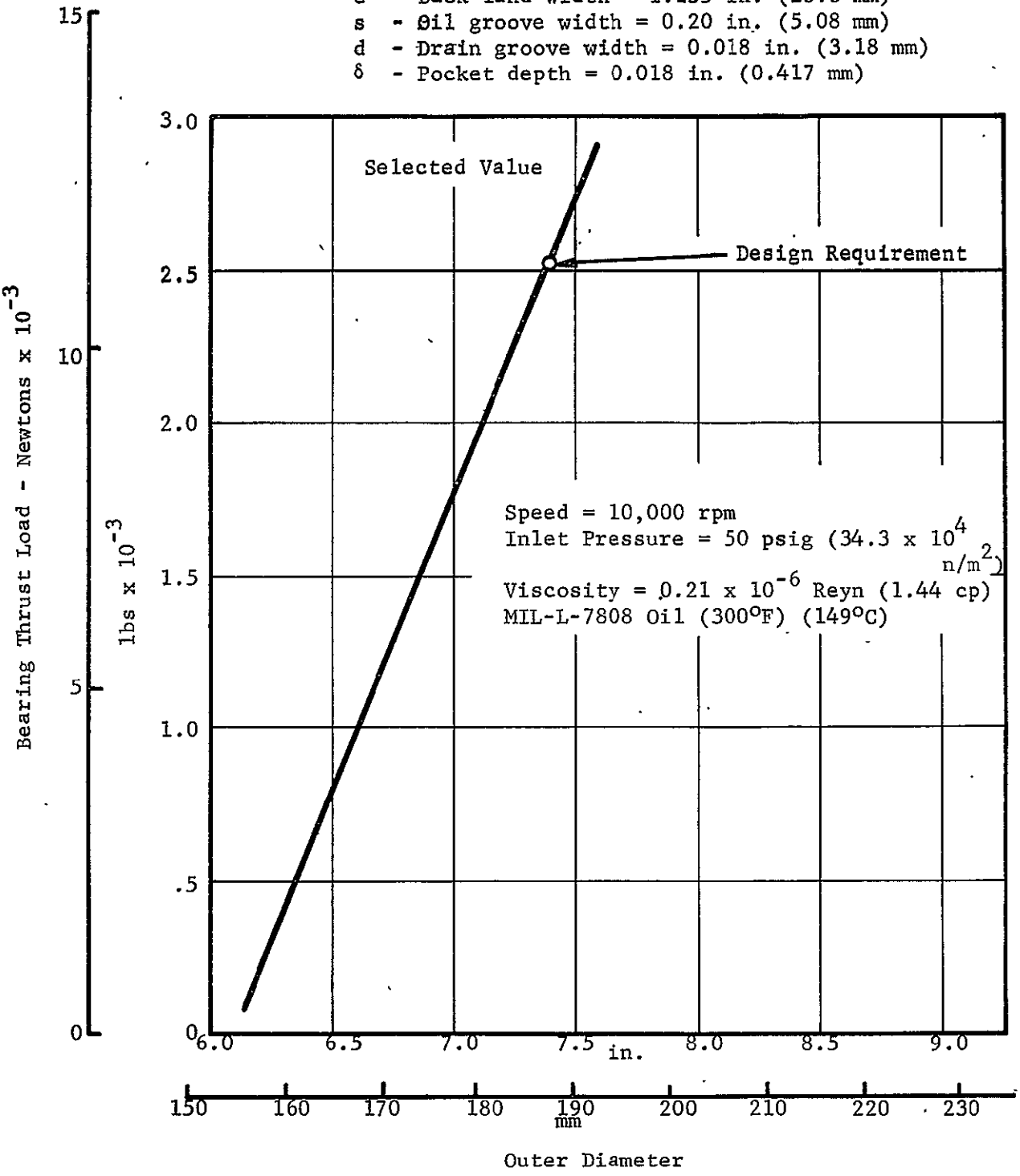

Fig. 5 Bearing Thrust Load vs. Outer Diameter for Planar Shrouded-Step Thrust Bearing

MTI-9165

3.1.1.2 Production Calculations for Optimized Planar Thrust Bearing

With the resulting optimized geometry, the detailed dimensions of which are shown in Fig. 5, production computer runs were made to determine the performance of the bearing at other viscosities, speeds, lubricant supply pressures, and film thicknesses. The ranges of these variables are as follows:

Viscosity:	0.21×10^{-6} (1.44), 0.456×10^{-6} (3.14), 1.45×10^{-6} (10.0) reyns (cp)
Speed:	4,000, 6,000, 8,000, and 10,000 rpm
Supply Pressure:	10 (6.92) 25 (17.1), and 50 (34.3) psig (Newtons/$m^2 \times 10^{-4}$)
Film Thickness:	0.0005 (.0127), 0.001 (.0254), 0.002 (.0508), 0.003 (.0762) and 0.004 (.1016) in. (mm)

Results of these calculations are presented in Figs. 6 through 14. The optimized load vs. film thickness characteristics of the planar thrust bearing were combined with the load vs. deflection ball bearing curve at various conditions. The resulting load-sharing capabilities of the combination are shown and discussed in later sections.

3.1.1.3 Axial Load vs. Axial Film Thickness for Conical Thrust Bearing

Fig. 15 shows the relationship between axial thrust load capacity and axial film thickness for cone angles between 0 and 60 degrees (the planar bearing cone angle is 0 degrees). The following dimensions and operating characteristics were assumed for these calculations:

- Projected dimensions corresponding to the planar thrust bearing with 7.4 in. (187.96 mm) outer diameter
- Runner Speed = 10,000 rpm
- Viscosity = 0.21×10^{-6} reyn (1.44 cp) (MIL-L-7808 at 300° F (149° C)
- Inlet Pressure = 50 psig (34.3×10^4 Newtons/m^2)

It should be pointed out that the assumption of constant projected dimensions such as land, pocket width, and outer diameter, together with increasing cone angles results in increasing values of bearing

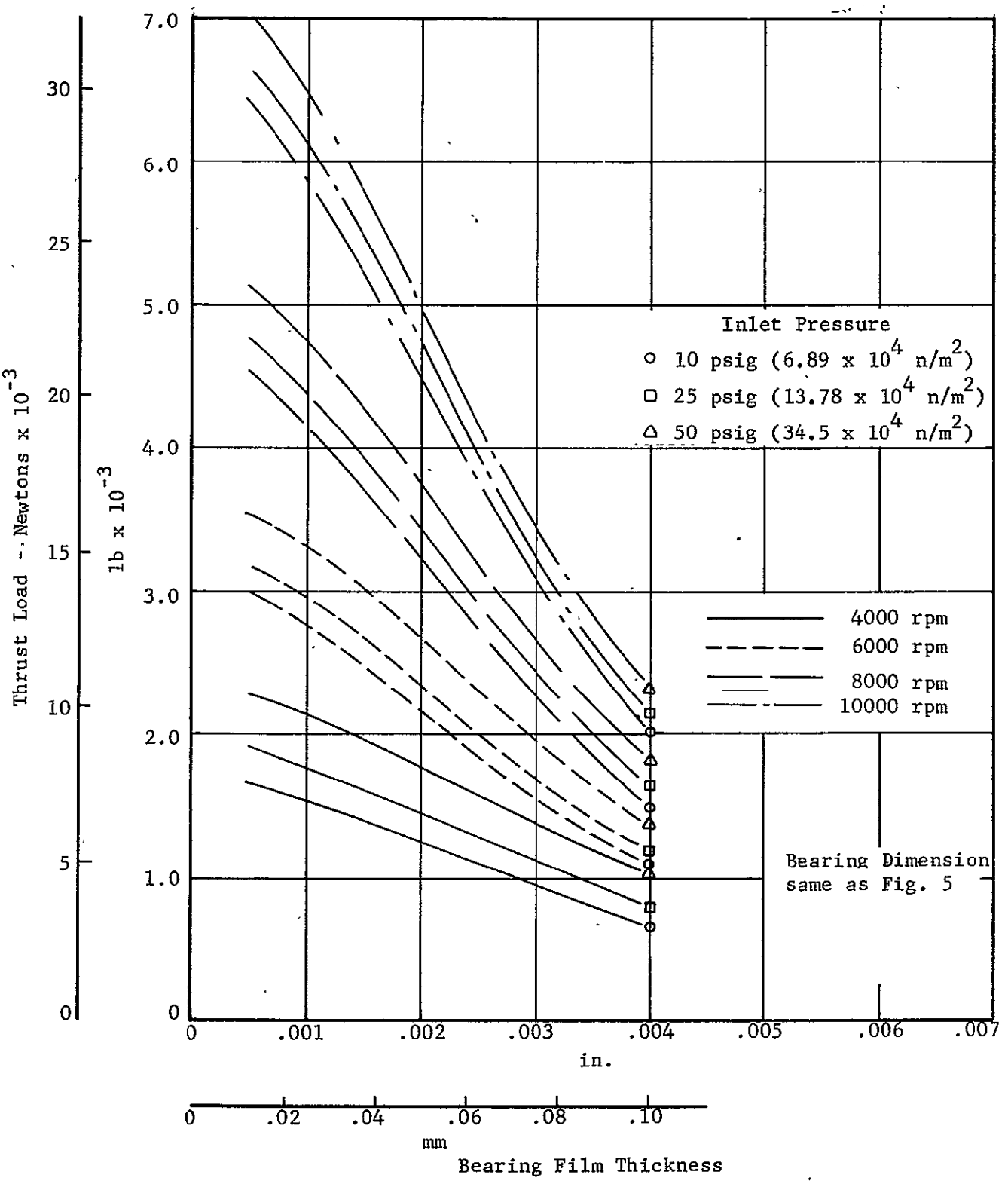

Fig. 6 Thrust Load vs. Film Thickness for Optimized Planar Fluid-Film Thrust Bearing at 100F (37.8C).

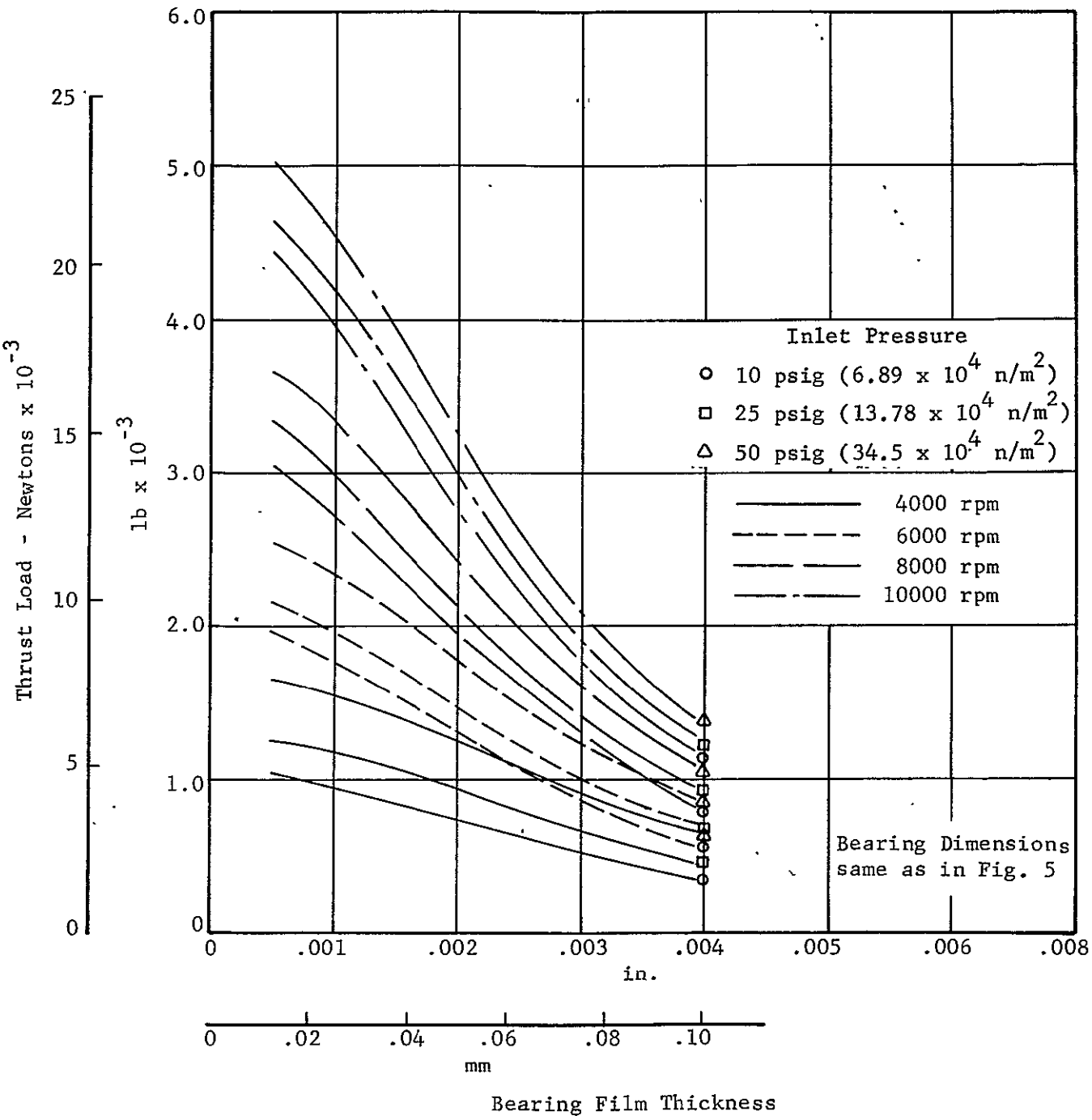

Fig. 7 Thrust Load vs. Film Thickness for Optimized Planar Fluid-Film Thrust Bearing at 200F (93.3C).

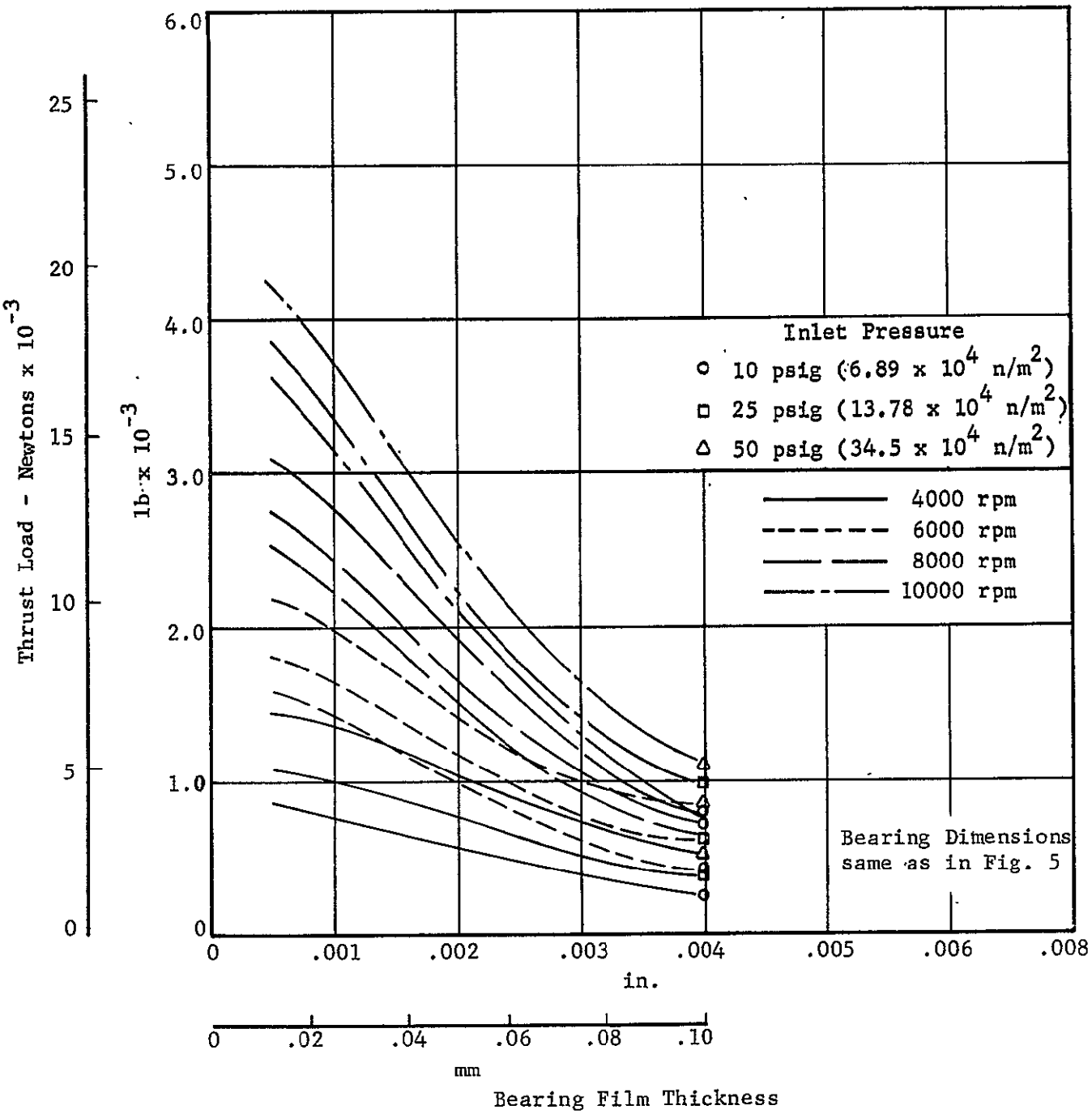

Fig. 8 Thrust Load vs. Film Thickness for Optimized Planar Fluid-Film Thrust Bearing at 300F (148.9C).

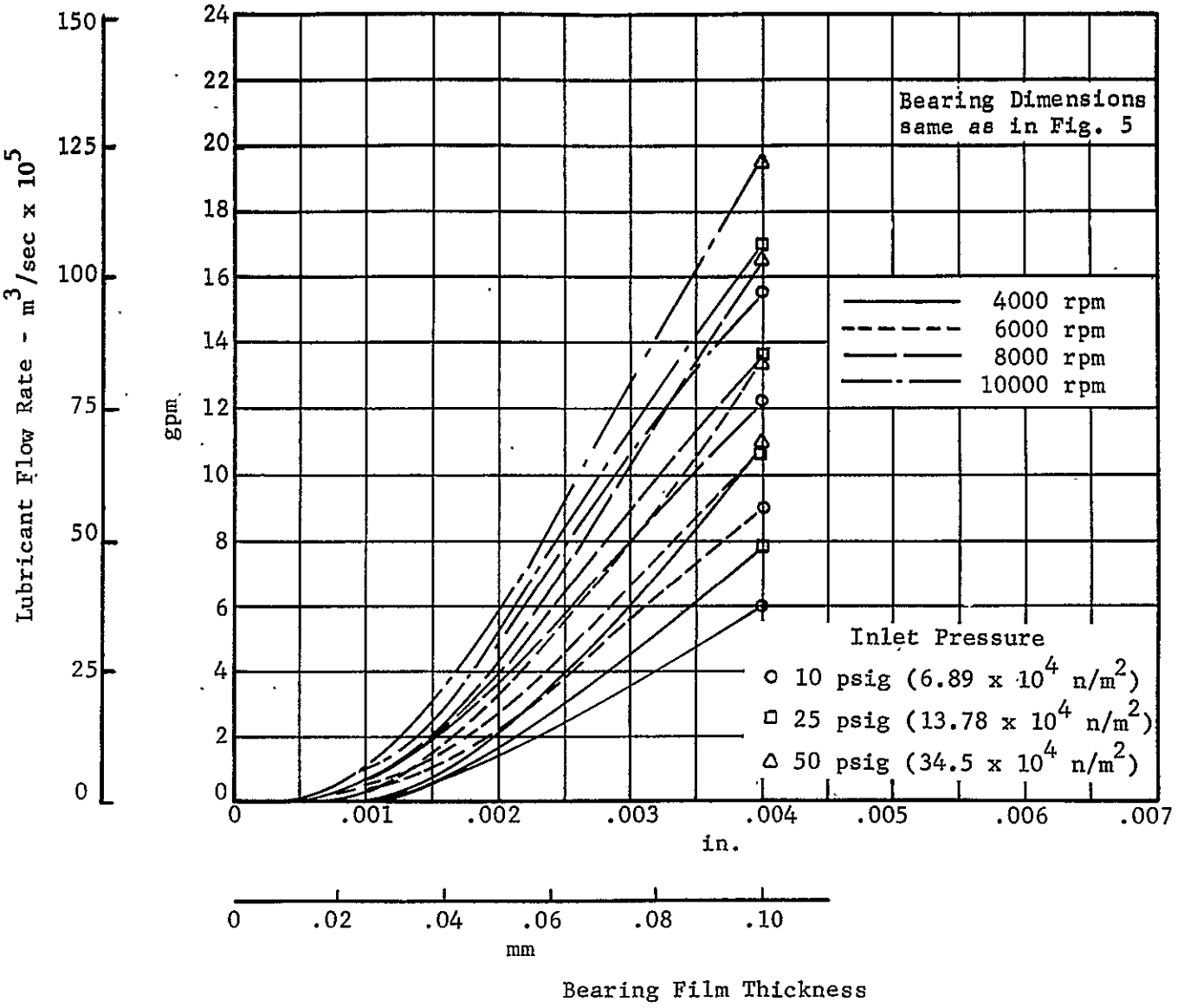

Fig. 9 Lubricant Flow Rate vs. Film Thickness for Optimized Planar Fluid-Film Thrust Bearing. at 100F (37.8C).

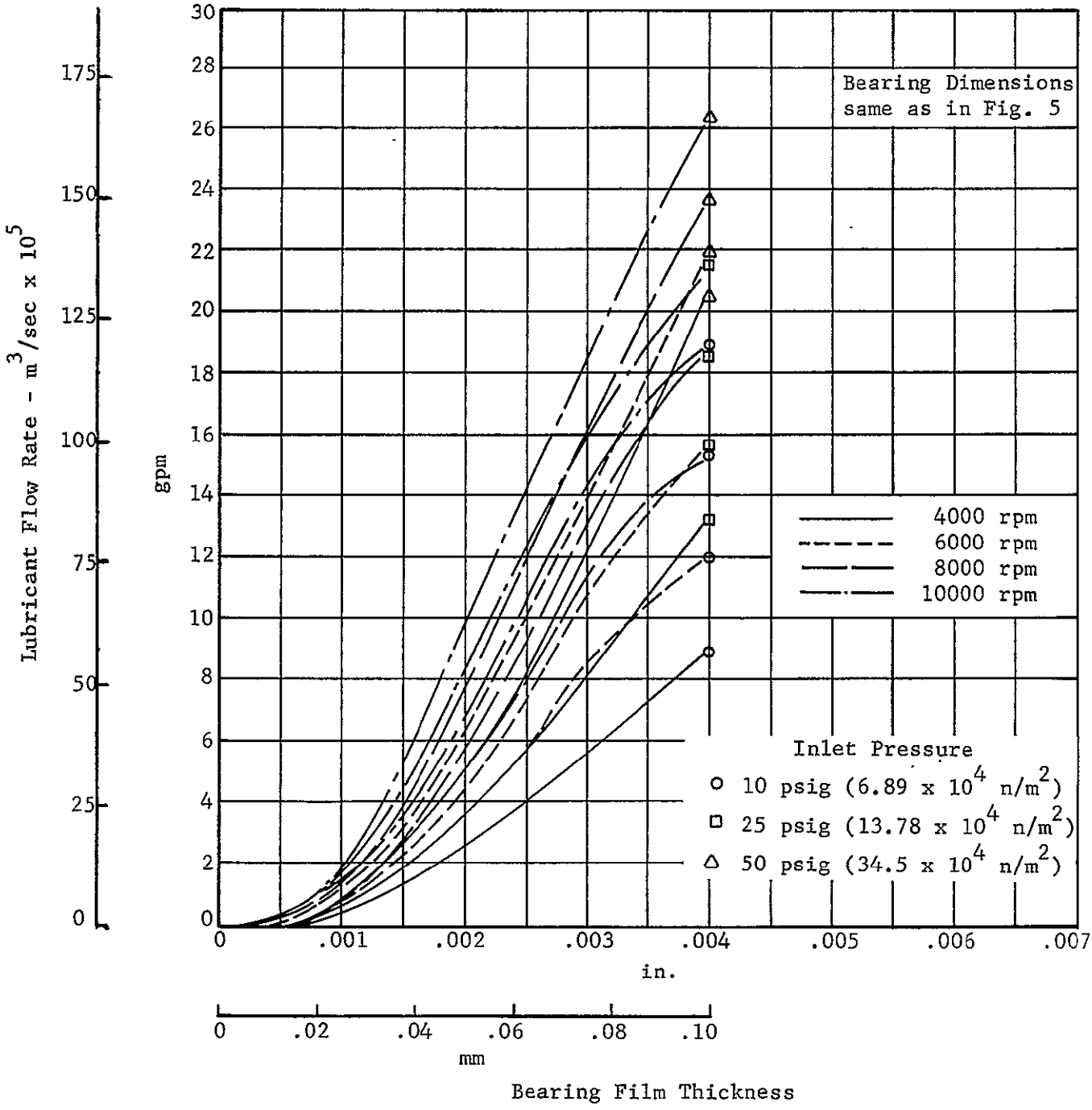

Fig. 10 Lubricant Flow Rate vs. Film Thickness for Optimized Planar Fluid-Film Thrust Bearing at 200F (93.3C).

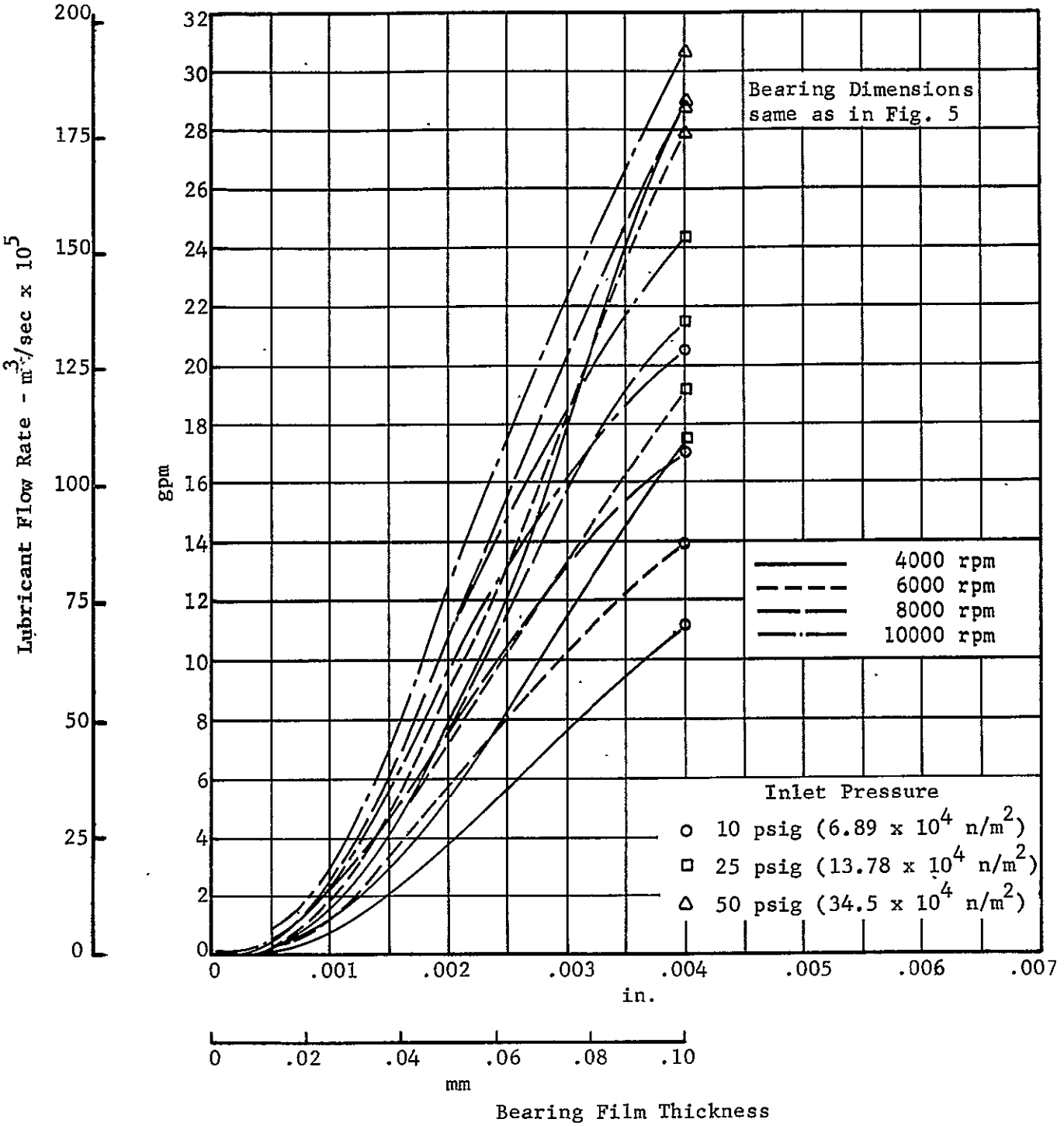

Fig. 11 Lubricant Flow Rate vs. Film Thickness for Optimized Planar Fluid-Film Thrust Bearing at 300F (148.9C).

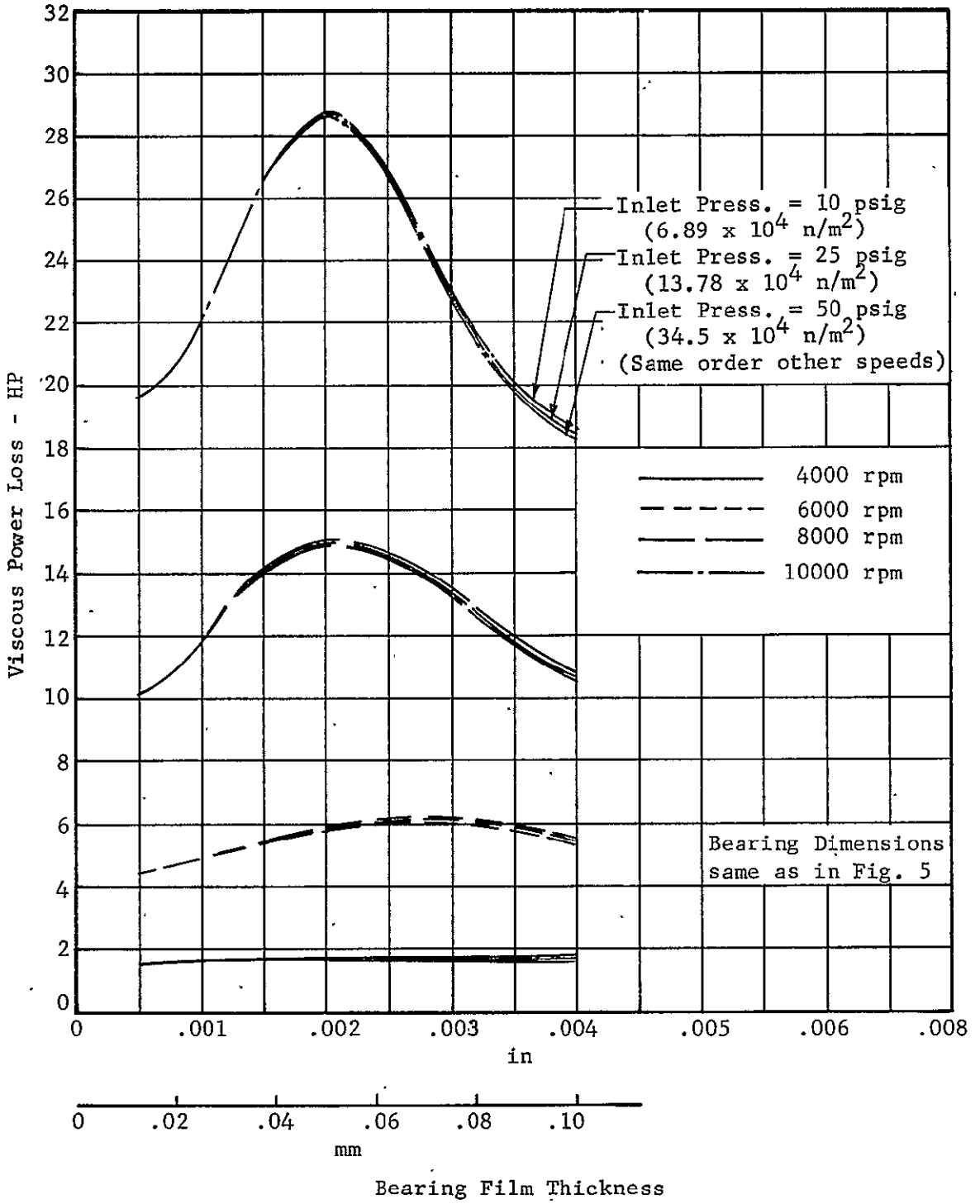

Fig. 12 Viscous Power Loss vs. Film Thickness for Optimized Planar Fluid-Film Thrust Bearing. at 100F (37.8C).

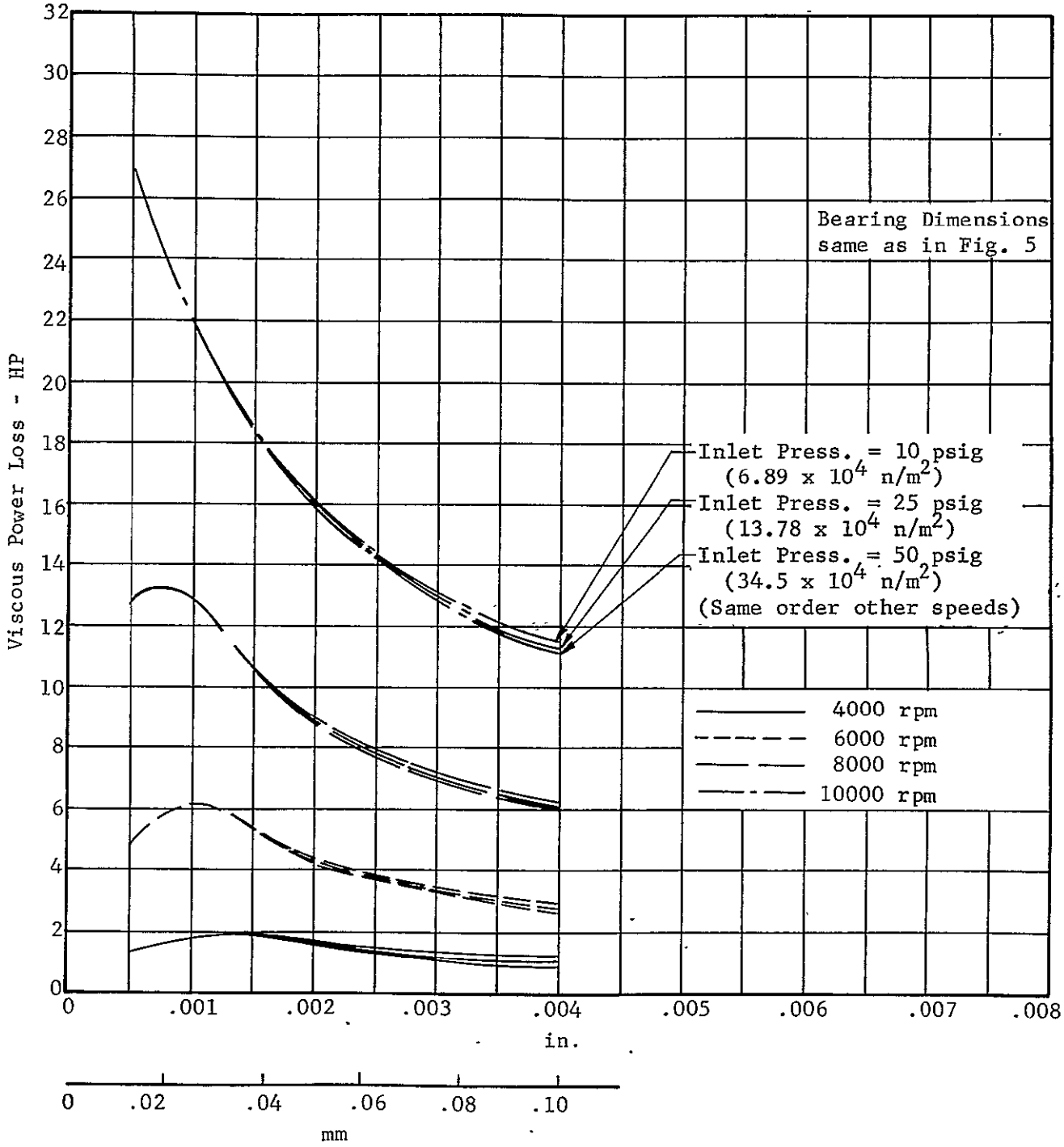

Fig. 13 Viscous Power Loss vs. Film Thickness for Optimized Planar Fluid-Film Thrust Bearing at 200F (93.3C).

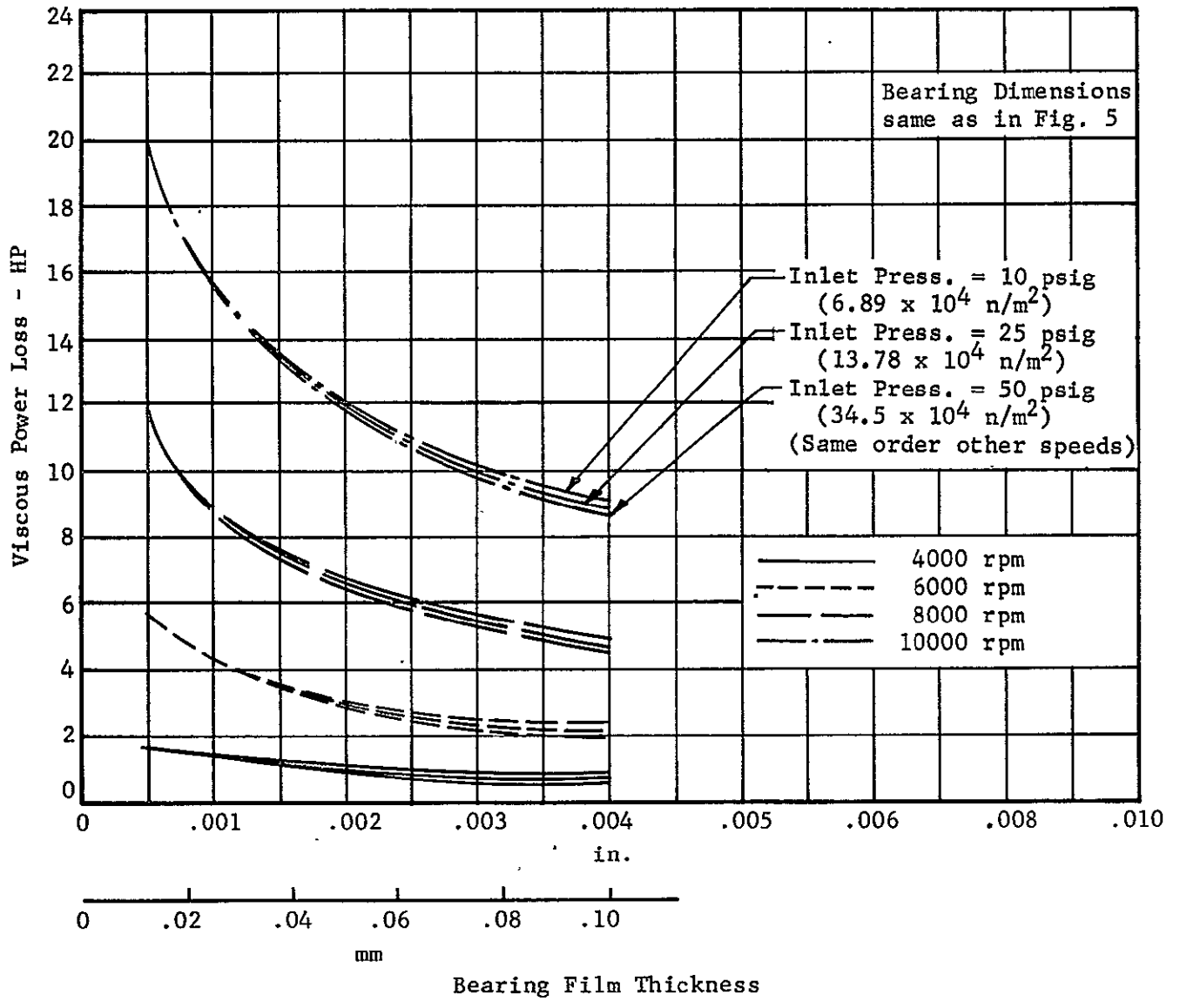

Fig. 14 Viscous Power Loss vs. Film Thickness for Optimized Planar Fluid-Film Thrust Bearing at 300F (148.9C).

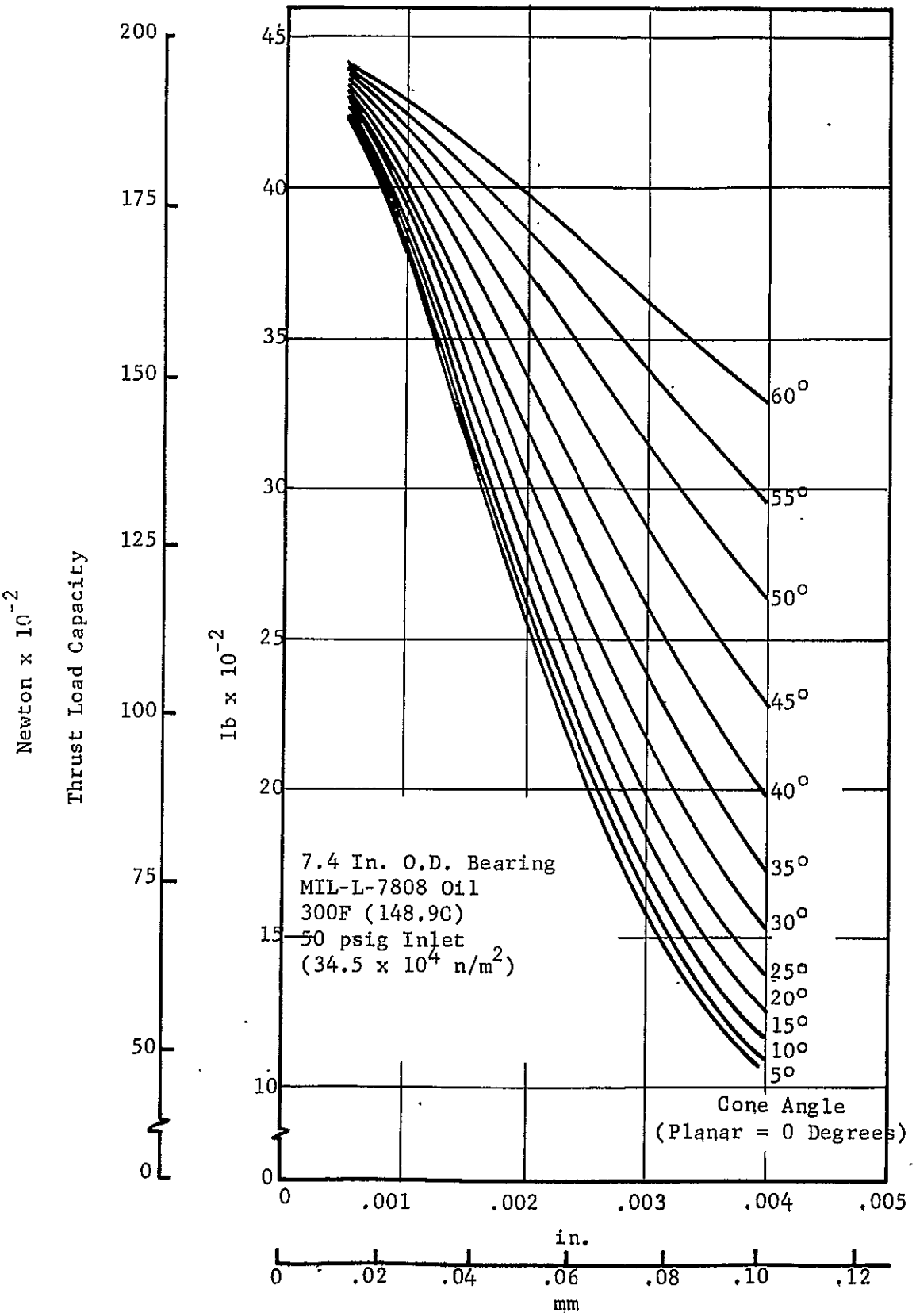

Fig. 15 Conical Fluid-Film Bearing Thrust Load vs. Axial Film Thickness at 300 F (148.9C) for Various Cone Angles.

width, measured along the cone, as well as decreasing perpendicular film thicknesses for a given axial film thickness.

Thus, while the resulting axial load component increases with cone angle over the range of cone angles considered, the bearing begins to occupy more and more axial space within the test vehicle. It is to be expected, on the other hand, that axial load support capacity would reach a maximum value and then decrease as cone angle increased if the conical bearing length was held constant and outer diameter allowed to decrease. This variation, however, would also be subject to increasingly unacceptable small perpendicular film thicknesses for cone angles greater than 45 degrees. The working angle of 45 degrees was selected based upon this fact, and the desire to limit the bearing axial length requirement in the test vehicle to approximately the same as that of the test ball bearing.

For the conical bearing with 45 degree cone angle with the operating conditions indicated in Fig. 15, and with an axial film thickness of 0.0035 in. (.089 mm), the lubricant flow rate is 16.0 gal/min (10.1×10^{-4} m^3/sec), the power loss is 16.1 hp, and the resulting lubricant temperature rise is $10.1^{\circ}F$ ($5.6^{\circ}C$).

3.1.1.4 Calculations for 45 Degree Conical Bearing with Same Gross Dimensions as Final Planar Bearing

With a cone angle of 45 degrees, production computer runs were made to determine the performance of the conical bearing at other viscosities, speeds, lubricant supply pressures, and film thicknesses. The ranges covered for these quantities are the same as those for the planar production runs. The results of the calculations performed at 10,000 rpm for lubricant inlet conditions of 300° F ($149^{\circ}C$) and 50 psig (34.3×10^4 Newtons/m^2) are presented in Figs. 16 through 18.

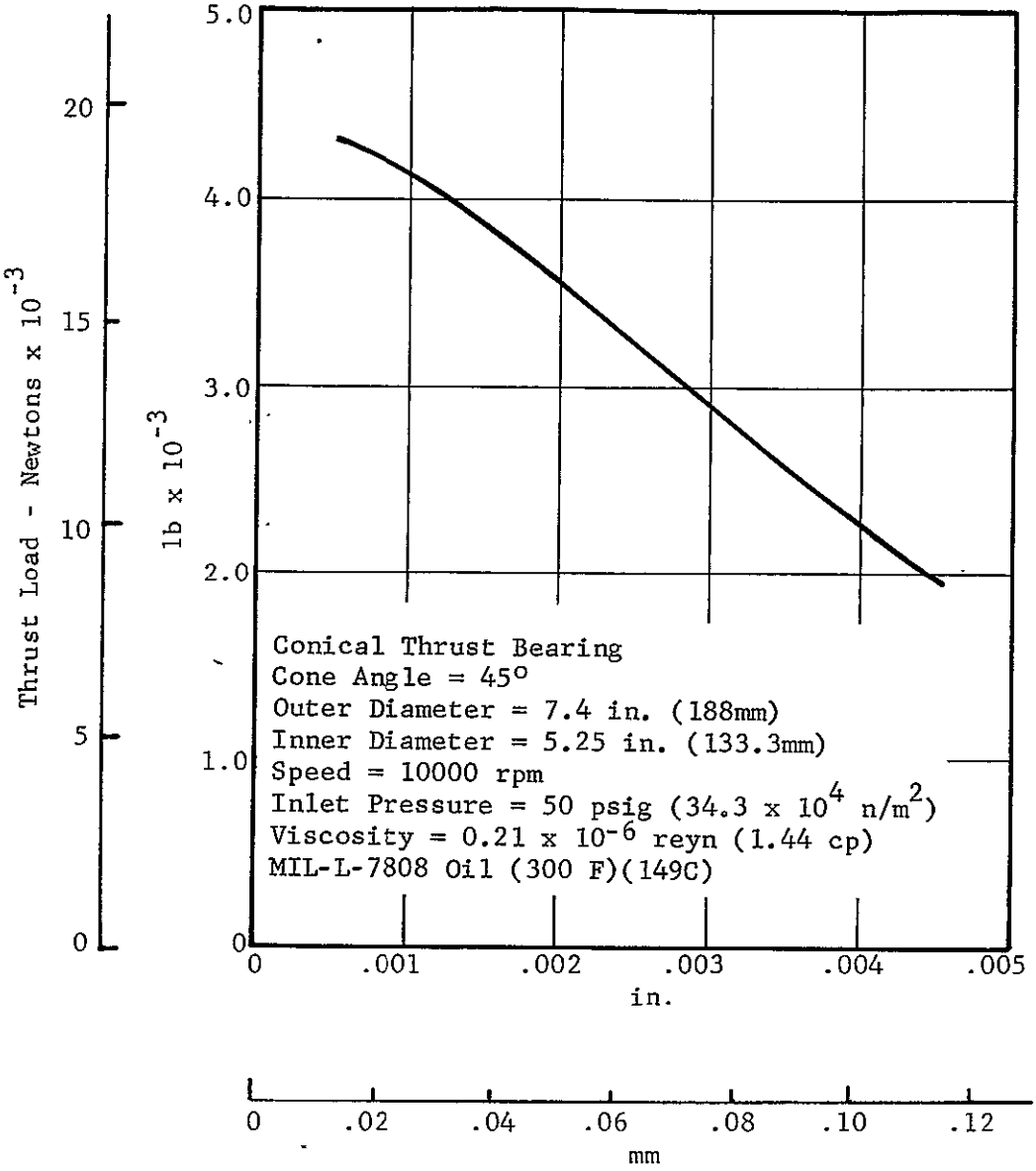

Fig. 16 Bearing Thrust Load vs. Axial Film Thickness for Conical Shrouded-Step Thrust Bearing with 7.4 in. (188 mm) Outer Diameter

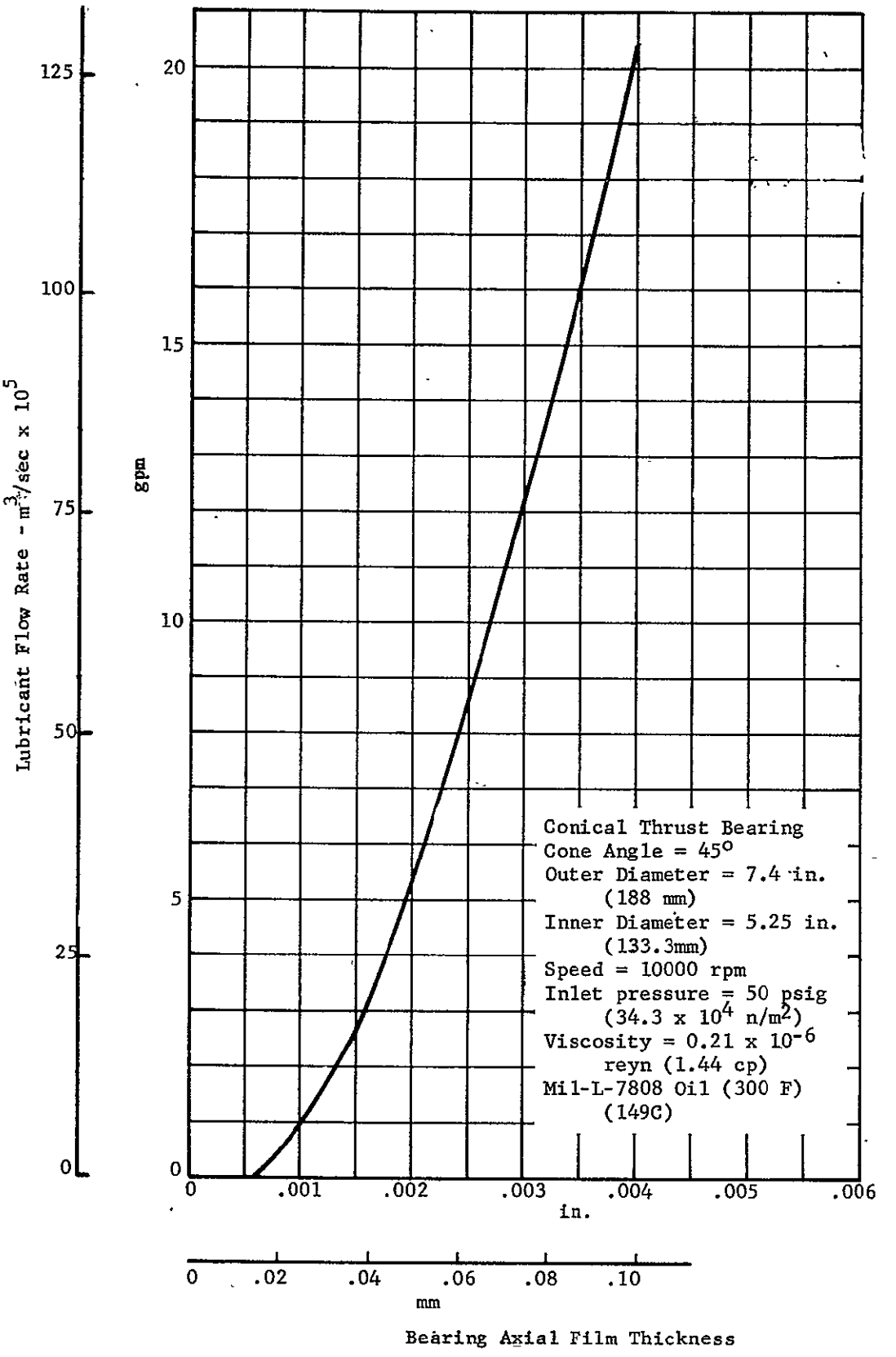

Fig. 17 Lubricant Flow Rate vs. Axial Film Thickness for Conical Shrouded-Step Thrust Bearing with 7.4 in. (188 mm) Outer Diameter.

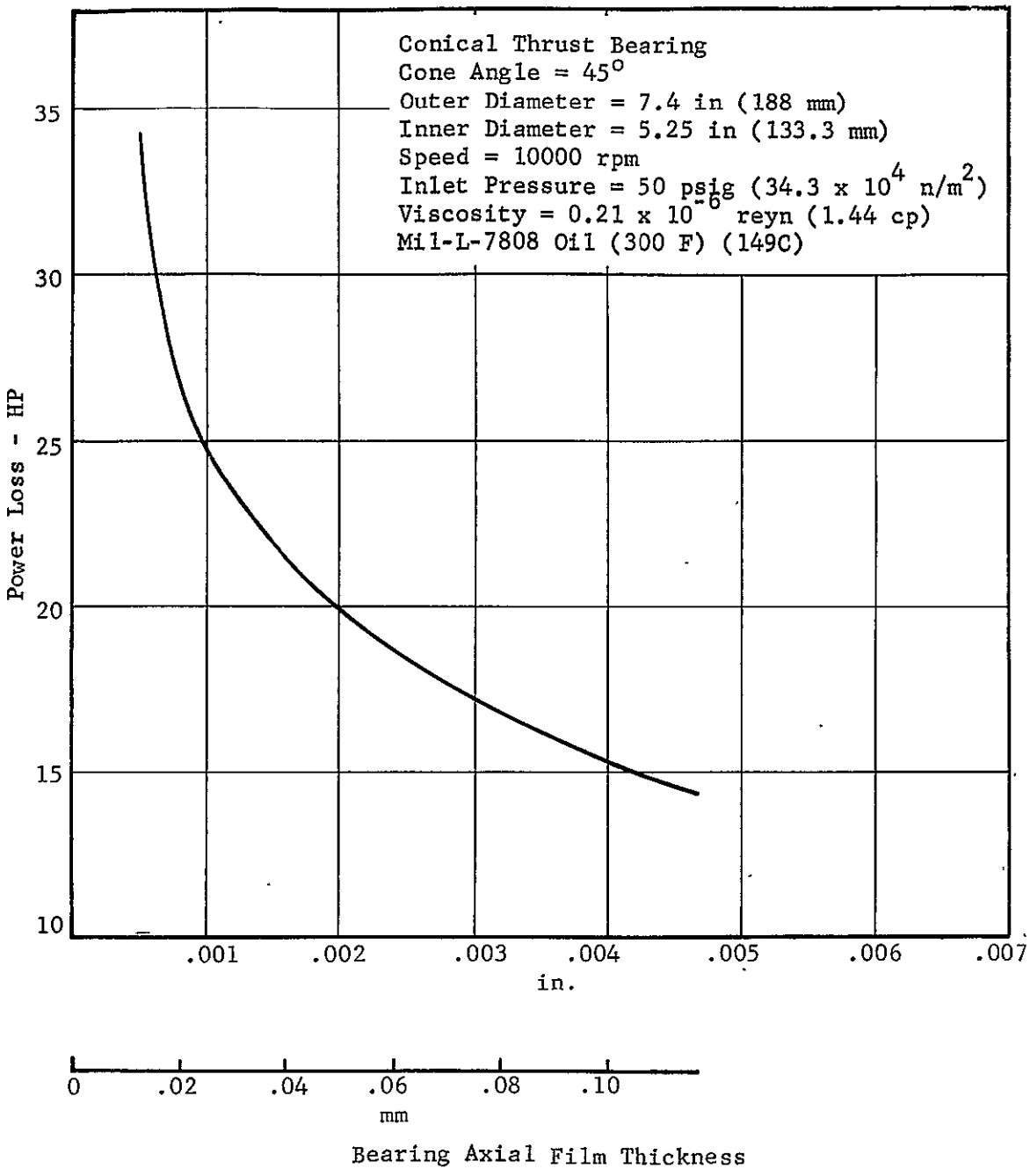

Fig. 18. Power Loss vs. Axial Film Thickness for Conical Shrouded-Step Thrust Bearing with 7.4 in. (188mm) Outer Diameter.

The calculated load vs. film thickness characteristics of the 45 degree conical thrust bearing were combined with the load vs. deflection ball bearing curve at 10,000 rpm. The resulting load-sharing capabilities of the combination are shown and discussed in later sections.

3.1.1.5 Conical Bearing Calculations with Outer Diameter of 7.0 Inches (178.5 mm)

Calculations for the conical bearing with 7.4 inch (187.96 mm) outer diameter predict axial load support capacity in excess of that desired. Unfortunately, operation at the relatively low loads and large diameters required for evaluation of hybrid bearing performance will be at relatively high values of film thickness. The calculated flow rates for these conditions are excessive as are the power losses. In an attempt to achieve lower flow rates and lower power loss, at the expense of load capacity, smaller outer diameters were investigated. The inner diameter was left unchanged in each case, and other diameters were reduced in proportion. Circumferentially measure quantities, such as pocket length, were also reduced in direct proportion. The results of the calculations at an outer diameter of 7.0 in. (177.7 mm) are shown in Figs. 19, 20 and 21 for 10,000 rpm, 50 psig (34.3×10^4 Newtons/m^2) and 300°F (149°C).

3.1.1.6 Production Conical Bearing Calculations with Outer Diameter of 6.5 Inches (165.1 mm)

Calculations similar to those described in the preceding section (3.1.1.4) were also performed at an outer diameter of 6.5 in. (165.1 mm). Proportional reductions in diameters and circumferential dimensions were again made. Results of these calculations are shown in Figs. 22 through 30, for the full temperature and pressure range. Figure 22 also provides a list of the pertinent bearing dimensions.

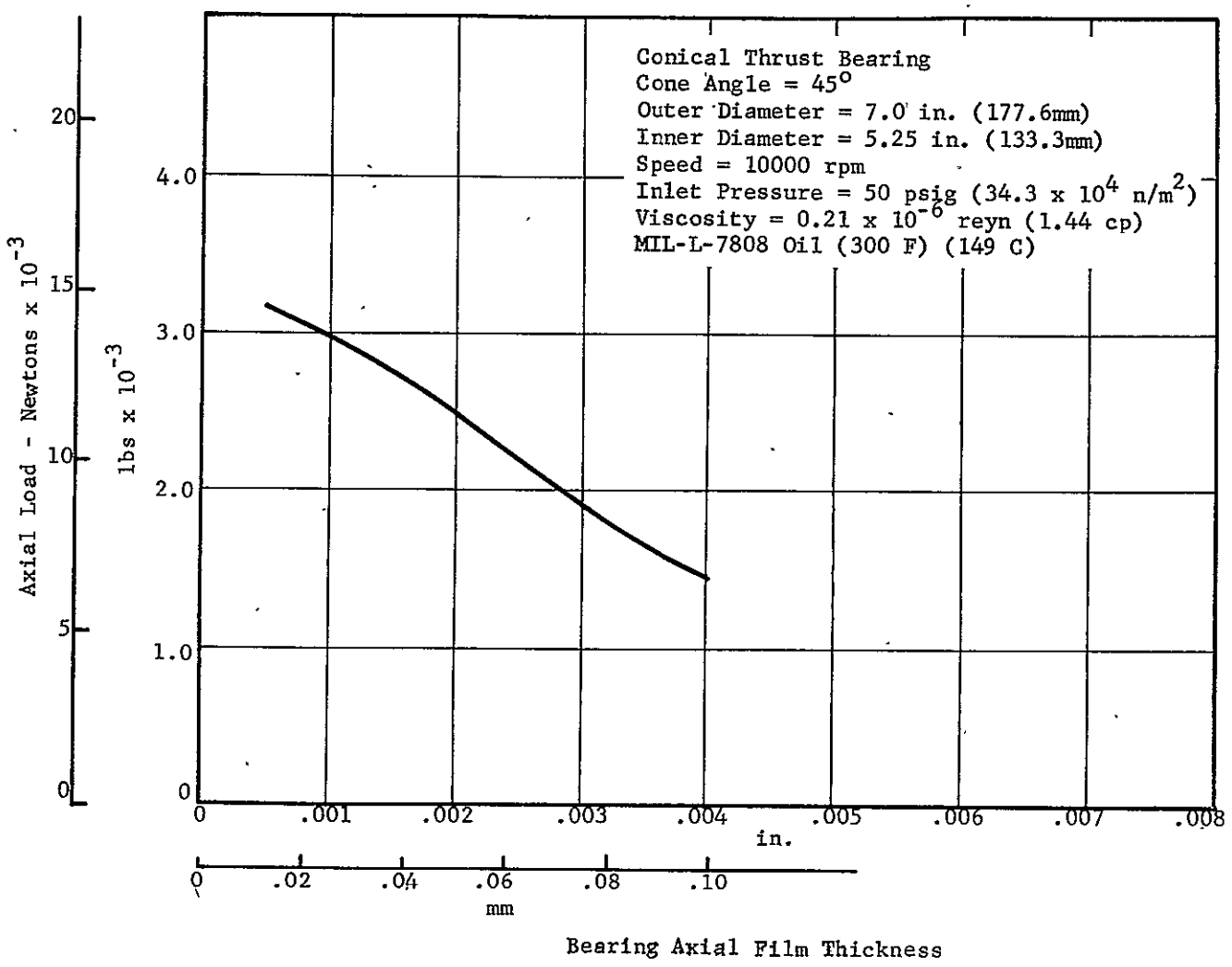

Fig. 19 Bearing Thrust Load vs. Axial Film Thickness for Conical Shrouded-Step Thrust Bearing with 7.0 in. (177.7mm) Outer Diameter.

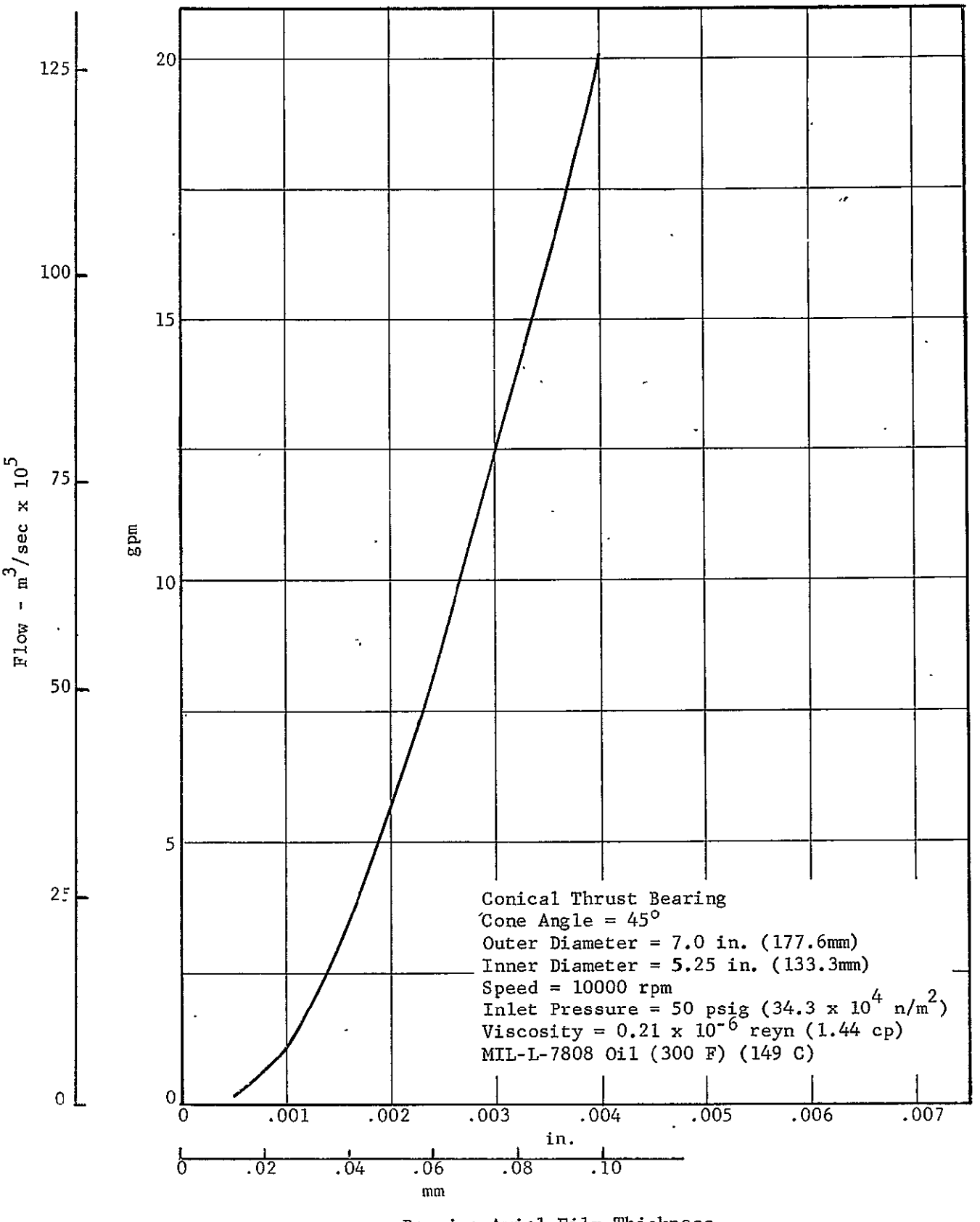

Fig. 20 Lubricant Flow Rate vs. Axial Film Thickness for Conical Shrouded-Step Thrust Bearing with 7.0 in. (177.7 mm) Outer Diameter

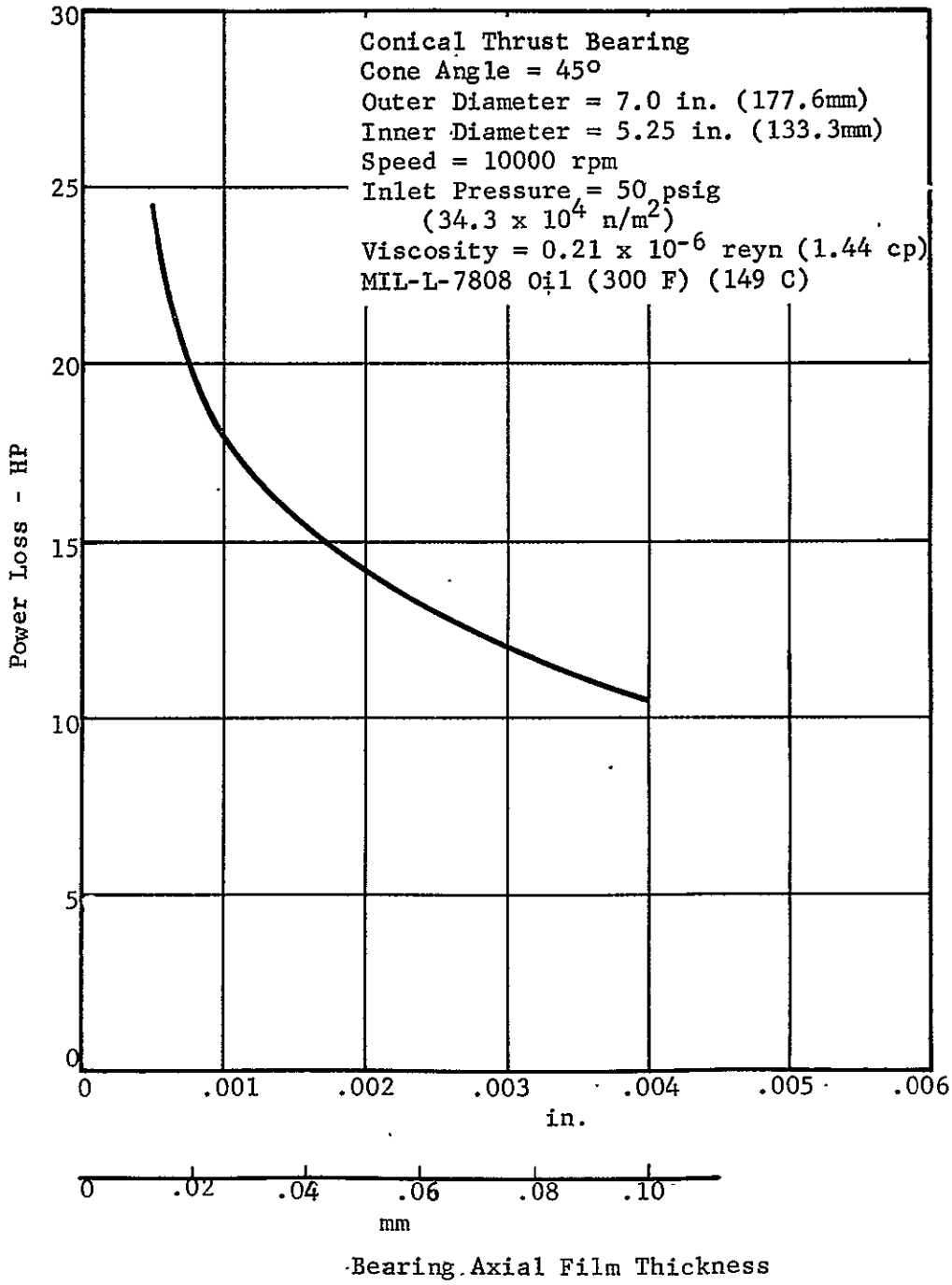

Fig. 21 Power Loss vs. Axial Film Thickness for Conical Shrouded-Step Thrust Bearing with 7.0 in. (177.7 mm) Outer Diameter.

MTI-9171

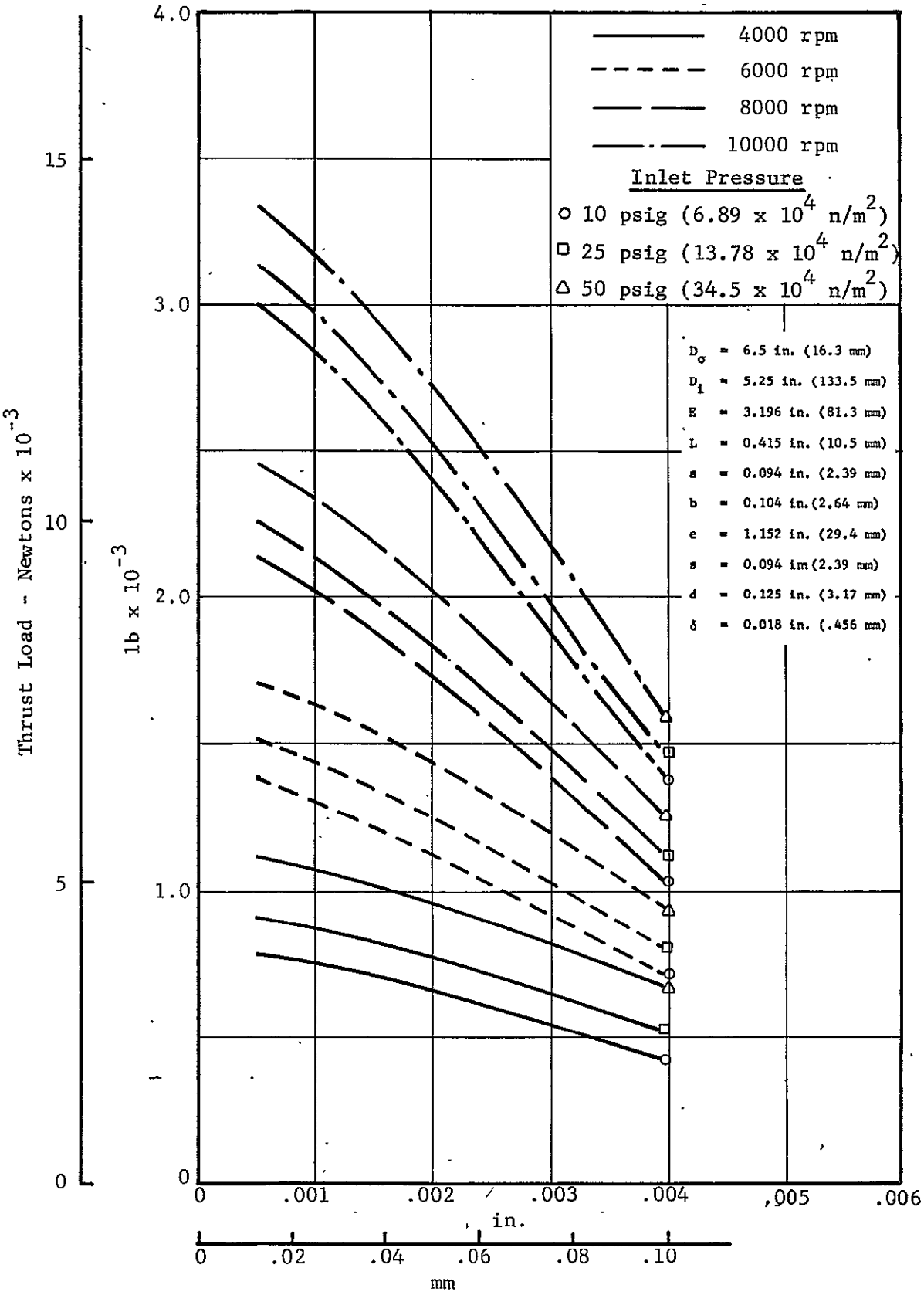

Fig. 22 Thrust Load vs. Film Thickness for 45 Degree Conical Fluid-Film Thrust Bearing with 6.5 in. (165 mm) Outer Diameter at 100°F (37.8°C)

MTI-9172

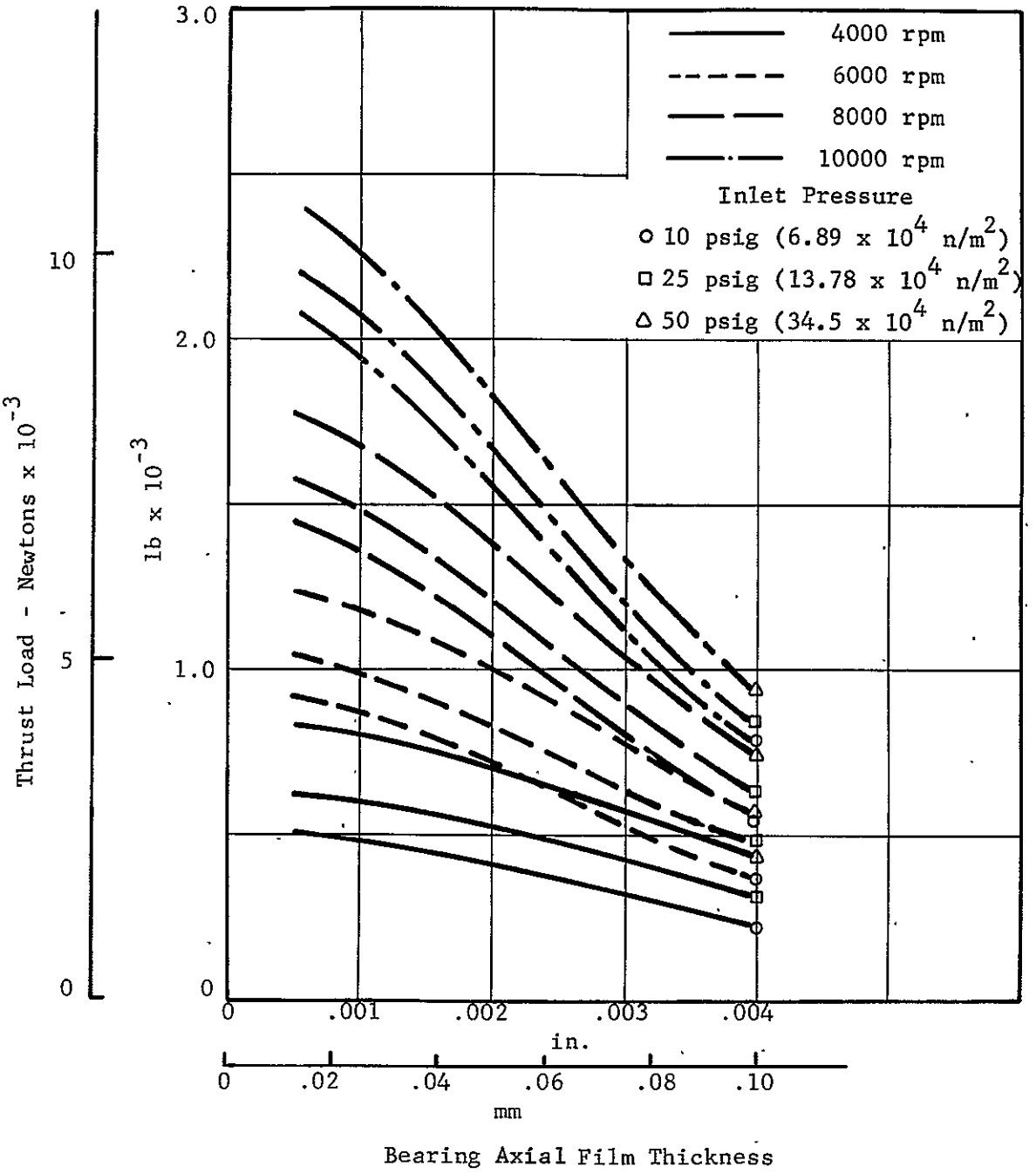

Fig. 23 Thrust Load vs. Film Thickness for 45 Degree Conical Fluid-Film Thrust Bearing with 6.5 in. (165 mm) Outer Diameter at 200°F (93.3°C)

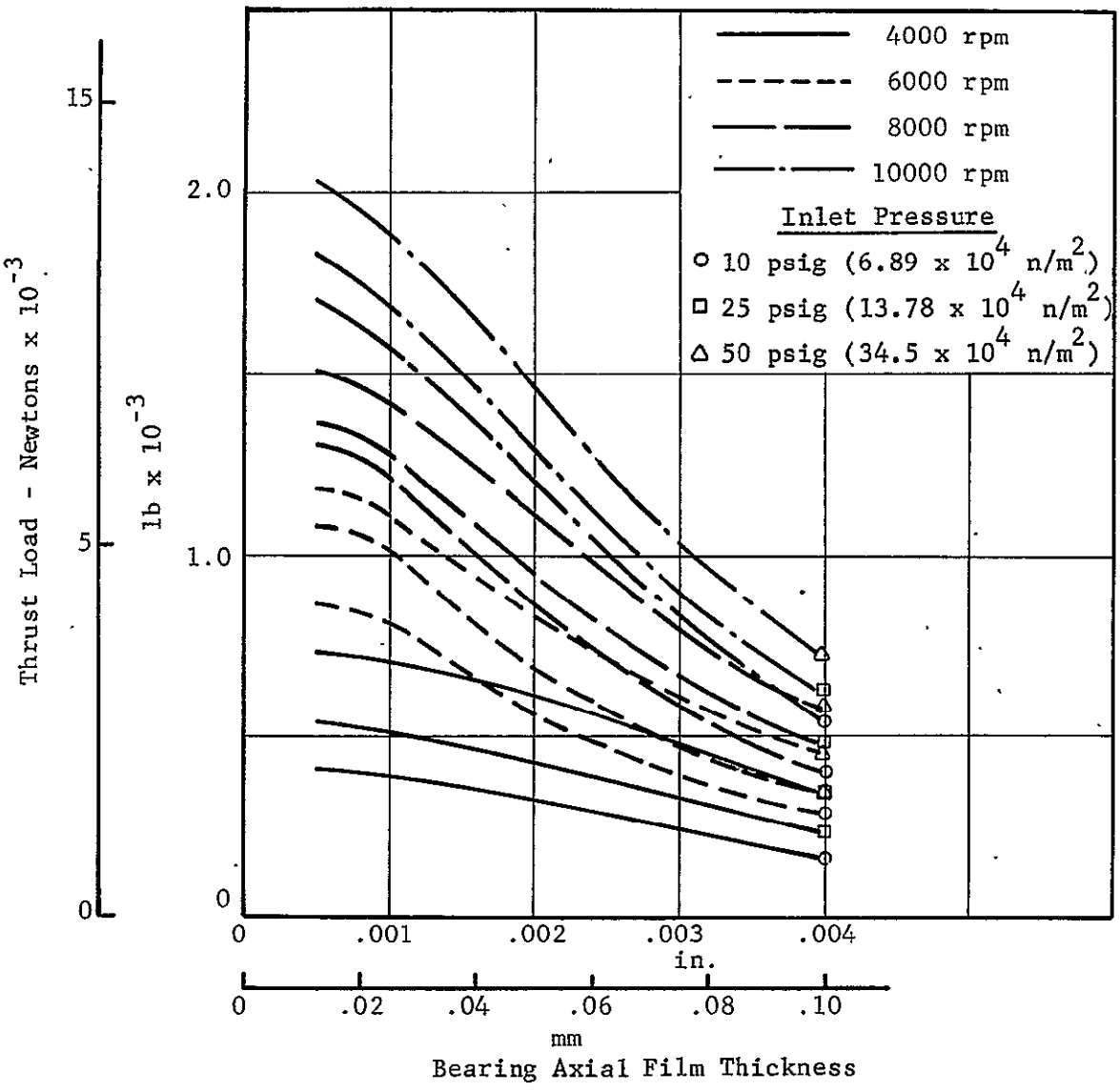

Fig. 24 Thrust Load vs. Film Thickness for 45 Degree Conical Fluid-Film Thrust Bearing with 6.5 in. (165 mm) Outer Diameter at 300°F (149°C)

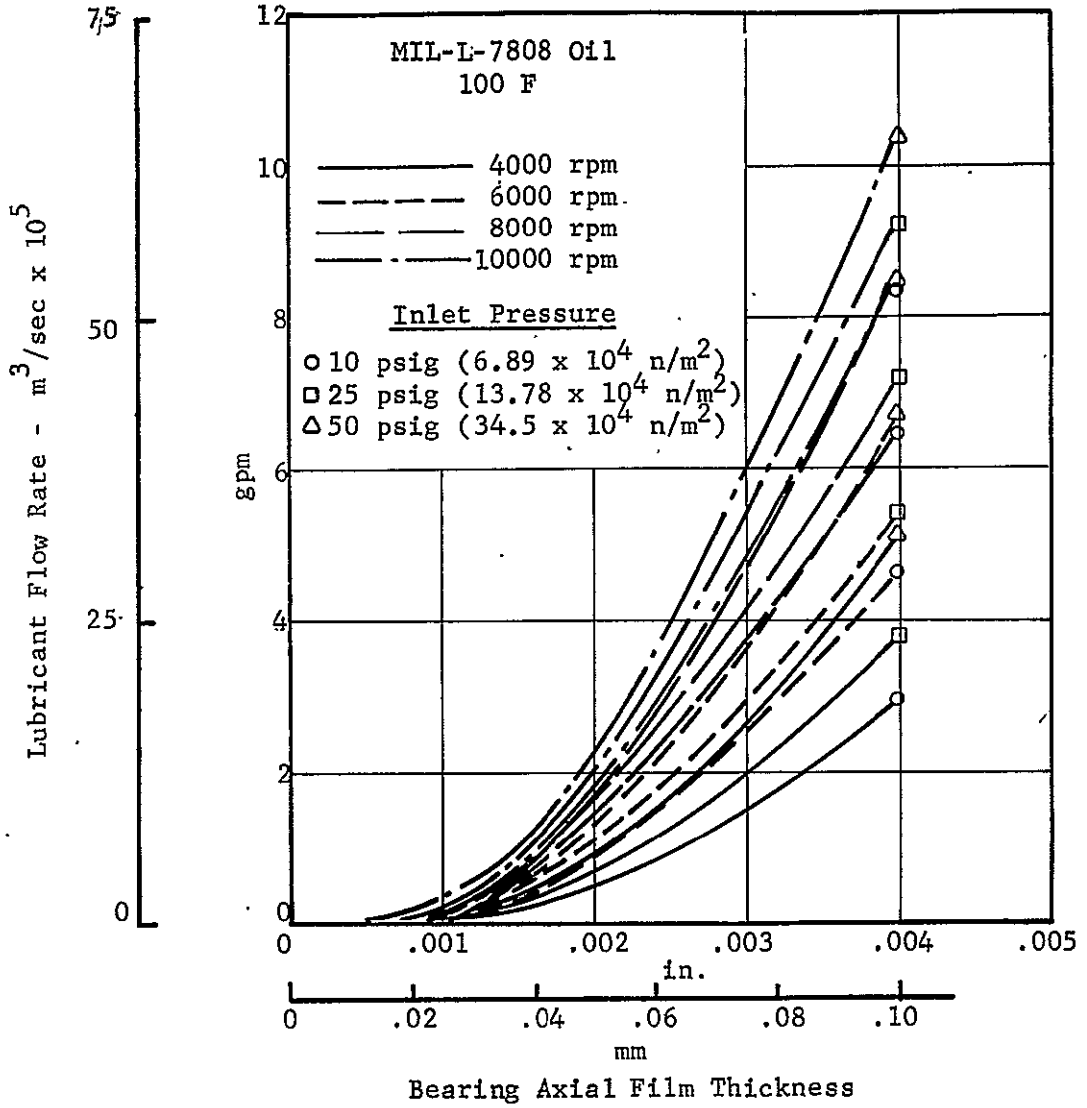

Fig. 25 Lubricant Flow Rate vs. Film Thickness for 45-Degree Conical Fluid-Film Thrust Bearing with 6.5 in. (165 mm) Outer Diameter at 100°F (37.8°C)

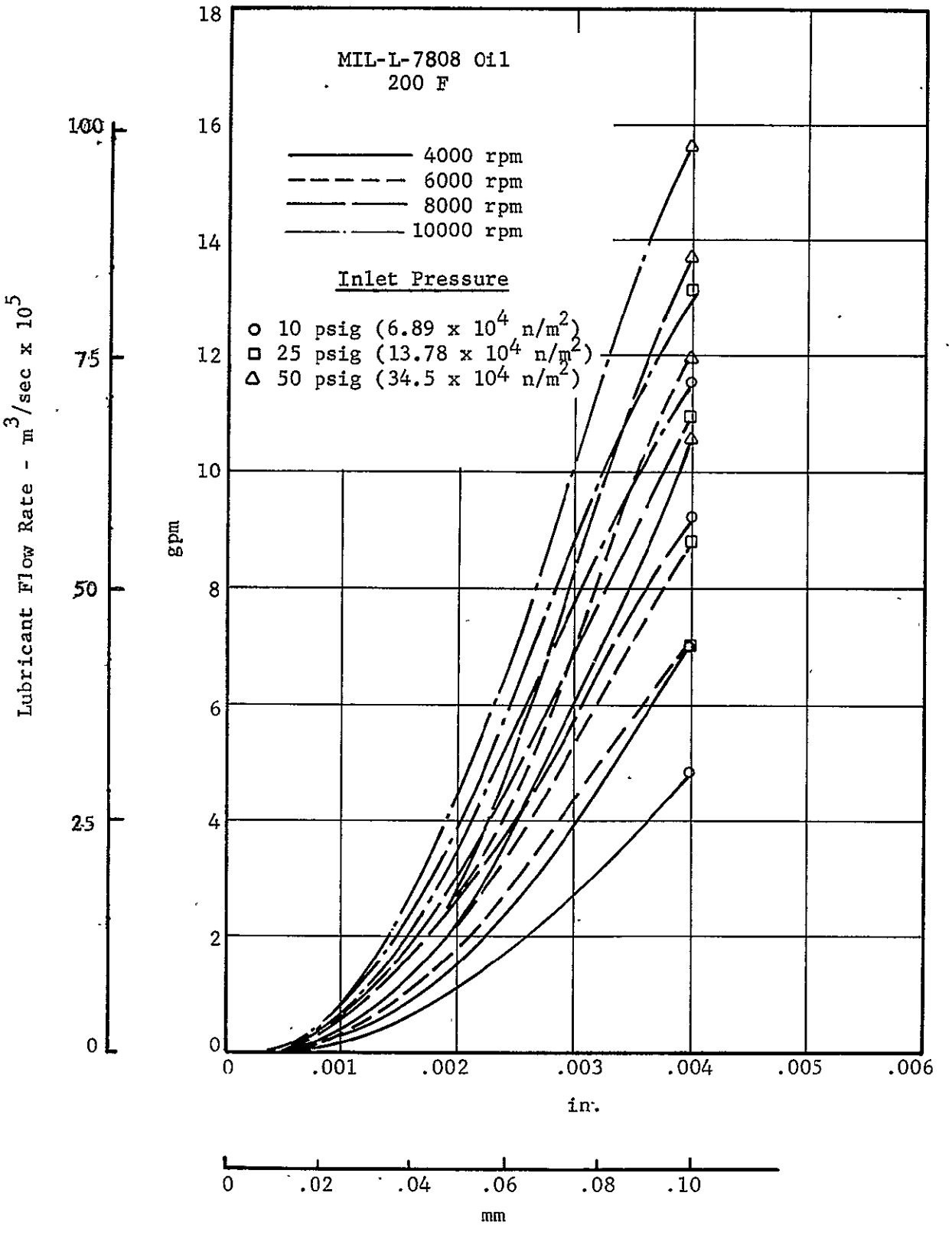

Fig. 26 Lubricant Flow Rate vs. Film Thickness for 45 Degree Conical Fluid-Film Thrust Bearing with 6.5 in. (165 mm) Outer Diameter at 200°F (93.3°C)

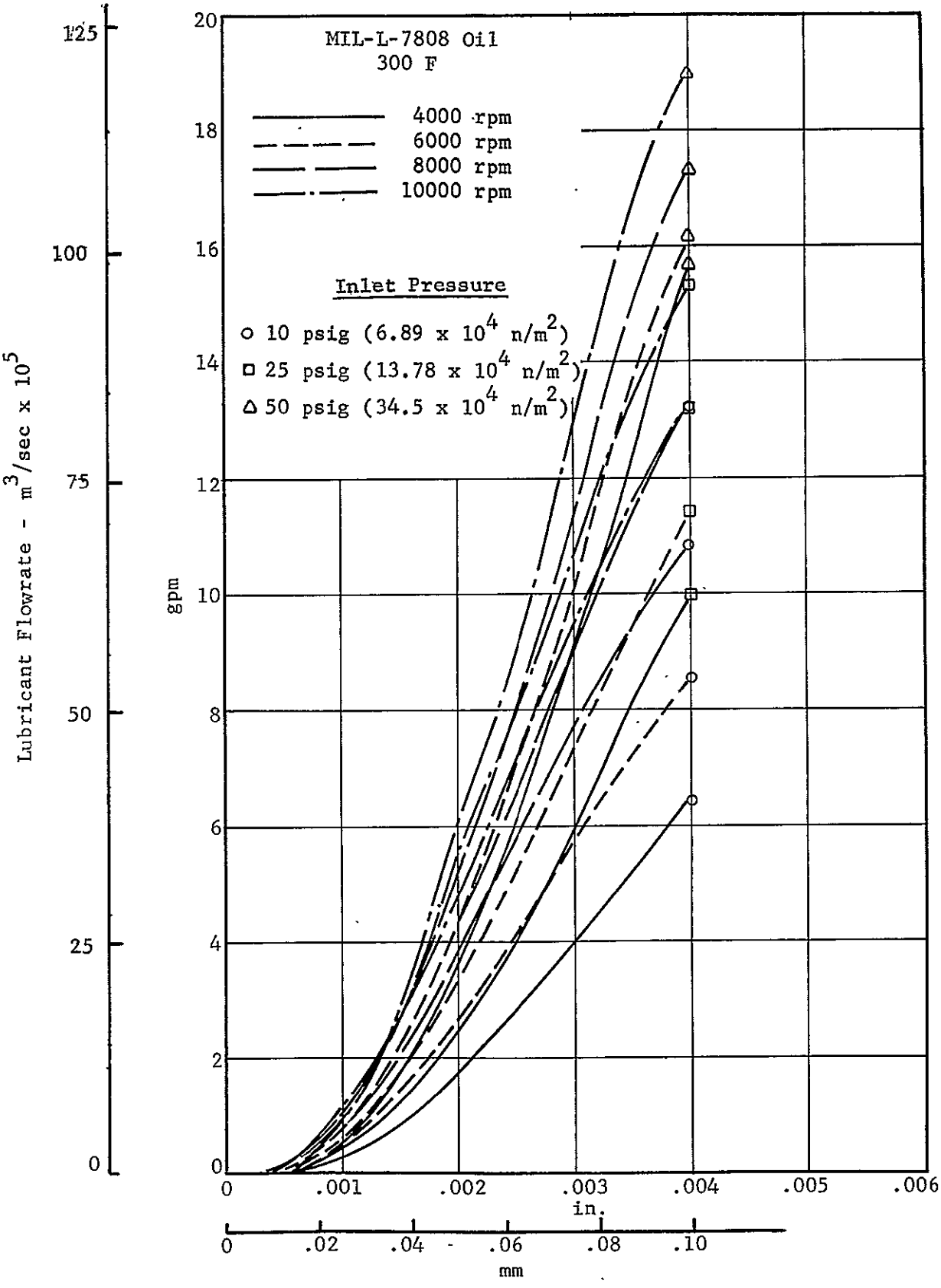

Fig. 27 Lubricant Flow Rate vs. Film Thickness for 45 Degree Conical Fluid-Film Thrust Bearing with 6.5 in. (165 mm) Outer Diameter at 300°F (149°C)

MTI-9184

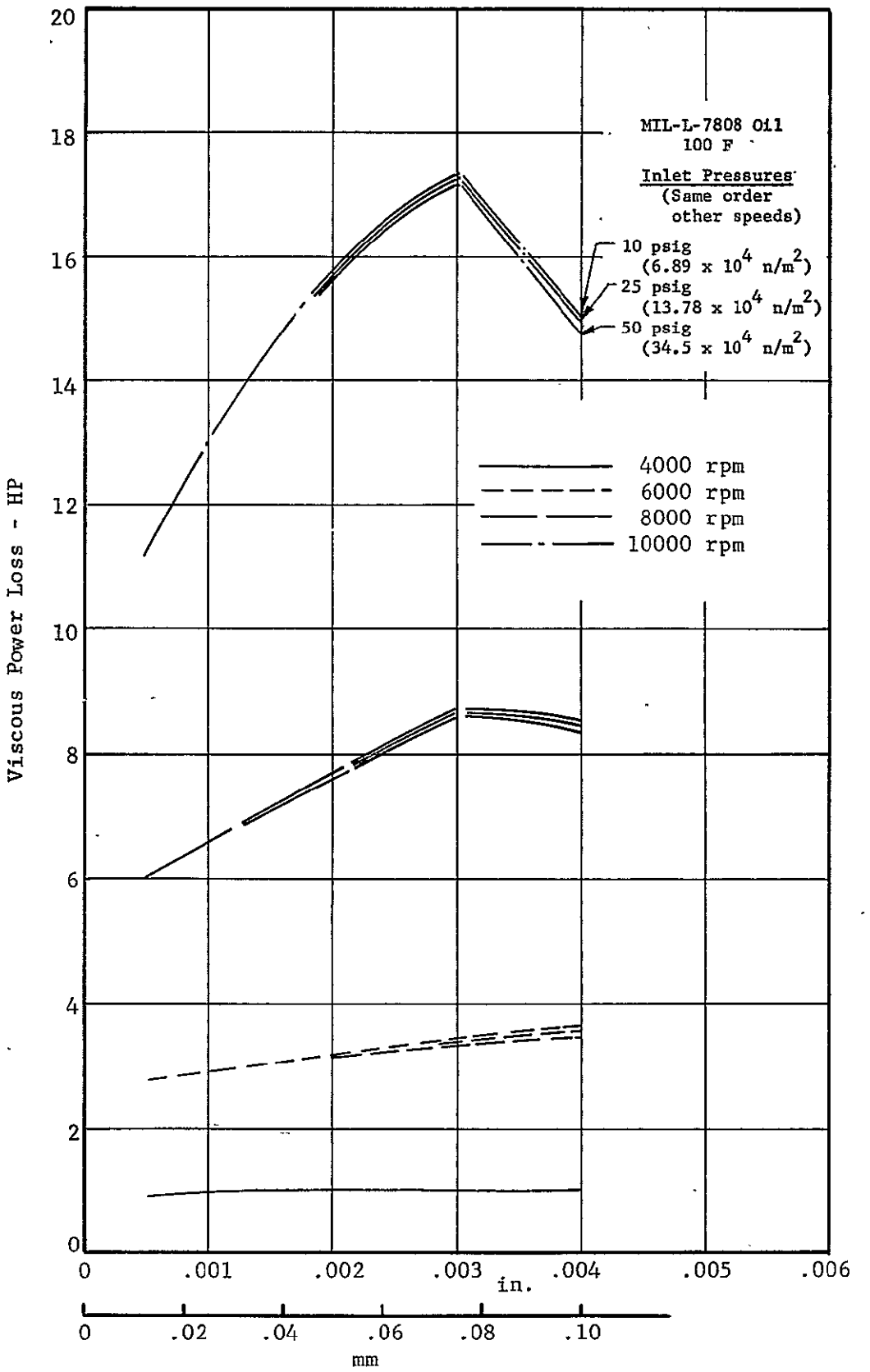

Fig.28 Viscous Power Loss vs. Film Thickness for 45-Degree Conical Fluid-Film Thrust Bearing with 6.5 in. (165 mm) Outer Diameter at 100°F (37.8°C)

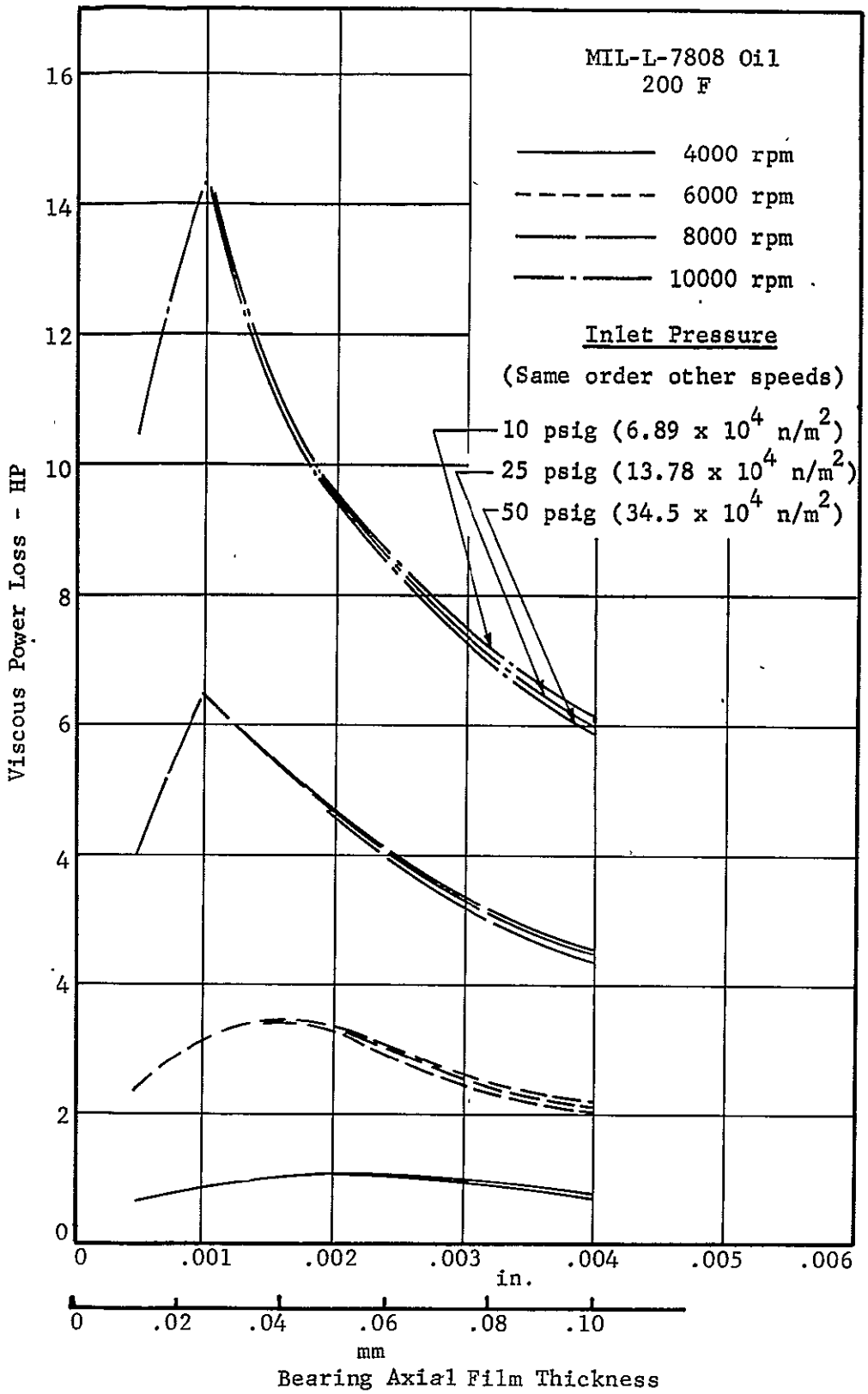

Fig. 29 Viscous Power Loss vs. Film Thickness for 45-Degree Conical Fluid-Film Thrust Bearing with 6.5 in. (165 mm) Outer Diameter at 200°F (93.3°C)

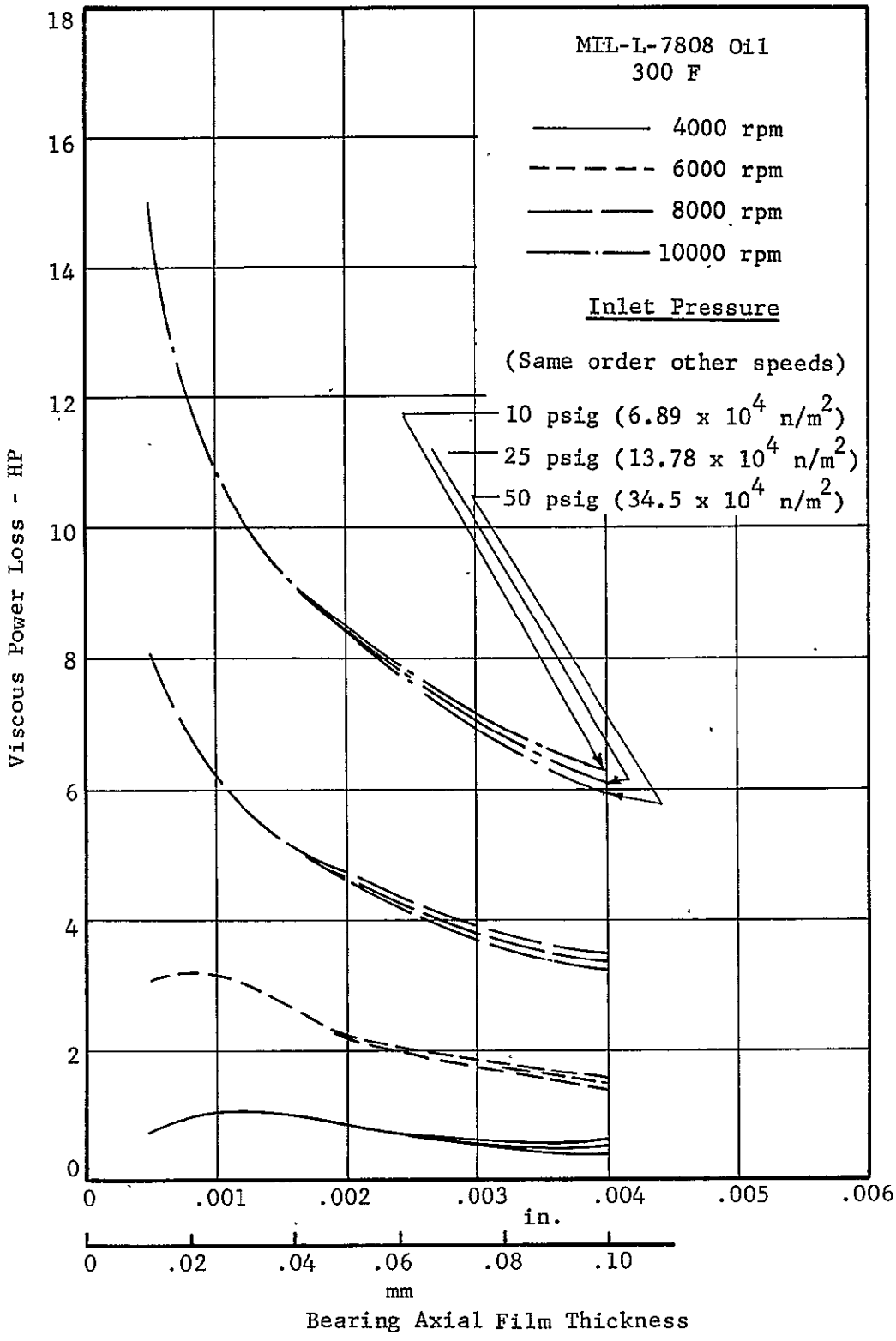

Fig. 30 Viscous Power Loss vs. Film Thickness for 45 Degree Conical Fluid-Film Thrust Bearing with 6.5 in. (165 mm) Outer Diameter at 300°F (149°C)

3.1.1.7 Effects of Runner Eccentricity in Conical Configuration (O.D. = 7.4 Inches)(187.96mm)

For non-concentric operation of the conical shrouded-step thrust bearing, a radial force and a bending moment in the shaft will exist. The case of radial eccentricity in a 45 degree conical bearing is shown graphically in Fig. 31. The nominal axial clearance is denoted by quantity h_f. For the pocket orientation shown, introduction of radial eccentricity e is equivalent to increasing the axial film thickness of the top pad by e. Similarly, the axial film thickness of the bottom pad is reduced by e. The axial film thickness of the two side pads are essentially unchanged.

Radial force and shaft bending moment were investigated by considering various amounts of eccentricity for several different axial film thicknesses. Eccentricity, as a percentage of concentric axial clearance ($\varepsilon_c := e/h_f$), is introduced. The resulting net radial force acts in the plane of the eccentricity, as does the resulting moment. The radial force acts so as to decrease the eccentricity. The results of the calculations are contained in Table I for ε_c = 0.25, 0.50, and 0.75:

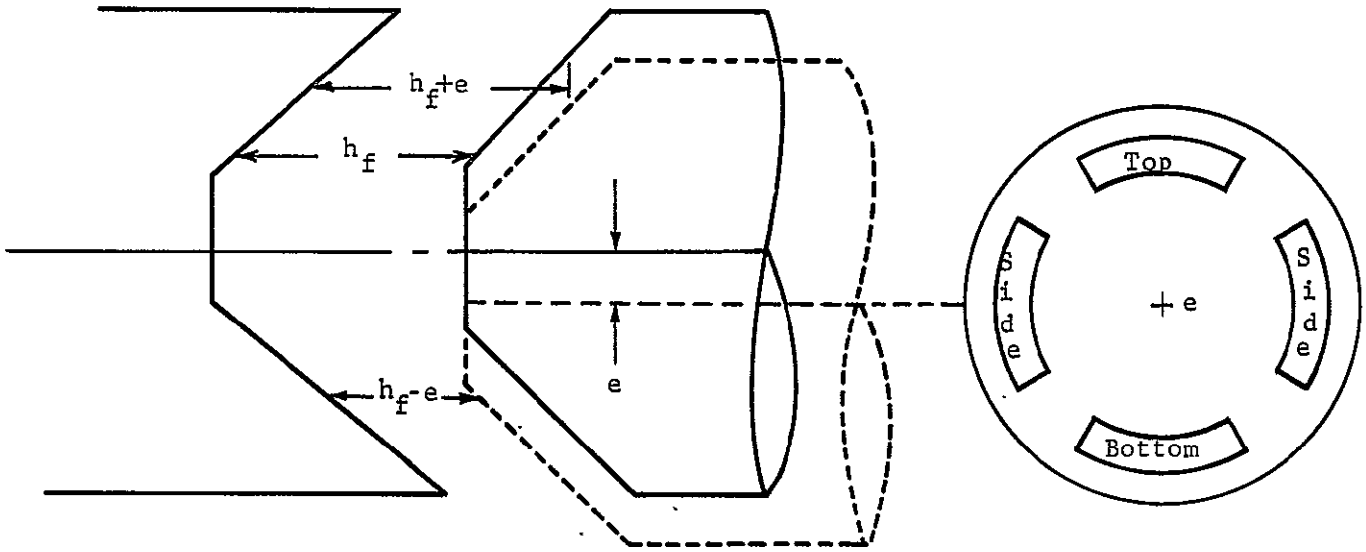

Fig. 31 Radial Eccentricity in Conical Bearing With 45^{o} Cone Angle.

TABLE I

EFFECTS OF RUNNER ECCENTRICITY

(10,000 rpm, 300 F (149°C), 50 psig (34.3 x 10^4 Newton/m^2))

Concentric Axial Clear. in. (mm)	Concentric Thrust Load Lb (Newtons)	Eccentricity in. (mm)	Eccentricity Thrust Load Lb (Newtons)	Net Radial Force Lb (Newtons)	Misalignment Torque lb-in (Newton-Meters)
.0005 (.0127)	4320 (19,224)	.000125 (.0031)	4323 (19,237)	22.5 (100)	148 (16.72)
		.000250 (.0063)	4323 (19,237)	42.5 (189)	279 (31.53)
		.000375 (.0095)	4315 (19,202)	65.0 (289)	427 (48.25)
.001 (.0254)	4120 (18,334)	.000250 (.0063)	4120 (18,334)	60.0 (267)	394 (44.52)
		.000500 (.0127)	4108 (18,280)	112.5 (500)	740 (83.62)
		.000750 (.0190)	4090 (18,201)	175.0 (778)	1150 (129.95)
.002 (.0508)	3560 (15,842)	.000500 (.0127)	3553 (15,811)	162.5 (723)	1070 (120.91)
		.001000 (.0254)	3530 (15,709)	310.0 (1,380)	2038 (230.29)
		.001500 (.0381)	3503 (15,588)	437.5 (1,947)	2875 (324.88)
.003 (.0762)	2880 (12,816)	.000750 (.0190)	2890 (12,861)	240.0 (1,068)	1576 (178.09)
		.000150 (.0038)	2901 (12,909)	472.5 (2,103)	3105 (350.87)
		.000225 (.0057)	2855 (12,705)	645.0 (2,870)	4240 (479.12)
.004 (.1016)	2280 (10,146)	.001000 (.0254)	2283 (10,159)	297.5 (1,324)	1955 (220.92)
		.002000 (.0508)	2300 (10,235)	610.0 (2,715)	4010 (453.13)
		.003000 (.0762)	2295 (10,213)	905.0 (4,027)	5950 (672.35)

As can be seen the effect of eccentricity on the thrust load capacity is negligible. The resulting bending moment could be taken up with ease by the roller bearings existing within an actual engine system. On test this moment load will be shared by the ball bearing and axial load applicator.

3.1.2 Ball Bearing Component

The ball bearing component of the hybrid boost bearing, supplied by NASA, had previously been utilized by another NASA contractor for evaluation testing. It was a 120 mm (4.724 in.) bore angular contact split inner race bearing, and had the dimensions shown in Table II.

TABLE II

TEST BALL BEARING CHARACTERISTICS

Outside Diameter	7.4800 in. (190 mm)
Bore Diameter	4.7242 in (120 mm)
Pitch Diameter	6.1024 in. (155 mm)
Width of Bearing	1.437 in. (36.5 mm)
Outer Race Curvature	0.52
Inner Race Curvature	0.54
Number of Balls	15
Ball Diameter	0.8125 in. (20.64 mm)
Split Inner Race Shim Thickness	0.0068 in. (.1737 mm)
Material (Balls and Races)	M-50 Tool Steel
Cage Material	Unknown
Initial Contact Angle (Degrees)	22^{o}

The ball bearing was analyzed using a computer program developed by Mr. A. B. Jones. Ref. 2 discusses the basic mathematical analysis used by this program. The model used for calculation purposes is shown in Fig. 32. The outer ring is assumed fixed in space, the deflections of the inner ring are referred to an orthogonal XYZ-coordinate system. The

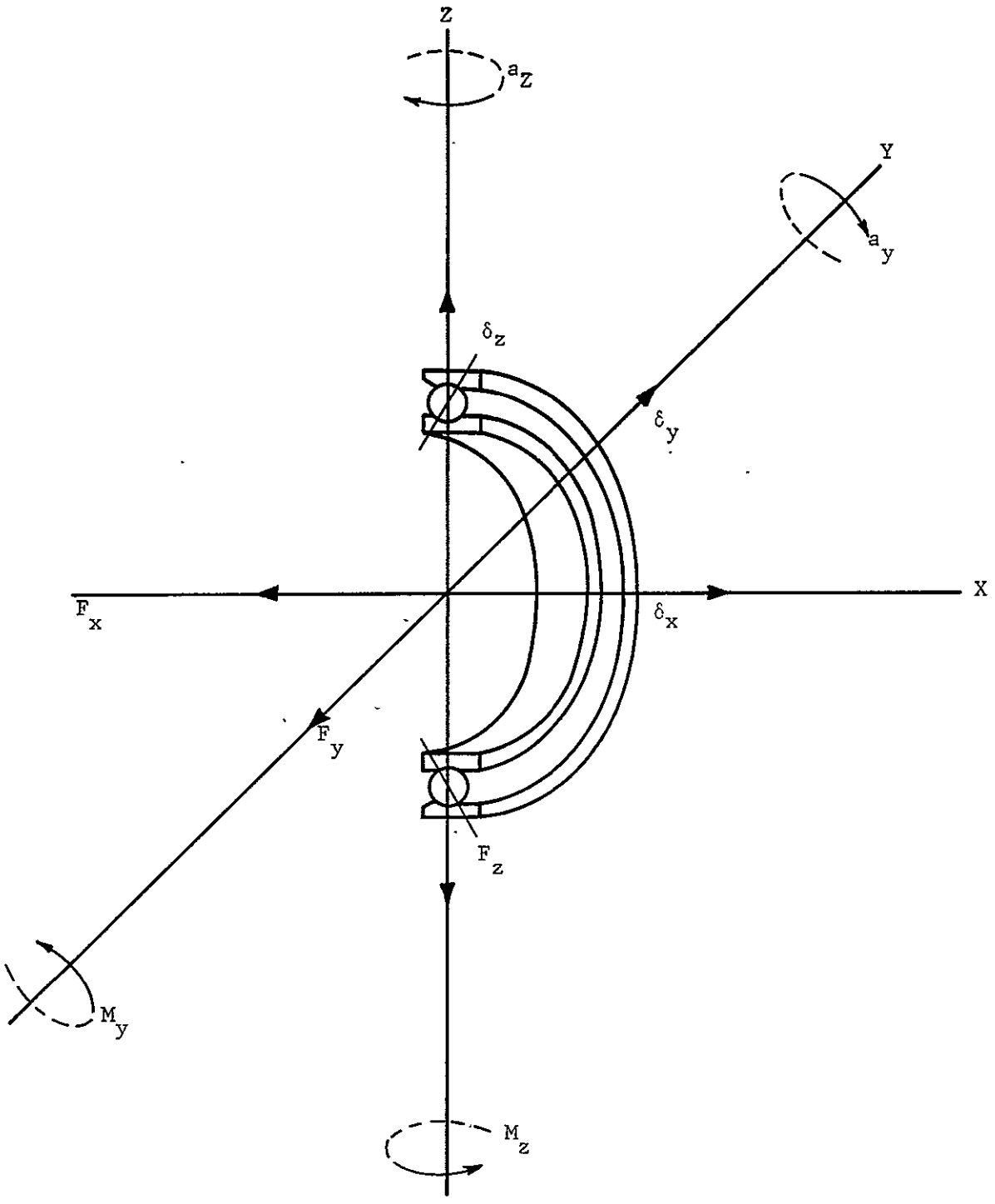

Fig. 32 Ball Bearing Analytical Model (Indicated directions are positive).

program considers centrifugal and gyroscopic load effects on each of the rolling contact elements over the full 360 degree azimuth. Cage effects are neglected.

Using the bearing data specified above, the operating characteristics of the bearing were calculated at speeds of 10, 4000, 6000, 8000, and 10,000 rpm. Thrust load at each shaft speed was varied between 500 lbs (2,225 Newtons), and 3000 lbs. (13,350 Newtons) and the radial load was assumed to be constant at 50 lbs (223 Newtons). The latter represents an initial guess at the weight of the floating test housing. The actual weight turned out to be 75 lbs (334 Newtons).

Since the output of the ball bearing computer program is extremely detailed and lengthy only the most pertinent design data were selected for reproduction in this report. These data are summarized in Table III.

The factor of immediate interest in the design of the hybrid boost bearing is the load vs. deflection characteristic over the speed range of interest. These characteristics plotted in Fig. 33, are typical of high-speed bearings. Note that the effect of speed on bearing deflection is quite pronounced at low axial loads, and increases in speed at constant load may produce negative deflections (negative deflection is in the direction of the applied load). The negative deflections occur as a result of an increase in ball inertia loading with increasing speed and subsequent change in contact angle at the outer race. As will be shown later, this behavior must be taken into consideration in the design of the hybrid boost bearing.

3.1.3 Combined Hybrid Boost Bearing Performance

The basic hybrid boost bearing concept can be schematically represented as shown in Fig. 34. Neglecting the radial stiffness of the ball bearing, the system is described as consisting of three springs arranged in a series-parallel pattern. The three springs are identified as having stiffness, ball bearing axial stiffness and fluid film thrust bearing stiffness

TABLE III

STIFFNESS CHARACTERISTICS OF TEST BALL
BEARING COMPONENT OF HYBRID BOOST BEARING

N Speed (rpm)	F_a Axial Load Lb.(Newtons)	F_z Radial Load Lb.(Newtons)	δ_x Ax. Displ. Mils (mm)	K_B Axial Stiff. Lb/in (Newt./mm) x 10^{-5}	K_z Rad. Stiff. Lb/in (Newt./mm) x 10^{-5}
10	- 500 (2,225)	50 (223)	1.282 (.0325)	6.3 (1.10)	1.2 (.21)
	-1000 (4,450)	50 (223)	1.953 (.0496)	8.6 (1.51)	2.2 (.39)
	-2000 (8,900)	50 (223)	2.928 (.0743)	12.0 (2.10)	3.7 (.65)
	-3000 (13,350)	50 (223)	3.679 (.0934)	14.7 (2.57)	4.9 (.86)
	-4000 (17,800)	50 (223)	4.308 (.1094)	17.1 (2.99)	5.9 (1.03)
4000	- 500 (2,225)	50 (223)	1.160 (.0294)	5.0 (.88)	1.2 (.21)
	-1000 (4,450)	50 (223)	1.916 (.0486)	8.1 (1.42)	2.2 (.39)
	-2000 (8,900)	50 (223)	2.916 (.0740)	11.8 (2.07)	3.7 (.65)
	-3000 (13,350)	50 (223)	3.672 (.0932)	14.6 (2.56)	4.9 (.86)
6000	- 500 (2,225)	50 (223)	.850 (.0215)	3.7 (.65)	1.1 (.19)
	-1000 (4,450)	50 (223)	1.797 (.0456)	7.1 (1.24)	2.1 (.37)
	-2000 (8,900)	50 (223)	2.877 (.0730)	11.4 (1.996)	3.7 (.65)
	-3000 (13,350)	50 (223)	3.652 (.0927)	14.4 (2.52)	4.9 (.86)
8000	- 500 (2,225)	50 (223)	.439 (.0111)	3.1 (.54)	1.0 (.175)
	-1000 (4,450)	50 (223)	1.574 (.0399)	6.0 (1.05)	2.0 (.35)
	-2000 (8,900)	50 (223)	2.789 (.0708)	10.6 (1.86)	3.6 (.63)
	-3000 (13,350)	50 (223)	3.605 (.0915)	13.9 (2.43)	4.8 (.84)
10,000	- 500 (2,225)	50 (223)	.079 (.0020)	3.1 (.54)	0.97(.17)
	-1000 (4,450)	50 (223)	1.290 (.0327)	5.4 (.95)	1.9 (.33)
	-2000 (8,900)	50 (223)	2.645 (.0671)	9.7 (1.698)	3.5 (.61)
	-3000 (13,350)	50 (223)	3.520 (.0894)	13.2 (2.31)	4.8 (.84)

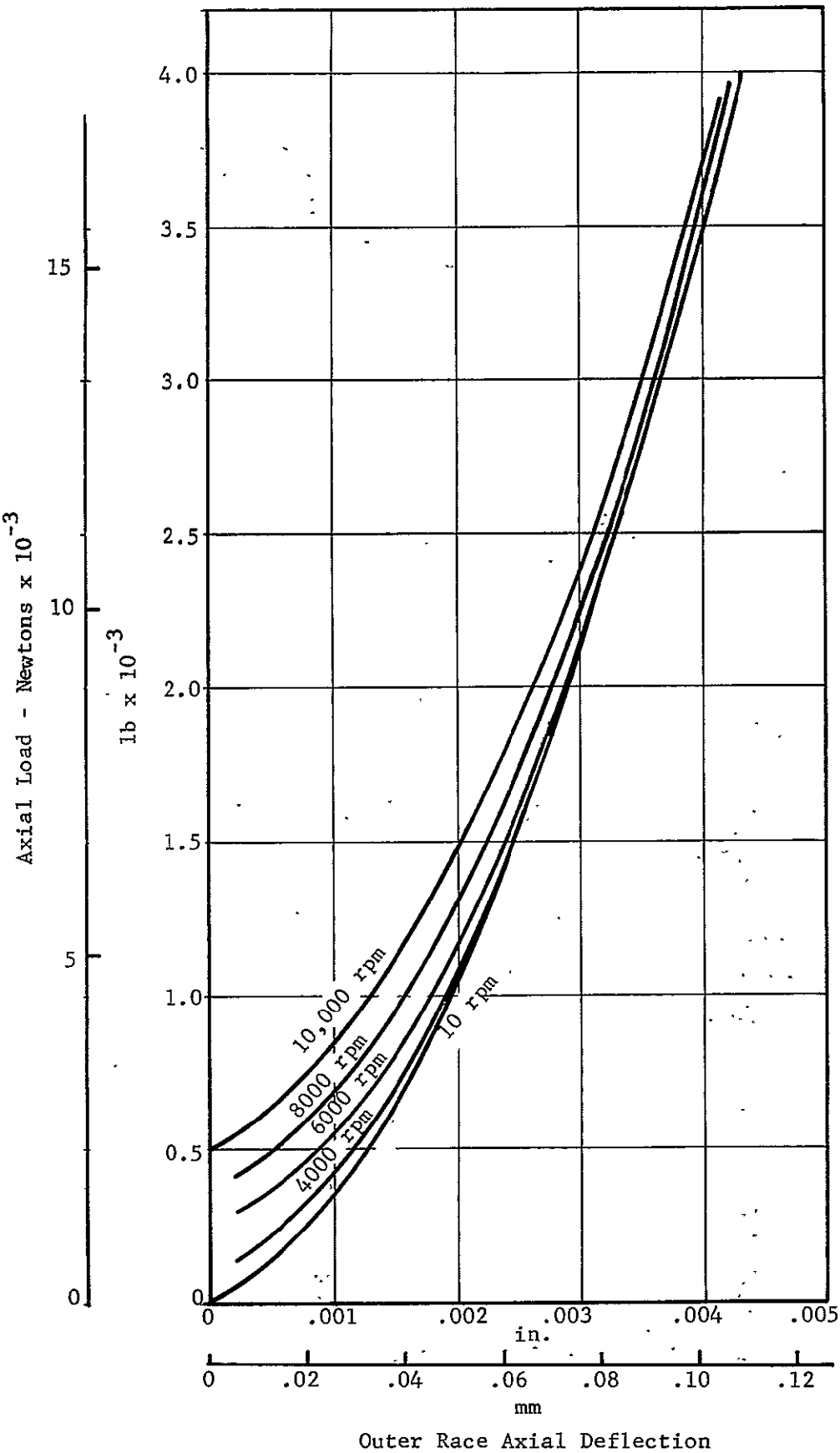

Fig. 33 Axial Deflection vs. Load at Various Speeds for 120 mm Bore Ball Bearing Selected for Test - Inner Race Fixed.

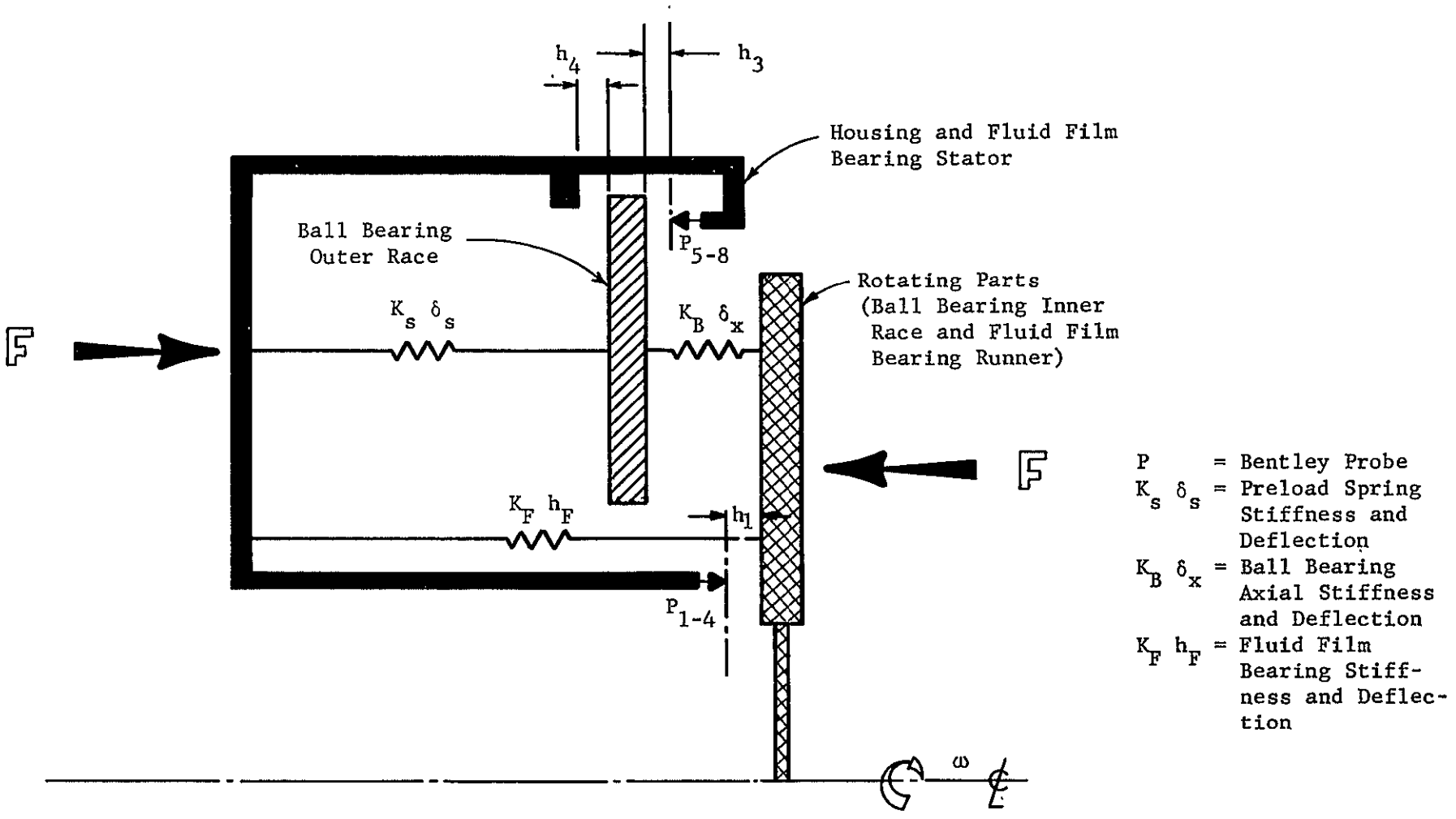

Fig. 34 Hybrid Boost Bearing Schematic

MTI-8555

respectively. Spring stiffness K_S is in series with the ball bearing stiffness K_B. Thus, the equivalent stiffness K_e of the rolling element bearing is given by the expression:

$$\frac{1}{K_e} = \frac{1}{K_S} + \frac{1}{K_B} = \frac{K_B + K_S}{K_S K_B} \tag{2}$$

This expression holds for the conditions where $h_4 > 0$, that is, while the preload spring is not fully deflected. Once the preload spring is bottomed, the equivalent stiffness becomes

$$K_e \approx K_B \tag{3}$$

Since the fluid film bearing stiffness K_F is in parallel with the equivalent ball bearing stiffness, the overall effective hybrid bearing stiffness K_e' is given by the expression:

$$K_e' = K_e + K_F = \frac{K_S K_B}{K_S + K_B} + K_F \tag{4}$$

Again, this expression is valid only where $h_4 > 0$. For the case where the preload spring is bottomed ($h_4 = D$):

$$K_e' = K_f + K_B \tag{5}$$

3.1.3.1 Planar Configuration

Because of the nonlinear characteristics of the stiffness of the fluid film bearing and the ball bearing, the performance characteristics of the combined hybrid boost bearing are best presented in graphical form. A graphical solution of the load capacity of the planar hybrid boost bearing is shown in Fig. 35. Here, for a speed of 10,000 rpm a lubricant viscosity of 0.21×10^{-6} reyn (1.44 cp) and an inlet pressure of 50 psig ($34,3 \times 10^4$ Newtons/m^2), the load

vs. deflection characteristics of the individual hybrid boost bearing are given for several setup clearances. The bearing D_o = 7.4 inches.

The zero reference for the ball bearing curve is taken at static conditions at a point where the internal play is eliminated by a slight preload and the initial contact angle materializes. It so happens that this point is equivalent to the 500 lb (2,225 Newtons) point at 10,000 rpm hence over this range of load, the conditions of Equation (3) are met, and the stiffness is that of the ball bearing only.

The relative positions between the fluid film bearing and the ball bearing indicated in Fig. 3 5 are established by locating the two components so that the clearance of the fluid film bearing is at a prescribed value at static conditions when the initial contact angle is in effect. This clearance is set to permit continuance of operation without rubs on fluid film bearing components should the oil supply be lost at a thrust load of 3000 lbs. (13,350 Newtons). Characteristics for three such clearances are shown. Having established the reference points for the fluid film and ball bearing components, the load vs. deflection characteristics for each are plotted as shown, and numerically added as to yield the equivalent load vs. deflection curve for the specific hybrid boost bearing at the given set of conditions.

Referring again to Fig. 35, assume that at the indicated conditions of operation a load of 3000 lbs (13,350 Newtons) (point A) is imposed. It can be seen then that at this load level the fluid film bearing will carry about 1930 lbs (8,588 Newtons) (point B) and the ball bearing about 1070 lbs (4,762 Newtons) (point C). Should oil system failure occur, the fluid film bearing will become ineffective and the entire load will be shifted onto the ball bearing component. Following the horizontal 3000 lb (13,350 Newton) load line to point D, the ball bearing will take over the load, deflecting until the

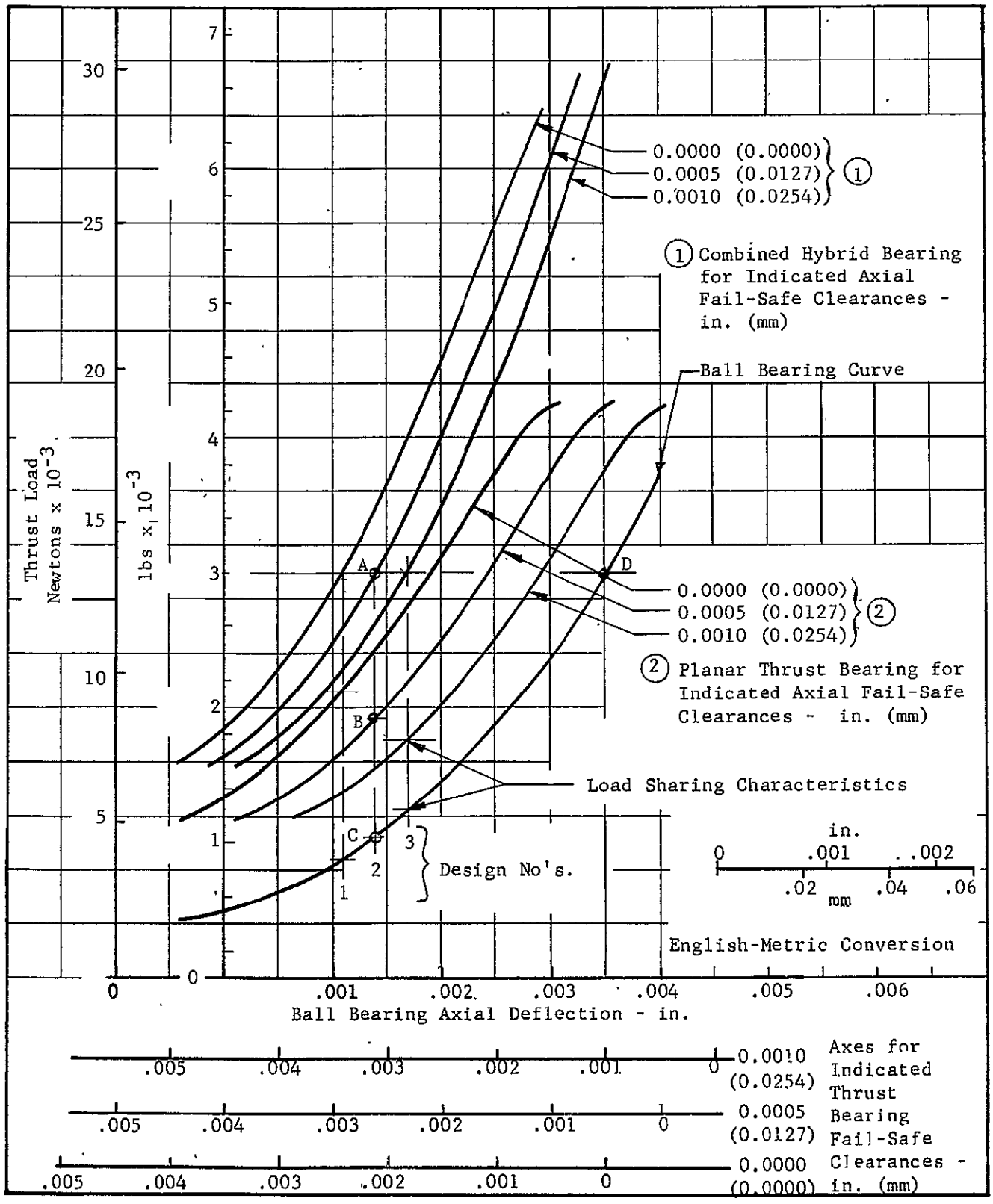

Fig. 35 Thrust Load Characteristics for Ball Bearing, Planar Thrust Bearing, and Several Hybrid Combinations at 10,000 rpm, 300 F, (149 C) and 50 psig (34.5 x 10^4 n/m^2).

fluid film bearing clearance is reduced to 0.0005 inches (.0127 mm). This remaining clearance is sufficient to provide a margin of separation between the rotating and stationary components of the fluid film bearing under ideal conditions of flatness and runout, and thus to satisfy the fail-safe requirements of a jet engine system. The effects of ± 0.0005 inch (.0127 mm) shift in initial stack up either due to manufacturing tolerances or thermal changes, are also shown in Fig. 35. For the same axially applied load of 3000 lbs (13,350 Newtons) the following changes in load distribution will take place as a result of a ± 0.0005 inch (.0127 mm) change in initial gap setting:

	Ball Bearing Load, lbs. (Newtons)	Fluid Film Bearing Load, lbs. (Newtons)
Increase in Gap by 0.0005 inch (.0127 mm)	1240 (5,518)	1760 (7,832)
Nominal Gap of 0.0005 inch (.0127 mm)	1070 (4,761)	1930 (8,589)
Decrease in Gap by 0.0005 inch (.0127 mm)	880 (3,916)	2120 (9,434)

The load division between the fluid film and ball bearing components of the hybrid boost bearing may be altered by about 20 percent by decreasing the initial gap setting by 0.0005 in. (.0127 mm). The fail-safe provision is, however, completely eliminated by such a change. It is apparent that, in the event of lube system failure, contact between the stationary and rotating parts of the fluid film bearing will occur because of loss of clearance. This can be seen clearly by following the horizontal 3000 lb. (13,350 Newton) load line to the intersection of the ball bearing curve. On the other hand a shift in the direction of gap increase will also increase the load share of the ball bearing, but will result in a larger margin of safety at lube system failure (.001 inch) (.0254 mm).

3.1.3.2 Conical Configuration

As with the planar bearing, the stiffness of the fluid-film and ball bearing components are nonlinear with respect to thrust load.

The performance characteristics are thus best presented in graphical form. Graphical solutions for the three conical bearing configurations discussed earlier (outer diameters of 7.4 (187.96), 7.0 (177.7), and 6.5 (165.1) inches (mm), other dimensions proportionally reduced) are presented in Figs. 36 through 38, respectively.

As before, operating characteristics were 10000 rpm, viscosity of 0.21×10^{-6} reyn (1.44 cp) (MIL-L-7808 at $300^{\circ}F$)($149^{\circ}C$), and inlet pressure of 50 psig (34.3×10^{4} Newtons/m^2). The ball bearing curve is again plotted together with the fluid-film bearing load curves for several fail-safe clearance values and the curves added numerically to produce the total load vs. deflection characteristics for the combined hybrid bearing configurations. The zero reference curve for the ball bearing is the same as used before, and the fail-safe clearances have identical meanings. Note here, however, that axial film thicknesses and clearances are considered in the results.

The data shown in Table IV, are abstracted from the results tables for the one planar and three conical bearings considered in order to present a comparison of performance characteristics. The selected fail-safe clearance was 0.001 (.0254 mm) inch (see points A, B, C, D, E on Figs. 35, 36, 37 and 38.

Based on these calculated results, the preliminary conclusion may be drawn that both the planar and the conical hybrid bearing configurations are feasible for use in effecting a considerable reduction in ball-bearing thrust load. The power losses and flow requirements are however, prohibitively high for the larger diameter bearings. Of the configurations examined the 6.5 inch (165.1 mm) diameter bearing does offer a good compromise in terms of sacrificing a somewhat more favorable load distribution for reasonably low power losses and flow requirements.

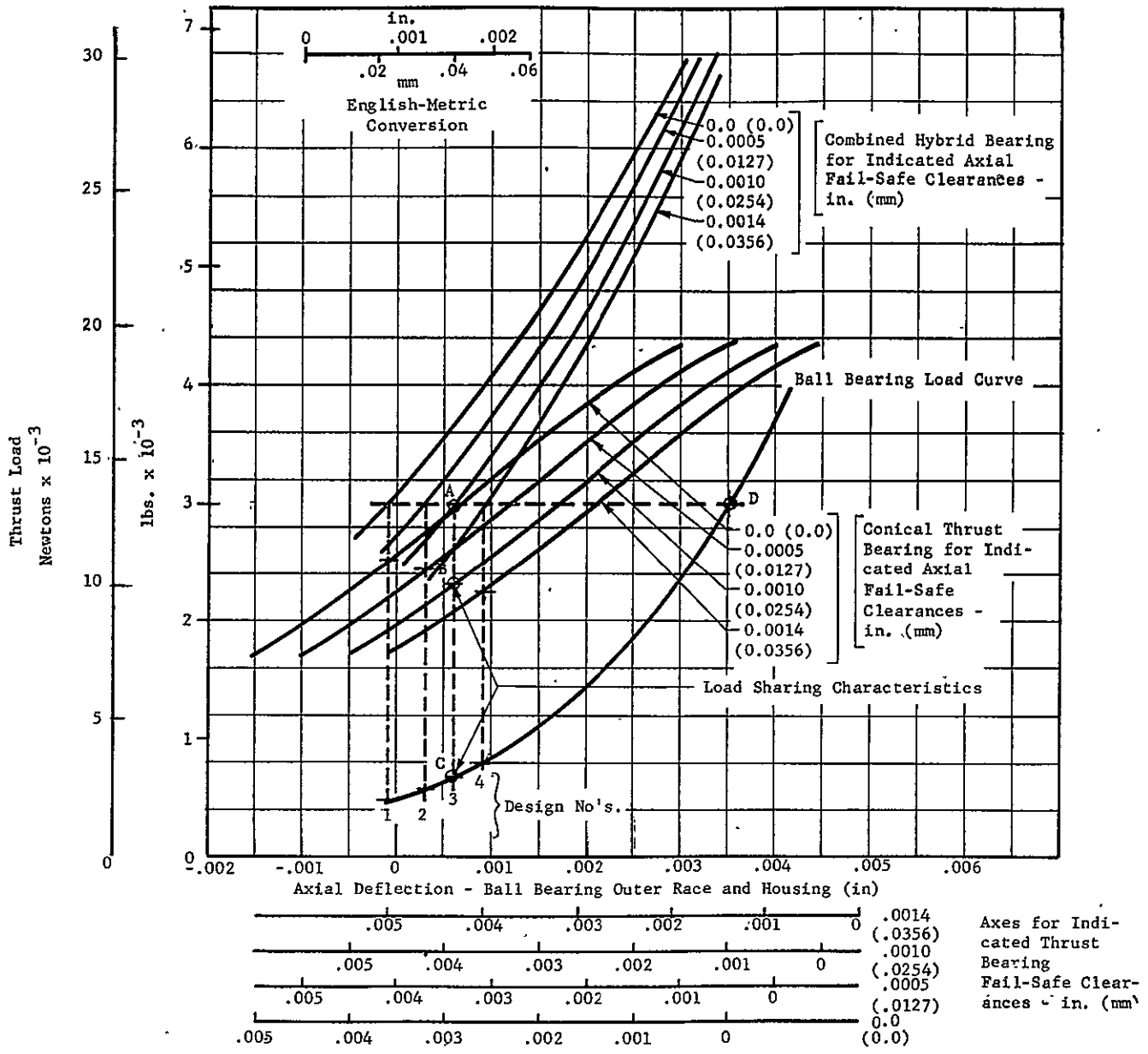

Fig. 36 Thrust Load Characteristics for Ball Bearing, 45° Conical Bearing, and Several Hybrid Combinations at 10000 RPM, 300F, and 50 psig, ID = 5.25 in., OD = 7.40 in.

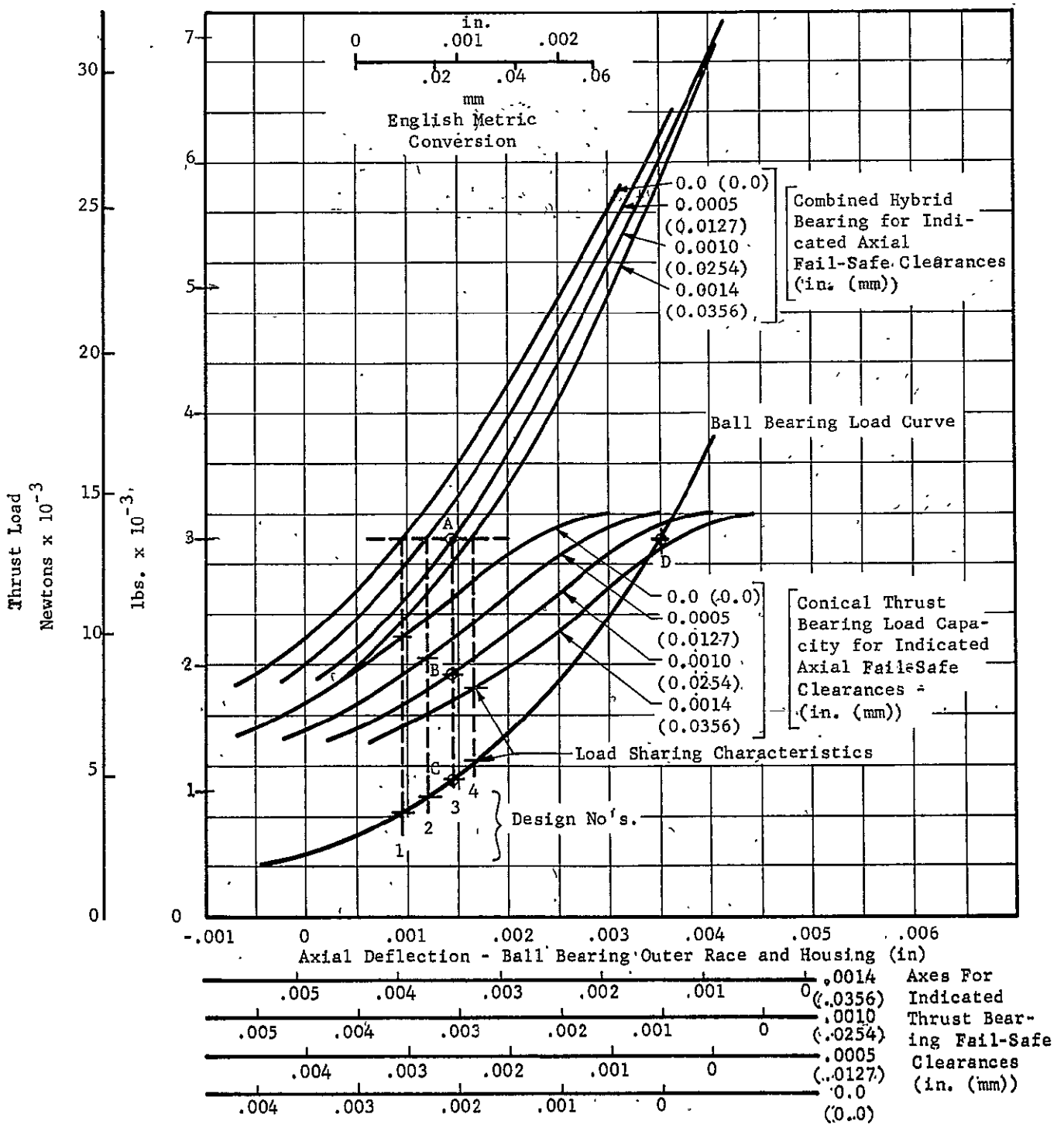

Fig. 37 Thrust Load Characteristics for Ball Bearing, 45° Conical Bearing with 7.0 in. (177.7 mm) Outer Diameter, and Several Hybrid Combinations at 10000 rpm, 300 F (149 C) and 50 psig (34.5×10^4 n/m^2).

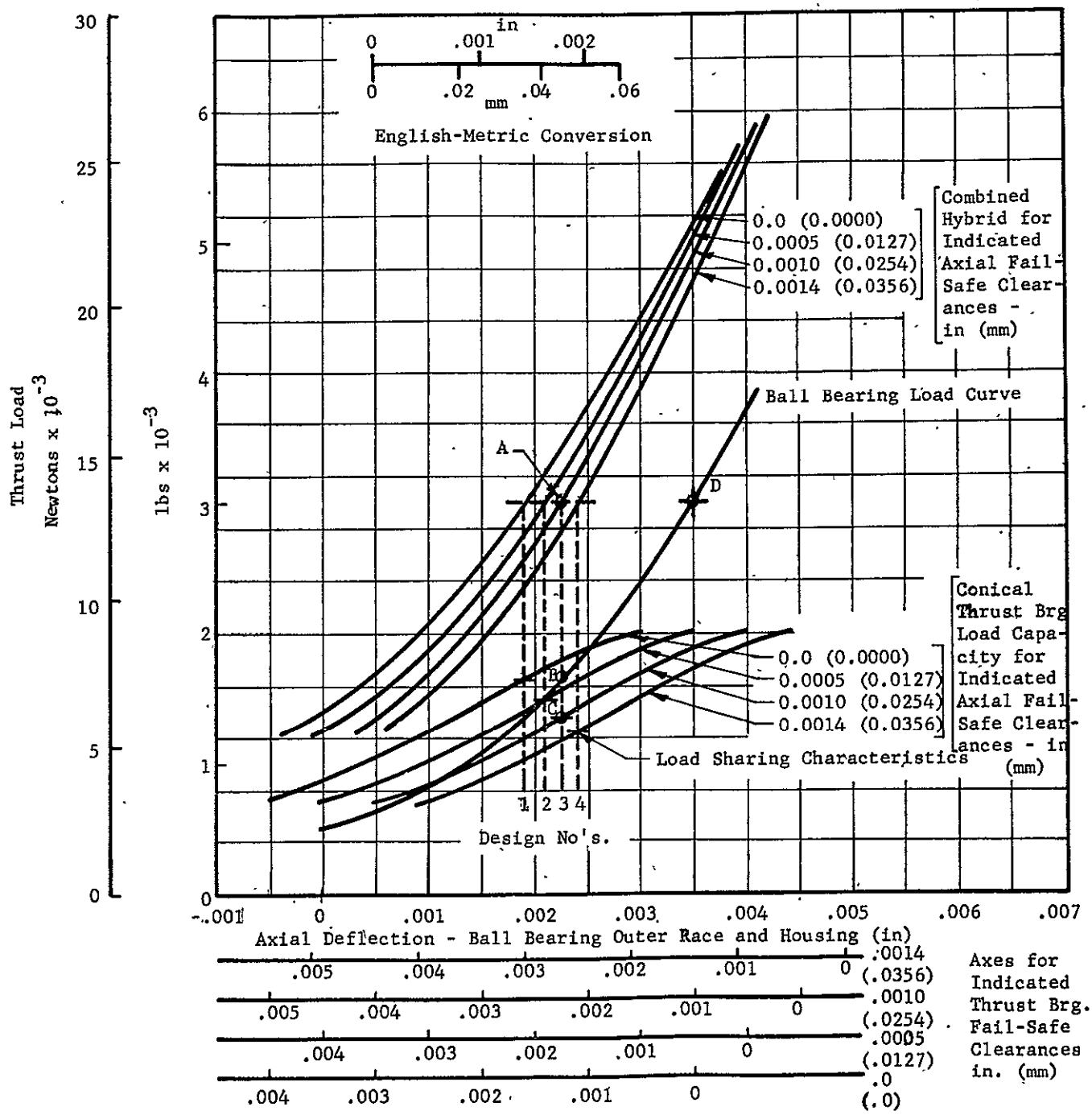

Fig. 38 Thrust Load Characteristics for Ball Bearing, 45° Conical Bearing with 6.5 in. Outer Diameter, and Several Hybrid Combinations at 10,000 RPM, 300°F and 50 psig

TABLE IV

HYBRID BOOST BEARING RESULTS (FAIL-SAFE CLEARANCE: 0.001 IN. T=300F (149°C)

Bearing Type	Outer Dia. in.(mm)	Thrust Load Lb(Newtons)	Ball Brg. Load Lb(Newtons)	Axial Fluid-Film Thickness in.(Mils)	Power Loss (HP)	Flow Rate GPM(M^3/sec x 10^4)	Temp. Rise °F (°C)
Planar	7.4 (187.96)	3000 (13,350)	1240 (5,518)	.00280 (.0711)	9.1	20.2 (12.6)	5.1 (2.8)
45° Conical	7.4 (187.96)	3000 (13,350)	680 (3,026)	.00390 (.099)	13.7	19.6 (12.2)	8.5 (4.7)
45° Conical	7.0 (187.96)	3000 (13,350)	1080 (4,806)	.00305 (.0774)	12.0	12.8 (8.0)	9.8 (5.4)
45° Conical	6.5 (165.1)	3000 (13,350	1610 (7,165)	.00225 (.0571)	7.9	8.2 (5.16)	11.2 (6.2)

3.2 Mechanical Analysis and Design of Bearing System

3.2.1 Thermal Analysis

Thermal mapping calculations were performed for both the planar and conical hybrid-boost bearing configurations at both 100°F (37°C) and 300°F (149°C) oil inlet temperatures to the fluid-film bearing component. Inputs included the heat generation rates and bearing flow rates determined from the combined bearing performance curves presented in the preceeding sections. In all, some ten complete calculations were performed for these configurations and temperature conditions in order to determine both nominal results and also the effects of deviations of various temperatures and flow rates upon nominal temperature distributions.

In each of the following sections, the thermal modeling assumptions are listed, and the resulting temperature distribution is presented.

3.2.1.1 Planar Bearing Configuration

The finite-element thermal model utilized in thermal mapping studies for the planar hybrid boost configuration with outer diameter of 7.4 inches (187.96 mm) and fail-safe clearance of 0.001 inch (.0254 mm) is shown in Fig. 39. The operating characteristics for this bearing are shown in Table IV. Fig. 39 shows the grid used for the model, the forced convection flow streams (Roman numerals) and the boundary condition types assumed to exist. The actual boundary condition values follow in Tables V and VI. The results of the planar bearing thermal mapping calculations for the two temperature extremes are presented in Figs. 40 and 41. Note in both these figures the relatively low thermal gradients that exist in both runner and stator. Also, in each case, the flow of lubricant in Streams I, II and III (through the ball bearing) provides the very important function of heat removal, as may be seen by its elevated temperature of 30-40°F (17°-22°C) above the surrounding materials. The peak operating temperatures appear in the area of the ball bearing outer race, which indicates that the heat conduction paths in that region

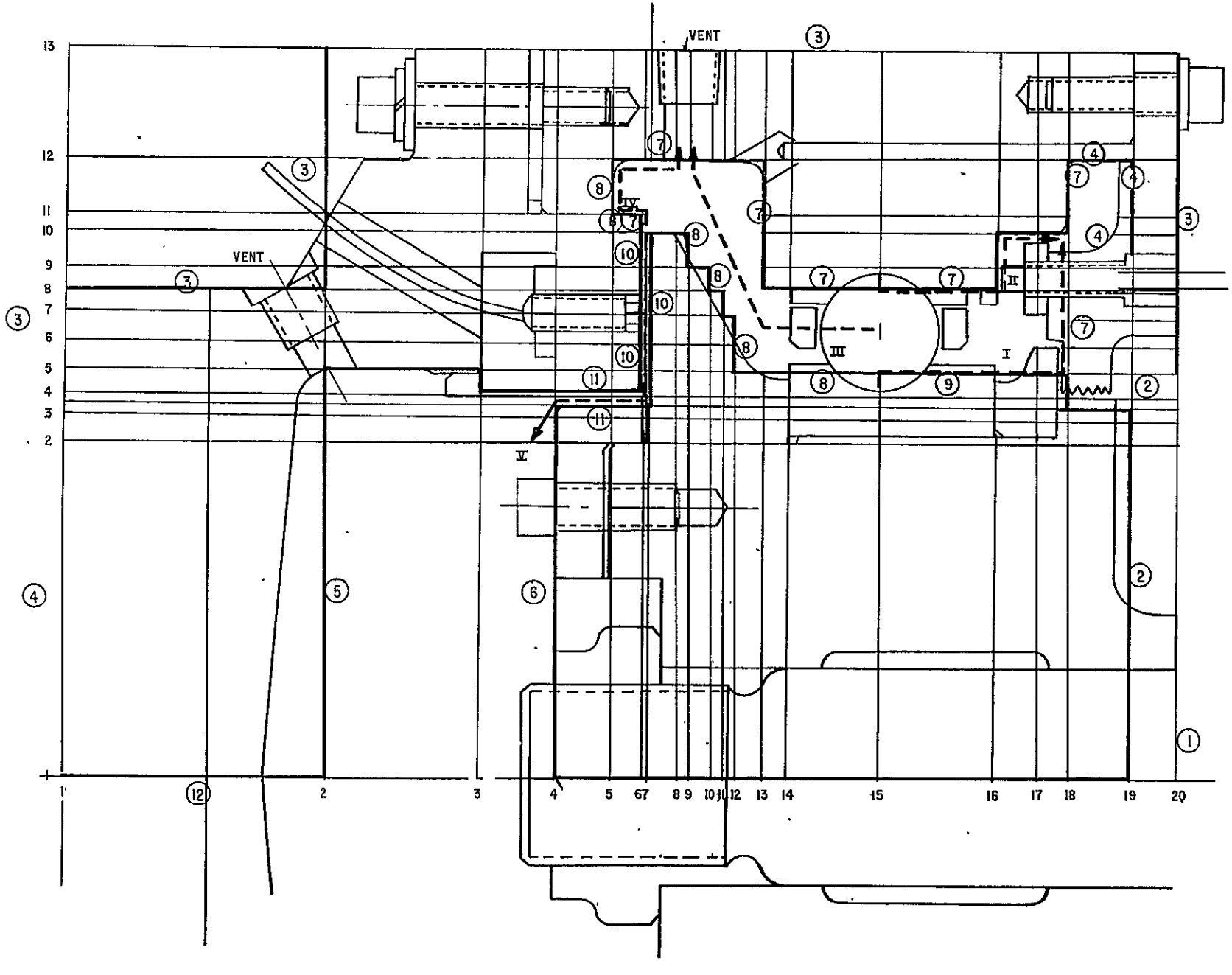

Fig. 39 Boundary Condition Types and Forced Convection Flows for Planar Hybrid Boost Bearing.

MTI-9193

TABLE V

$100^{\circ}F$ ($37^{\circ}C$) INLET TEMPERATURE PLANAR BEARING THERMAL MAPPING

Runner Rotational Speed	10,000 rpm
Fail-Safe Clearance	0.001 in (.0254 mm)
Lubricant Inlet Pressure	50 psig (34.3×10^4 Newtons/m^2)
Lubricant Inlet Temperature	$100^{\circ}F$ ($37^{\circ}C$)
Lubricant Inlet Viscosity	1.45×10^{-6} reyn (10 cp)

Lubricant Flow Data:

Flow Stream No.	Lubr. Specific Heat BTU/lb-F (joule/kg°C)	Flow Rate GPM (m^3/sec x 10^4)	Heat Capacity BTU/hr (joule/sec)
I	0.56 (2340)	0.375 (.236)	88.0 (25.8)
II	0.56 (2340)	0.375 (.236)	88.0 (25.8)
III	0.56 (2340)	0.75 (.472)	176.0 (51.6)
IV	0.56 (2340)	9.7 (6.11)	2200.0 (645)
V	0.56 (2340)	9.2 (5.79)	2110.0 (618)

Heat Generation Data:

Ball Bearing Power Loss	6.3 HP
Fluid-Film Bearing Power Loss	18.4 HP

Boundary Condition Data:

Boundary Condition No.	Type	Ambient Temp. °F (°C)	Film Coefficient BTU/hr-ft^2-°F (joule/sec.-m^2-°C)
1	Const. Temp.	200 (93)	—
2	Nat. Conv.	140 (60)	15.0 (85)
3	Nat. Conv.	80 (27)	2.5 (14.2)
4	Nat. Conv.	100 (37)	5.0 (28.4)
5	Nat. Conv.	110 (44)	8.0 (45.3)
6	Nat. Conv.	110 (44)	17.0 (96.3)
7	Forced Conv.	—	15.0 (85)
8	Forced Conv.	—	30.0 (170)
9	Forced Conv.	—	30.0 (170)
10	Forced Conv.	—	500.0 (2830)
11	Forced Conv.	—	350.0 (1980)
12	Insulated	—	—

TABLE VI

300°F (149°C) INLET TEMPERATURE PLANAR BEARING THERMAL MAPPING

Runner Rotational Speed	1000 rpm
Fail-Safe Clearance	0.001 in. (.0254 mm)
Lubricant Inlet Pressure	50 psig (34.3×10^4 Newtons/m^2)
Lubricant Inlet Temperature	300°F (149°C)
Lubricant Inlet Viscosity	0.21×10^{-6} reyn (1.44 cp)

Lubricant Flow Data:

Flow Stream No.	Lubr. Specific Heat BTU/lb-F (joule/kg°C)	Flow Rate GPM (m^3/sec x 10^4)	Heat Capacity BTU/hr (joule/sec.)
I	0.56 (2340)	0.375 (.236)	88.0 (25.8)
II	0.56 (2340)	0.375 (.236)	88.0 (25.8)
III	0.56 (2340)	0.75 (.472)	176.0 (51.6)
IV	0.56 (2340)	10.2 (6.3)	2410.0 (706)
V	0.56 (2340)	10.0 (6.2)	2320.0 (680)

Heat Generation Data:

Ball Bearing Power Loss	4.5 HP
Fluid-Film Bearing Power Loss	10.2 HP

Boundary Condition Data:

Boundary Condition No.	Type	Ambient Temp. °F (°C)	Film Coefficient BTU/hr-ft^2-°F (Joule/sec.-m^2-°C)
1	Const. Temp.	200 (93)	–
2	Nat. Conv.	140 (60)	15.0 (85)
3	Nat. Conv.	80 (27)	2.5 (14.2)
4	Nat. Conv.	100 (37)	5.0 (28.4)
5	Nat. Conv.	285 (141)	8.0 (45.3)
6	Nat. Conv.	285 (141)	17.0 (96.3)
7	Forced Conv.	–	15.0 (85)
8	Forced Conv.	–	30.0 (170)
9	Forced Conv.	–	30.0 (170)
10	Forced Conv.	–	500.0 (2830)
11	Forced Conv.	–	350.0 (1980)
12	Insulated	–	–

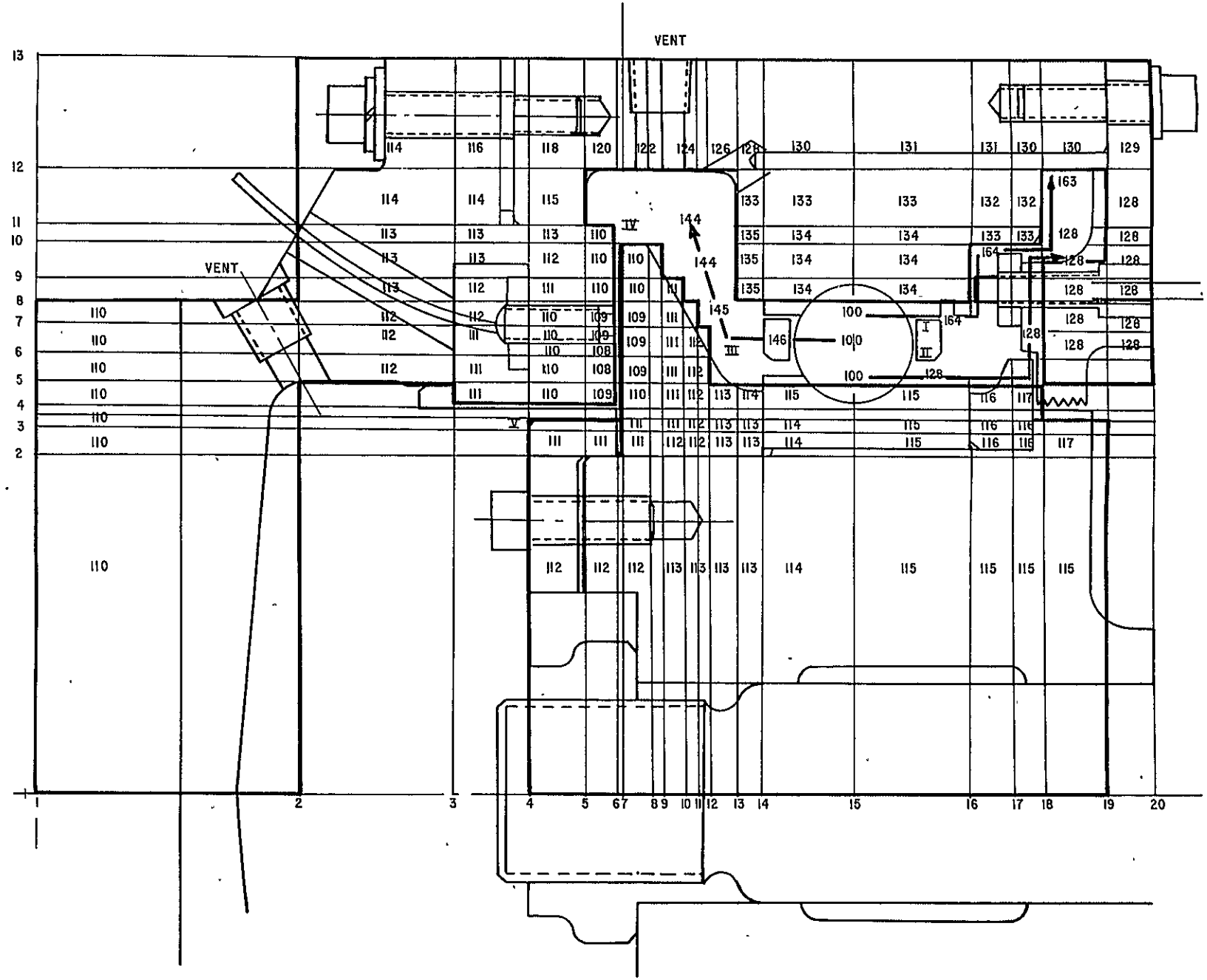

Fig. 40 Planar Hybrid Boost Thermal Map with 100 F Lubricant Inlet.

MTI-9192

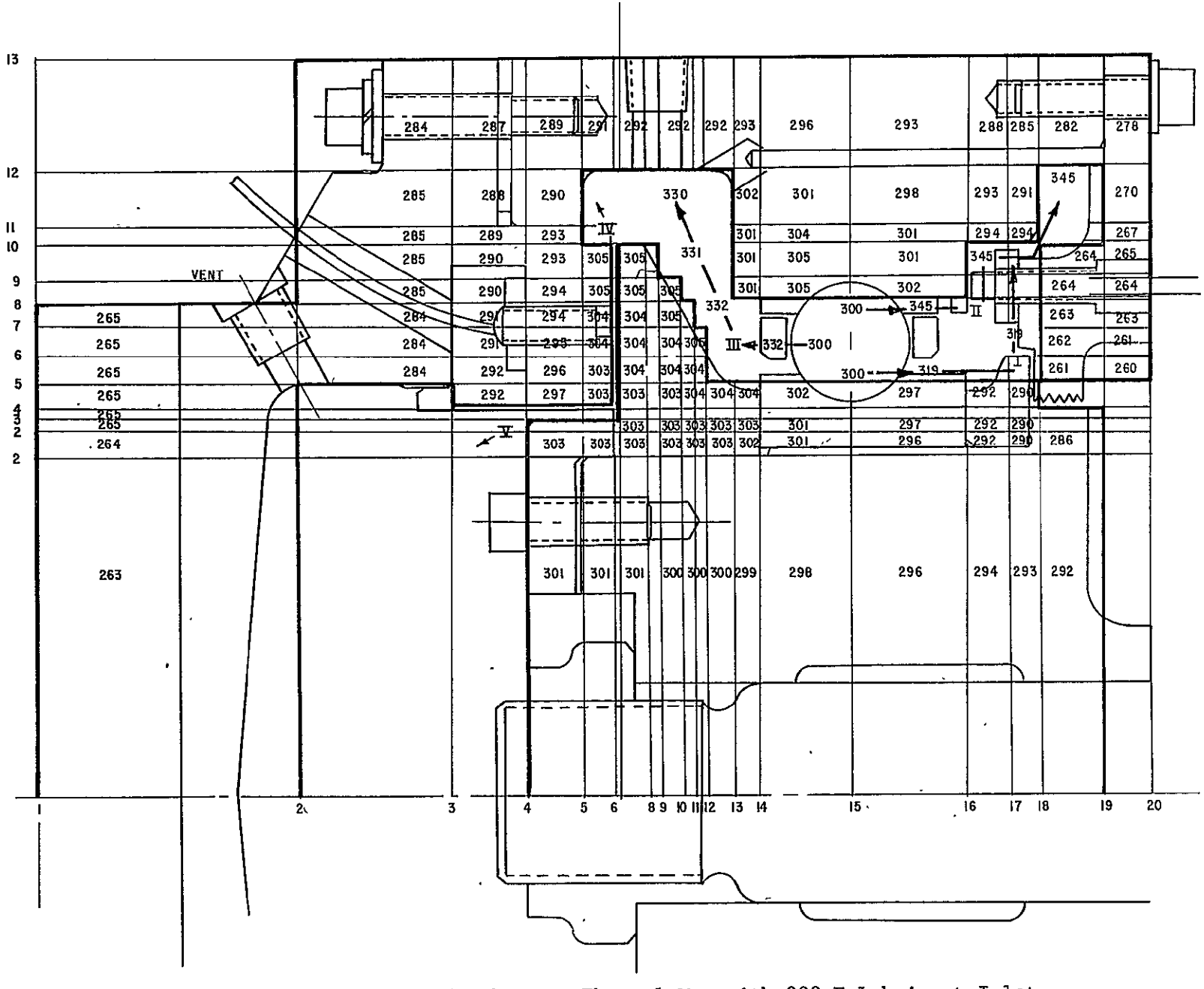

Fig. 41 Planar Hybrid Boost Thermal Map with 300 F Lubricant Inlet

may become critical should fits be looser than desired. This in fact may be the case around the bearing outer race mounting cartridge, which will deflect slightly under axial loading.

In general, the thermal predictions look reasonable, and provide no indication that operation of the planar hybrid boost bearing will be other than satisfactory.

3.2.1.2 Conical Bearing Configuration

The finite element thermal model utilized in thermal mapping studies for the conical hybrid boost configuration with axial fail-safe clearance of 0.001 in. (.0254 mm) and 6.5 in. (165.1 mm) outer diameter is similar to that shown in Fig. 39 for the planar configuration. Boundary condition types and forced convection flows are located as before. The major difference is in the representation of the thrust surface. Computer program input limitations required that the 45 degree thrust surface be modeled as a series of short steps for the thermal calculations. While such a procedure does obviously affect the local temperatures near the thrust surface, the use of an adequate number of grids, in the region should prevent the thrust surface representation from affecting the overall conditions within the runner and stator.

The boundary condition values for the 100°F (37°C) and 300°F (149°C) lubricant inlet temperatures are shown in Tables VII and VIII for the conical hybrid configuration. The results of the thermal mapping calculations for the two extremes are present in Figs. 42 and 43.

Note in both figures the relatively low axial thermal gradients which exist in both runner and stator, as was the case in the planar bearing. Now, however, radial gradients on the order of 10-20° F (6-11°C) exist in the runner.

Again the forced convection flows through the ball bearing appear

TABLE VII

100^{o}F (37^{o}C) INLET TEMPERATURE CONICAL BEARING
(6.5 in. (165.1 mm) outer diameter) THERMAL MAPPING

Runner Rotational Speed	10,000 rpm
Fail-Safe Clearance	0.001 in. (.0254 mm)
Lubricant Inlet Pressure	50 psig (34.3×10^{4} Newtons/m^2)
Lubricant Inlet Temperature	100^{o} F (37^{o}C)
Lubricant Inlet Viscosity	1.45×10^{-6} reyn (10 cp)

Lubricant Flow Data:

Flow Stream No.	Lubr. Specific Heat BTU/lb-F (joule/kg^{o}C)	Flow Rate GPM (m^3/sec. x 10^4)	Heat Capacity BTU/hr (joule/sec)
I	0.56 (2340)	0.375 (.236)	88.0 (25.8)
II	0.56 (2340)	0.375 (.236)	88.0 (25.8)
III	0.56 (2340)	0.75 (.472)	176.0 (51.6)
IV	0.56 (2340)	3.3 (2.07)	767.0 (225)
V	0.56 (2340)	3.1 (1.94)	737.0 (216)

Heat Generation Data:

Ball Bearing Power Loss	6.3 HP
Fluid-Film Bearing Power Loss	16.9 HP

Boundary Condition Data:

Boundary Condition No.	Type	Ambient Temp. ^{o}F (^{o}C)	Film Coefficient BTU/hr-ft^2 - ^{o}F (joule/sec.-m^2-^{o}C)
1	Const. Temp.	200 (93)	–
2	Nat. Conv.	140 (60)	15.0 (85)
3	Nat. Conv.	80 (27)	2.5 (14.2)
4	Nat. Conv.	100 (37)	5.0 (28.4)
5	Nat. Conv.	110 (44)	8.0 (45.3)
6	Nat. Conv.	110 (44)	17.0 (96.3)
7	Forced Conv.	–	15.0 (85)
8	Forced Conv.	–	30.0 (170)
9	Forced Conv.	–	30.0 (170)
10	Forced Conv.	–	500.0 (2830)
11	Forced Conv.	–	350.0 (1980)
12	Insulated	–	–

TABLE VIII

300°F (149°C) INLET TEMPERATURE CONICAL BEARING
(6.5 in. (165.1 mm) outer diameter) THERMAL MAPPING

Runner Rotational Speed	10,000 rpm
Fail-Safe Clearance	0.001 in. (.0254 mm)
Lubricant Inlet Pressure	50 psig (34.3×10^4 Newtons/m^2)
Lubricant Inlet Temperature	300°F (149°C)
Lubricant Inlet Viscosity	0.21×10^{-6} reyn (1.44 cp)

Lubricant Flow Data:

Flow Stream No.	Lubr. Specific Heat BTU/lb-F (joulé/kg°C)	Flow Rate GPM (m^3/sec. x 10^4)	Heat Capacity BTU/hr (joule/sec.)
I	0.56 (2340)	0.375 (.236)	88.0 (25.8)
II	0.56 (2340)	0.375 (.236)	88.0 (25.8)
III	0.56 (2340)	0.75 (.472)	176.0 (51.6)
IV	0.56 (2340)	4.2 (2.64)	982.0 (288)
V	0.56 (2340)	4.0 (2.52)	943.0 (276)

Heat Generation Data:

Ball Bearing Power Loss	4.5 HP
Fluid-Film Bearing Power Loss	7.9 HP

Boundary Condition Data:

Boundary Condition No.	Type	Ambient Temp. °F (°C)	Film Coefficient BTU/hr-ft^2 - °F (joule/sec.-m^2-°C)
1	Const. Temp.	200 (93)	—
2	Nat. Conv.	140 (60)	15.0 (85)
3	Nat. Conv.	80 (27)	2.5 (14.2)
4	Nat. Conv.	100 (37)	5.0 (28.4)
5	Nat. Conv.	285 (141)	8.0 (45.3)
6	Nat. Conv.	285 (141)	17.0 (96.3)
7	Forced Conv.	—	15.0 (85)
8	Forced Conv.	—	30.0 (170)
9	Forced Conv.	—	30.0 (170)
10	Forced Conv.	—	500.0 (2830)
11	Forced Conv.	—	350.0 (1980)
12	Insulated	—	—

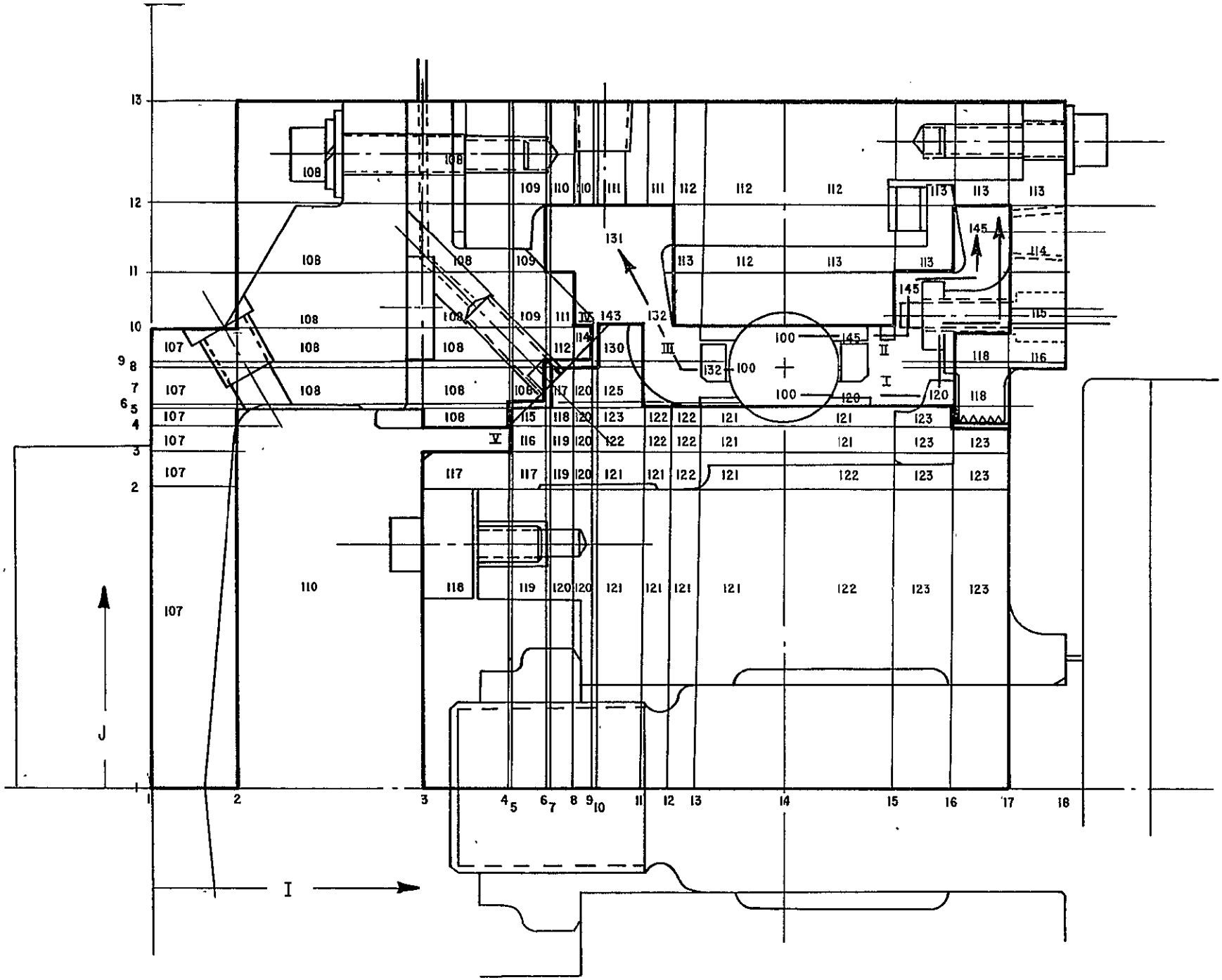

Fig. 42 Conical Hybrid Boost Thermal Map with 100 F Lubricant Inlet. (D_o = 6.5 inches).

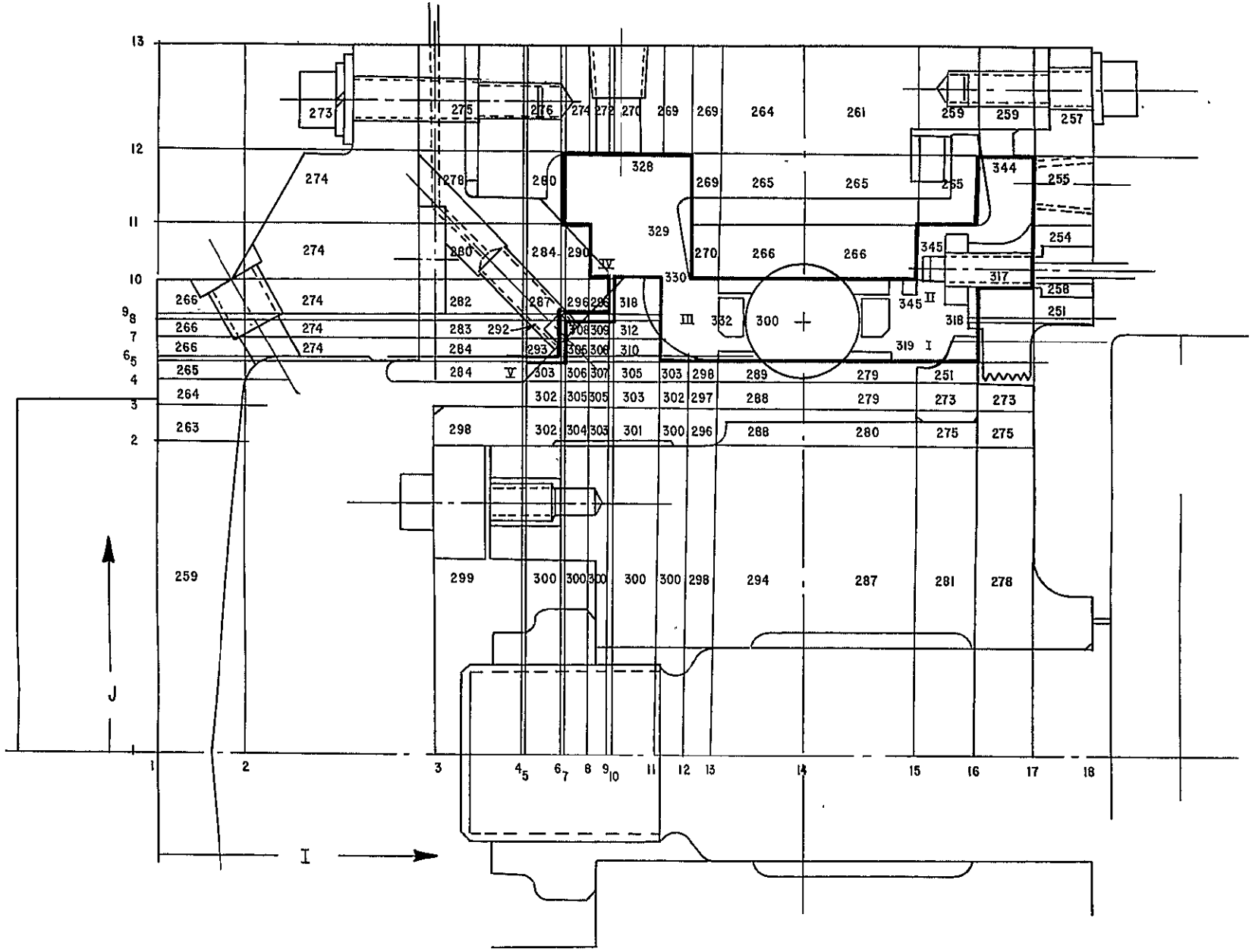

Fig. 43 Conical Hybrid Boost Thermal Map with 300 F Lubricant Inlet (D_o=6.5 inches).

MTI-9195

to be serving the important function of heat removal, judging by the elevated temperatures about 30°F (17°C) in the 100°F (37°C) case and approximately 50-60°F (28-33°C) in the 300°F (149°C) case. In the latter case, it appears that the introduction of the ball bearing lubricant at 300°F (149°C) is the major reason for the elevated lubricant temperatures.

The peak metal temperatures in both the 100°F (37°C) and 300°F (149°C) lubricant inlet conditions appear in the runner for the conical bearing, whereas in the planar bearing they appeared in the area of the outer ball bearing race. The reason for this difference may be seen by comparing Table V with Table VII, and Table VI with Table VIII. In these comparisons it will be noted that while the power loss in the fluid film component is roughly the same for the two configurations, the heat removal capacity of the conical bearing is only one-third to one-half that of the planar. This is due solely to the lower lubricant flow rates of the conical bearing. In general, the predictions appear reasonable, and no indication appears that operation of the conical hybrid boost bearing configuration will be other than satisfactory.

3.2.2 Thermoelastic Deformation Analysis

Thermoelastic deformation calculations were performed for both runner and stator for the hybrid boost bearing planar and conical configurations. Each component was subjected to a 3000 lb. (13,350 Newtons) thrust load alone, the thrust load combined with the 100°F (37°C) lubricant inlet temperature thermal distribution at 10000 rpm, and the thrust load combined with the 300°F (149°C) lubricant inlet temperature thermal distribution at 10000 rpm. In addition, the effect of rotational speed alone was calculated for the planar runner.

3.2.2.1 Planar Bearing Configuration

The thermoelastic deformation model for the planar bearing runner is shown in Fig. 44. The runner centerline is at the top, and

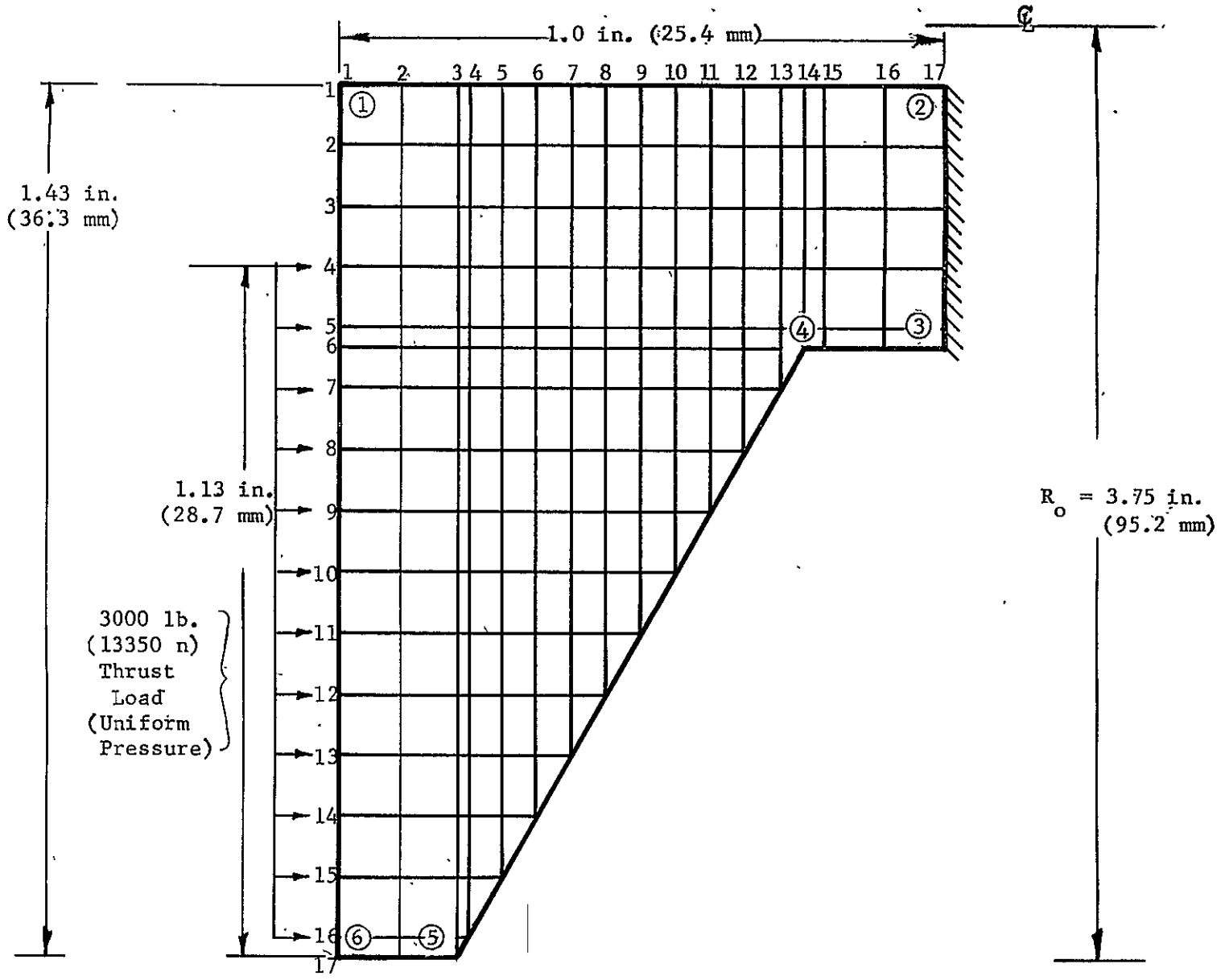

Fig. 44 Planar Hybrid Boost Bearing Runner Thermal Deformation Model

MTI-9130

axial restraint is provided at the right edge between model stations 2 and 3 as shown. Bearing thrust load is applied along the left edge between grid points (17,1) and (4,1), as indicated by the arrows. Temperature distributions calculated earlier are applied at the grids.

The planar runner thermal deformation calculations indicate that the 3000 lb. (13,350 Newtons) thrust force alone causes a departure from flatness of less than .0001 in. (.0025 mm), with a deflection such that the bearing would open outward. With 100°F (37°C) lubricant inlet conditions and 3000 lb. (13,350 Newtons) thrust load, the thrust surface remains flat within 8×10^{-5} in. (.00203 mm), (without rotation, bearing opens inward and vice versa). The effect of rotation at 10,000 rpm acts to oppose the temperature gradient effects, resulting in a maximum axial deflection of .0001 in. (.0025 mm) at the outer radius due to this cause (open outward). With 300°F (149°C) lubricant inlet conditions as well as thrust and rotation, the planar runner begins to depart more significantly from the flat condition, with an axial deflection difference of 0.0005 in. (.0127 mm) between the inner and outer radii (opening outward). Thus, the bearing axial clearance is greater at the outside than at the inside.

The thermoelastic deformation model for the planar bearing stator and housing is shown in Fig. 45. The housing centerline is again at the top, and axial restraint is provided along the left edge between grids 1 and 2 as shown. Bearing thrust load is applied between model points 6 and 7 (grid points (4,10), and (10,10) as shown. Temperature distributions calculated earlier are applied at the grids.

Planar housing thermal deformation calculations were performed for the three load conditions indicated above. Little, if any deviation from a flat surface was noted for each case.

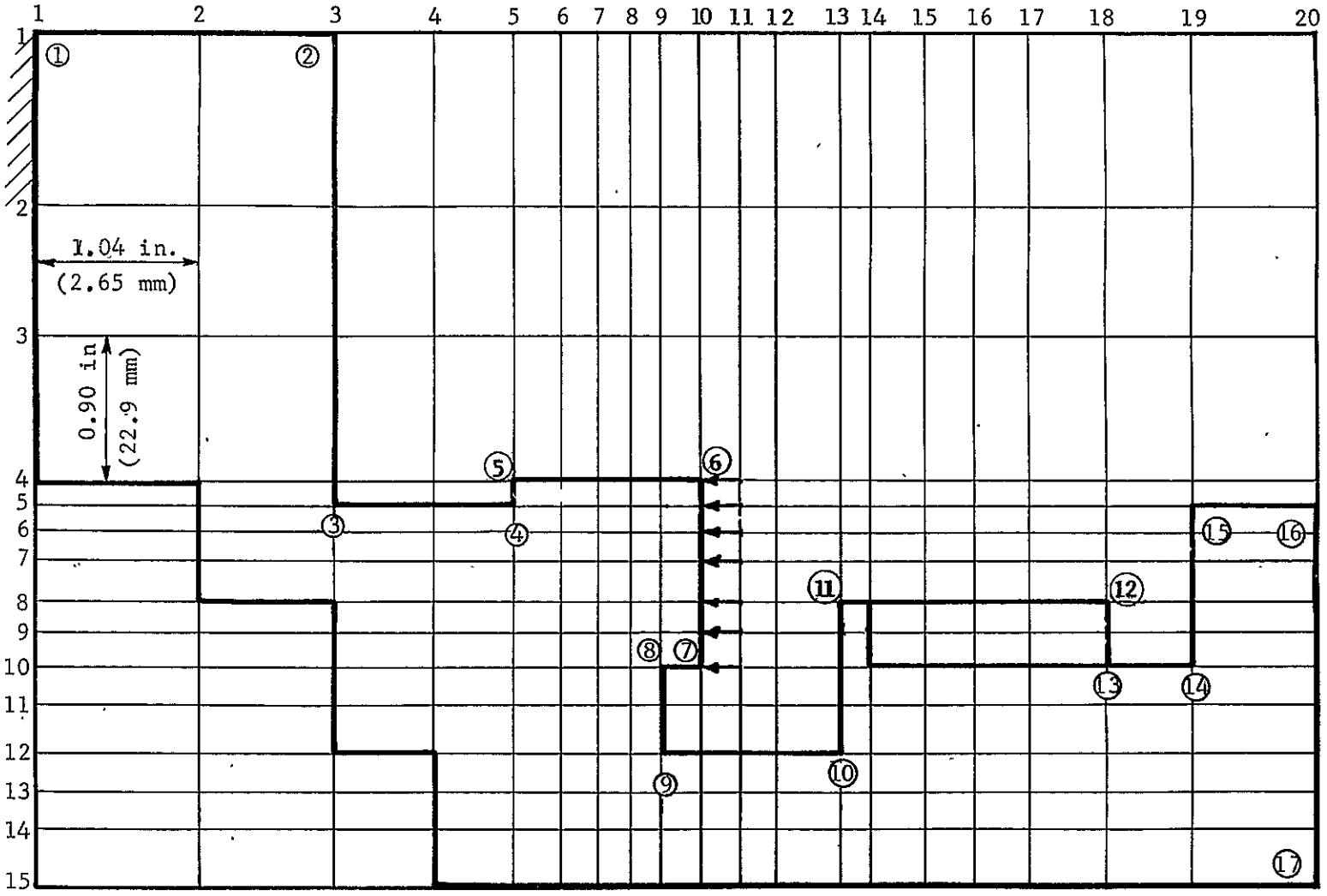

Fig. 45 Planar Hybrid Boost Bearing Housing Thermal Deformation Model.

On the basis of the foregoing results, in which a maximum relative axial deformation of 0.0005 in. (.0127 mm) was predicted for the outer radius of the runner (opening outward), little, if any degradation of performance of the planar configuration should result because of deformations in or near the bearing surfaces.

3.2.2.2 Conical Bearing Configuration

The thermoelastic deformation model for the conical bearing runner calculations is shown in Fig. 46. The thrust area diagonal boundaries may be modeled exactly for this calculation, and thus no need exists for the step approximations used in the thermal mapping calculations. Again, the axis of revolution is at the top and the thrust area, between model points 10 and 11, as indicated by the arrows. Axial restraint is provided at the right edge and radial restraint at the inner radius, as shown. For reference, points on the boundary of the model are again indicated by number. Bearing pressure loading is as indicated by the arrows between model points 10 and 11. Temperature distributions calculated earlier are then applied at the grids.

Thermal deformation calculations were performed for the conical runner for the three loading conditions considered earlier: thrust, thrust with 100°F (37°C) lubricant inlet temperature and thrust with 300°F (149°C) lubricant inlet temperature. While the deviation from a flat surface was important for the planar bearing, the key quantity here is the deviation of the bearing surface from a true 45 degree cone. With the thrust load alone, the maximum axial and radial components of deflection of the runner thrust surface were less than 10^{-5} in. (.00025 mm). The results of the runner deformation calculations for the other two loading conditions are presented, together with those for the housing, in Figs. 48 and 49 in order to facilitate comparison. These figures are discussed below.

The thermoelastic deformation model for the conical bearing stator

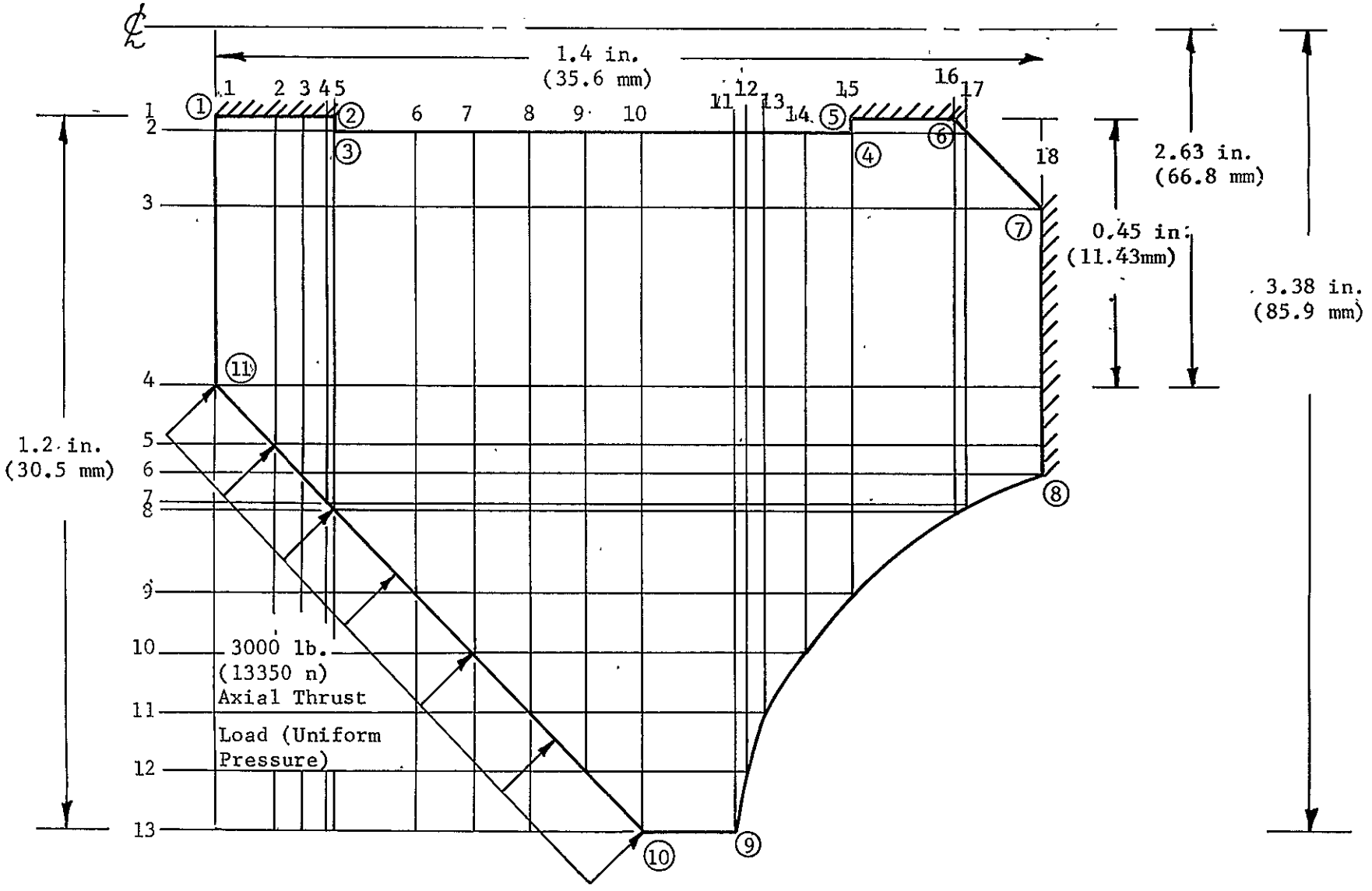

Fig. 46 Conical Hybrid Boost Bearing Runner Thermal Deformation Model

MTI-9187

and housing is shown in Fig. 47. The housing centerline is again at the top and axial restraint is provided along the left edge between grids 1 and 2 as shown. Bearing thrust load is applied between model points 6 and 7 as indicated by the arrows. Temperature distributions calculated earlier are applied at the grids. Thermal deformation calculations were performed for the three loading conditions indicated above.

With the thrust load alone, the maximum axial and radial components of deflection of the housing thrust surface were less than 10^{-4} in. (.0025 mm). The results of the housing deformation calculations for the other loading conditions are presented with the results of the runner calculations in Figs. 48 and 49 for comparison.

In Figs. 48 and 49, the displacement and distortion of the thrust surfaces, which are indicated by the relative locations of the "original" and "deformed" thrust surfaces (deformation scale) may be interpreted as the change in dimensions from the fixed boundaries of the appropriate model, and should be viewed in that light. The important quantities to be noted are the effect of the imposed conditions on the thrust surface flatness and deviation from the true 45 degree cone. The absolute motion of the thrust surface during operation is an independent variable which may be controlled during testing to obtain the desired loading. Note that in each case, the parallelism of the surfaces is not materially altered by the combined temperature, speed, and thrust force effects.

On the basis of the foregoing results, no degradation in conical bearing performance should result because of deformations in or near the bearing surfaces.

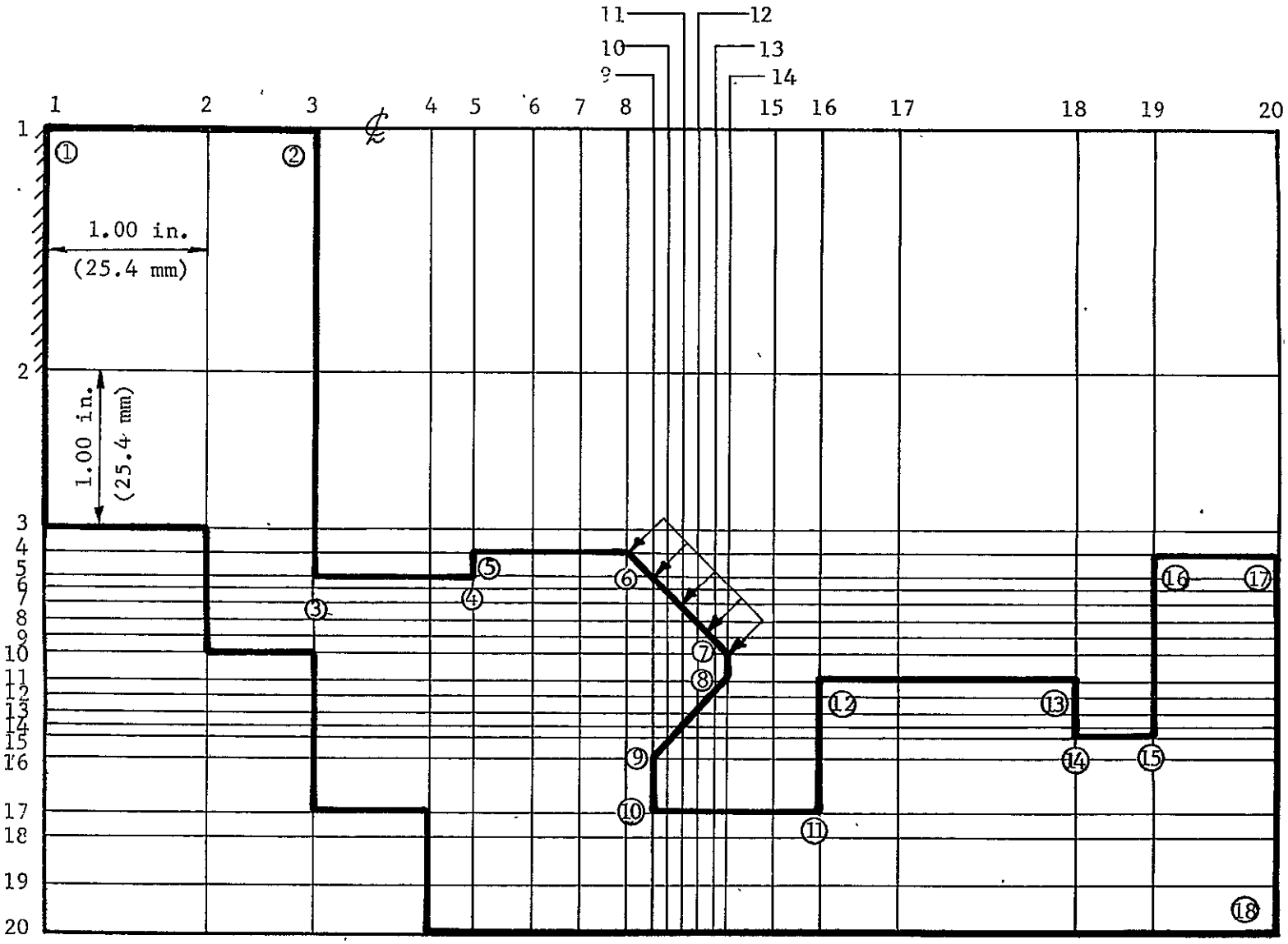

Fig. 47 Conical Hybrid Boost Bearing Housing Thermal Deformation Model.

MTI-9188

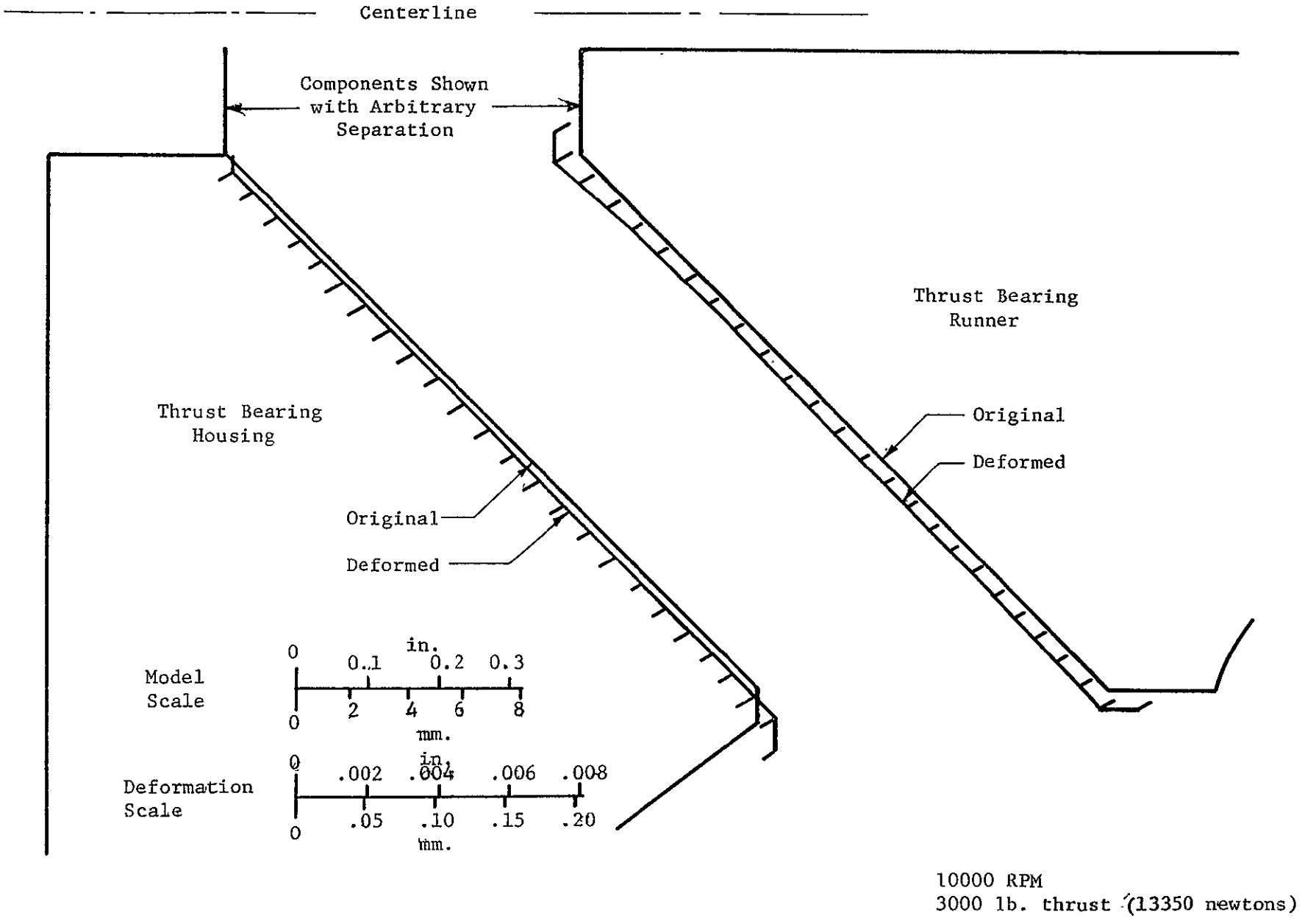

Fig. 48 Conical Hybrid Boost Bearing Thermal Deformation Results - 100 F (37.8C) Lubricant Inlet Temrerature

MTI-9189

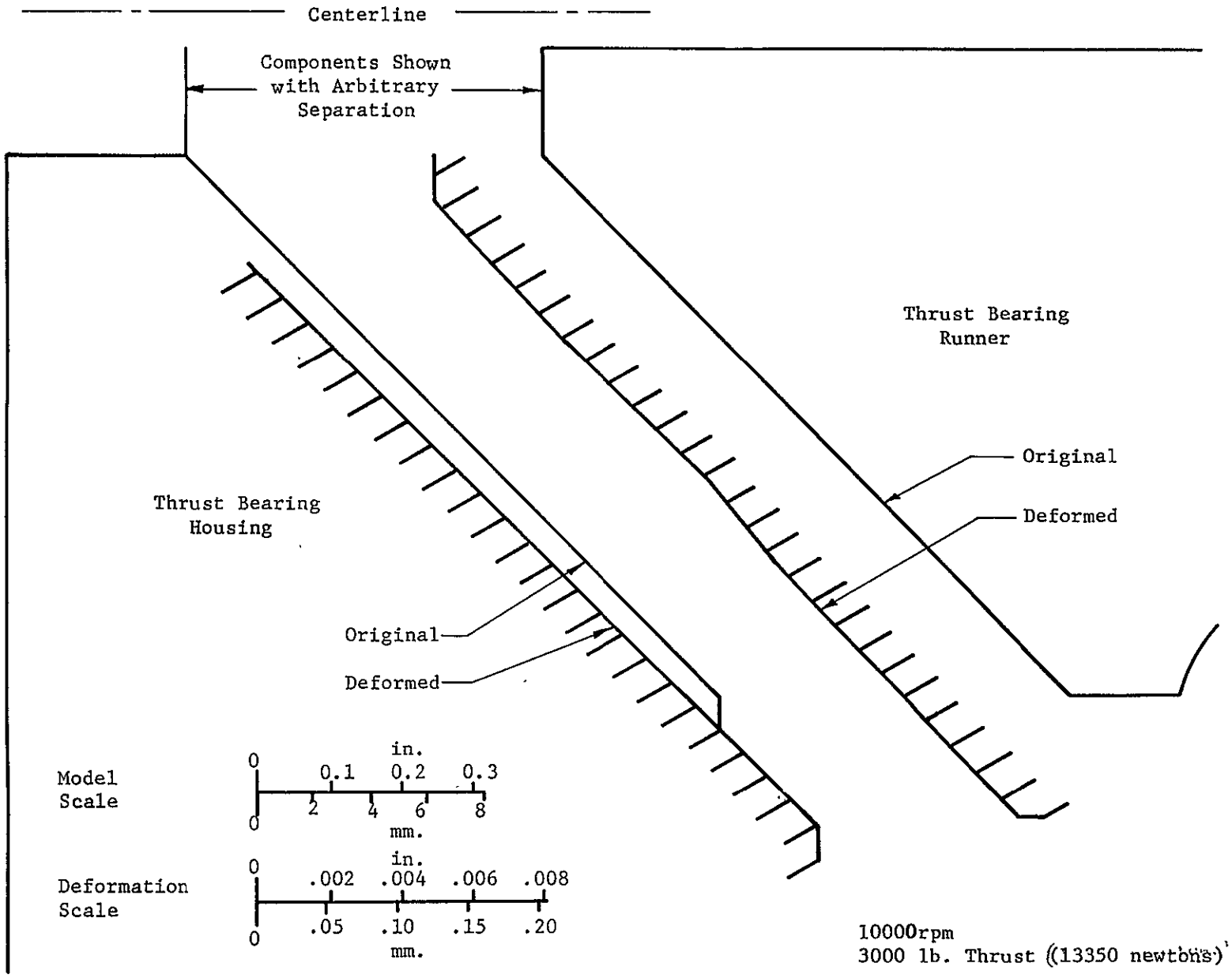

Fig. 49 Conical Hybrid Boost Bearing Thermal Deformation Results - 300 F (148.9C) Lubricant Inlet Temperature.

MTI-9199

3.2.3 Ball Bearing Outer-Race Retainer Cartridge Design

During preliminary design of the hybrid-boost bearing test rig, it appeared that the device used for axial loading of the ball bearing outer race would interfere with the axial flow of lubricating oil from the ball bearing. In addition, relatively large amounts of axial deflection appeared likely to result from the cantilever ring geometry utilized under earlier, lower thrust load tests of a similar bearing. A cylindrical retainer, loaded in tension, was thus designed to apply the axial thrust load to the outer race. Several potential designs were evaluated analytically. Axial deflections under 3000 lb (13,350 newtons) loading were calculated for each. The final design exhibits less than 0.0001 in (2.54×10^{-3} mm) deflection between thrust surfaces under these conditions.

Figure 50 shows a cross-sectional view through half of the analytical model of the axisymmetric retainer, showing the axis of symmetry at the top. The grid used for the calculations is shown, together with points (denoted by circled numbers) at which axial deformation is examined. A plot of axial deformation for the final design is shown in Fig. 51. Note particularly the deflections of points 3 and 4 and of points 10 and 11, the two areas where thrust loading is applied. Approximately 30 microinches (7.6×10^{-4} mm) of coning is apparent at each thrust application point due to the cantilever ring effect, while total axial deformation between point 4 (assumed fixed in axial and radial directions) and point 11 is about 55 microinches (13.9×10^{-4} mm). These results are satisfactory from the standpoint of system flexibility requirements, which dictate a high axial stiffness for this member.

3.2.4 Ball Bearing Preload Spring Design

The preload spring configuration used is shown in Fig. 52. This circular spring can be divided into four equal beams. The stiffness of each beam can be calculated from

$$\frac{W}{\delta_S} = \frac{192\ EI}{L^3} \qquad (6)$$

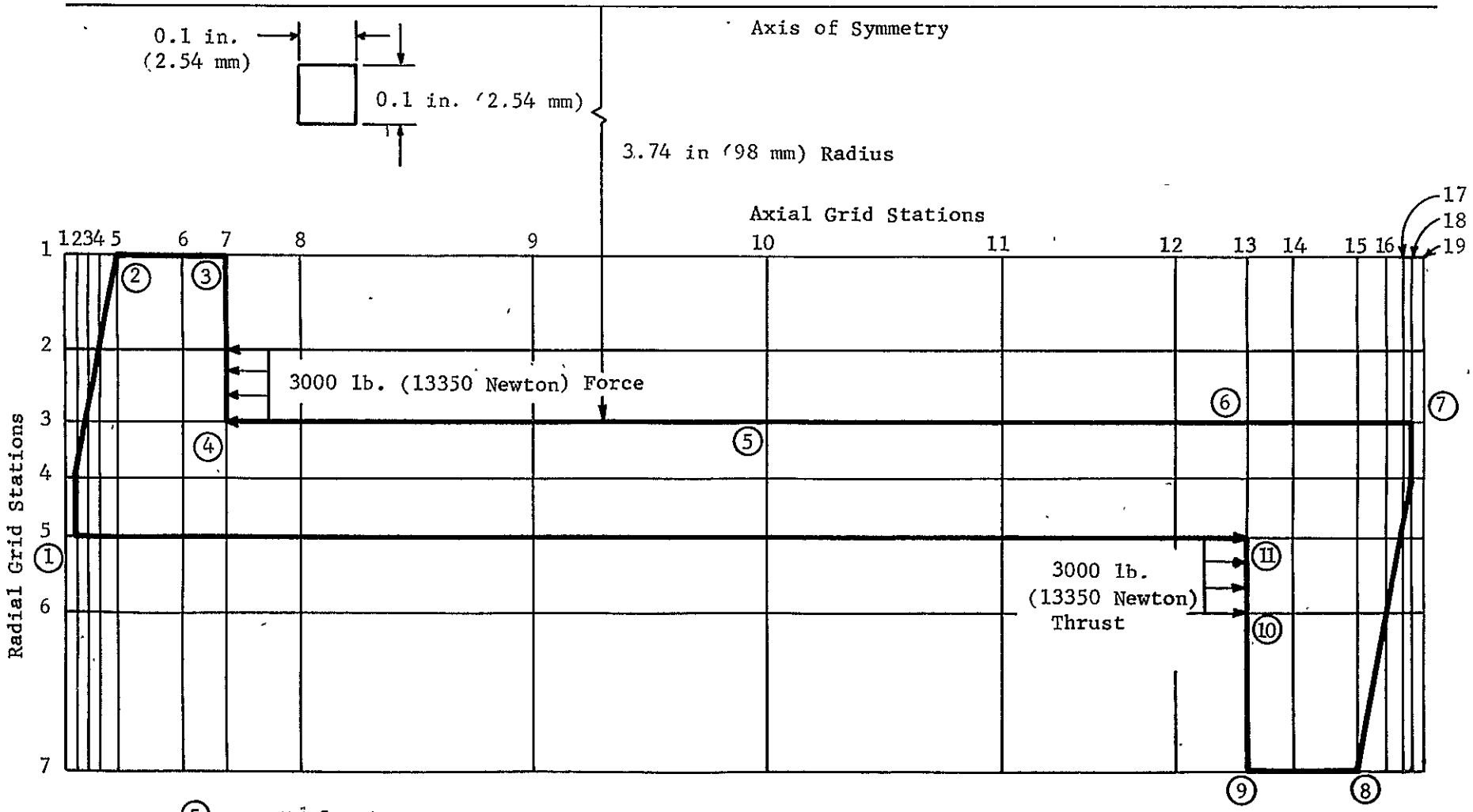

(5) - Model Station Number

Shear Modulus = 1.15×10^6 psi (7.93×10^9 Newton/m^2)
Poisson Ratio = 0.3
Thermal Expansion Coefficient = 6.4×10^{-6} in/in$^\circ$F (11.5×10^{-6} mm/mm$^\circ$C)
Density = 0.28 lb/in^3 (20 kg/m^3)
Uniform Temperature

Fig. 50 Thermoelastic Deformation Model for Ball Bearing Outer-Race Retainer Cartridge

MTI-9198

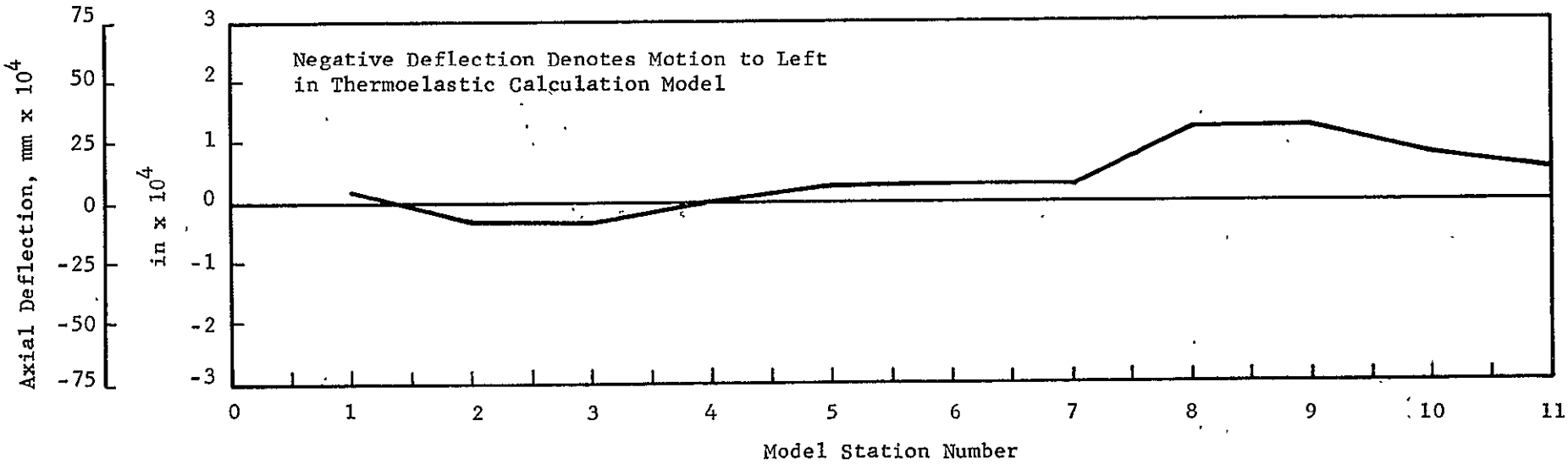

Fig. 51 Axial Deformation at Various Points on Ball Bearing Outer-Race Retainer Under 3000 lb (13350 Newton) Axial Load

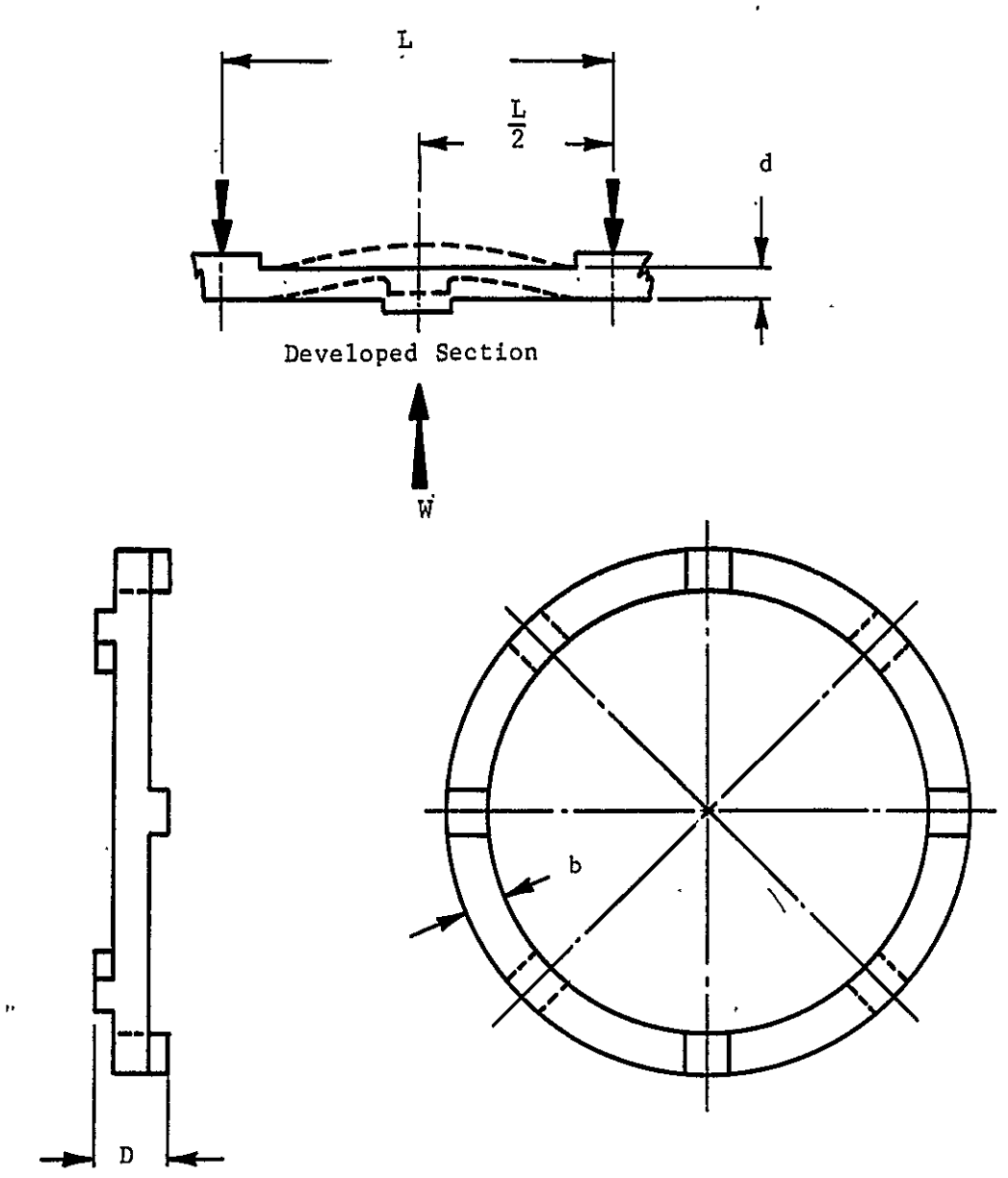

Fig. 52 Preload Spring Drawing (not to scale)

where $I = \frac{b\ d^3}{12}$

$$K_S = \frac{W}{\delta_S} = \frac{16\ E\ bd^3}{L^3} \qquad (7)$$

Substituting $E = 30 \times 10^6$ psi (20.6×10^{10} newtons/m^2), b = 0.3125 inches (7.9 mm), d = 0.185 inches (4.7 mm) and L = 6.63 inches (168 mm) into Equation (7),

$$\frac{W}{\delta_S} = K_S = 3250 \text{ lb/in } (5.72 \times 10^5 \text{ newtons/m}) \qquad (8)$$

Since four parallel beams constitute the spring, the total spring stiffness is 13000 lb/in(22.8×10^5 newtons/m). A comparison between the calculated and actual preload spring stiffness is shown in Fig. 53. Considering the fact that the calculated characteristics are based upon nominal spring tolerances, the agreement between calculated and actual values is very good. Fig. 53 also shows the maximum bending stress plotted against load. The design stress is approximately 52,000 psi (3.58×10^8 newtons/m^2) reasonably low for this application.

3.2.5 Critical Speed Analysis of Hybrid-Boost Test Rig Drive Spindle

A critical speed analysis was performed on the test spindle utilized in Task III efforts prior to its fabrication. This analysis was directed at the calculation of the critical speeds of the spindle and test ball-bearing assembly as functions of the spindle mount bearing stiffness, resulting in a system critical speed map. Actual values of bearing stiffnesses were then calculated and superimposed upon the critical speed map. Intersections of the bearing stiffness and critical speed curves thus obtained provide a good indication of the actual system critical speeds.

Radial stiffness of the test ball bearing is reasonably insensitive to speed at thrust loads between 500 lbs. (2224 newtons) and 3000 lbs. (13,350 newtons). Typical values (calculated by Mr. A. B. Jones, Jones and Harris Associates, Newington, Conn.) are 110,000 lb/in. (1.925×10^7 newtons/m)

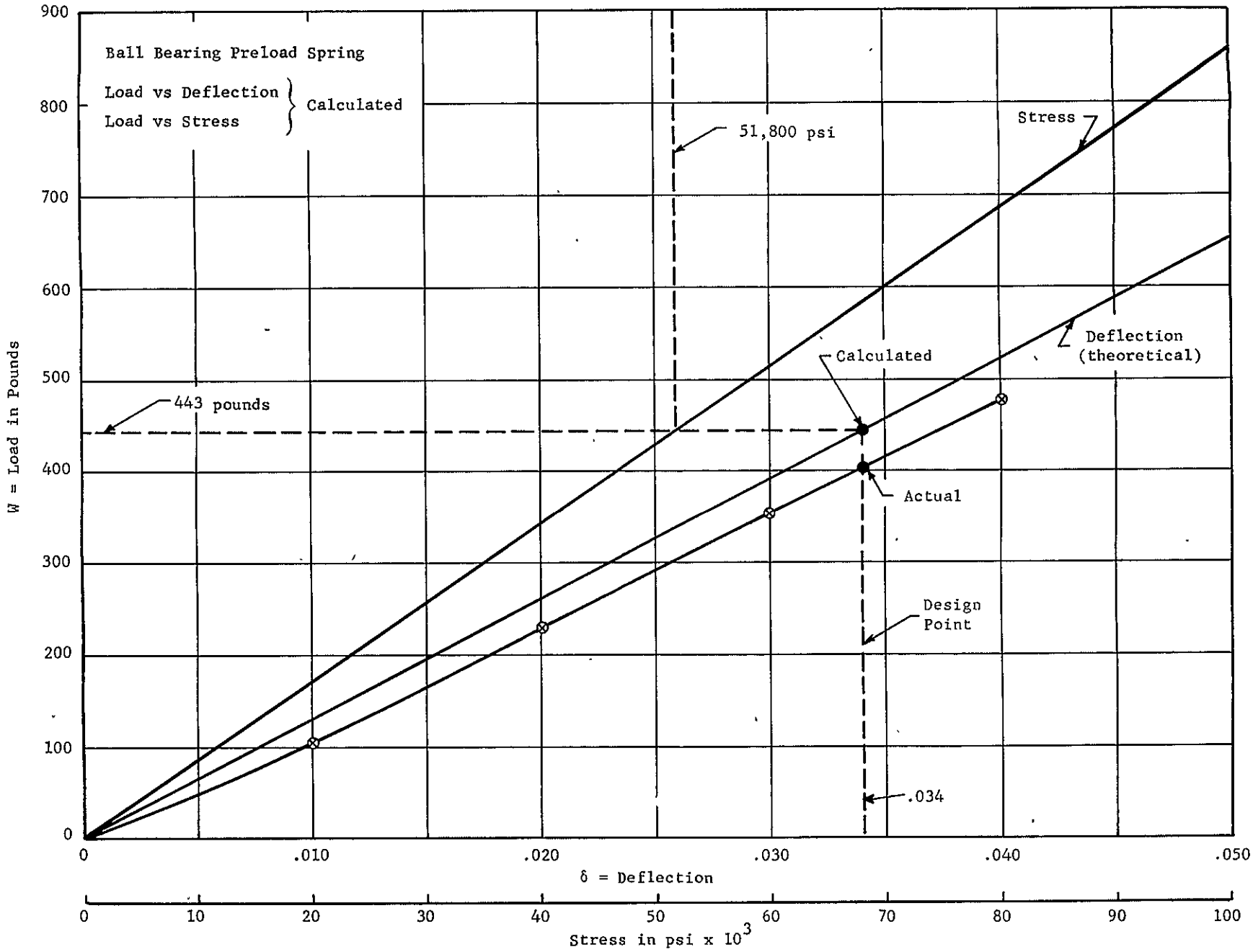

Fig. 53 Spring Load vs. Deflection and Stress for Test Ball Bearing Preload Spring

at 500 lbs. (2224 newtons), 200,000 lb/in. (3.5×10^7 newtons/m) at 1000 lbs. (4448 newtons),360,000 lb/in. (6.3×10^7 newtons/m) at 2000 lbs. (8896 newtons), and 490,000 lb/in. (8.57×10^7 newtons/m) at 3000 lb. (13,350 newtons). This stiffness was considered as a parameter in the study, with calculations done for values of 100,000 lb/in. (1.75×10^7 newtons/m), 400,000 lb/in. (7.0×10^7 newtons/m) and 1.0×10^6 lb/in. (1.75×10^8 newtons/m). The second major parameter considered was the weight of the loader housing. Estimated weight of this portion of the system was 50 lb. (22.7 kg) to 70 lbs. (31.8 kg), with critical speed mapping calculations performed for each of these values.

The four spindle support bearings were expected to be of approximately equal radial stiffness. Earlier similar spindle bearing designs were found to exhibit radial stiffnesses of between 1.6×10^6 lb/in. (2×10^8 newtons/m) at 5000 rpm and 400,000 lb/in. (7.0×10^7 newtons/m) at 25,000 rpm. Thus, for completeness the support bearing stiffness range for consideration was taken as 1×10^4 lb/in. (1.75×10^6 newtons/m) to 1×10^7 lb/in. (1.75×10^9 newtons/m).

Fig. 54 presents the most important results of the critical speed study. In this act of calculations test bearing stiffness K_B was taken as 1×10^6 lb/in. (1.75×10^8 newtons/m), and loader weight was 70 lbs. (31.8 kg). Typical speed vs. stiffness characteristics (K_1, K_2, K_3, K_4) for the spindle support bearings are shown. For this mapping calculation, K_B' and W_H were held constant at the above values) and K_1, K_2, K_3 and K_4 were varied together between 1×10^4 lb/in. (1.75×10^6 newtons/m) and 1×10^7 lb/in. (1.75×10^9 newtons/m). The resulting critical speeds were then plotted vs. stiffness. Actual increasing speed operation of the system would result in bearing stiffness values moving upward along the characteristic curves, with the first critical speed being encountered at about 11,500 to 12,000 rpm.

Similar results were obtained for other values of K_B' and W_H. This may be summarized by noting the support bearing stiffness at which the first

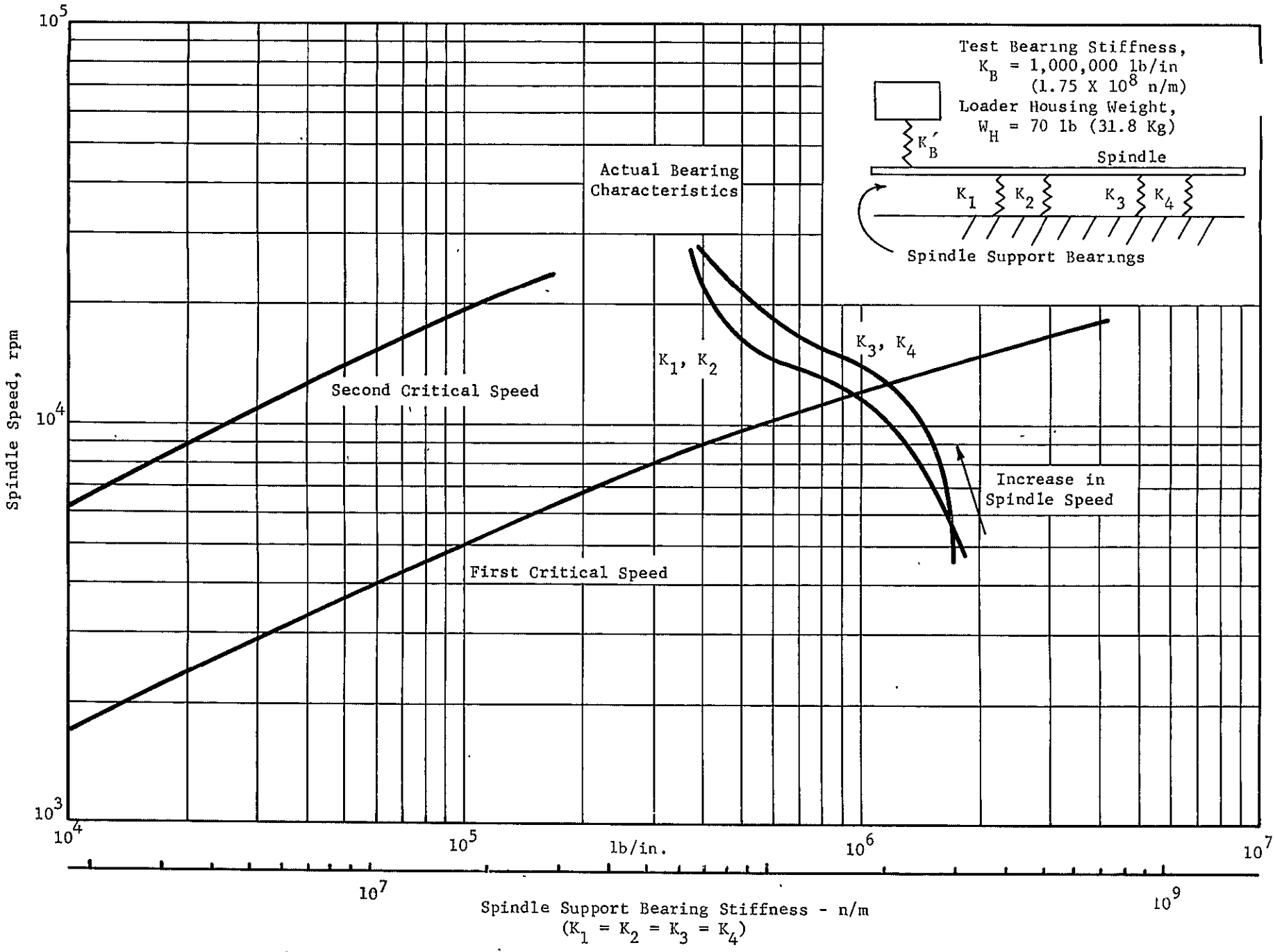

Fig. 54 Critical Speed Map - Proposed Hybrid Boost Spindle and Test Ball-Bearing System

MTI-9128

critical speed passes through 10,000 rpm, the top test speed for the system.

Loader Housing Weight - lb (kg)	Test Bearing Stiffness - lb/in (newtons/m)	Support Bearing Stiffness in lb/in (n/m) at which First Critical Speed Exceeds 10,000 rpm
50 (22.7)	400,000 (7×10^7)	530,000 (9.27×10^7)
50 (22.7)	1×10^6 (1.75×10^8)	400,000 (7×10^7)
70 (31.8)	1×10^6 (1.75×10^8)	560,000 (9.8×10^7)

While the system first critical speed exceeded the top test speed of 10,000 rpm for these three cases, it did not for the lower test ball bearing radial stiffness of 100,000 lb/in. (1.75×10^7 newtons/m)(500 lbs. (2224 newtons) thrust equivalent). In fact, two critical speeds between about 7,000 and 9,000 rpm were calculated for this case (50 lbs. (22.7 kg) loader housing). This result may at first appear to be unsatisfactory, but further examination indicates that system operation should be adequate. Of primary importance is the fact that system radial damping is neglected in the critical speed mapping calculations. In fact, significant radial damping is present, both in the spindle support bearings because of the oil mist lubrication and especially in the test ball bearing and thrust bearing area because of the thrust bearing lubricant. It was thus anticipated that little, if any, significant system vibration should be noted in this region for operation at these speeds and thrust loads because of this effect.

More important, the existance of critical speeds below 10,000 rpm is limited to only one portion of the load-speed operating regime. This condition is estimated to encompass speeds above about 7,500 rpm for thrust loads below

about 1,000 lbs. (4448 newtons) to 1500 lbs. (6670 newtons). The majority of test points are thus attainable without penetration of this critical speed area. Subsequent testing confirmed the validity of these assumptions. The criticals present at low loads and high speed were hardly detectable and did not interfere with proper operation.

3.3 Selection of Test Configuration

An appraisal of the planar and conical bearing configurations indicated that while both fluid film thrust bearing configurations would be capable of satisfactory performance as devices for reducing the axial loading on the ball bearing component, the conical thrust bearing possesses certain inherent advantages over the planar bearing. In general, the following arguments can be advanced:

1. The conical bearing has greater load capacity with equal axially-projected dimensions and film thickness. At 10,000 rpm and with 300°F (149°C), and 50 psig (34.3 x 10^4 newtons/m^2) inlet oil conditions, the following operating characteristics were calculated:

Bearing	ID in. (mm)	OD in. (mm)	Axial Film Thickness in. (mm)	Load lb. (newtons)
Planar	5.25 (133.4)	7.40 (187.96)	.0020 (.0508)	2550 (11,348)
Conical	5.25 (133.4)	7.40 (187.96)	.0020 (.0508)	3560 (15,842)

2. The conical bearing has larger axial film thickness with equal axially-projected dimensions and load capacity. At 10,000 rpm and with 300°F (149°C) and 50 psig (34.3 x 10^4 newtons/m^2) oil inlet conditions, the following operating characteristics were calculated:

Bearing	ID in. (mm)	OD in. (mm)	Axial Film Thickness in. (mm)	Load lb. (newtons)
Planar	5.25 (133.4)	7.40 (187.96)	.0020 (.0508)	2550 (11,348)
Conical	5.25 (133.4)	7.40 (187.96)	.0035 (.0889)	2550 (11,348)

The larger film thickness affords an increased safety margin for "fail-safe" operation.

3. The conical bearing possesses self alignment capability.

4. The conical configuration results in net radial forces when operation is non-concentric. While no detailed study of the interaction of these forces with the test housing has been performed, it was anticipated that the shrouded-step configuration would behave dynamically as a simple spring system. This is because the direction of each of the radial forces exerted upon the shaft by the several bearing segments is fixed with time. Hydrodynamic instability effects of the type encountered with journal bearings was thus not expected to be encountered.

5. The conical bearing surfaces are more complex than the planar surfaces, and thus would be more difficult and costly to fabricate. Preliminary estimates indicated that the present manufacturing capabilities were adequate for this task at a reasonable cost.

6. Both planar and conical bearings have similar steady-state temperature maps for representative extreme conditions of speed and lubricant inlet temperature. Thermoelastic deformation studies indicate that the conical bearing runner and housing experience considerable amounts of gross thrust surface displacement relative to the assumed fixed points on the bodies. Little deviation from the true 45 degree cone surface exists in either body, however. Thus, thermal and thermoelastic effects were not a significant factor in selection of a test configuration.

Based upon the results outlined above, and particularly upon the potential of the conical configuration as a high thrust load device, it was the recommendation of MTI that the conical fluid-film bearing with 6.5 in. (165.1 mm) outer diameter be selected as the test bearing. NASA Technical Project Management concurred in this selection, subject to the condition that the conical bearing surfaces could be manufactured successfully at reasonable cost. Subsequent investigations indicated that this was possible and manufacture was begun.

4.0 TEST FACILITY

An overall view of the test facility on which the hybrid boost bearing tests were performed is shown in Fig. 55. The facility was comprised of a test rig, auxiliary lubrication systems, heating and cooling systems, loading systems, and instrumentation. Details of the overall set-up are discussed in the following sections.

4.1 Test Facility Description

An overall schematic of the test system used is shown in Fig. 56. The system consists of a mounting base upon which a DC motor drive is mounted. The drive in turn is coupled onto a 6.34:1 step-up gear box, which in turn is coupled onto a spindle. The spindle has a overhanging cantilevered shaft on which the test bearings are mounted. The area comprising the test bearing is shown as a box marked "Test Head". The test head in turn is loaded through the use of an actuator. The test bearing is lubricated by a MIL-L-7808 oil system which is temperature controlled. The spindle is lubricated through air-oil mist lubricators and the gearbox and DC motor drives have self-contained lubricating systems.

4.1.1 Description of Test Head

An assembly drawing of the test head is shown in Fig. 57. The head consists basically of a housing (11) containing a ball bearing retainer (12) which in turn houses the test ball bearing (38). A preload spring (15) is inserted between the housing and the retainer to keep the ball bearing under load at all times so as to prevent skidding. The total preload amounts to 400 lbs. The preload spring was designed and manufactured by MTI and statically checked for its load vs. deflection characteristics. A comparison between the calculated and actual preload spring characteristics is shown in Fig. 53. A loose fit is maintained between the bearing retainer and the outer housing, while the fit between the ball bearing outer diameter to the retainer is close to line-to-line.

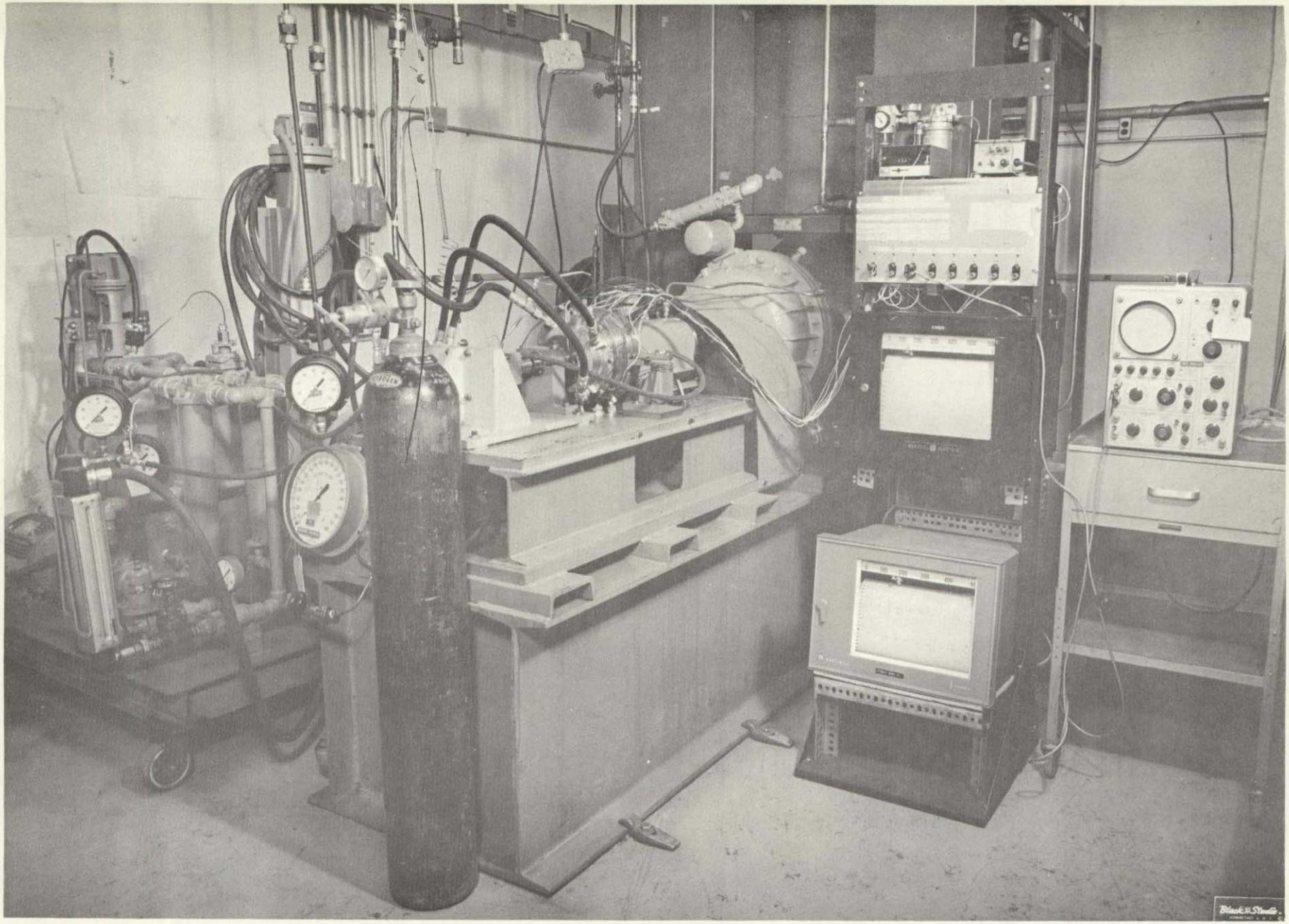

Fig. 55 Overall View of Test Facility

MTI-8899

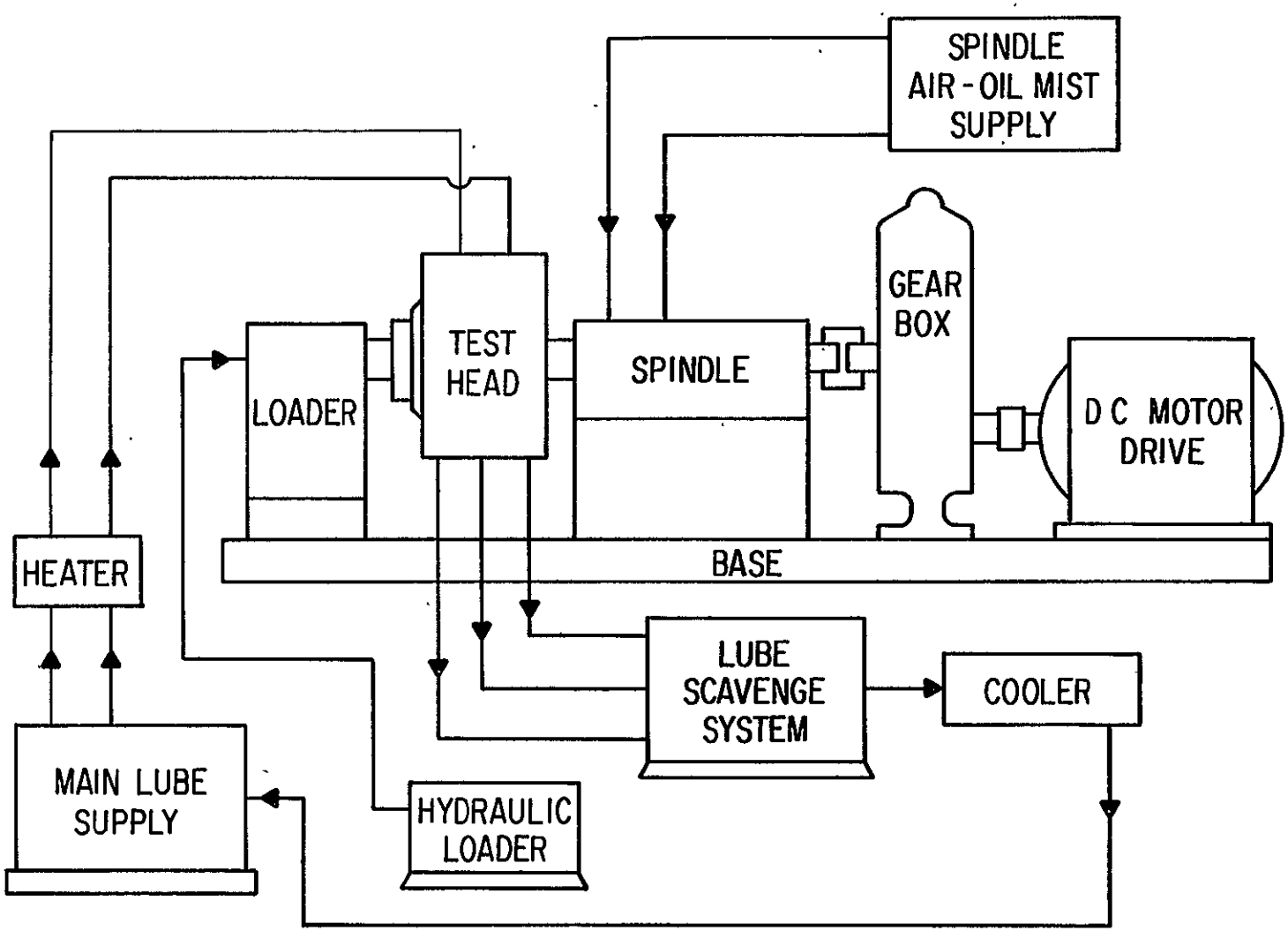

Fig. 56 Test System Schematic

MTI-7344

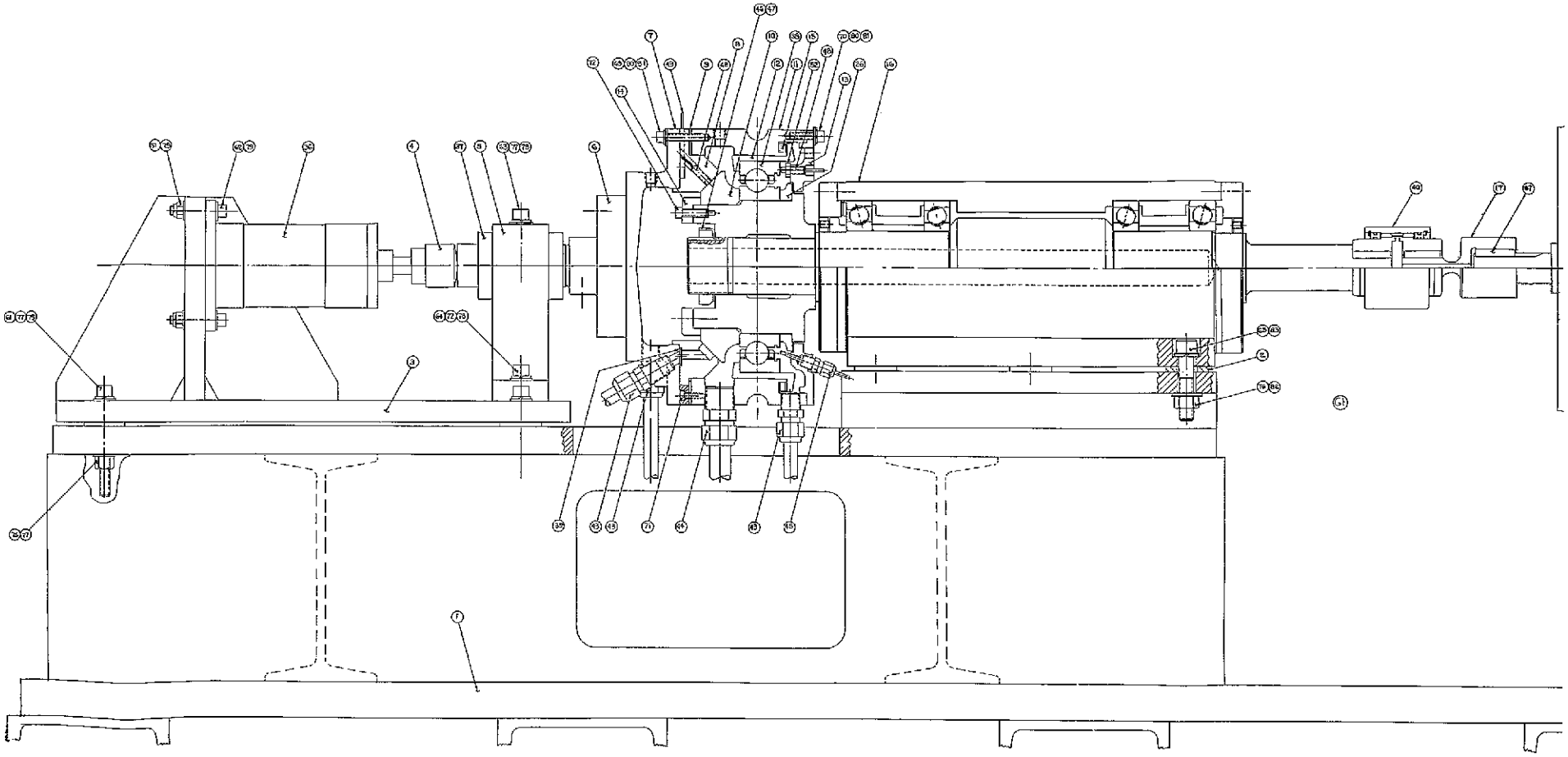

PRECEDING PAGE BLANK NOT FILMED

FOLDOUT FRAME 1

FOLDOUT FRAME 2

Fig. 57 Assembly Drawing

The fluid film bearing is comprised of a runner (10) and a stator (8). The fluid film bearing runner is mounted on the shaft with a line-to-line to .001" loose fit and secured in place through a spacer and locknut as shown. The fluid film bearing stator is secured to the housing through the use of four small bolts and fastened in place through six bolts which also are used to lock the housing end plate (7) to the housing itself. Oil is supplied to the fluid film bearing through four oil inlet lines (43) and two ball bearing jets located 180 degrees apart (45). The oil is scavenged from the housing through three scavenge lines (43, 44) each of the lines being connected to two scavenge ports located on the bottom of the housing. The runner and stator of the fluid film bearing shown in Fig. 57 are of the conical design discussed previously in Section 3 .

Fig. 58 shows a fluid film bearing with a planar runner (28) and a stator (27) design. Other details of this design configuration are otherwise the same as those described for the conical bearing.

Fig. 59 presents an end view of the test housing. This view discloses the torque arms (24) which restrain the housing from rotation. Each arm contains a ball located in a ball socket. The balls transmit the force to the strain gage beam (33). The full deflection of the strain gage beam is limited through the insertion of a spacer (22) so as to provide a torque resisting surface in case of bearing failure without permanently distorting the strain gage beam arrangement. The strain gage beams are mounted on posts (20) which in turn are mounted on the test base. This view also shows in more detail the oil supplies to the fluid film bearing as well as those to the ball bearing. The double porting for each scavenge line can also be easily descended. A close-up of the test head is shown in Fig. 60.

4.1.2 Lubrication Systems

A schematic representation of the lubrication system employed in this series of tests is shown in Fig. 61. This system basically consists of a 20 gal. capacity oil tank which is equipped with calrod immersion

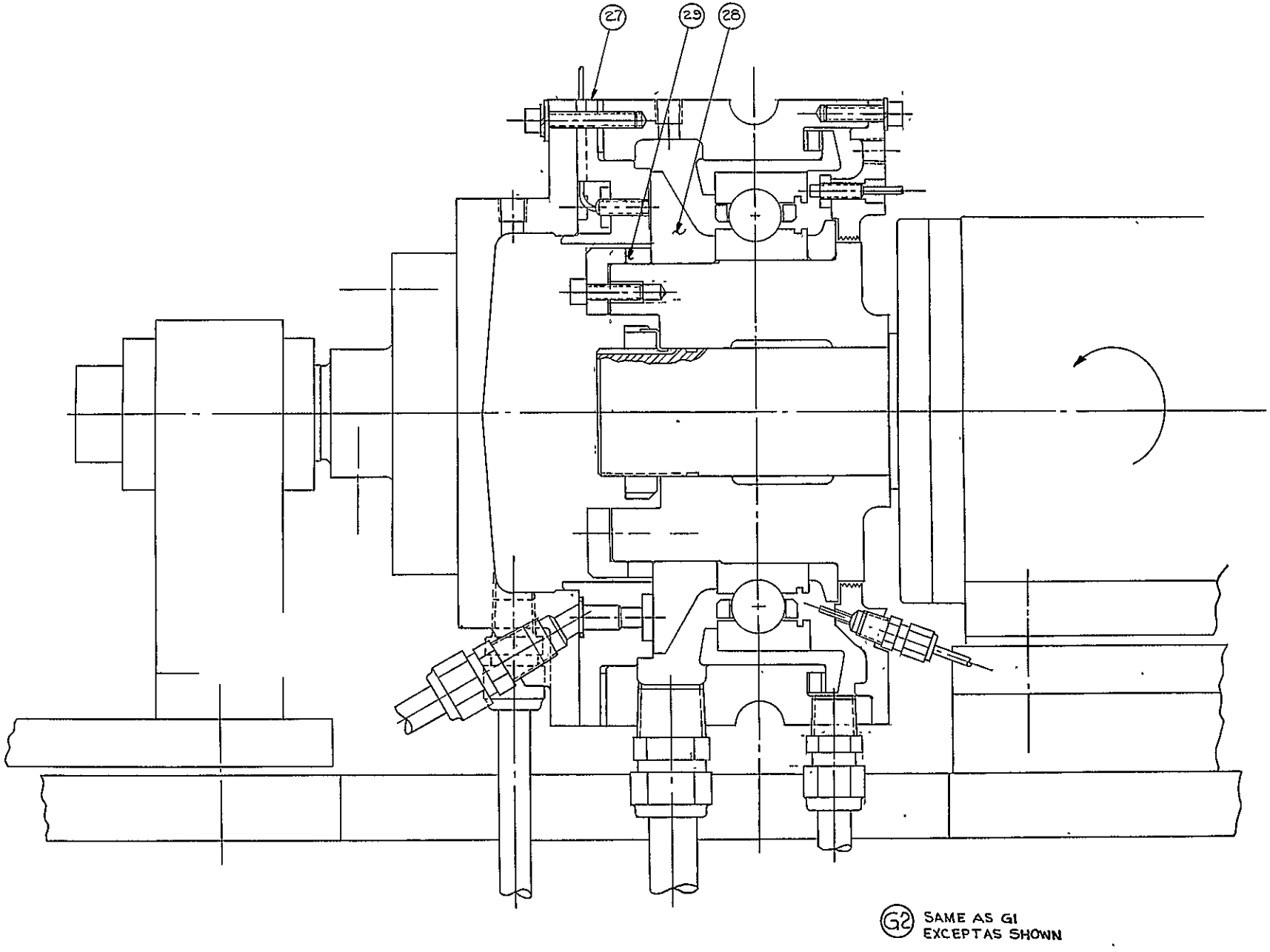

Fig. 58 Hybrid Boost Bearing With Planar Fluid Film Bearing Configuration

MTI-8896

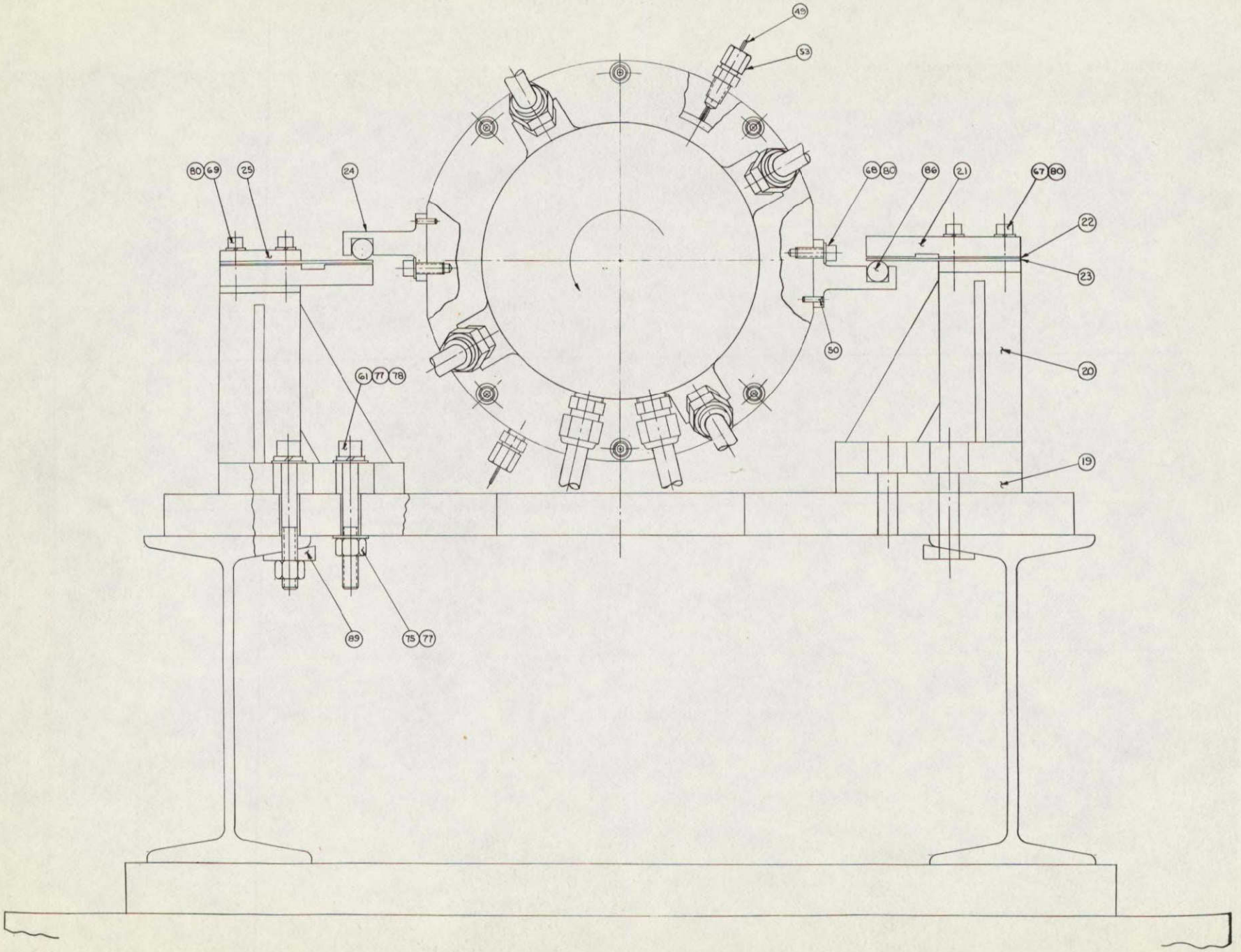

Fig. 59 Test Head End View Showing Oil Supply Lines and Torque Arms

MTI-8897

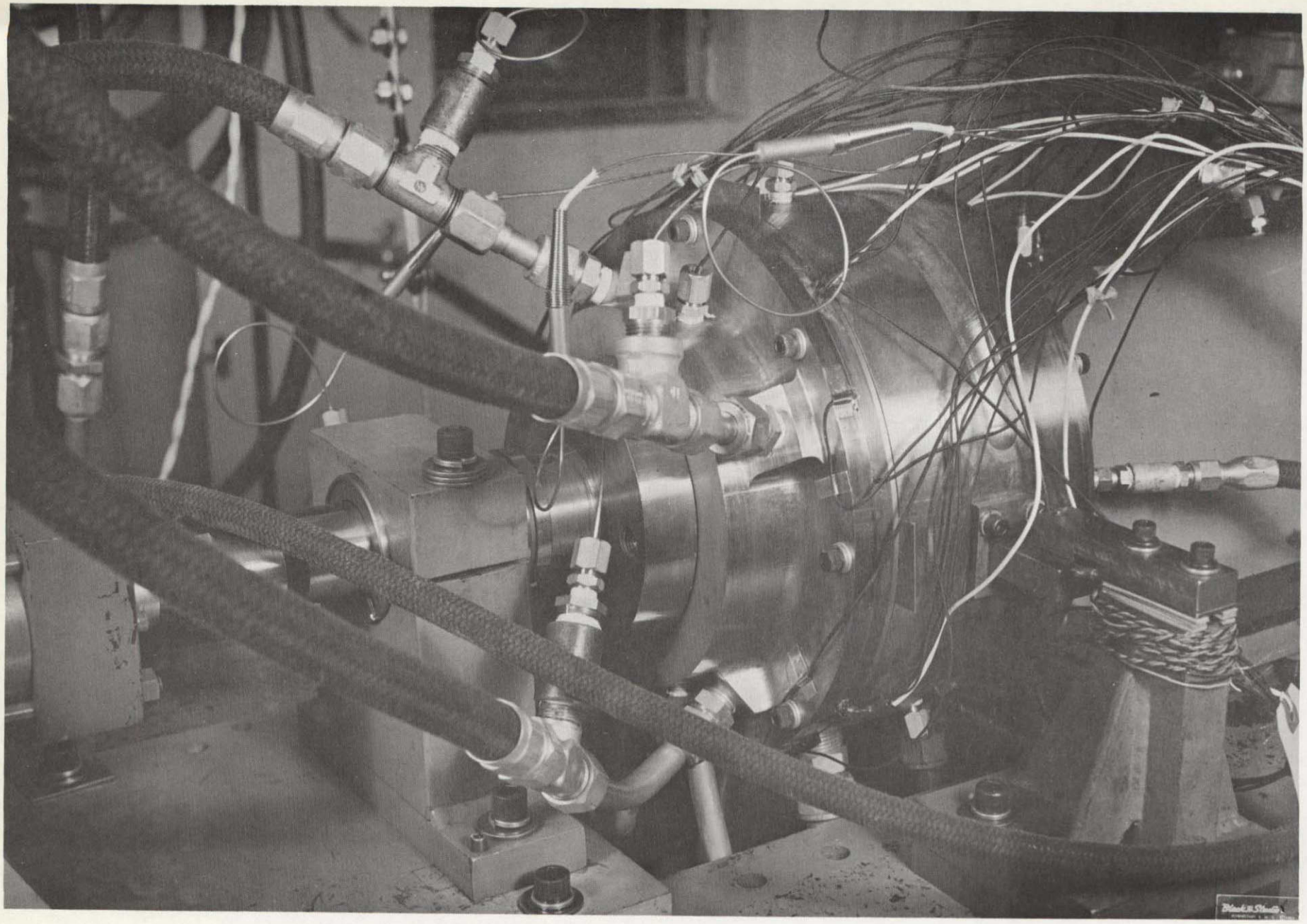

Fig.60 Closeup of Test Head Assembly

MTI-8898

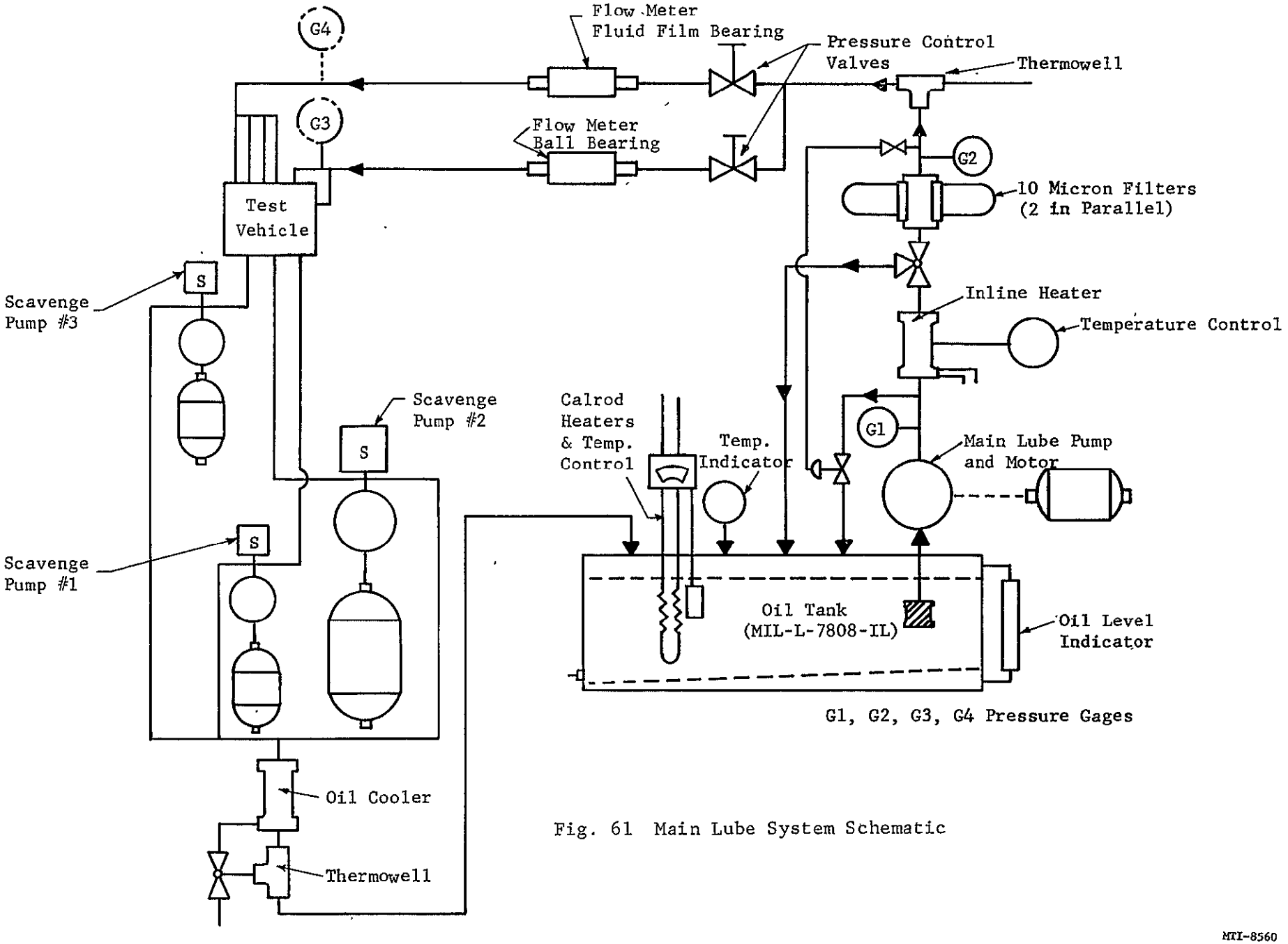

Fig. 61 Main Lube System Schematic

heaters and a temperature control, an immersion dial thermometer, a side glass showing the level of the oil in the tank, and various oil line connections.

The oil is delivered from the tank through a strainer onto the main lube pump. The output of the main lube pump goes to an in-line heater through a three-way by-pass valve onto two parallel filters (both filters employing 10 micron screens). Downstream of the filters the oil passes a thermoweld which controls the heater temperatures, and branches off into two lines — one of these lines supplies oil to the fluid film bearing through a fluid flowmeter which measures the total flow to the fluid film bearing, and the other line supplies the oil to the ball bearing again through a fluid flow meter which measures the total flow to the ball bearing. Oil connections external to the test rig are provided for oil supply lines to each of the four pockets comprising the fluid film bearing, and to each of the two oil jets supplying the oil to the ball bearing. Pressure gages are located throughout the oil path in the places indicated in Fig. 61 .

The oil discharge from the test vehicle is accomplished by three scavenge pumps, each pump connecting to a major sump cavity within the bearing system. The sump connections are shown in more detail in Fig. 57 . The total capacity of all three scavenge pumps combined is approximately 35 gallons/minute. The output of the scavenge pumps passes through a temperature controlled water cooler back into the main oil tank.

4.2. Instrumentation and Measurements

The instrumentation employed on the test set up discussed above consisted of pressure gages, thermocouples, inductance proximity probes, flowmeters, two 24 point temperature recorders, speed indicators, and a CRO to provide a display of the output of one of the inductance probes used in the fluid film bearing. The latter has been employed to determine the dynamic behavior of

the fluid film bearing stator with respect to the rotor. Torque measurements were accomplished through the use of two strain gaged beams described in Section 4.1.1. All of the instruments have been precalibrated and the calibrations were rechecked periodically as the test progressed.

The inductance probes turned out to be extremely temperature sensitive, hence in order to obtain a high degree of reading accuracy, the probes were precalibrated in fixtures which were made up of exactly the same material as the bearing parts into which they were to be installed. Also the geometry in the immediate environment of the probe was closely simulated. Calibration was performed in oil at the temperature levels indicated in the test, i.e. 100, 200, and 300 F. Once calibrated, each probe was also spot checked for calibration as well as repeatability in the actual installation. Thermocouples were located in the vicinity of each probe to afford a close interpolation of the probe readings. The probe reading accuracy thus obtained is estimated to be within ± 0.0002". The proximity probe and the thermocouple arrangements employed in each pad of the fluid film bearing are shown in Figs. 62 a and b. Figure "a" represents the initial set up where one proximity probe was installed in the pocket of each pad and recessed to be flush with the pockets bottom. To the right of this probe (clockwise direction) are three thermocouples located radially in line to pick up readings of the pocket outer land and inner land temperatures. The front (upstream) land is also provided with a thermocouple located close to the land's center.

Additionally, four proximity probes were installed in the oil drain grooves as shown in Fig. 62b, after completion of the ball bearing component tests when it became apparent that the existing probes were gradually failing at 300° F, and the remaining probes were insufficient to provide good axial alignment accuracy.

Four proximity probes were also installed in the rear seal plate to detect

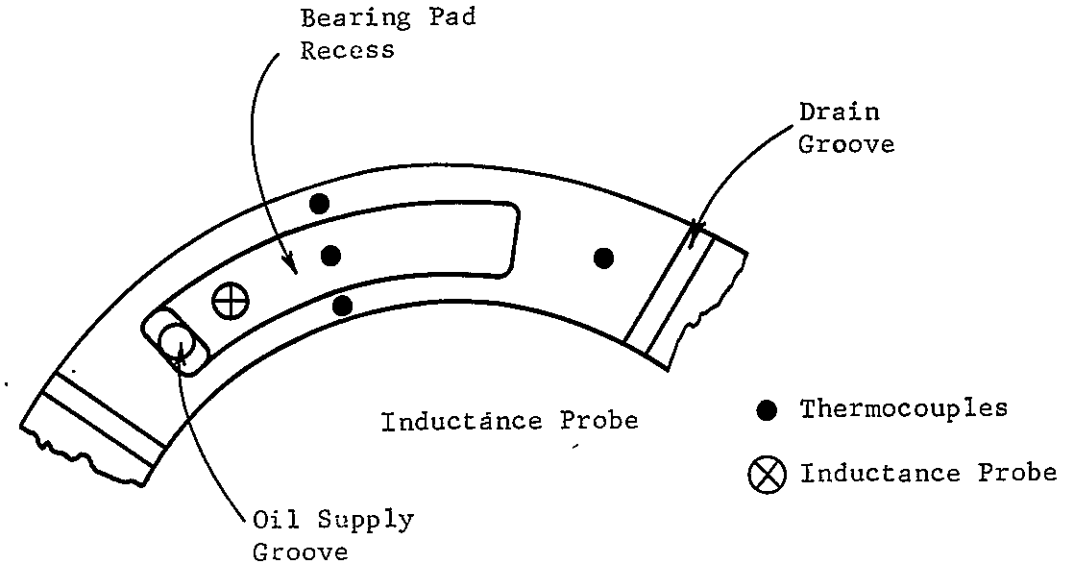

a. Initial Arrangement

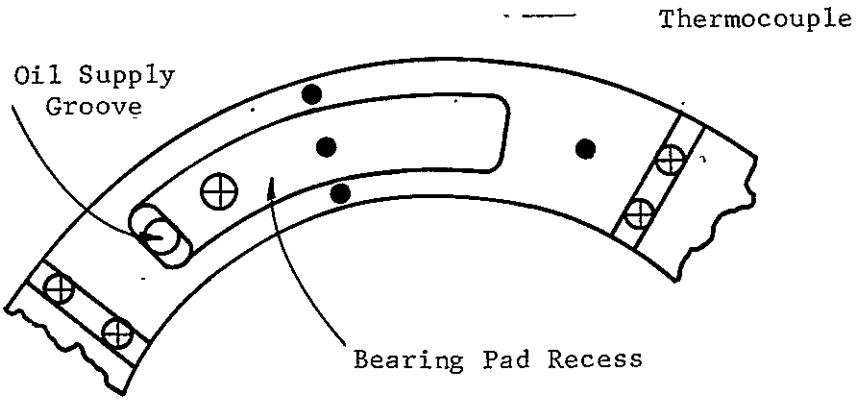

b. Revised Probe Arrangement

Fig. 62 Fluid Film Bearing Pad Instrumentation

and measure displacements between the housing and ball bearing outer race. These readings were employed to correct the displacement values obtained within the fluid film bearing area so that the net displacements between the inner and outer races of the ball bearing could be determined. This net displacement when plotted vs. the axially applied load produced ball bearing stiffness characteristics curves which could then be compared with the predicted characteristics arrived at through the use of the ball bearing computer program.

Thermocouples were also installed on the back end of the fluid film bearing stator, various housing locations and ball bearing outer race. The true position layout is described in Appendix A.

4.3 Test Plan

A detailed test plan including assembly and check-out procedures instrumentation procedures as well as test procedures was carried out and submitted for NASA approval prior to testing. The test sequence consisted of:

1. Ball Bearing Tests. Tests of the ball bearing component at speeds of 4000, 6000, 8000, and 10,000 rpm with loads of 500, 1000, 2000, and 3000 lbs. applied at each speed. These tests were run with oil flow rates of .75, 1.0, and 2.0 gpm at temperatures of 100, 200, and 300 F.
2. Hybrid Boost Bearing Tests. A series of full hybrid boost bearing tests at conditions identical to the ones given in 1 above with the exception of the fact that oil flow was maintained at 1 gal/min. and the fluid film supply pressure was kept at 50 psig.
3. Fail-Safe Tests. The fail-safe test sequence consisted of five start-stop tests simulating engine starts and stops. The speed was gradually increased to 10,000 rpm, the oil pressure to 50 psig, and the load to 3000 lbs. Note that although the test plan called for the 1000 lb. loading, this load level was increased inasmuch as it was felt as the test progressed, that the bearing arrangement could safely tolerate the 3000 lb. load.

Oil interruption tests were also performed, during which the oil was shut off while the unit was operating at full speed and load conditions for a period up to 5 minutes. Again here, although the maximum load indicated was 1000 lbs. the oil interruption tests were performed at all test load levels up to 2000 lb. loads at all speeds and all oil temperatures.

4.4 Test Bearing Geometry and Stack Up

The geometry of the fluid film bearing was for all practical purposes identical to the geometry arrived at in Section 3.1.1.6. A list of all design parameters is given in Fig. 22. The bearing design point was selected as being T_{in}=300°F (149°C), W = 3000 lb (13,350 n) and N = 10,000 rpm. The fail safe clearance at these conditions was assumed to be 0.001 inch (0.0254 mm). To achieve this clearance at the above listed conditions, the initial static axial clearance between the rotating and stationary members of the fluid film bearing should be 0.0046 inches (0.117 mm). This number is easily arrived at by following in Fig. 38 a vertical line passing through the zero (0) ball bearing deflection (which is equivalent to the reference position of the ball bearing under a 500 lb. (2225 n) axial preload) down to the 0.001 inch (0.0254 mm) fail safe scale.

5.0 DISCUSSION OF TEST RESULTS

The test set-up, calibration, and test procedures have been discussed in Section 4.0. This section concerns itself mainly with the reduction and analysis of the data obtained within this test program. The discussion of the results will be divided into three separate sections. The first section contains a discussion of the results obtained on the ball bearing component. The fluid film bearing component by itself is treated in the second section, and the combined hybrid boost bearing performance is discussed in the last section. The lubricant used in this series of tests was Esso Turbo-Oil 2389, a MIL-L-7808F oil with 3.38 cs viscosity at 210°F (99 C) and 14.2 cs at 100°F (37 C).

5.1 Discussion of Ball Bearing Test Results

The testing of the hybrid boost bearing commenced with the evaluation of the performance characteristics of the ball bearing by itself. In order to facilitate this evaluation and prevent rubbing between the fluid film bearing surfaces, should that happen to occur at high loading, a spacer was used to space the stator from the rotor at a safe enough distance so as to preclude any accidental rubs. Static tests were then performed to establish the degree and extent of housing deflection which may contribute to an increase in overall measured ball bearing deflection, thus softening the ball bearing axial stiffness.

5.1.1 Axial Deflection Tests

To establish the gross deflection, measurements were taken at zero load condition, of the relative deflection between inner and outer races as determined by the outputs of the proximity probes located in the fluid film bearing stator. These probes can be considered as being part of the bearing outer race and moving in unison with it. The probe target area is located on the fluid film bearing runner which in turn may be considered as being part of the ball bearing inner race. The relative movement between the outer and inner races can thus easily be determined through the measurement of the distance between the stator and the runner of the fluid film bearing. This measurement, however, assumes that no

additional displacement between the housing and outer race occurs. To establish the extent of the additional displacement between the bearing and housing via the bearing retainer, probes were located, as described in Section 4.0, on the test housing rear plate and targeted on to the ball bearing outer race thus measuring the relative displacement between outer race and housing. This displacement, when subtracted from the full fluid film bearing measurement, yields the net displacement between the inner and outer races of the ball bearing.

From the point of view of hybrid boost bearing operation, it is the overall or aggregate displacement that is of importance inasmuch as this determines the load distribution between the fluid film and ball bearings. In order, however, to compare the calculated ball bearing axial deflection with actual axial deflection of the ball bearing component used on test, the housing deflection corrections have to be imposed upon the ball bearing measurement results. This housing deflection characteristic is not expected to change with speed, hence the corrections for housing deflection were obtained at zero speed and subsequently utilized to correct the deflections also at speeds other than zero. It must also be pointed out at this time that the proximity probes located in the conical fluid film bearing stator read the shortest, i.e., perpendicular distance between the fluid film bearing stator and rotor surfaces. This reading does not represent the axial movement between the outer and inner races and has to be divided by the cosine of the cone angle, which in this case is 45 degrees. From hereon, whenever the distance between the stationary and rotating fluid film bearing parts is given, it will be given in terms of axial rather than perpendicular distance of the two components, the axial distance being measured on a line parallel to the shaft center.

The corrections to the deflections between the outer and inner races for the ball bearing component that were obtained on test are shown in Table IX,

TABLE IX

BALL BEARING - AXIAL DEFLECTION

Zero Speed - 100°F (37°C)

Load lb (Newtons)	Fluid Film Bearing Clearance mils (mm)	Displacement between inner race and housing mils (mm)	Rear Probe Clearance mils (mm)	Displacement between housing and outer race mils (mm)	Net Ball Bearing Displacement Between Inner and Outer Races mils (mm)
500(2,225)	22.0(0.56)	1.3(0.033)	42.5(0.11)	0	1.30(0.033)
1000(4,450)	21.3(0.54)	2.0(0.057)	42.54(0.11)	0.04(0.001)	1.96(0.050)
2000(8,900)	20.21(0.52)	3.09(0.079)	42.54(0.11)	0.04(0.001)	3.05(0.078)
3000(13,350)	19.13(0.48)	4.17(0.106)	42.84(0.12)	0.34(0.0086)	3.81(0.097)

The corrected ball bearing test results obtained on the first series of tests with a large spacer, are shown in Fig. 63. As can be seen, the agreement between the test points plotted in that figure with calculations performed through the use of the A. B. Jones Rolling Element Bearing Computer Program, is very good.

The displacement from the initial contact angle is taken as 1.3 mils (.33 mm) at 500 lbs. (2225 Newtons). Note that the displacement between the housing and bearing outer race at low loads is practically nil. Only at 3000 lbs. (13,350 n) does the displacement reach 0.34 mils (.1 mm).

Subsequent to these tests, the spacer which permitted large clearances between the stator and rotor of the fluid film bearing was removed and machined down to yield an initial clearance between the stator and rotor of 6.4 mils (0.163 mm) at an initial preload of 500 lbs. (2,225 Newtons), a temperature of 100° F, (37°C), and a shaft speed of 0 rpm. This initial clearance is somewhat larger than the contemplated clearance of 4.6 mils (.121 mm) based upon the analytical results. The reason for the increase was due to the facts that the anticipated bearing stiffness did not materialize due to slight housing deflections, and misalignment could cause local decreases in clearance. The clearance was thus increased to assure the fail-safe features discussed in Section 3.0.

5.1.2 Ball Bearing Performance Tests

With the hybrid boost bearing fully assembled, tests were now performed at all indicated speeds, loads, and temperature levels, and the data generated in a way which would introduce the least possibility of error. Thus, for each test point and at each individual load, speed,

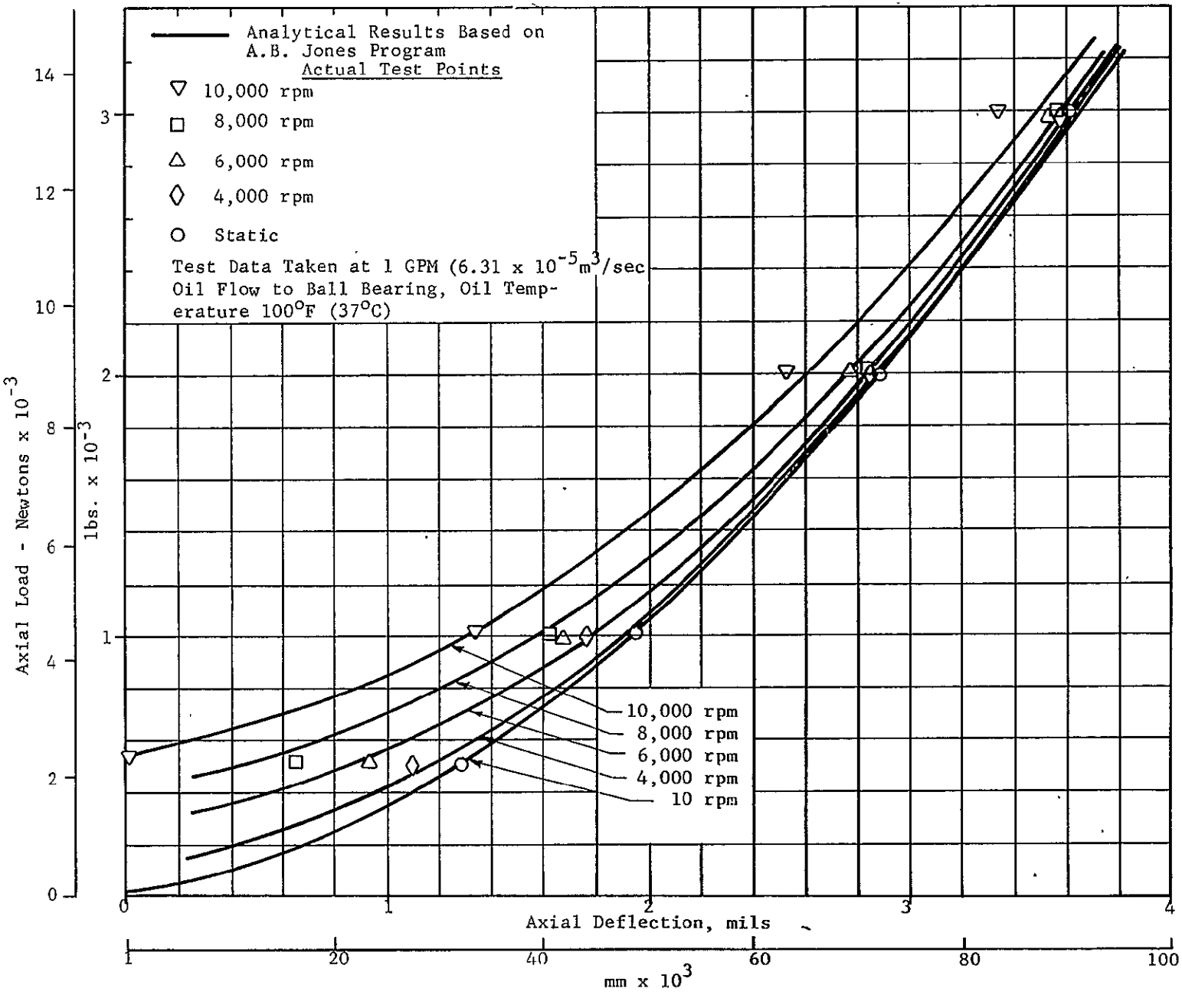

Figure 63

MTI-9135

and temperature the axial fluid film thickness was measured with and without supply to the fluid film bearing. This permitted the instantaneous evaluation of the fluid film bearing's contribution to the load carrying capacity of the entire hybrid boost bearing and also permitted the separation of the ball bearing characteristics from those of the fluid film bearing. The ball bearing performance data thus obtained is shown in Tables X, XI, XII, for 100, 200 and 300 F, respectively. The tables list speed, load, fluid film bearing thickness (in axial direction), horsepower (test and calculated), and outer race temperatures. The calculated horsepower is based on the following formula (Ref. 3).

$$q = 3.19 \times 10^{-8} (dN)^{1.5} F_a^{0.007} \mu^{0.25} m^{0.42}$$

where q = bearing heat rejection to oil, in BTU/min

d = bearing bore in mm

N = bearing speed in rpm

F = bearing load in lbs.

μ = oil viscosity in centipoises

m = oil flow in lb/min

Converting this equation to horsepower

$$HP = 7.52 \times 10^{-10} (dN)^{1.5} F^{0.07} \mu^{0.25} m^{0.42}$$

TABLE X

BALL BEARING PERFORMANCE DATA

Q_B = 1 gpm (.63 x 10^{-4} m^3/sec.) T_{in} = 100°F (37°C)

N RPM	F_a LBS. (NEWTONS)	h_f MILS (mm)	HP TEST	HP CALC.	T_{or} °F (°C)
4,000	340 (1,513)	6.73 (.171)	—	1.90	100 (37)
↓	690 (3,070)	5.74 (.146)	1.00	1.98	109 (43)
	1,420 (6,319)	4.31 (.109)	.96	2.07	113 (45)
	2,220 (9,879)	3.23 (.082)	1.00	2.08	115 (46)
6,000	360 (1,602)	7.16 (.182)	—	3.43	117 (47)
↓	690 (3,071)	6.02 (.153)	2.26	3.60	124 (51)
	1,350 (6,008)	4.54 (.115)	2.25	3.73	126 (52)
	2,100 (9,345)	3.44 (.087)	2.17	3.78	127 (53)
8,000	270 (1,202)	7.57 (.192)	—	5.25	117 (47)
↓	550 (2,448)	6.24 (.158)	3.89	5.51	132 (56)
	1,130 (5,029)	4.78 (.121)	3.70	5.69	138 (59)
	1,800 (8,010)	3.66 (.093)	3.74	5.73	141 (61)
10,000	250 (1,113)	8.38 (.213)	—	7.38	134 (57)
↓	640 (2,848)	6.75 (.171)	7.90	7.61	147 (64)
	1,350 (6,008)	4.71 (.119)	7.84	7.86	147 (64)
	2,170 (9,657)	3.38 (.086)	7.39	7.91	158 (88)

TABLE XI

BALL BEARING PERFORMANCE DATA

Q_B = 1 gpm (.63 x 10^{-4} m^3/sec.) T_{in} = 200°F (93°C)

N RPM	F_a LBS. (NEWTONS)	h_f MILS (mm)	HP TEST	HP CALC.	T_{or} °F (°C)
4,000	400 (1,780)	5.78 (.147)	—	1.30	204 (96)
↓	880 (3,915)	4.98 (.126)	.60	1.36	204 (96)
↓	1,810 (7,054)	3.79 (.096)	.55	1.43	204 (96)
↓	2,760 (12,282)	2.66 (.068)	.50	1.47	204 (96)
6,000	390 (1,835)	6.0 (.152)	—	2.39	205 (96)
↓	780 (3,471)	5.13 (.130)	1.16	2.51	211 (99)
↓	1,640 (7,298)	3.80 (.097)	1.18	2.63	211 (99)
↓	2,510 (11,169)	2.86 (.073)	1.08	2.71	212 (100)
8,000	400 (1,780)	6.40 (.163)	—	3.71	202 (94)
↓	760 (3,382)	5.27 (.134)	1.66	3.89	202 (94)
↓	1,440 (6,408)	4.02 (.102)	1.84	4.08	218 (103)
↓	2,120 (9,434)	3.11 (.079)	1.88	4.20	218 (103)
10,000	400 (1,780)	6.70 (.170)	—	5.24	212 (100)
↓	740 (3,293)	5.22 (.133)	3.76	5.49	212 (100)
↓	1,460 (6,497)	3.64 (.092)	3.81	5.76	227 (108)
↓	2,160 (9,612)	2.67 (.068)	3.81	5.93	234 (112)

TABLE XII

BALL BEARING PERFORMANCE DATA

Q_B = 1 gpm (.63 x 10^{-4} m^3/sec.) T_{in} = 300°F (149°C)

N RPM	F_a LBS. (NEWTONS)	h_f MILS (mm)	HP TEST	HP CALC.	T_{or} °F (°C)
4,000	480 (2,136)	5.70 (.144)	—	.99	304 (151)
↓	960 (4,272)	4.76 (.120)	.13	1.03	304 (151)
	1,940 (8,633)	3.52 (.089)	.15	1.08	298 (148)
	2,840 (12,640)	2.55 (.064)	.31	1.12	298 (148)
6,000	470 (2,091)	5.73 (.145)	—	1.82	296 (147)
↓	940 (4,183)	4.70 (.119)	.51	1.91	296 (147)
	1,870 (8,322)	3.42 (.086)	.62	2.01	301 (149)
	2,700 (12,015)	2.50 (.063)	.83	2.07	301 (149)
8,000	460 (2,047)	6.18 (.156)	—	2.83	295 (146)
↓	940 (4,183)	5.02 (.127)	1.57	2.98	295 (146)
	1,780 (8,680)	3.69 (.093)	1.73	3.14	302 (150)
	2,620 (11,660)	2.56 (.065)	1.94	3.23	302 (150)
10,000	470 (2,091)	6.75 (.170)	—	4.0	294 (146)
↓	820 (3,648)	5.42 (.137)	2.33	4.17	309 (154)
	1,600 (7,120)	3.83 (.097)	2.46	4.40	309 (154)
	2,500 (11,125)	2.60 (.066)	2.69	4.50	309 (154)

As can be seen, the measured power loss [at 1 gpm ($.63 \times 10^{-4}$) oil flow to the bearing] shows extremely low load dependence, as expected from the above empirical formula. In some cases, however, particularly at the high speed, the power loss appears to be decreasing with load rather than increasing which could be explained by an increase in temperature within the bearing and a subsequent slight drop in viscosity. In general, the calculated power loss of the bearing at 100 F (37 C) is higher than the actually measured loss.

The effect of flow on ball bearing performance at speeds up to 6,000 rpm was totally negligible within the range of flow tested [.75 gpm (4.7×10^{-4} m^3/sec) and 2.0 gpm (1.26×10^{-4} m^3/sec)]. The differences between the .75 gpm ($.47 \times 10^{-4}$ m^3/sec) and the 1.0 gpm ($.63 \times 10^{-4}$ m^3/sec) lie within the limits of measuring accuracy, and are for all practical purposes negligible. At 2 gpm (1.26×10^{-4} m^3/sec) the power loss increases over that measured at 1 gpm ($.63 \times 10^{-4}$ m^3/sec) by 30% and 50% respectively for 8,000 and 10,000 rpm.

The outer race temperatures show a load and speed dependence, the speed dependence being less pronounced than that of load at speeds of 6,000 rpm and higher. This is surprising since the opposite would usually be expected. Since, however, the load changes were performed at constant speed, it is possible that the temperature rise attributed to the load effect merely represents the rise to steady state conditions at the given speed.

The test loads for the ball bearings do not appreciably exceed 2,000 lbs. inasmuch as the tests at 3,000 lbs. were performed with the full hybrid boost bearing only and no attempts were made to simulate failure of oil supply to the fluid film bearing.

5.2 Fluid Film Bearing Test Results

The fluid film bearing performance data were obtained by a process of deduction. As explained in the Section 5.1, above, at each test point the performance characteristics of the full hybrid boost bearing and the ball bearing were established

by a full hybrid boost bearing test followed by one with the oil supply to the fluid film bearing shut off. The fluid film bearing capacity was determined through the subtraction of the ball bearing's load share determined in the test above from that of the full hybrid boost bearing. Similarly, the power loss involved in the fluid film bearing has also been determined through the subtraction of the power loss measured in the ball bearing from that measured in the full hybrid boost bearing. Although the supply pressure to the fluid film bearing component was maintained at 50 psi (34.3×10^4 Newtons/in^2), the actual pocket pressure was subject to considerable variations. Since provisions for measurement of pocket pressures were not included calibrations of flow vs. pressure were performed at 100 (37), 200 (93), and 300 F (149 C) temperature levels to establish the pressure drops experienced through the lines. To include the restrictive effects of the fluid film bearing clearance on the flow and thus also on the pocket pressure, static measurements of the fluid film bearing were performed (see Section 5.3 for more particulars). Thus the supply pressures shown in Tables XIII through XV are the product of extrapolation based upon the static runs and flow checks through the lines. Note that at high oil temperatures and large clearances the pocket pressure is particularly low as shown by little or no change in operating clearance when the supply to the fluid film bearing is cut at zero speed conditions (see Fig. 81).

5.2.1 Load Carrying Capacity of Fluid Film Bearing

The fluid film bearing performance data are summarized in Tables XIII, XIV, and XV for 100 (37), 200 (93), and 300 F (149 C) respectively. These tables contain a listing of the speed in revolutions/minute, viscosity in reyns and centiposes, film thickness in mils and millimeters, supply pressure in psi and newtons/m^2, load in lbs. and newtons, horsepower and flow to the bearing in gal/minute and m^3/sec. The variations in viscosity shown are due to variations in the land temperatures observed on test. All calculated values which are given for the purpose of comparison with test values are based upon the temperatures measured within the fluid film area and the indicated supply pressures.

TABLE XIII

FLUID FILM BEARING PERFORMANCE DATA
T_{in} = 100°F (37°C)

N RPM	μ REYNS x 10^7 (CP)	h_F MILS (MM)	P_s PSI (NEWTONS/M^2 x 10^{-4})	F_a LBS. (NEWTONS)		HP		Q_F GPM (M^3/SEC. X 10^4)	
				TEST	CALC.	TEST	CALC.	TEST	CALC.
4,000	20.0 (13.7)	6.73 (.171)	10.4 (7.2)	160 (712)	223 (992)	—	1.25	9.47 (5.96)	5.61 (3.53)
↓	19.3 (13.3)	5.74 (.146)	18.7 (12.8)	310 (1,379)	316 (1,406)	1.72	1.40	7.69 (4.84)	5.30 (3.34)
	18.8 (13.0)	4.31 (.109)	35.3 (24.2)	580 (2,581)	519 (2,310)	1.84	1.69	4.82 (3.04)	3.91 (2.46)
	17.3 (11.9)	3.23 (.082)	50.0 (34.3)	780 (3,471)	693 (3,084)	1.88	1.87	2.70 (1.68)	2.42 (1.51)
6,000	18.0 (12.4)	7.16 (.182)	6.0 (4.12)	140 (623)	243 (1,081)	—	2.36	—	7.82 (4.92)
↓	18.0 (12.4)	6.02 (.153)	15.0 (10.2)	310 (1,380)	366 (1,629)	3.25	2.65	9.03 (5.68)	7.25 (4.56)
	17.3 (12.0)	4.54 (.115)	33.0 (22.6)	650 (2,893)	602 (2,679)	3.13	3.44	5.73 (3.60)	5.57 (3.50)
	16.4 (11.3)	3.44 (.087)	50.0 (34.3)	900 (4,005)	831 (3,698)	3.59	4.45	3.60 (2.26)	3.60 (2.26)
8,000	17.7 (12.2)	7.57 (.192)	4.0 (2.7)	230 (1,024)	401 (1,784)	—	5.12	—	9.81 (6.17)
↓	17.2 (11.8)	6.24 (.158)	13.0 (8.9)	450 (2,003)	471 (2,096)	6.91	5.16	—	10.39 (6.40)
	16.3 (11.2)	4.78 (.121)	29.0 (19.8)	870 (3,872)	751 (3,342)	7.60	6.18	8.10 (5.09)	8.23 (5.17)
	15.0 (10.3)	3.66 (.093)	46.0 (31.5)	1200 (5,340)	1058 (4,708)	7.36	7.07	5.83 (3.66)	5.77 (3.63)
10,000	18.3 (12.6)	8.38 (.213)	—	250 (1,113)	351 (1,562)	—	7.41	—	15.29 (9.50)
↓	17.3 (12.0)	6.75 (.171)	10 (6.9)	360 (1,602)	572 (2,545)	10.45	8.37	—	15.02 (9.30)
	14.9 (10.2)	4.71 (.119)	30 (20.5)	650 (2,893)	1132 (5,037)	9.70	10.41	10.85 (6.70)	13.14 (8.10)
	13.5 (9.3)	3.38 (.086)	50 (34.3)	830 (3,694)	1812 (8,063)	8.20	13.74	8.62 (5.42)	8.27 (5.20)

TABLE XIV

FLUID FILM BEARING PERFORMANCE DATA
T_{in} = 200°F (93°C)

N RPM	μ REYNS x 10^7 (CP)	h_F MILS (MM)	P_s PSI (NEWTONS/M^2 x 10^{-4})	F_a LBS. (NEWTONS)		HP		Q_F GPM (M^3/SEC. X.10^4)	
				TEST	CALC.	TEST	CALC.	TEST	CALC.
4,000	4.7 (3.24)	5.78 (.147)	3.0 (2.05)	100 (445)	107 (476)	—	.489	—	6.62 (4.17)
	4.8 (3.30)	4.98 (.126)	6.0 (4.12)	120 (534)	155 (690)	.62	.552	—	6.33 (3.98)
	4.85 (3.33)	3.79 (.096)	14.0 (9.50)	190 (846)	276 (1,228)	1.03	.720	8.5 (5.35)	5.19 (3.27)
	4.85 (3.34)	2.66 (.068)	19.0 (13.0)	240 (1,068)	413 (1,838)	.99	.945	4.9 (3.08)	2.69 (1.68)
6,000	4.75 (3.28)	6.0 (.152)	2.0 (1.36)	110 (490)	154 (685)	—	1.27	—	9.86 (6.20)
	4.75 (3.28)	5.13 (.130)	5.0 (3.43)	220 (979)	224 (997)	2.38	1.41	—	9.47 (5.96)
	4.75 (3.28)	3.80 (.097)	14.0 (9.50)	360 (1,602)	416 (1,851)	2.36	1.76	9.0 (5.67)	7.66 (4.82)
	4.65 (3.20)	2.86 (.073)	18.0 (1.23)	490 (2,181)	596 (2,652)	2.21	2.18	6.0 (3.77)	4.83 (3.04)
8,000	4.64 (3.20)	6.40 (.163)	2.0 (1.36)	100 (445)	255 (1,135)	—	2.89	—	12.94 (8.0)
	4.57 (3.14)	5.27 (.134)	3.5 (2.22)	240 (1,068)	282 (1,255)	5.49	2.72	—	12.81 (7.90)
	4.57 (3.14)	4.02 (.102)	13.0 (8.9)	560 (2,492)	514 (2,287)	5.31	3.30	10.4 (6.40)	11.23 (6.90)
	4.52 (3.12)	3.11 (.079)	18.0 (1.23)	880 (3,916)	765 (3,404)	4.94	3.97	7.85 (4.94)	7.98 (5.0)
10,000	4.90 (3.38)	6.70 (.170)	—	100 (445)	245 (1,090)	—	5.05	—	16.51 (10.20)
	4.57 (3.14)	5.22 (.133)	5.0 (3.43)	260 (1,157)	393 (1,749)	9.14	5.07	—	16.32 (10.10)
	4.57 (3.14)	3.64 (.092)	15.0 (10.2)	540 (2,403)	799 (3,556)	9.79	6.13	—	12.81 (8.0)
	4.45 (3.06)	2.67 (.068)	19.0 (13.0)	840 (3,738)	1209 (5,380)	8.19	7.55	10.3 (6.40)	7.99 (5.0)

TABLE XV

FLUID FILM BEARING PERFORMANCE DATA
T_{in} = 300°F (149°C)

N RPM	μ REYNS x 10^7 (CP)	h_F MILS (MM)	P_s PSI (NEWTONS/M^2 x 10^{-4})	F_a LBS. (NEWTONS)		HP		Q_F GPM (M^3/SEC. X 10^4)	
				TEST	CALC.	TEST	CALC.	TEST	CALC.
4,000	2.06 (1.42)	5.70 (.144)	–	20 (89)	53 (236)	–	.31	–	6.24 (3.93)
↓	2.00 (1.38)	4.76 (.120)	–	40 (178)	75 (334)	.61	.33	–	5.62 (3.53)
	2.00 (1.38)	3.52 (.089)	4 (2.74)	60 (267)	147 (655)	.46	.41	–	5.02 (3.16)
	2.03 (1.40)	2.55 (.064)	20 (13.7)	160 (710)	316 (1,405)	.13	.51	7.42 (4.67)	4.50 (2.83)
6,000	2.03 (1.40)	5.73 (.145)	–	30 (134)	102 (454)	–	1.08	–	9.46 (5.96)
↓	2.03 (1.40)	4.70 (.119)	–	60 (267)	141 (628)	1.85	1.08	–	8.71 (5.48)
	2.03 (1.40)	3.42 (.086)	5 (3.43)	130 (578)	259 (1,150)	1.86	1.14	–	7.74 (4.87)
	2.06 (1.42)	2.50 (.063)	21 (14.4)	300 (1,335)	488 (2,170)	1.40	1.41	7.93 (4.99)	6.12 (3.85)
8,000	2.03 (1.40)	6.18 (.156)	–	40 (178)	228 (1,015)	–	3.28	–	11.60 (7.2)
↓	2.06 (1.42)	5.02 (.127)	–	60 (267)	219 (975)	3.76	2.72	11.0 (6.8)	11.83 (7.3)
	2.12 (1.46)	3.69 (.093)	2 (1.37)	220 (980)	346 (1,539)	4.23	2.64	12.0 (7.4)	10.36 (6.4)
	2.12 (1.46)	2.56 (.065)	19 (13.0)	380 (1,690)	656 (2,915)	4.02	2.87	8.58 (5.40)	8.26 (5.2)
10,000	2.04 (1.41)	6.75 (.170)	–	30 (134)	211 (939)	–	5.02	–	16.16 (10.0)
↓	2.17 (1.48)	5.42 (.137)	–	180 (802)	316 (1,405)	7.27	5.52	–	14.85 (9.2)
	2.17 (1.48)	3.83 (.097)	2 (1.37)	400 (1,780)	490 (2,180)	8.01	5.35	–	13.08 (8.1)
	2.17 (1.48)	2.60 (.066)	18 (12.30)	500 (2,225)	870 (3,870)	7.89	5.36	9.72 (6.12)	10.38 (6.4)

Since the temperatures shown were measured by thermocouples embedded in the face of the bearing, the chances are that these reflect the metal skin temperatures, rather than the temperatures of the actual fluid film separating the stator and runner of the fluid film bearing.

The performance of the fluid film bearing with regard to load carrying capacity, is plotted in Figs. 64, 65, and 66 for 100 (37), 200 (93), and 300 F (149 C) respectively. Note that at 100 F (37 C), the 4,000, 6,000, and 8,000 rpm curves show the normally anticipated behavior with regard to speed and clearance, i.e., the load carrying capacity increases with increase in speed and with decrease in clearance. The 10,000 rpm curve, however, crosses the other curves indicating an effectively lower stiffness characteristic. This behavior demonstrates the drop-off in load carrying capacity obtained at high shear stresses. Turning to Figs. 65 and 66, one may observe that this effect diminishes as the inlet oil temperature is increased. An increase in inlet oil temperature would reduce the local viscosity and thus also decrease the shear stresses present within the fluid film. The effect of a decrease in shear stress could result in decreased heat dissipation and consequently also in a lowering of the thermal gradient within the oil film.

A comparison between the calculated and measured load carrying capacity of the bearing is shown in Fig. 67. This figure presents plots at three different temperatures, of the load carrying capability obtained on test as a function of speed at constant clearances. Three clearances which fell within the range of the test data were selected for comparison; these are 0.003" (.077 mm), 0.0045" (.114 mm), and 0.006" (154 mm). Note that the load vs. speed agreement between the calculated and test values at high temperatures and high speeds is much better than that at the lower temperatures and high speeds. At low temperatures a substantial drop in load carrying capacity is indicated on test as a function of speed at speeds above 8,000 rpm for a given constant film thickness. This behavior of the fluid film bearing implies that there is a limit in terms of the load carrying capacity of the bearing, beyond which the load carrying capacity cannot be improved by mere increases in speed or viscosity. As

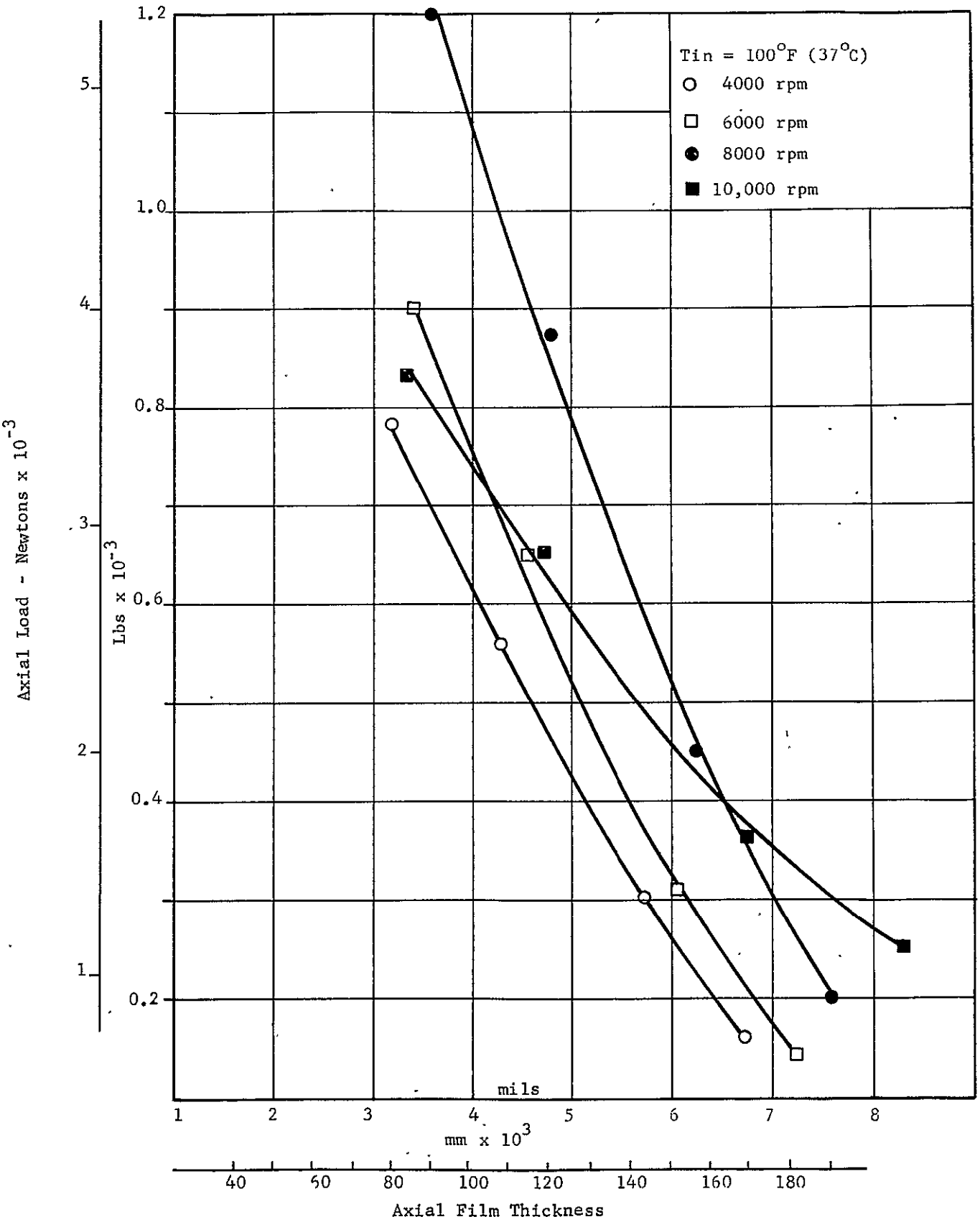

Fig. 64 Fluid Film Bearing Load vs. Film Thickness

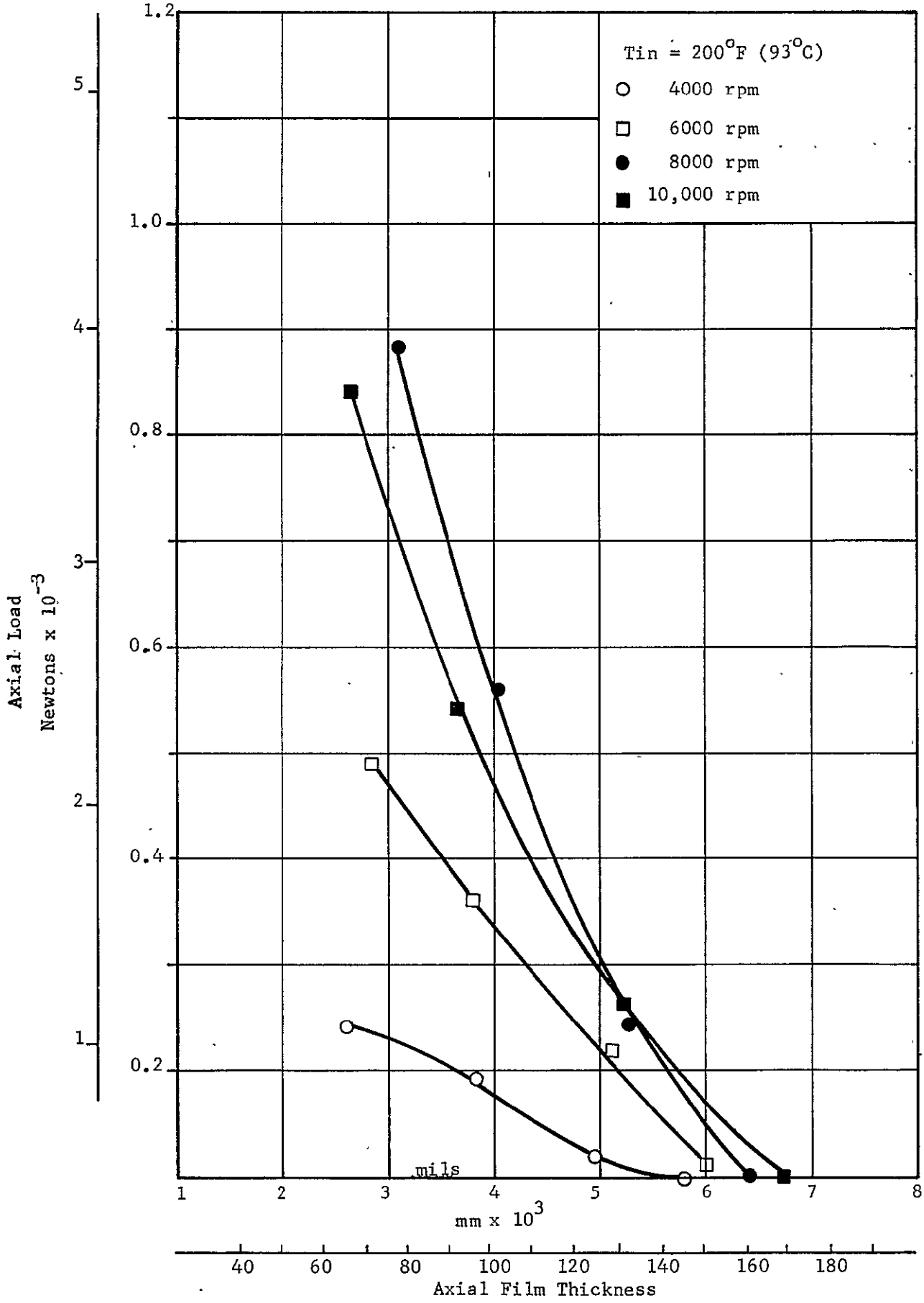

Fig. 65 Fluid Film Bearing Load vs. Film Thickness

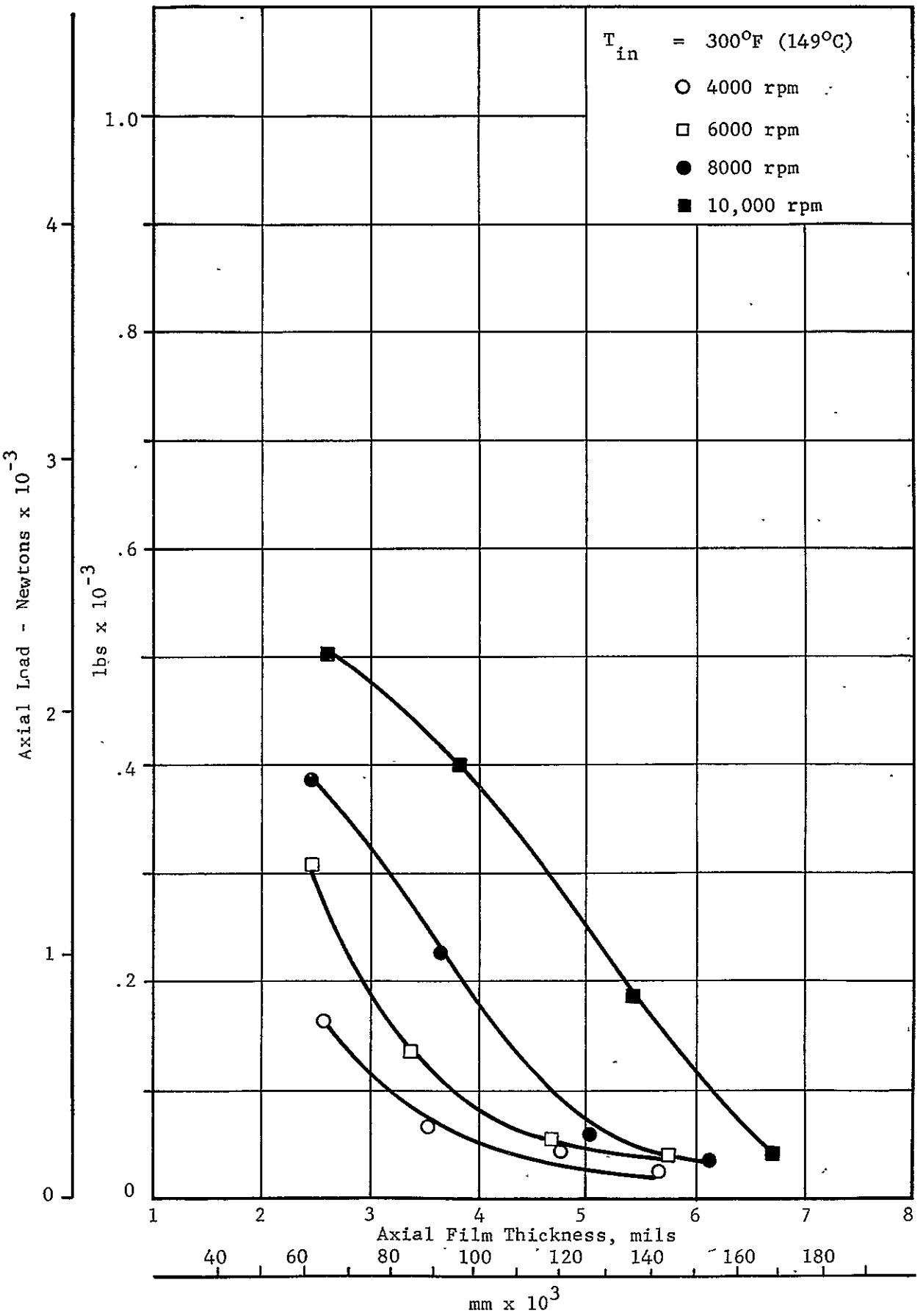

Fig. 66 Fluid Film Bearing Load vs. Film Thickness

MTI-9201

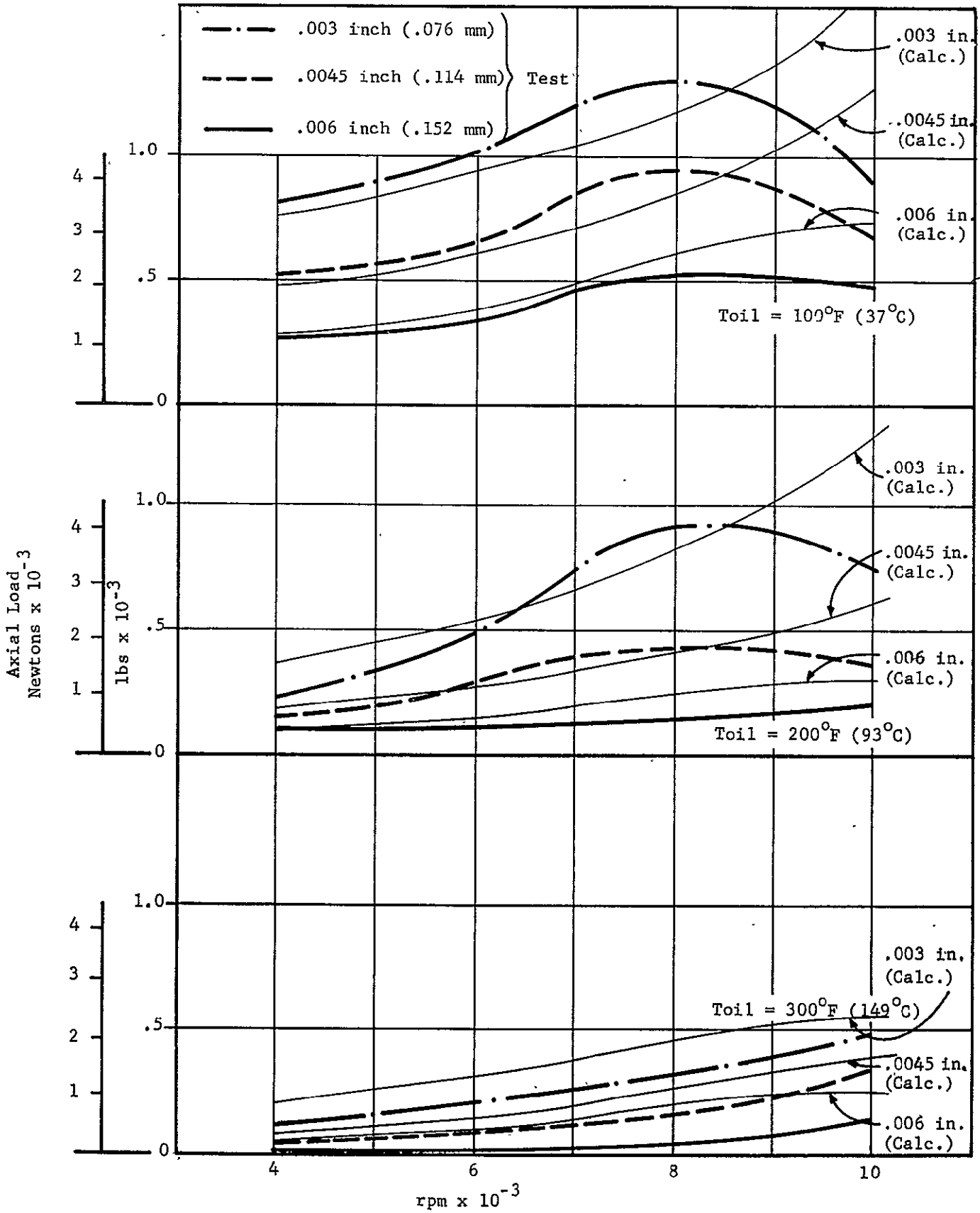

Fig. 67 Fluid Film Bearing Load vs. Speed

a matter of fact, the actual load capacity may even drop as a result of further increases in speed and/or decreases in temperature. Similar results were obtained by the authors on planar thrust bearing tests of a similar configuration before (Ref. 4). Interestingly enough, this type of behavior has been predicted by Mr. J. Boostma of the University of Delft in Holland in a paper published in Reference 5. He obtains this behavior by assuming a non-isothermal oil film condition which results from the velocity profile within the film.

This drop in load carrying capacity may seriously limit the load carrying and thus also the load sharing potential of the fluid film bearing component within the hybrid boost bearing arrangement. These limitations, however, can be overcome through a fluid film bearing arrangement which would mainly operate on a hydrostatic rather than a hydrodynamic principle.

5.2.2 Power Loss of the Fluid Film Bearing

With a few exceptions the measured power loss for the test bearing appears to be higher than the calculated one. Surprisingly, the test data on horsepower loss within the fluid film bearing does not appear to be varying appreciably with load, or more specifically, clearance. This is in direct contradiction to the normally expected analytical prediction which indicates that the power loss should increase with decreasing clearances. In some instances (particularly at high speed and high load at 100 F) the power loss actually decreases as a result of increased loading and decreased clearance.

It is worthwhile to note that at the points of power loss decrease, as a result of decrease in clearance at a given speed, the discrepancies between the calculated and actually measured loads also greatly increase. The non-isothermal oil film theory mentioned above, can also explain this recorded phenomenon — the oil film in effect is subject to thermal gradients which are sufficiently high to reduce the viscosity levels within the oil film so as to appreciably affect its load carrying capacity and decrease the heat generation and power loss. A comparison between calculated and test values of power loss is shown in Tables XIII through

XV. The test values are higher, most probably due to additional churning losses within the housing.

5.2.3 Oil Flow

Lack of test data with regard to flow at some of the test points is due to the fact that the flow exceeded the 11 gals/minute capacity of the flow meters which were used in this application. This occurred predominantly at large clearances and high temperature levels. In general, at low clearances, the agreement between measured and calculated oil flow is very good. The flows for high operational clearances are, at this stage, of strictly academic value inasmuch as the high flows required to satisfy the operation at light load conditions are impractical. The calculated and measured flows for the given test conditions are also shown in Tables XIII through XV.

5.3 Full Hybrid Boost Bearing Performance Data

As was pointed out in the prior two sections, the data obtained within the scope of this test program consisted of full hybrid boost bearing data and ball bearing data. The fluid film bearing characteristics were then deducted from those obtained for the complete hybrid boost bearing and the ball bearing component. The full hybrid boost bearing test data is presented in Tables XVI, XVII, and XVIII. As indicated in the test program, the speed was varied between 4,000 and 10,000 rpm, the load between 500 (2,225 newtons) and 3,000 (13,350 newtons) lbs., and the main measurements were those of fluid film thickness, power loss, and flow. The given flow measurements represent the aggregate total of the ball bearing flow and the fluid film bearing flow measured at the given test point. The load vs. deflection characteristics of the full hybrid boost bearing are plotted in Figs. 68, 69, and 70 for 100 (37), 200 (93), and 300 F (149 C) respectively. The decrease in the slope of the 10,000 rpm curve at the 100 and 200 F runs is primarily due to the unexpected low load carrying capacity of the fluid film bearing discussed before.

5.3.1 Axial Stiffness Characteristics of the Hybrid Boost Bearing

The stiffness characteristics of the hybrid boost bearing at small film

TABLE XVI

FULL HYBRID BOOST BEARING PERFORMANCE DATA
T_{in} = 100°F (37°C)

N RPM	F_a LBS. (NEWTONS)	Q GPM (m^3/sec. x 10^{-4})	H.P.	h_F MILS (mm)
4,000	500 (2,225)	10.46 (6.40)	2.72	6.73 (.171)
↓	1,000 (4,450)	8.68 (5.46)	2.72	5.74 (.146)
	2,000 (8,900)	5.81 (3.65)	2.80	4.31 (.109)
↓	3,000 (13,350)	3.69 (2.32)	2.88	3.23 (.082)
6,000	500 (2,225)	–	5.74	7.16 (.182)
↓	1,000 (4,450)	10.04 (6.20)	5.51	6.02 (.153)
	2,000 (8,900)	6.75 (4.25)	5.38	4.54 (.115)
↓	3,000 (13,350)	4.62 (2.91)	5.76	3.44 (.087)
8,000	500 (2,225)	–	10.71	7.57 (.192)
↓	1,000 (4,450)	–	10.80	6.24 (.158)
	2,000 (8,900)	9.17 (5.77)	11.30	4.78 (.121)
↓	3,000 (13,350)	6.85 (4.31)	11.10	3.66 (.093)
10,000	500 (2,225)	–	16.00	8.38 (.213)
↓	1,000 (4,450)	–	18.35	6.75 (.171)
	2,000 (8,900)	11.87 (7.30)	17.54	4.71 (.119)
↓	3,000 (13,350)	9.66 (6.08)	15.59	3.38 (.086)

TABLE XVII

FULL HYBRID BOOST BEARING PERFORMANCE DATA
T_{in} = 200°F (93°C)

N RPM	F_a LBS. (NEWTONS)	Q GPM (m^3/sec. x 10^{-4})	H.P.	h_F MILS (mm)
4,000	500 (2,225)	–	1.58	5.78 (.147)
↓	1,000 (4,450)	–	1.58	4.98 (.126)
	2,000 (8,900)	9.5 (5.98)	1.58	3.79 (.096)
↓	3,000 (13,350)	5.9 (3.71)	1.49	2.66 (.068)
6,000	500 (2,225)	–	3.81	6.00 (.152)
↓	1,000 (4,450)	–	3.54	5.13 (.130)
	2,000 (8,900)	9.95 (6.26)	3.54	3.80 (.097)
↓	3,000 (13,350)	7.05 (4.43)	3.29	2.86 (.073)
8,000	500 (2,225)	–	7.34	6.40 (.163)
↓	1,000 (4,450)	–	7.15	5.27 (.134)
	2,000 (8,900)	11.38 (7.0)	7.15	4.02 (.102)
↓	3,000 (13,350)	9.0 (5.67)	6.82	3.11 (.079)
10,000	500 (2,225)	–	12.60	6.70 (.170)
↓	1,000 (4,450)	–	12.90	5.22 (.133)
	2,000 (8,900)	–	13.60	3.64 (.092)
↓	3,000 (13,350)	11.3 (7.0)	12.00	2.67 (.068)

TABLE XVIII

FULL HYBRID BOOST BEARING PERFORMANCE DATA
T_{in} = 300°F (149°C)

N RPM	F_a LBS. (NEWTONS)	Q GPM (m^3/sec. x 10^{-4})	H.P.	h_F MILS (mm)
4,000	500 (2,225)	–	.79	5.70 (.144)
↓	1,000 (4,450)	–	.74	4.76 (.120)
	2,000 (8,900)	–	.61	3.52 (.089)
↓	3,000 (13,350)	8.46 (5.32)	.44	2.55 (.064)
6,000	500 (2,225)	–	2.22	5.73 (.145)
↓	1,000 (4,450)	–	2.36	4.70 (.119)
	2,000 (8,900)	–	2.48	3.42 (.086)
↓	3,000 (13,350)	8.95 (5.63)	2.23	2.50 (.063)
8,000	500 (2,225)	–	5.24	6.18 (.156)
↓	1,000 (4,450)	–	5.33	5.02 (.127)
	2,000 (8,900)	–	5.96	3.69 (.093)
↓	3,000 (13,350)	9.60 (6.04)	5.96	2.56 (.065)
10,000	500 (2,225)	–	9.18	6.75 (.170)
↓	1,000 (4,450)	–	9.60	5.42 (.137)
	2,000 (8,900)	–	10.47	3.83 (.097)
↓	3,000 (13,350)	10.74 (6.60)	10.58	2.60 (.066)

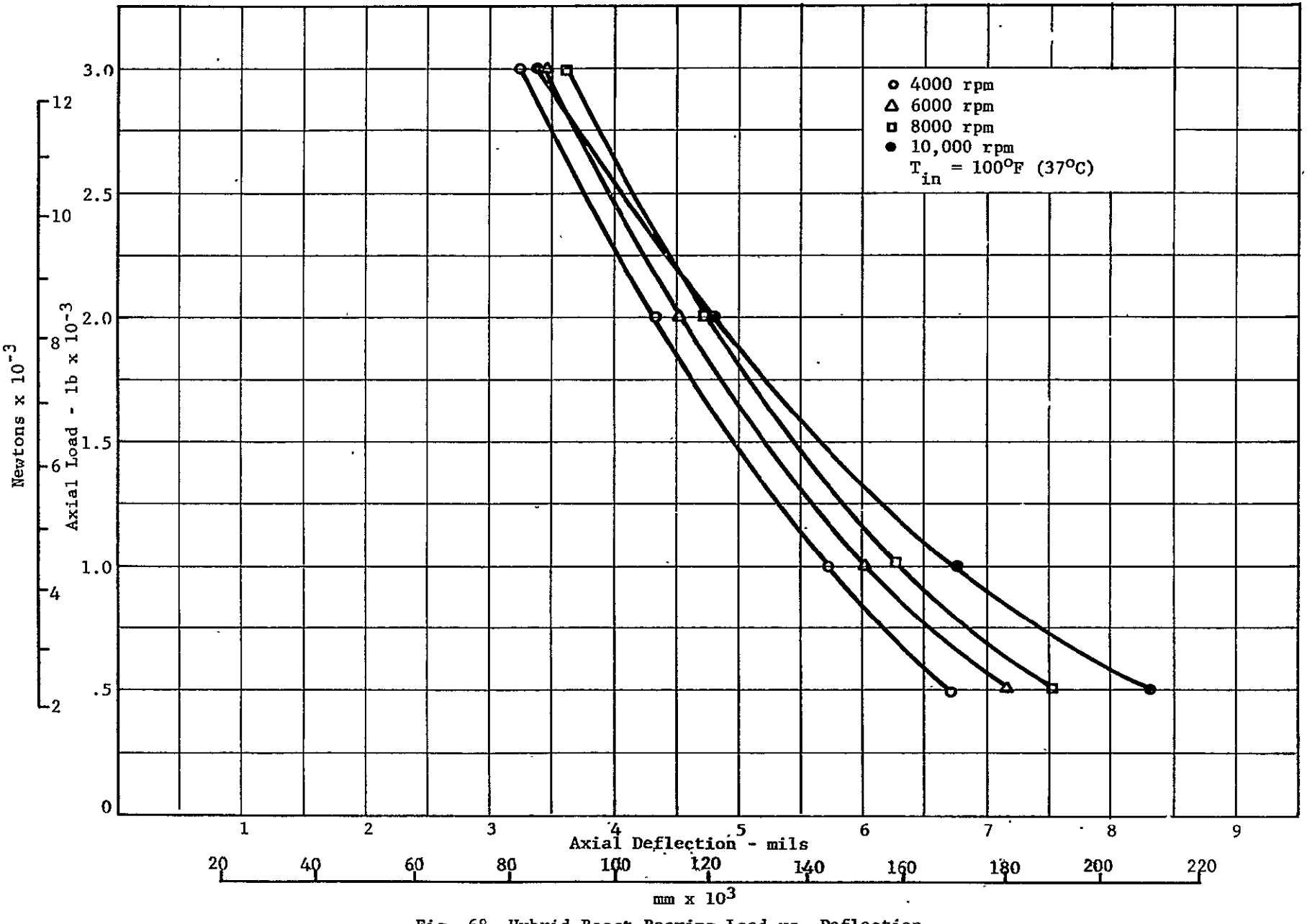

Fig. 68 Hybrid Boost Bearing Load vs. Deflection

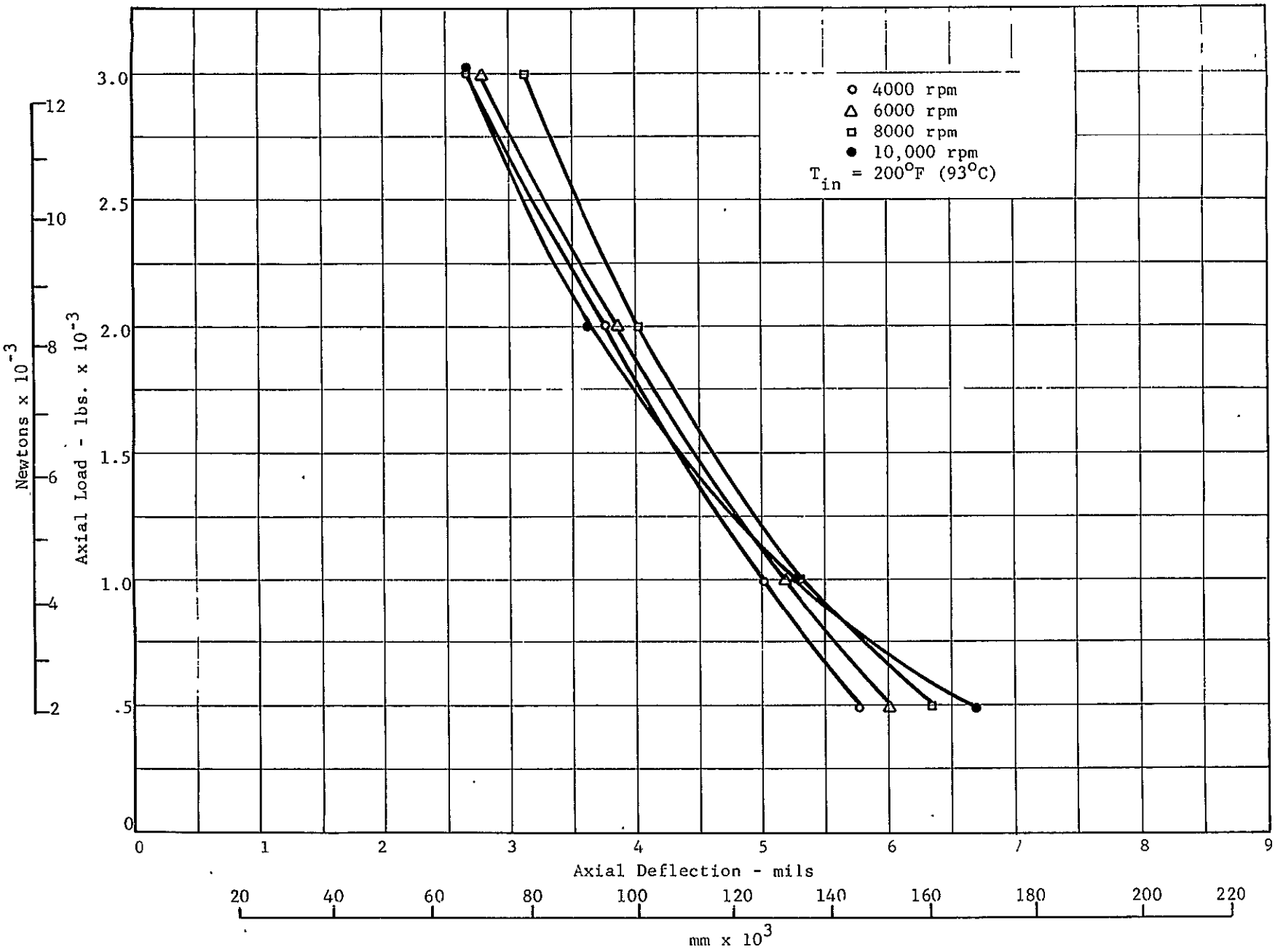

Fig. 69 Hybrid Boost Bearing Load vs. Deflection

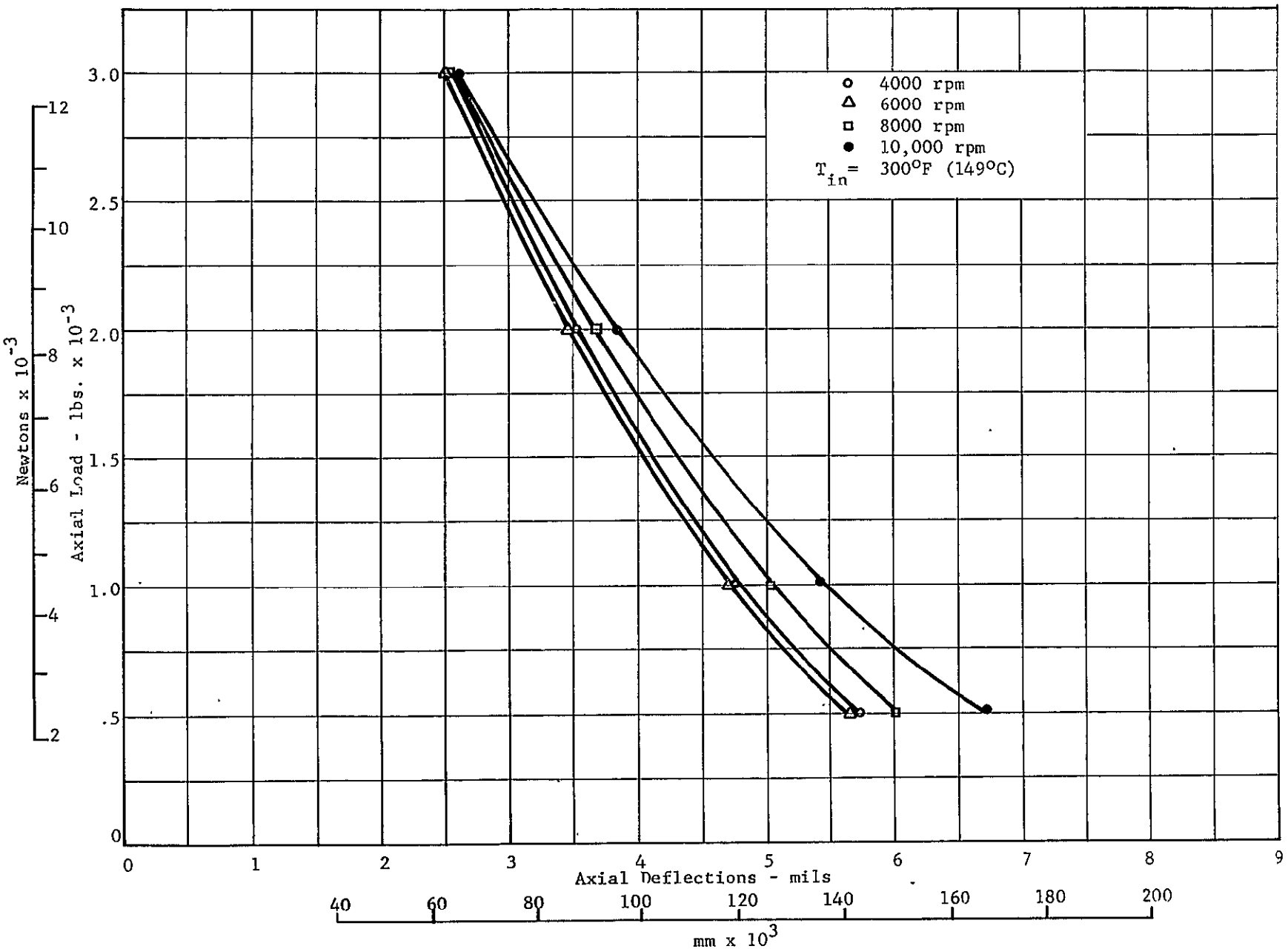

Fig. 70 Hybrid Boost Bearing Load vs. Deflection

thicknesses are fairly linear. On the average the stiffness values at 100 F, 200 F, and 300 F are about 1,000,000 lbs/in. These axial stiffness characteristics appear not to be appreciably affected by temperature. Stiffness generally decreases with increase in speed mainly due to the effects of the ball bearing and relative loss of load capacity of the fluid film bearing.

5.3.2 Load Capacity of the Hybrid Boost Bearing

Plots of load vs. deflection for each speed starting with a speed of 0 rpm and each temperature are given in Figs. 71 through 85 respectively. The 0 rpm plots are mainly representative of the hydrostatic effect present in the system. The hydrostatic load carrying component is a function of the pressure existing within the supply groove in the fluid film bearing area rather than the supply pressure measured at the inlet to the bearing housing. At high temperatures and large clearances the pressure drop across the bearing lands is minimal, hence the groove pressure is close to the ambient. At low oil temperatures the ΔP is high and the groove pressures are close to supply pressure. This can be clearly seen when the hydrostatic effects obtained at low temperatures are compared with those obtained at high temperatures for zero speeds and clearances. Thus, for instance, at a film thickness of 4 mils (.102 mm) 0 speed, at 100 F (37 C), the hydrostatic effect at a temperature of 100 F (37C) is responsible for approximately 380 lbs. (1690 newtons), about 160 lbs. (720 newtons) at a temperature of 200 F (93 C), and only about 30 lbs. (133 newtons) at a temperature of 300 F (149 C). The quoted values are obtained from Figs. 71, 76, and 81 respectively. The hydrodynamic effect at each one of the temperatures can be seen by comparing the results obtained at 0 speed with those obtained at higher speeds, thus for example, at 100 F the fluid film bearing share gradually increases due to the hydrodynamic action as shown in Figs. 72, 73, and 74, but in Fig. 75 which represents the results for 100 F (37 C) at 10,000 rpm, an actual drop in load carrying capacity is apparent. The same thing holds true for 200 F (93 C) but does not hold for the 300 F (149 C) series where the load carrying capacity gradually increases up to 10,000 rpm. The load carried by the fluid film bearing at each film thickness can easily be established by following a vertical line on any of the load carrying capacity curves shown in Figs. 71 through 86 at any

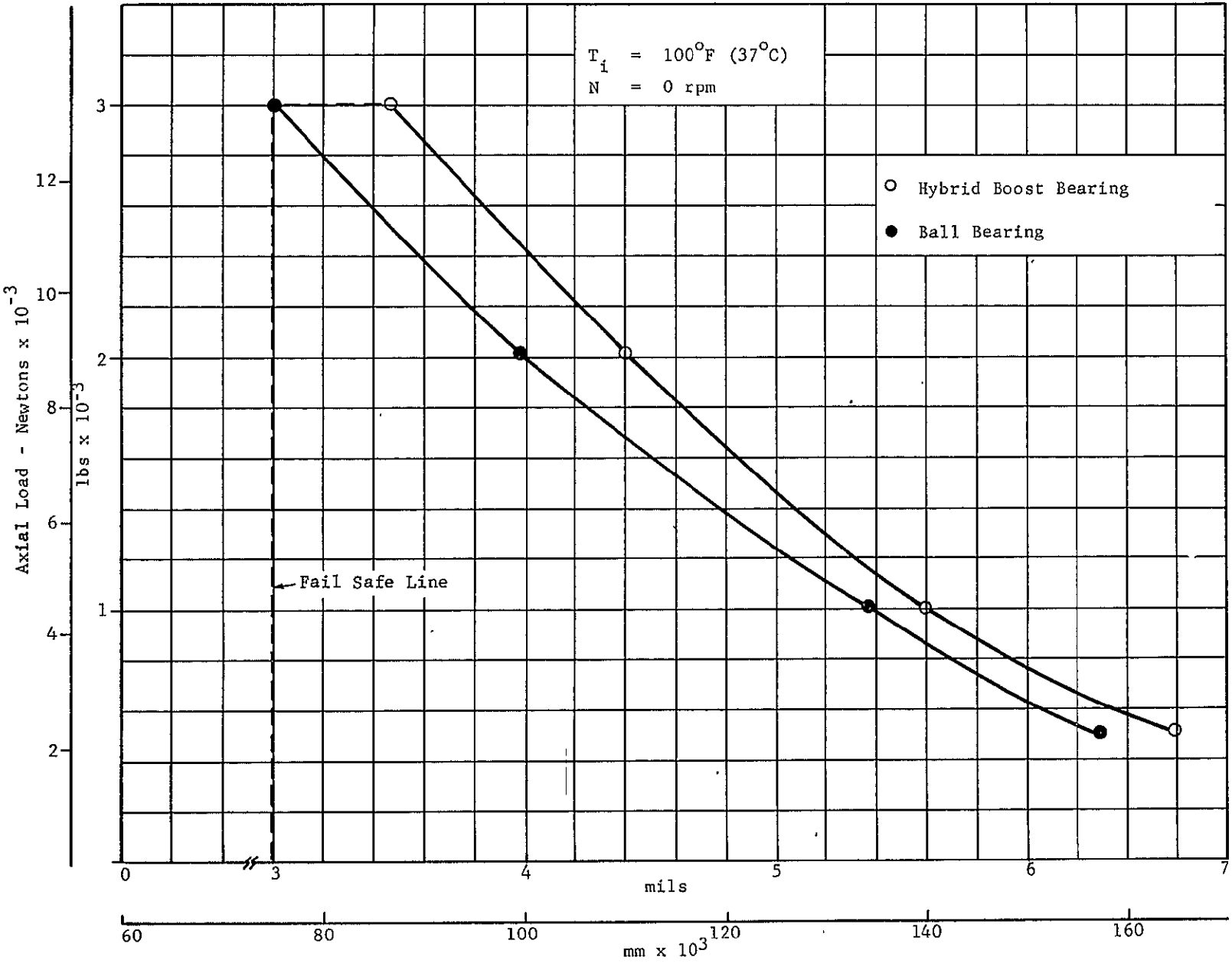

Fig. 71 Load vs. Deflection

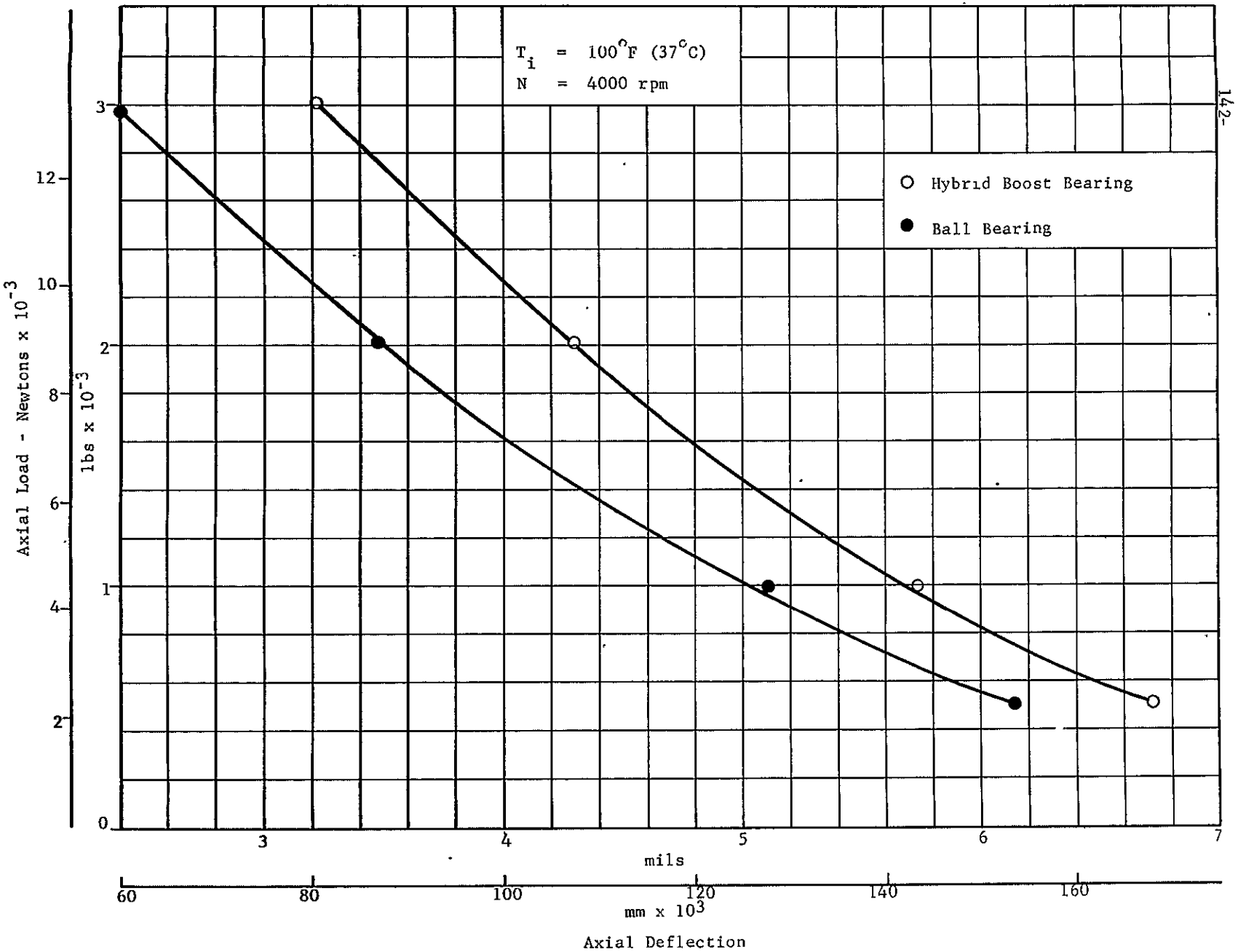

Fig. 72 Load vs. Deflection

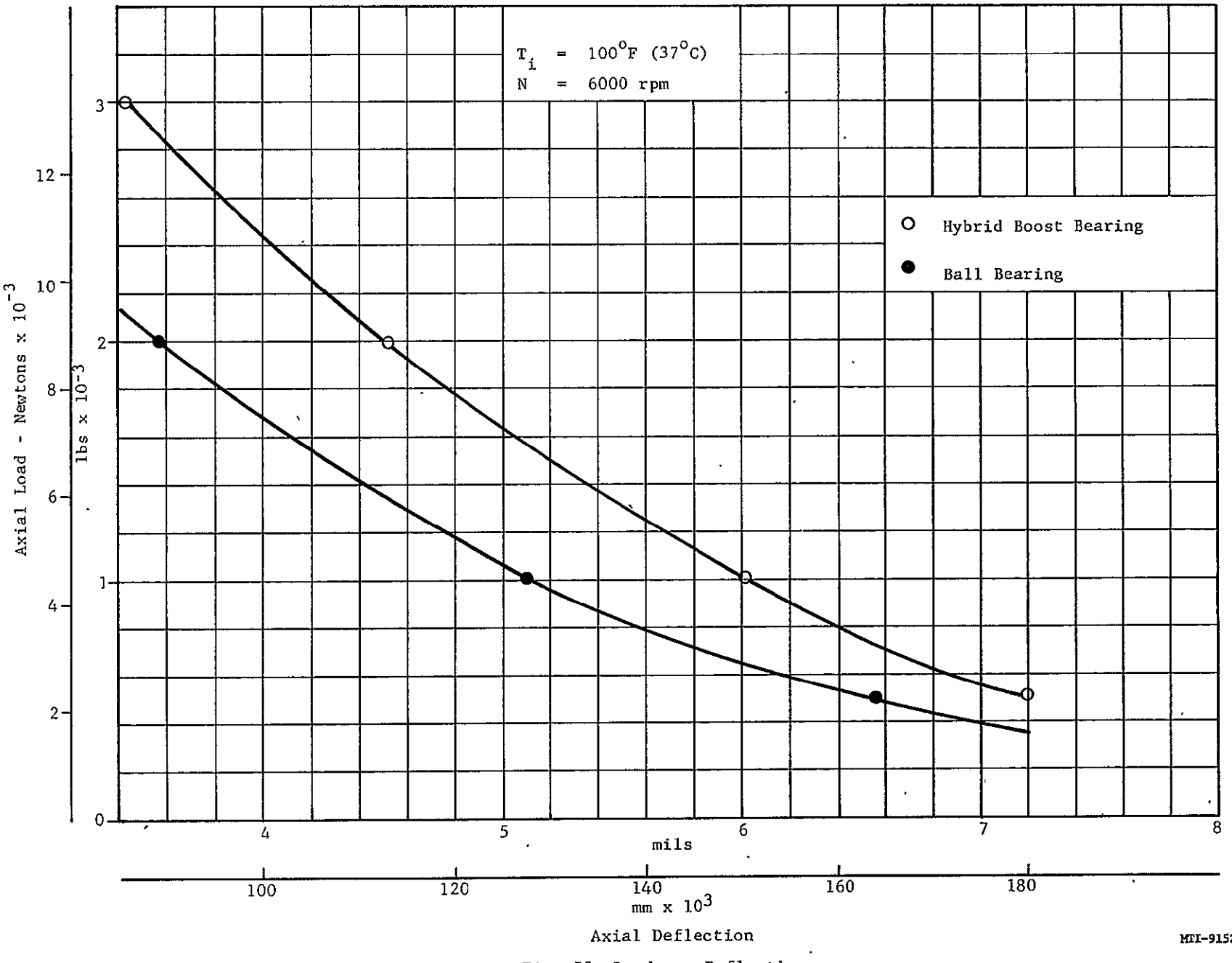

Fig. 73 Load vs. Deflection

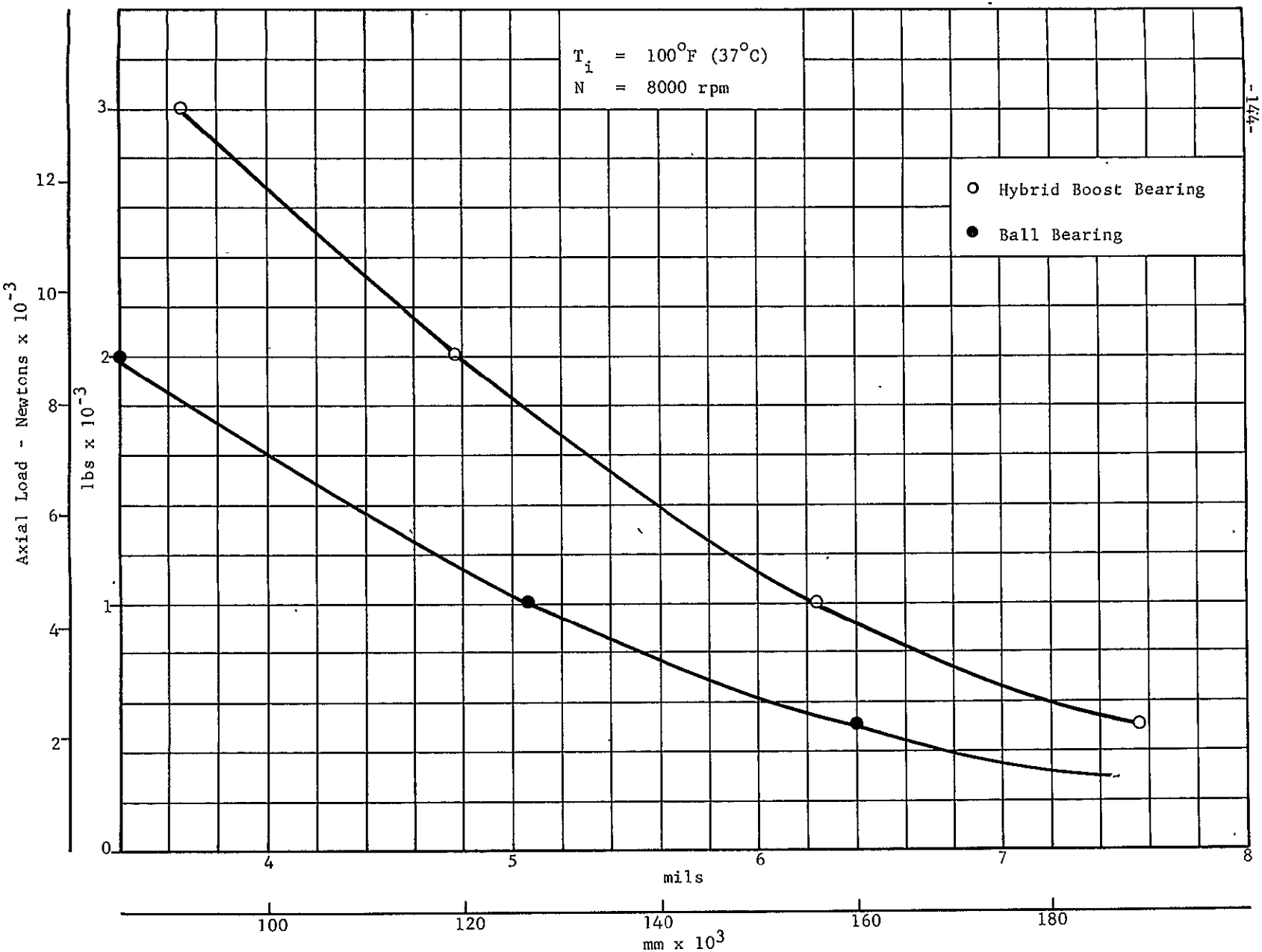

Fig. 74 Load vs. Deflection

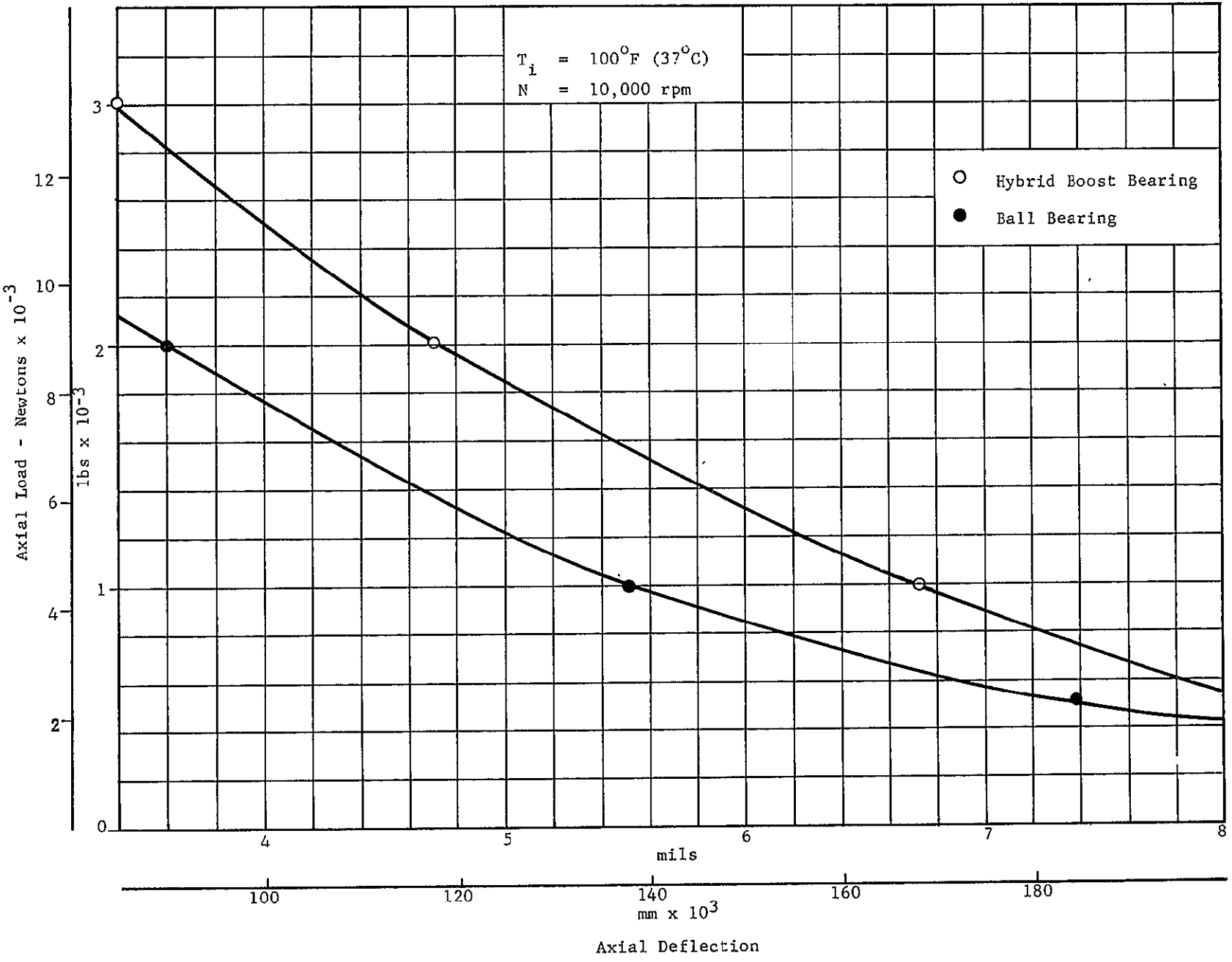

Fig. 75 Load vs. Deflection

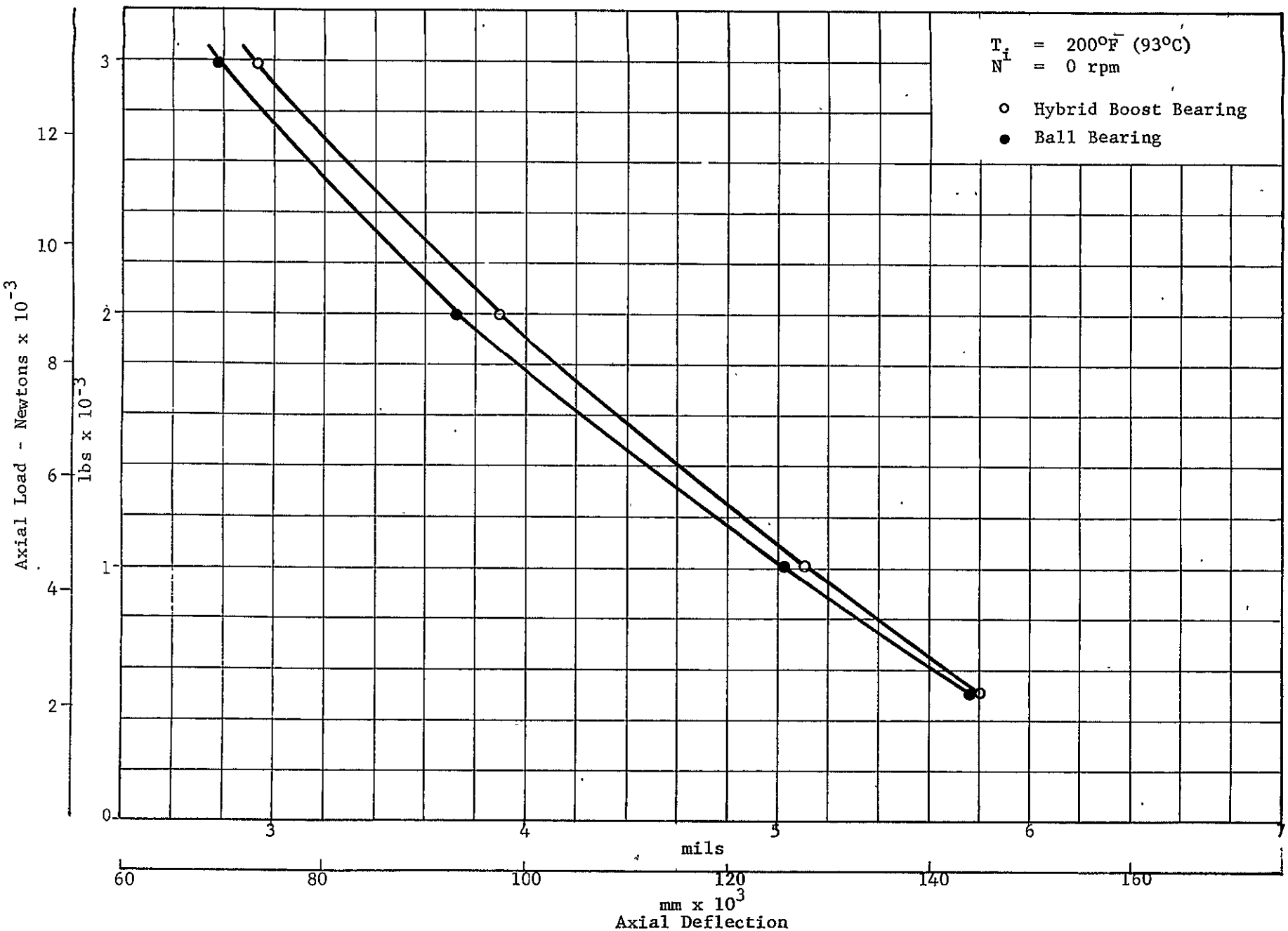

Fig. 76 Load vs. Deflection

MTI-9203

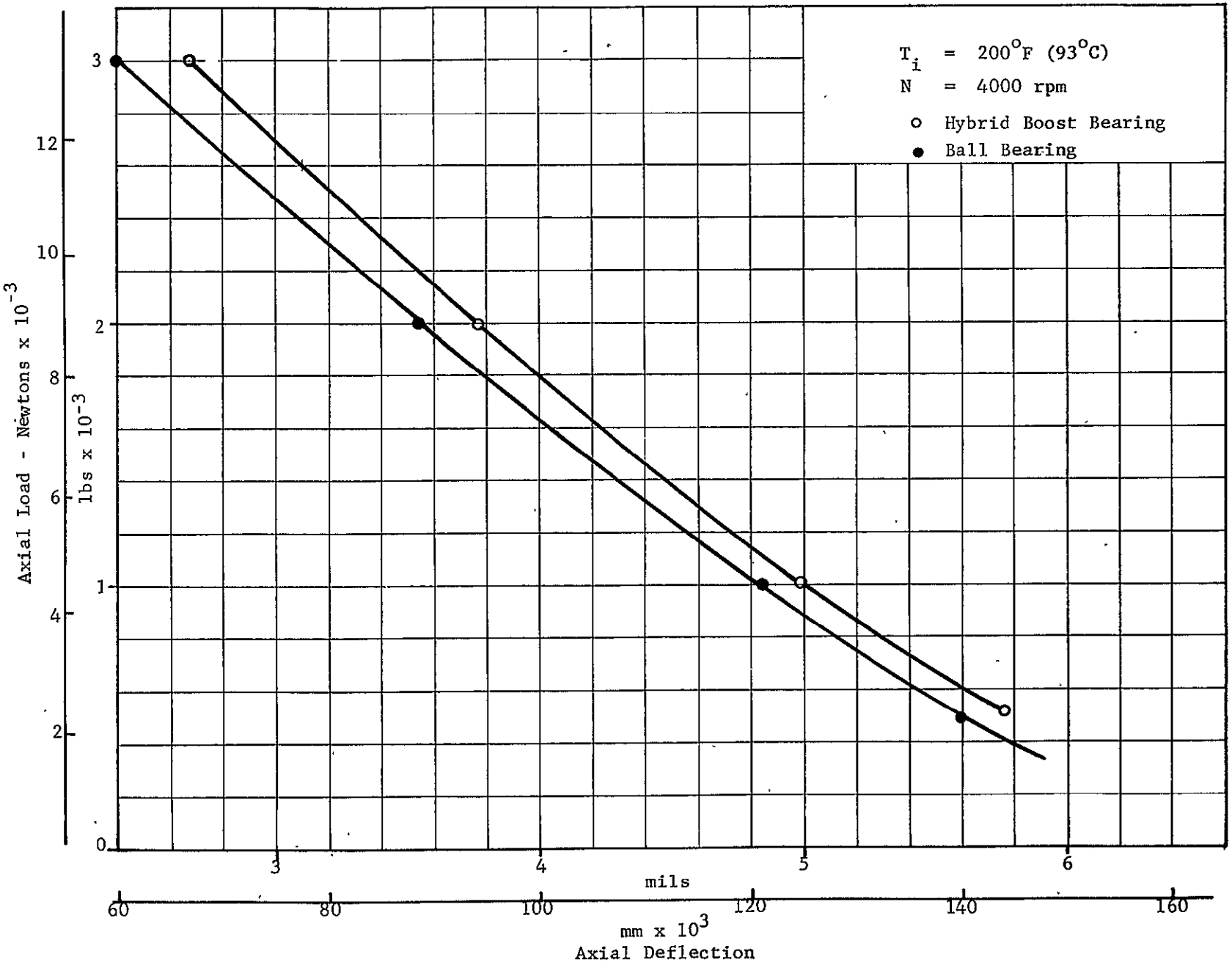

Fig. 77 Load vs. Deflection

MTI-9202

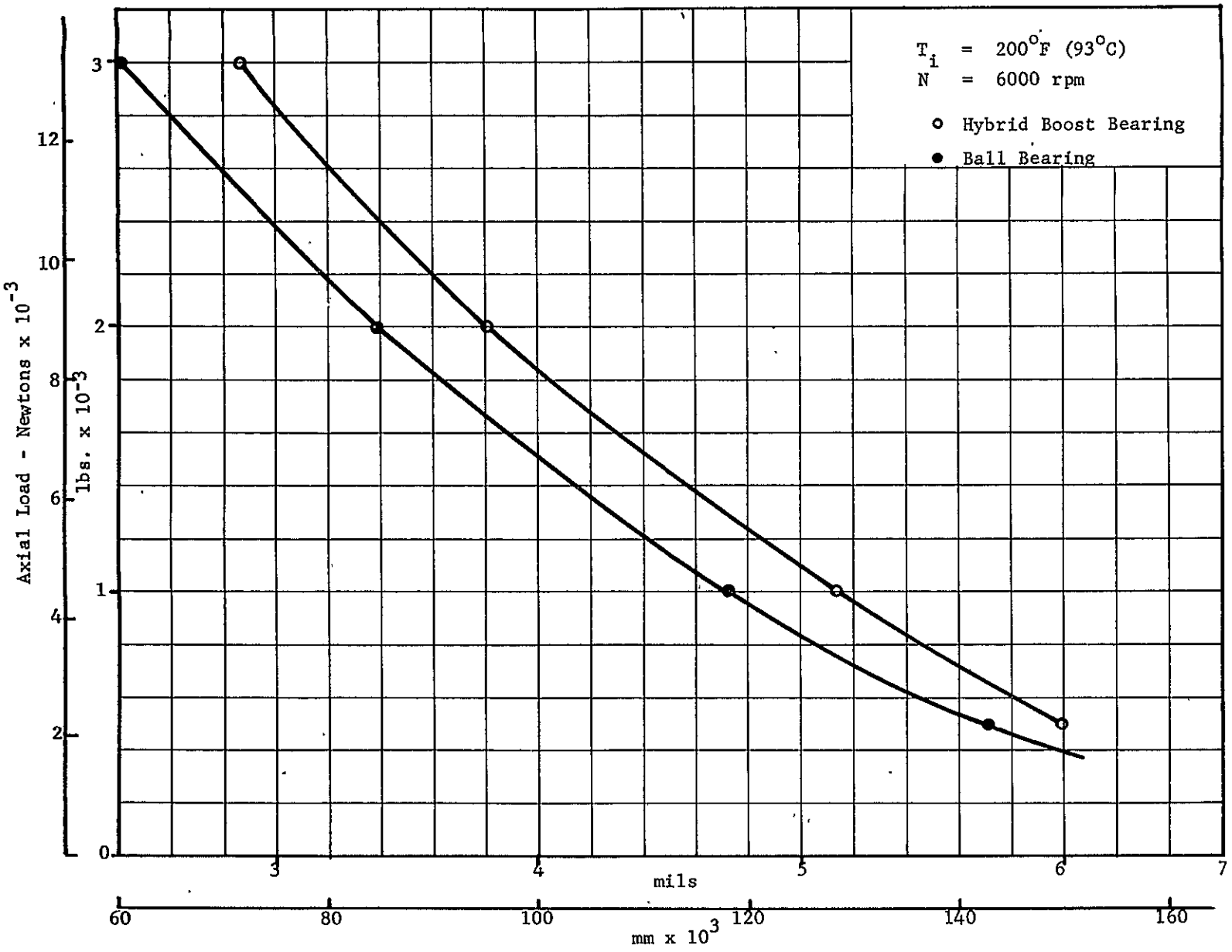

Axial Deflection

Fig. 78 Load vs. Deflection

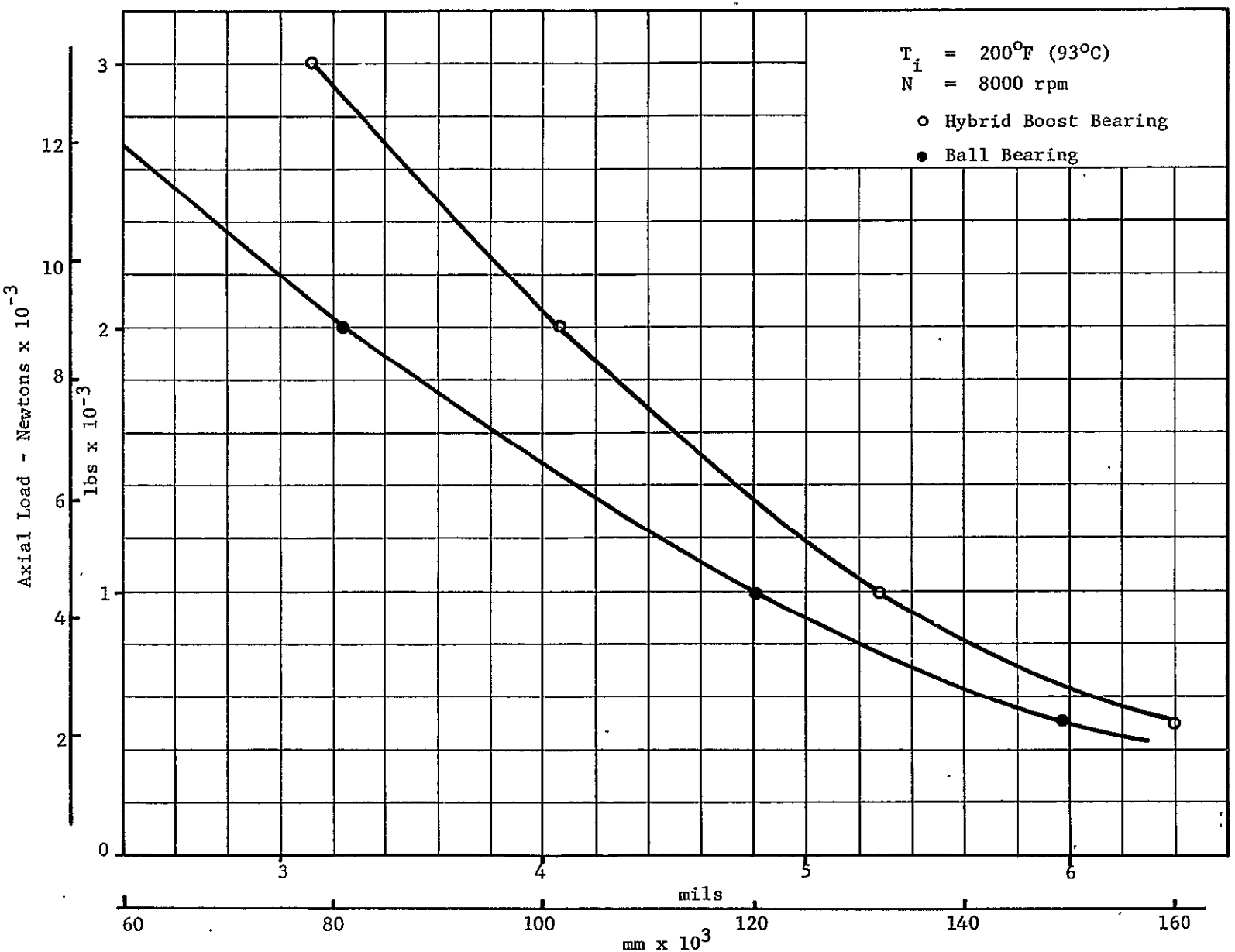

Fig. 79 Load vs. Deflection

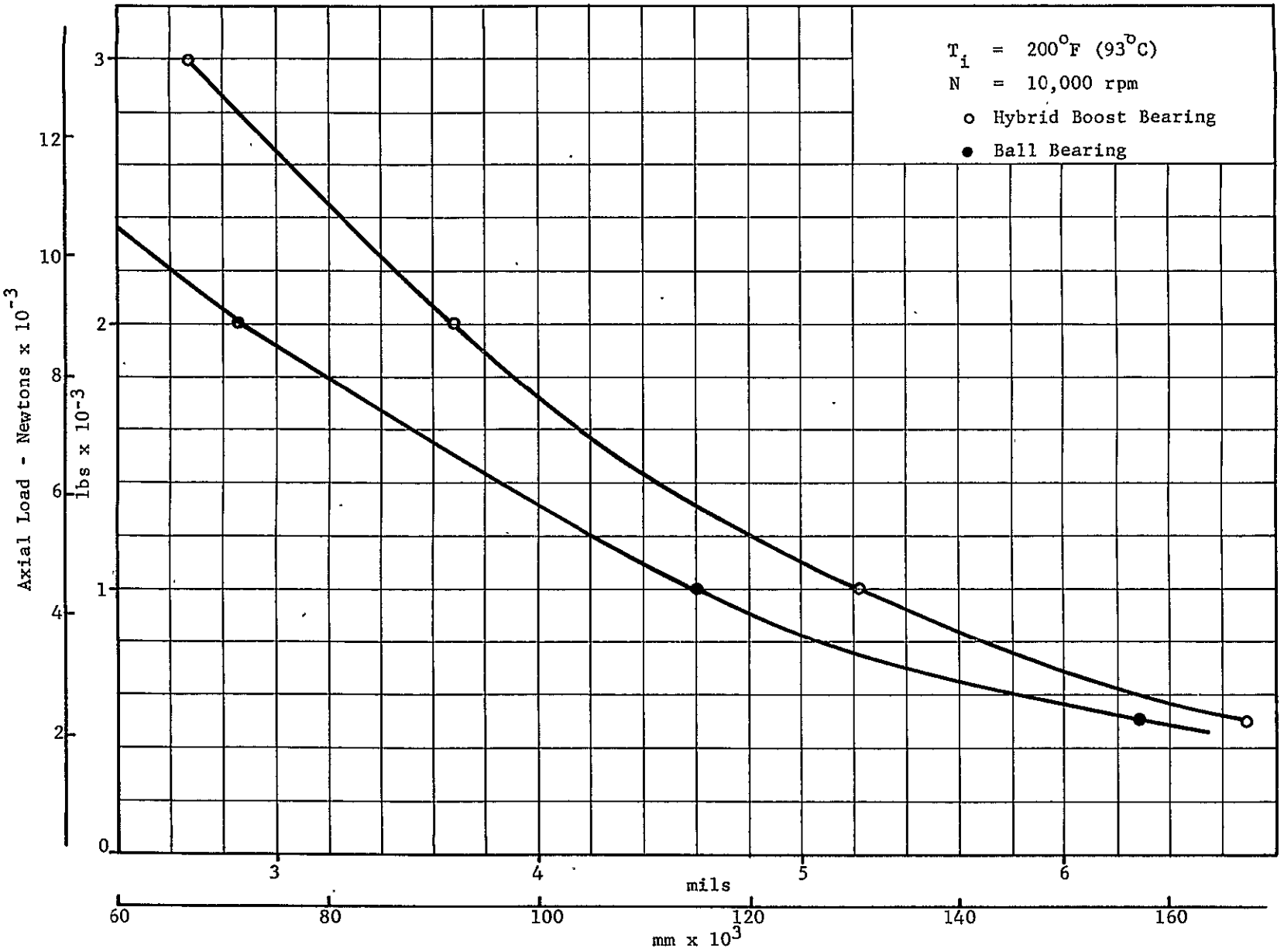

Axial Deflection

Fig. 80 Load vs. Deflection

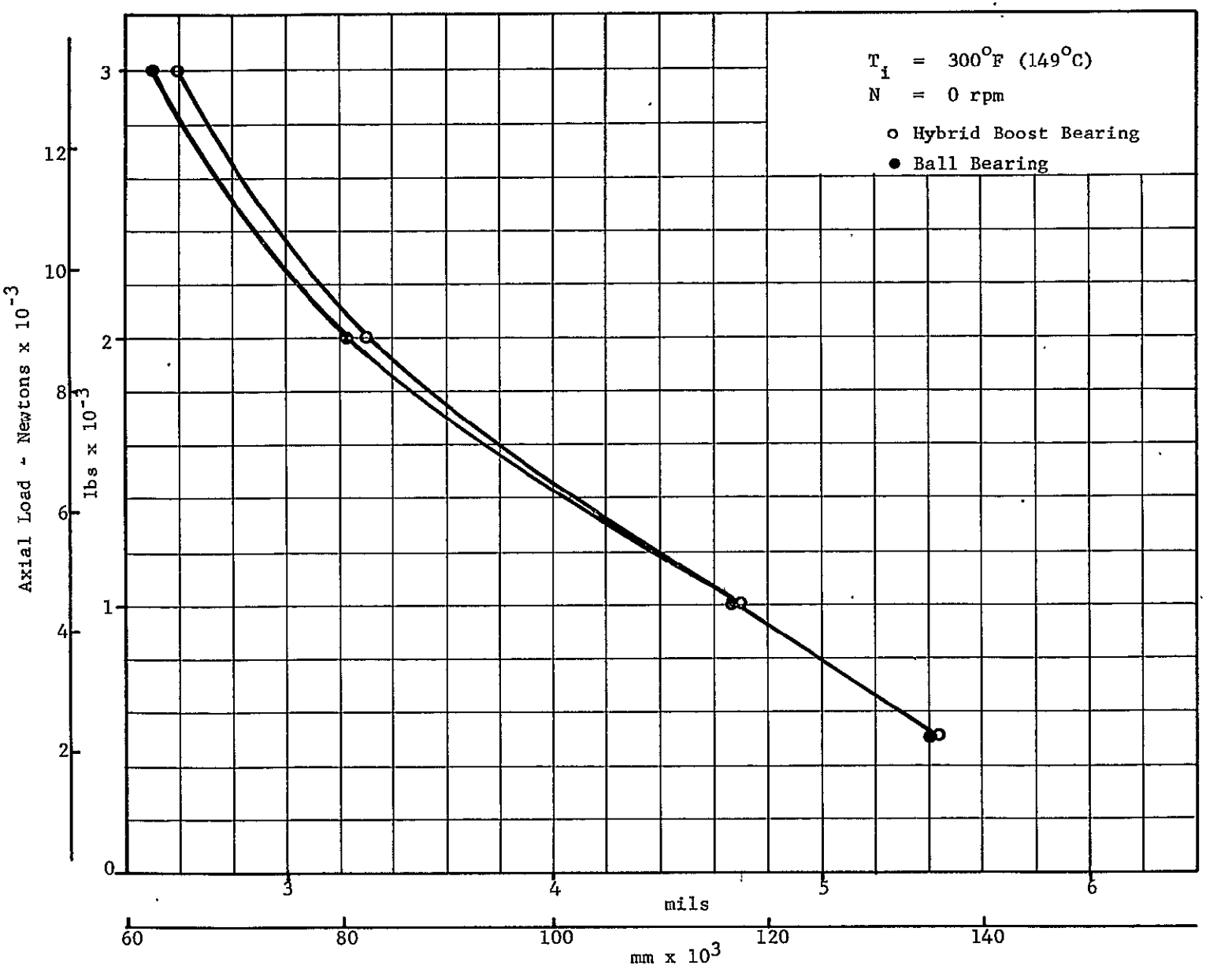

Fig. 81 Load vs. Deflection

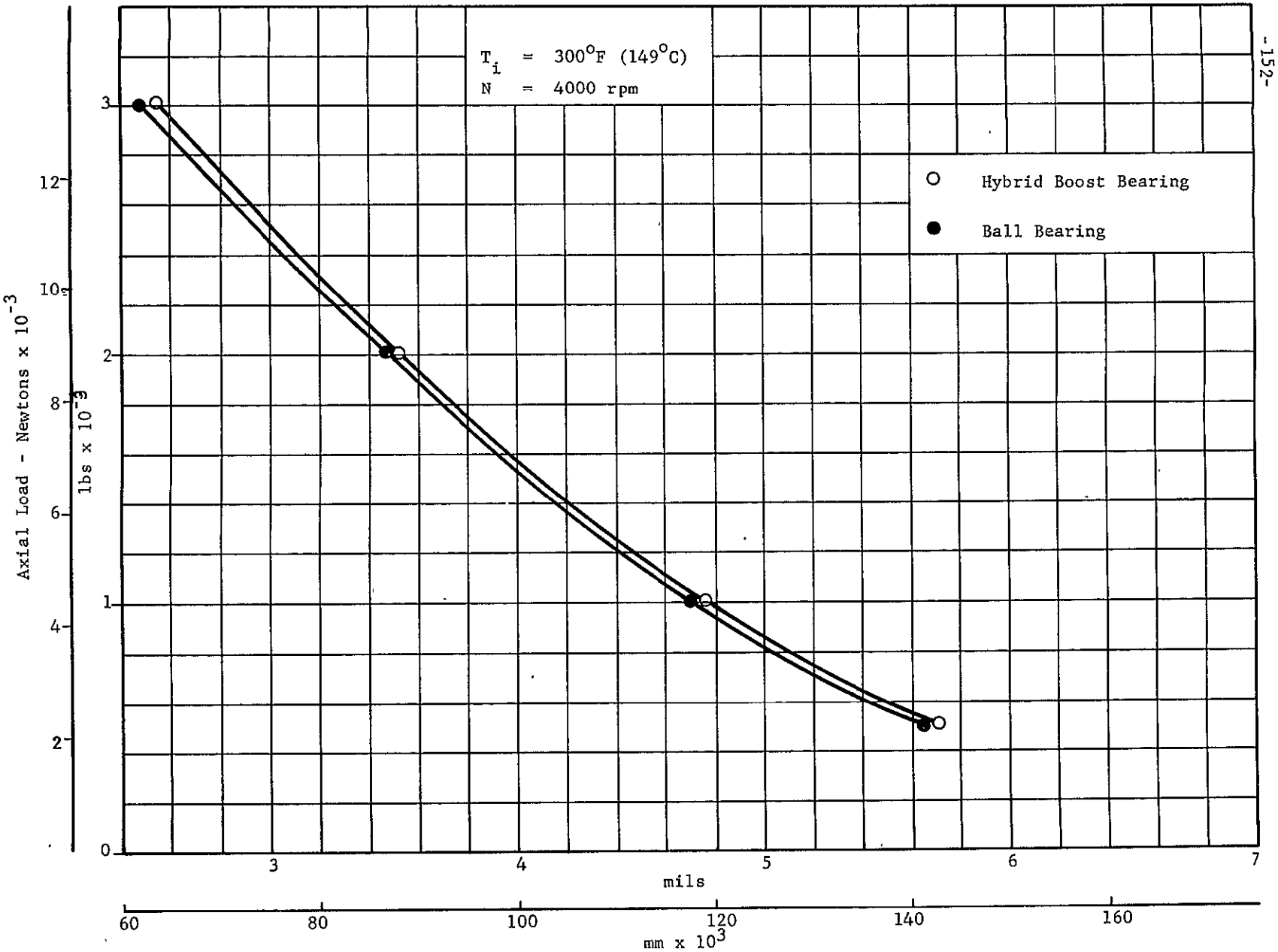

Fig. 82 Load vs. Deflection

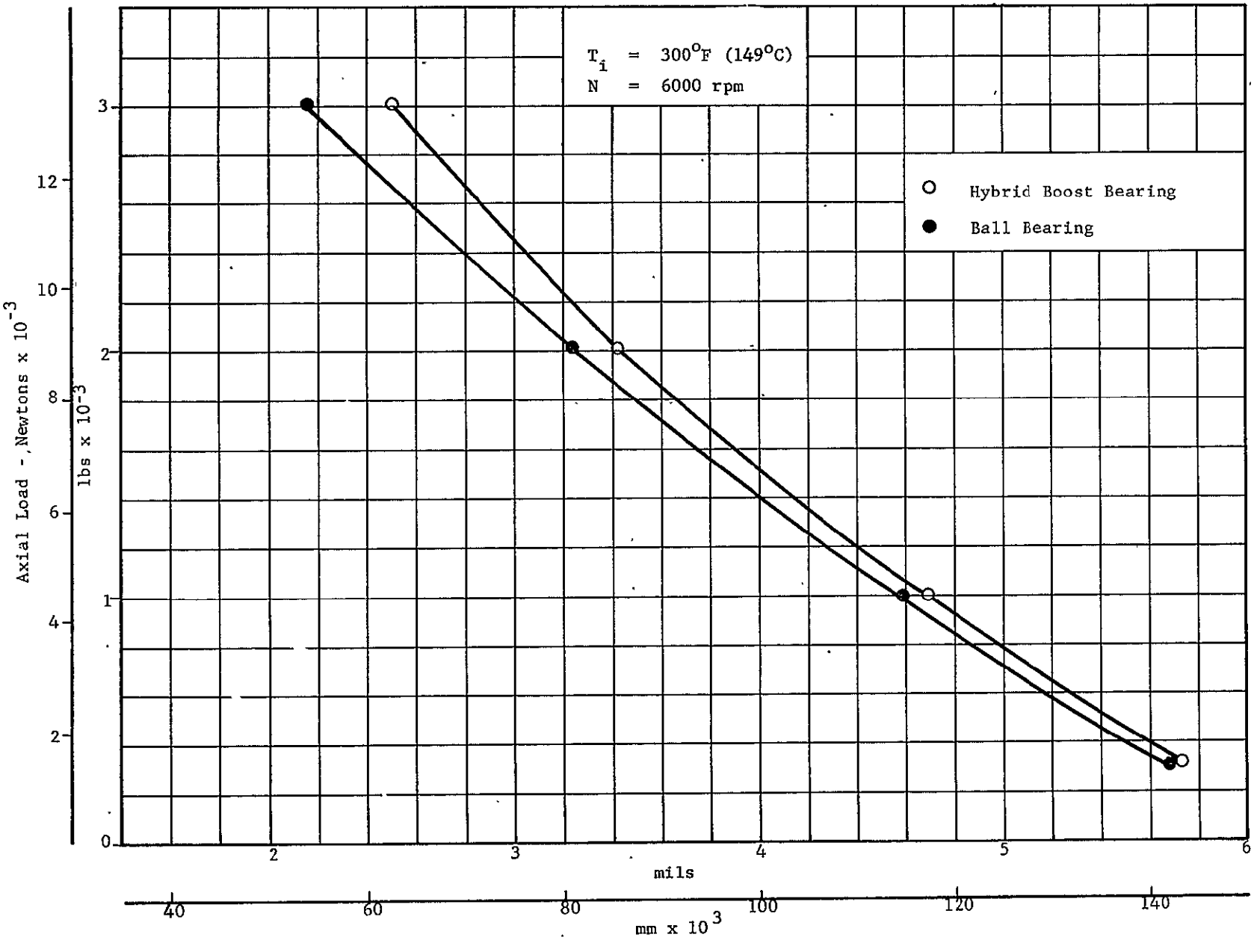

Fig. 83 Load vs. Deflection

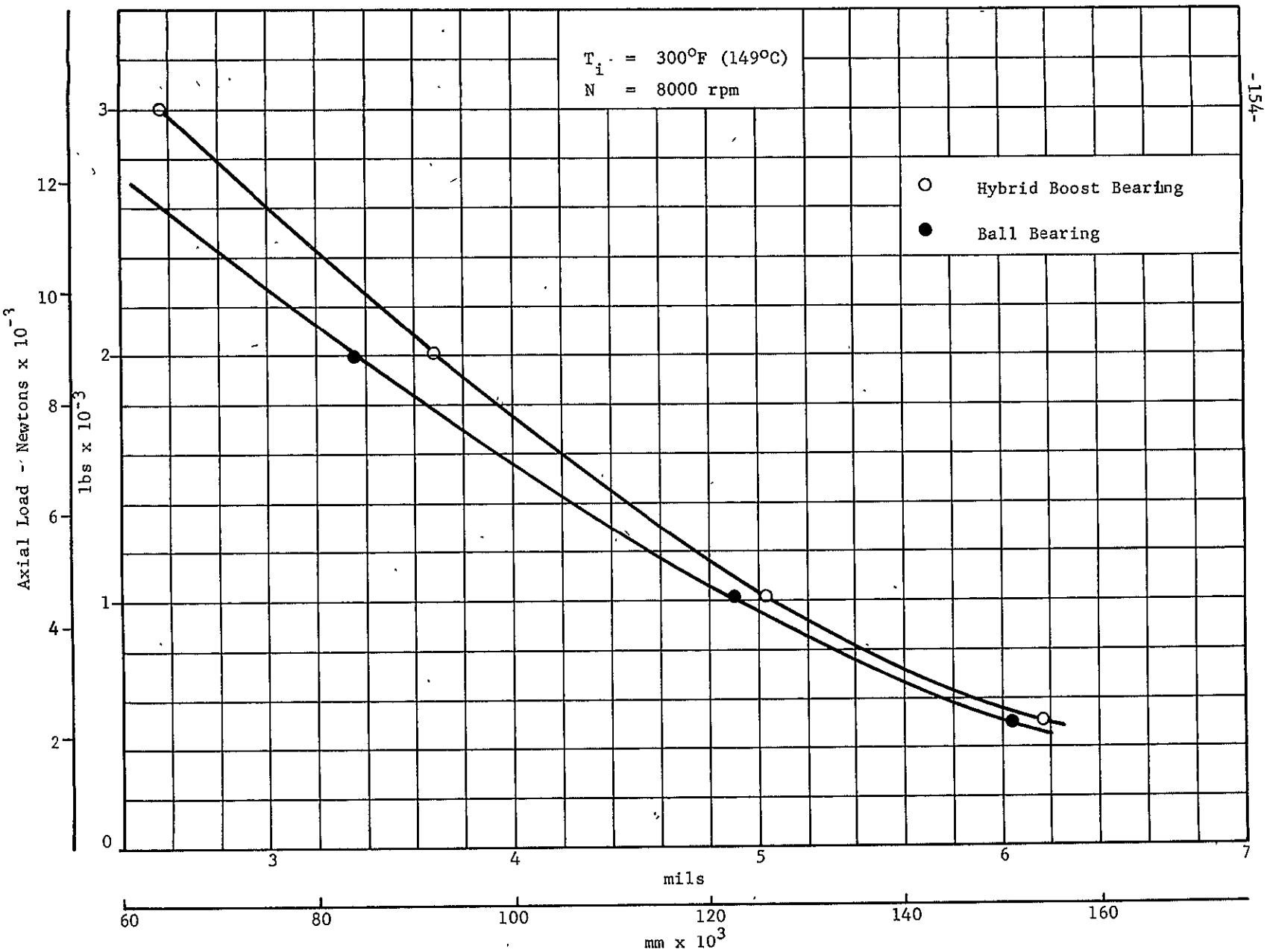

Fig. 84 Load vs. Deflection

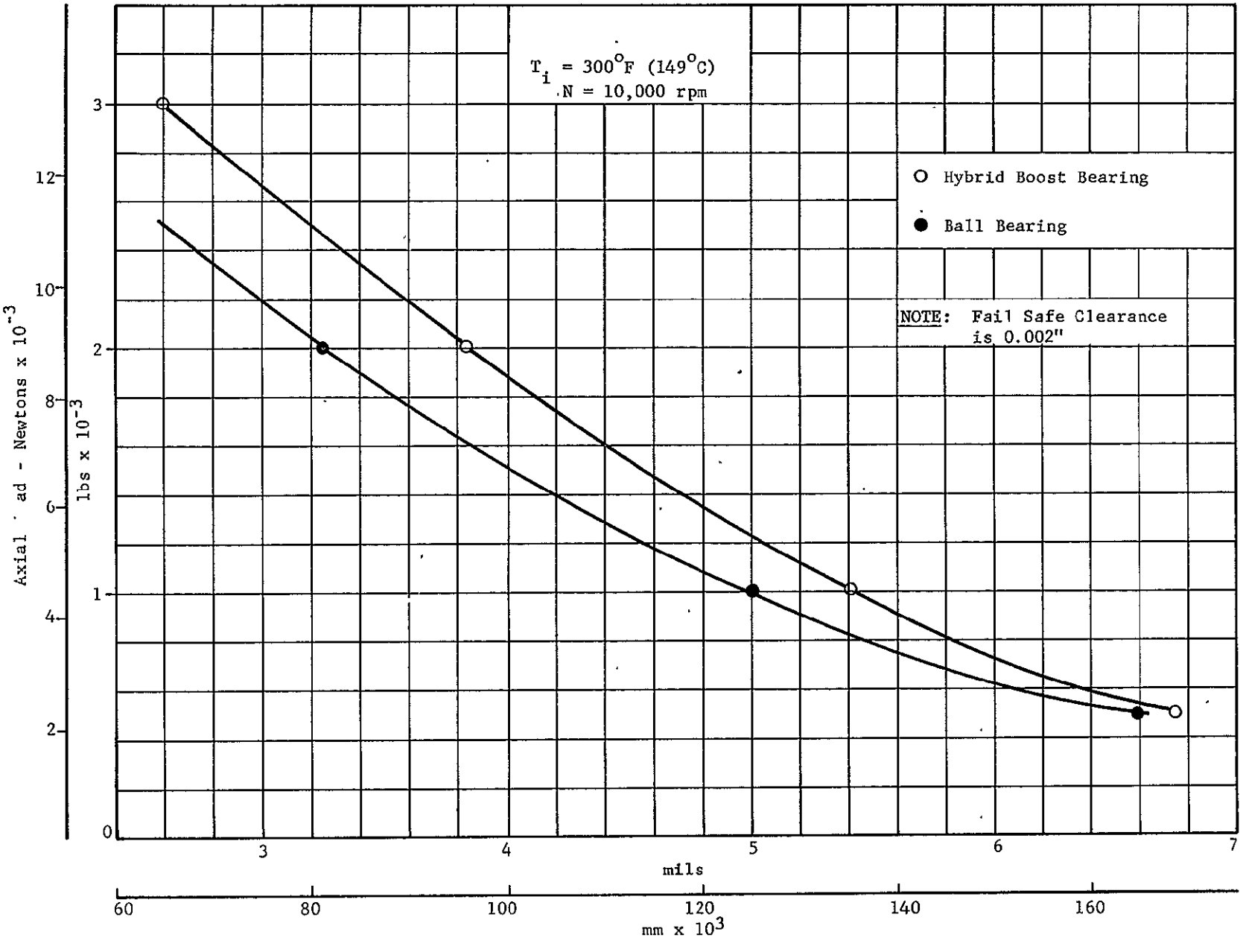

Fig. 85 Load vs. Deflection

given film thickness and measuring the difference between the full hybrid boost bearing capacity and that of the ball bearing. This difference obviously represents the share of the load carried by the fluid film bearing at the given conditions of operation. Note that at 300 F (149 C) the fluid film bearing capacity is relatively low because of the low viscosities of the lubricant prevalent at these conditions of operation, and low supply groove pressures.

5.3.3 Power Loss of the Hybrid Boost Bearing

The hybrid boost bearing torque and power losses are given in Fig. 86. The power loss as expected is highest at low temperatures where the viscosity of the fluid is highest and increases with speed.

A plot of horsepower loss vs. speed on log-log paper is shown in Fig. 87. It is interesting to note that an exponential relationship between horsepower and speed exists for the full hybrid boost bearing as shown by the straight lines obtained, the slope of which represents the exponent of speed. Since a definite variation in slope is indicated as a function of temperature, it is possible that the change in slope attributable to speed on this plot in reality comes about as a result of viscosity changes which in turn are a function of speed. These viscosity changes may materialize from changes in the churning oil heating rates. It may further be noted that the slope of the horsepower vs. speed curve on log-log paper appears to be increasing as the temperature increases in almost direct proportion to the temperature increase. Thus, the slope of the 100 F curve is 1.67, that of the 200 F curve, 2.3, and that for the 300 F curve, 3. The generally high oil flows present at the high temperature may well be responsible for this phenomenon.

A comparison of the component losses is shown in Fig. 88. Again, as before, due to the relatively low variation as a function of load an average power loss was plotted here vs. speed at the different temperatures of operation. On the average (with exception of the 10,000 rpm point) the fluid film bearing losses are twice as large as those of the ball bearing component.

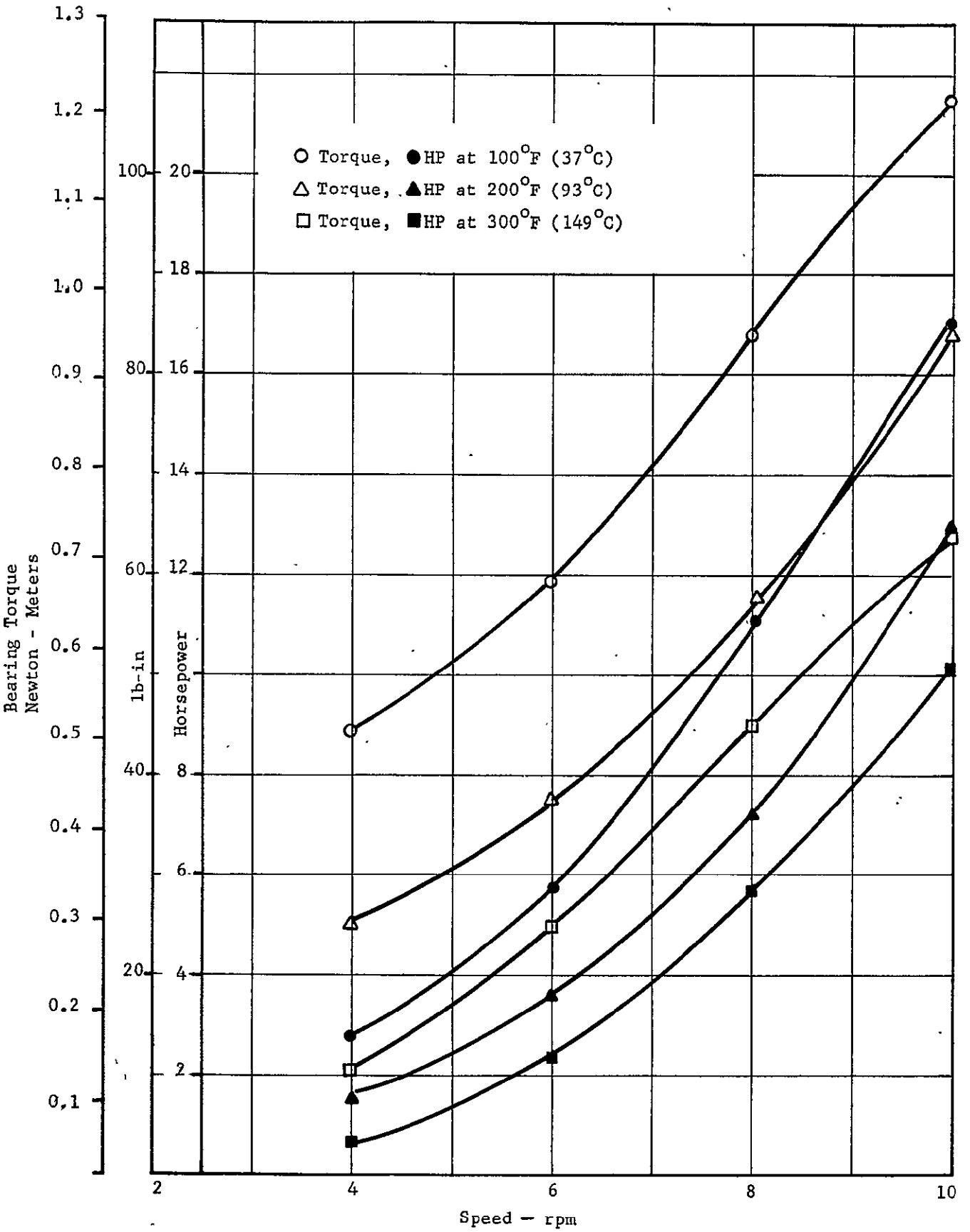

Fig. 86 Hybrid Boost Bearing Torque and Power Losses vs. Speed

MTI-8565

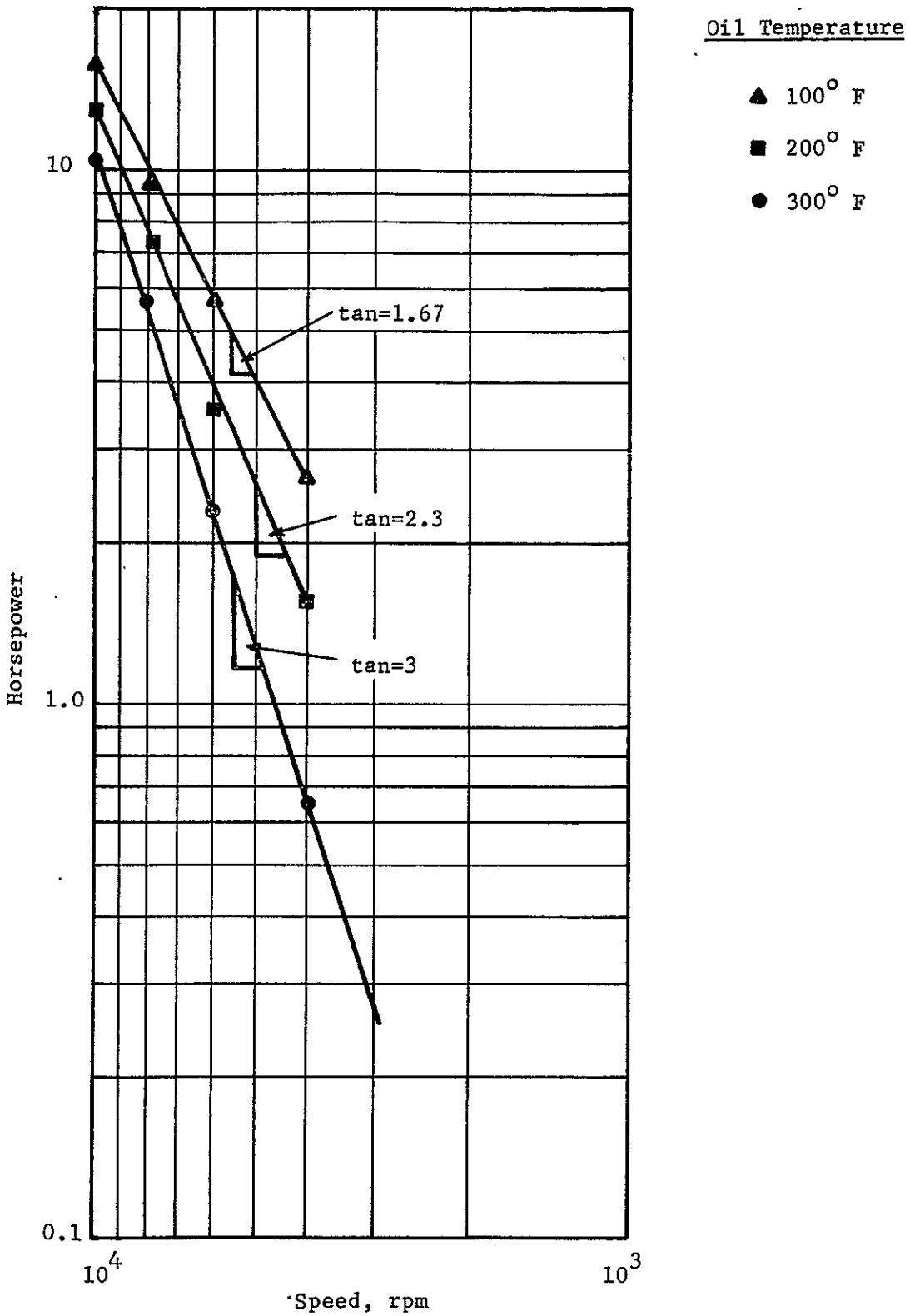

Fig. 87 Power Loss vs Speed for Hybrid Boost Bearing

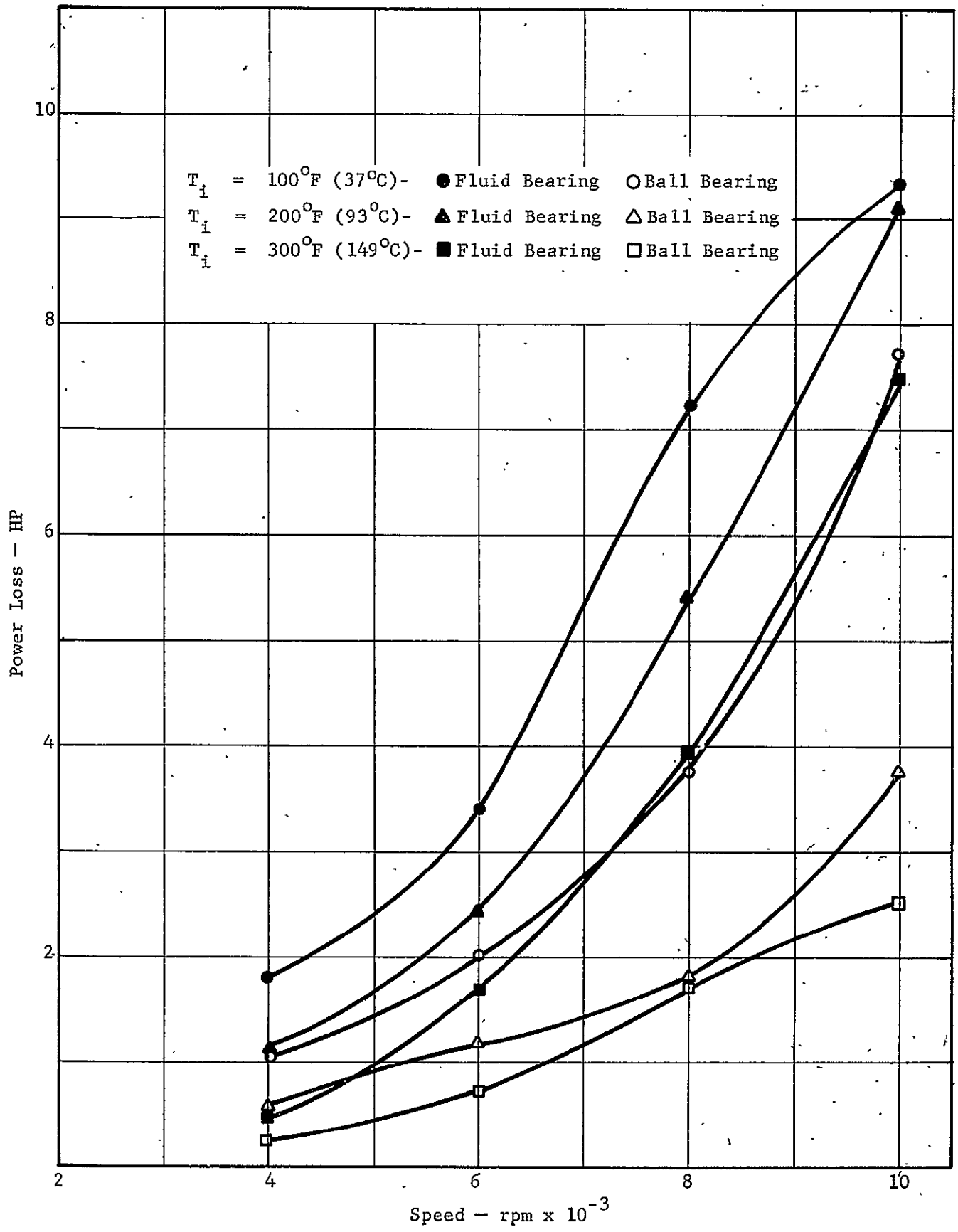

Fig. 88 Comparison of Ball Bearing and Fluid Film Bearing Power Losses

MTI-8570

5.3.4 Thermal Gradients

The temperature existing within the test rig during operation are shown in Tables XIX, XX and XXI. Inasmuch as the circumferential temperature gradients were negligible, the temperatures listed in these tables correspond to a cross-section through one of the fluid film bearing pockets only, along a plane parallel with the axis of rotation, i.e., the temperatures are measured in a plane similar to that used in the thermal analysis and shown in Figs. 42 and 43. The tables list the following factors for each test point: Speed in rpm (N), load (F_a) in lbs. and newtons, ball bearing outer race temperature (T_{OR}), the temperature at the fluid film bearing outer land (T_{OL}), the temperature at the fluid film bearing pocket center (T_P), the temperature at the fluid film bearing inner land (T_{IL}) and the temperature at the back surface of the fluid film bearing stator (T_B), all temperatures are given in degrees F and C. The location of the fluid film bearing temperatures is shown in Fig. 62.

A comparison between the measured temperature values presented in the above mentioned tables and the calculated values presented in Figs. 42 and 43 is difficult to draw since the calculated values are based upon isoviscous conditions corresponding to those present at 100°F (37°C) and 300°F (149°C) respectively. It is nevertheless of importance to note that the thermal gradients predicted on the analytical basis are much higher than those actually measured. Because the calculated values of thermal deformation (based on the higher thermal gradients) were still reasonably low, the actually measured lower thermal gradients across the stator in the axial direction will obviously further lower the thermal deformation, hence on the basis of the recorded measurements no thermal deformation problems are anticipated on the stator of the fluid film bearing.

The ball bearing outer race temperature measured on test is appreciably higher than the calculated one, and, as already mentioned in the discussion of the ball bearing test results, appears to be increasing with load. What portion of this increase is truly due to the effect of load and what portion to a slow ball temperature rise on its way to a thermal equilibrium

TABLE XIX

HYBRID BOOST BEARING TEMPERATURE DATA
T_{in} = 100°F (37°C)

N RPM	F_a LBS.(NEWTONS)	T_{OR} °F(°C)	T_{OL} °F(°C)	T_p °F(°C)	T_{IL} °F(°C)	T_B °F(°C)
4,000	500 (2,225)	100 (37)	96 (35)	96 (35)	97 (36)	97 (36)
	1,000 (4,450)	109 (43)	98 (37)	98 (37)	99 (37)	99 (37)
	2,000 (8,900)	113 (45)	100 (37)	101 (38)	101 (38)	101 (38)
	3,000(13,350)	115 (46)	105 (40)	106 (41)	107 (42)	106 (41)
6,000 ↓	500 (2,225)	117 (47)	103 (39)	104 (40)	104 (40)	105 (40)
	1,000 (4,450)	124 (51)	104 (40)	104 (40)	104 (40)	105 (40)
	2,000 (8,900)	126 (52)	105 (40)	106 (41)	106 (41)	108 (42)
	3,000(13,350)	127 (53)	107 (42)	108 (42)	111 (44)	111 (44)
8,000 ↓	500 (2,225)	117 (47)	105 (40)	104 (40)	105 (40)	106 (41)
	1,000 (4,450)	132 (55)	107 (42)	107 (42)	108 (42)	110 (43)
	2,000 (8,900)	138 (59)	109 (43)	108 (42)	110 (43)	112 (44)
	3,000(13,350)	141 (61)	113 (45)	113 (45)	115 (46)	114 (46)
10,000 ↓	500 (2,225)	134 (57)	107 (42)	106 (41)	108 (42)	108 (42)
	1,000 (4,450)	147 (64)	111 (44)	110 (43)	112 (44)	112 (44)
	2,000 (8,900)	147 (64)	118 (48)	114 (46)	115 (46)	115 (46)
	3,000(13,350)	158 (70)	118 (48)	118 (48)	119 (48)	120 (49)

TABLE XX

HYBRID BOOST BEARING TEMPERATURE DATA
T_{in} = 200°F(93°C)

N RPM	F_a LBS.(NEWTONS)	T_{OR} °F(°C)	T_{OL} °F(°C)	T_p °F(°C)	T_{IL} °F(°C)	T_B °F(°C)
4,000 ↓	500 (2,225)	204 (96)	204 (96)	204 (96)	205 (96)	202 (95)
	1,000 (4,450)	204 (96)	200 (93)	201 (94)	202 (95)	200 (93)
	2,000 (8,900)	204 (96)	201 (94)	202 (95)	202 (95)	200 (93)
	3,000(13,350)	204 (96)	200 (93)	200 (93)	201 (94)	200 (93)
6,000 ↓	500 (2,225)	205 (96)	203 (95)	203 (95)	204 (96)	202 (95)
	1,000 (4,450)	211 (99)	202 (95)	203 (95)	204 (96)	202 (95)
	2,000 (8,900)	211 (99)	203 (95)	203 (95)	204 (96)	203 (95)
	3,000(13,350)	212(100)	205 (96)	205 (96)	205 (96)	202 (95)
8,000 ↓	500 (2,225)	202 (95)	204 (96)	204 (96)	205 (96)	204 (96)
	1,000 (4,450)	202 (95)	205 (96)	205 (96)	206 (97)	205 (96)
	2,000 (8,900)	218(103)	205 (96)	205 (96)	206 (97)	206 (97)
	3,000(13,350)	218(103)	207 (97)	206 (97)	207 (97)	206 (97)
10,000 ↓	500 (2,225)	212(100)	202 (95)	202 (95)	204 (96)	202 (95)
	1,000 (4,450)	212(100)	207 (97)	207 (97)	207 (97)	206 (97)
	2,000 (8,900)	227(108)	208 (98)	207 (97)	208 (98)	207 (97)
	3,000(13,350)	234(112)	209 (98)	208 (98)	210 (99)	209 (98)

TABLE XXI

HYBRID BOOST BEARING TEMPERATURE DATA
T_{in} = 300°F(149°C)

N RPM	F_a LBS.(NEWTONS)	T_{OR} °F(°C)	T_{OL} °F(°C)	T_p °F(°C)	T_{IL} °F(°C)	T_B °F(°C)
4,000 ↓	500 (2,225)	304(152)	304(152)	305(152)	305(152)	301(150)
	1,000 (4,450)	304(152)	301(150)	302(151)	303(151)	300(149)
	2,000 (8,900)	298(148)	301(150)	302(151)	303(151)	300(149)
	3,000(13,350)	298(148)	303(151)	304(152)	305(152)	300(149)
6,000 ↓	500 (2,225)	296(147)	303(151)	303(151)	304(152)	300(149)
	1,000 (4,450)	296(147)	303(151)	303(151)	303(151)	300(149)
	2,000 (8,900)	301(150)	303(151)	303(151)	303(151)	300(149)
	3,000(13,350)	301(150)	304(152)	305(152)	305(152)	303(151)
8,000 ↓	500 (2,225)	295(146)	303(151)	303(151)	304(152)	301(150)
	1,000 (4,450)	295(146)	305(152)	305(152)	306(153)	303(151)
	2,000 (8,900)	302(151)	307(154)	307(154)	307(154)	306(153)
	3,000(13,350)	302(151)	307(154)	307(154)	307(154)	306(153)
10,000 ↓	500 (2,225)	294(146)	304(152)	304(152)	305(152)	303(151)
	1,000 (4,450)	307(154)	307(154)	307(154)	308(154)	305(152)
	2,000 (8,900)	307(154)	308(154)	308(154)	309(155)	307(154)
	3,000(13,350)	307(154)	308(154)	308(154)	309(155)	307(154)

is difficult to ascertain at this time. The lack of correlation between test and analysis results seems to be due to the assumption of overly optimistic heat transfer coefficients on the outer race and housing.

In general the measured temperatures within the fluid film bearing appear to be very uniform and the thermal gradients in the axial, radial and circumferential direction do not exceed $4^{\circ}F$ ($2.22^{\circ}C$).

5.4 Transient Testing

5.4.1 Starts and Stops

The test conditions for this program as well as the lubricant were initially established to simulate conditions existing within a jet engine. Since engine operation involves also starts and stops, to establish the behavior of the bearing at start and stop conditions, five start and stop tests were performed. The tests consisted of increase in oil pressure and load in proportion to the speed increase. All three factors were manually controlled. The rate of increase and decrease was approximately 8.5 rev/sec^2. This rate was used because it turned out to be the highest rate possible for the synchronous response of three people operating the knobs and valves controlling the three factors. The maximum speed reached in those transient tests was 10,000 rpm and the maximum loading 3,000 lbs (13,350 newtons). The tests were performed at $100^{\circ}F$ ($37^{\circ}C$) oil temperatures. The final steady state points at the maximum speed and maximum load corresponded closely to those obtained in previous tests. There was no indication of instabilities or contact between the fluid film bearing surfaces during the imposed transients. Disassembly of the unit after operation showed no indication of contact during operation between the stationary and rotating parts of the fluid film bearing. The ball bearing also appears to be in excellent condition. Pictures of the fluid film bearing and ball bearing components after test are shown in Figs. 89 and 90 respectively.

5.4.2 Fail-Safe Tests

The fail-safe tests were performed during the normal test runs as already

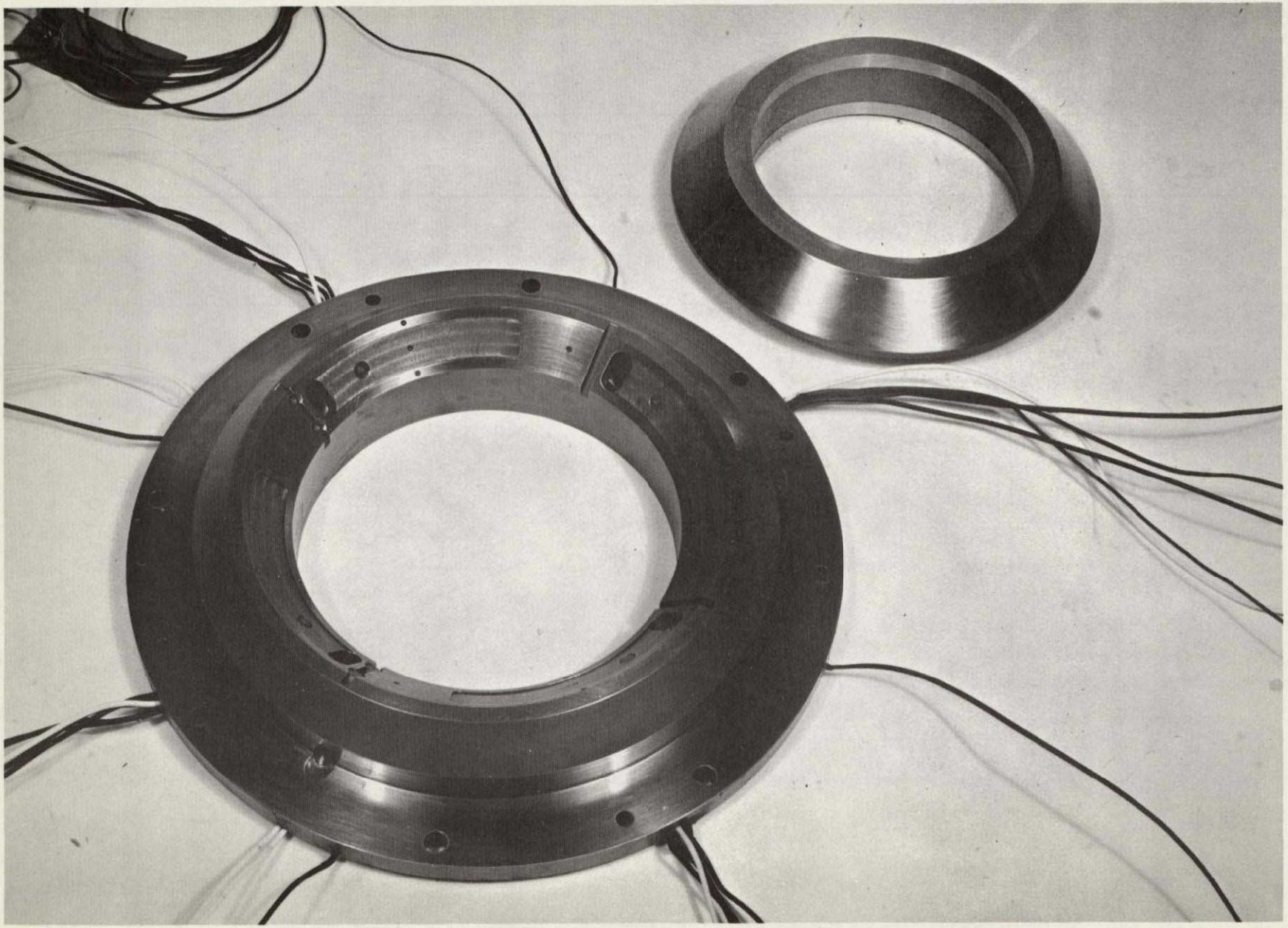

Fig. 89 Fluid Film Bearing Component After Test

MTI-8978

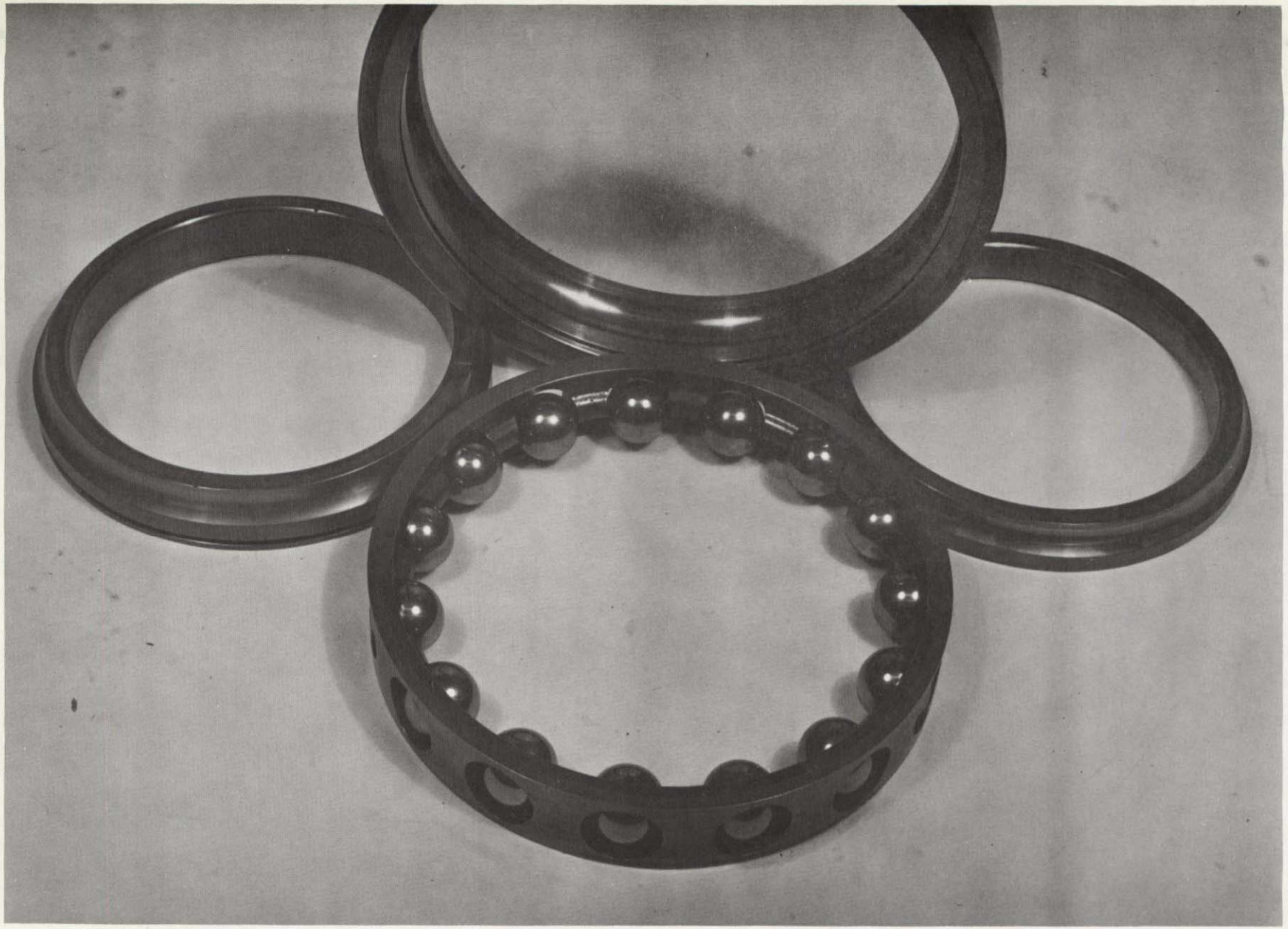

Fig. 90 Ball Bearing Component After Test

MTI-8979

indicated above, at each load point, each temperature, and each speed (up to loads of 3,000 lbs. (13,350 newtons))*. At each steady state condition the oil supply to the fluid film bearing was shut off at which time the ball bearing assumed the full loading being imposed on the system. Again, the bearings performed satisfactorily and no problems were encountered. The actual fail safe clearance at the design point was 0.002 in. (.0508mm). The fail safe clearance for each constant speed run can be found by extending the ball bearing curve to 3000 lb. and reading the film thickness at this point.

5.4.3 Constant Oil Flow Tests

In addition to the above tests, tests were also performed to determine the performance of the hybrid boost bearing system with a constant oil supply. The reason for constant oil supply desirability in an actual jet engine application goes back to the relative high flow requirements at high oil temperatures. The flow requirements are high when the fluid film bearing clearances are large and the latter are large when the loading is low. Consequently for a practical application the oil flow into the fluid film bearing can be limited to that required to support the high loading which is present in the engine at normal conditions of operation. To establish the feasibility of a constant flow system to the fluid film bearing, tests were performed at 100°F with a flow of 3.5 gpm which was maintained constant regardless of the clearances and/or externally applied loading. The unit was brought up to 6,000 rpm and the loading on the bearing (combined hybrid boost bearing) was varied between 500 (2225n) and 3000 lbs (13,350n) while the constant flow was maintained. Although cavitation may have taken place at the low load-high clearance conditions where the flow demand of the fluid film bearing exceeds by far the permitted flow, no derogatory effects on the performance were noted aside from the expected drop in the load carried by the fluid film bearing. Thus, at high load conditions where the flow requirement is low, the load division was the same as that with the normal oil supply since the flow requirements were fully satisfied with the 3.5 gpm flow that was made available. At low load conditions the flow was not satisfied and the light load existing at those conditions was fully carried by the ball bearing. Again, the hybrid boost bearing appeared to operate

---

* At speeds of 8000 and 10,000 rpm the maximum fail-safe load was limited to 2000 lb. for test safety reasons.

stably regardless of the unsatisfied flow conditions on its fluid film bearing component. No problems were experienced during this operation. The significance of these results lies in the fact that the high flow requirements which may mainly correspond to the large clearance-low load condition can be eliminated and the flow greatly reduced. This approach would gradually activate the fluid film bearing as the load carrying requirements on it increase.

5.5 Summary of Test Results

To summarize briefly the testing performed on the hybrid boost bearing and its components - tests have started with the ball bearing component evaluation. The axial deflection characteristics of the ball bearing which are of prime importance in the hybrid boost bearing setup have been shown to agree extremely well with those calculated using the A.B. Jones Rolling Element Computer Program. Subsequent testing of the hybrid boost bearing and its ball bearing component disclosed relatively good agreement in the load carrying capacity of the fluid film bearing component at low speeds and high temperatures. A noticeable drop in load carrying capacity was observed, however, at high speeds and low oil temperatures. This drop in load carrying capacity seems to impose some limitations on the load carrying capability of the fluid film bearing. The most reasonable explanation for that phenomenon at this time appears to be the possibility of non-isothermal temperature distribution within the oil film. In many designs, however, the load carried on the fluid film bearing within this test series (about 1,000 lbs.) may be sufficiently high to justify the use of a hybrid boost bearing in its present form.

The shortcomings of the hydrodynamic fluid film bearing component can be greatly improved through the use of a hydrostatic bearing arrangement whereby the load carrying capacity of the fluid film bearing component is determined by an externally supplied pressure source. Another possible limitation in the application of the hybrid boost bearing to aircraft engines is its relatively high flow requirement. Tests performed within the scope of this program, however, have shown that this problem can be by-passed when the bearing is designed for a

constant flow oil supply to the fluid film bearing. This means that the fluid film bearing component would become effective only in the instance where the load is highest (the high load magnitude to be established by specifications). During the low load stages of operation, the fluid film bearing would be simply supplied with oil at flow rates not exceeding that which is provided by the limited supply and the fluid film bearing will remain relatively inactive.

The measured power losses support the theory of non-isothermal flow inasmuch as the decrease in load carrying capacity is also accompanied by a decrease in the power loss. This decrease in the power loss can be explained by the fact that the actual oil film temperatures run higher than those of the fluid film bearing faces and consequently the effective viscosity is lowered and the power loss decreased. On the overall, the power loss within the fluid film bearing (or its heat rejection) is about twice that of the ball bearing component used. It is felt that with some design modifications this difference can be further reduced.

6.0 CONCLUSIONS

The hybrid boost bearing principle, employing parallel thrust loading of a conical fluid film bearing and a 120 mm bore ball bearing, was proven by test to be feasible. The tests performed within the scope of this program show that the fluid film bearing can operate stably when coupled in this manner with a ball bearing. Load sharing between the two bearings can be assured through proper spacing of the bearing components. Within the range of conditions tested, the fluid film bearing component was made to assure a maximum load of about 1200 lbs (5330 newtons) out of an externally imposed load of 3,000 lbs (13,350 newtons). The results furthermore, indicate that,

A. The existing fluid film bearing computer program used in the design analysis is adequate except in the low temperature, high speed portion of the test range. That program, which is based on isothermal, one-dimensional solutions, can be used to predict the load carrying capacity (load vs. film thickness as a function of geometry, speed and viscosity) fairly accurately at low speeds over the given oil temperature range of 100 (37C) to 300 F (149 C). The agreement at high speeds and high oil temperatures is also reasonably good. The measured load capacity is, however, substantially lower at speeds of 8,000 and 10,000 rpm when the oil used is of relatively high viscosity, i.e., at low inlet temperatures. Distinct limitations on the load capacity as a function of speed and oil temperature have been noted in this range. Present indications are that this behavior may be due to the non-isothermal temperature distribution within the oil film. This limitation can possibly be eliminated through the introduction of centrifugal pressure generation means, which in effect will result in hydrostatic fluid film bearing operation. Hydrostatic bearings are much less dependent on the local fluid film viscosities, and their load carrying ability is directly dependent on supply pressure.

B. Good agreement between calculated and actual measured temperatures within the fluid film bearing test housing was not obtained in all areas. For instance, the measured temperatures are generally higher in the outer race of the ball bearing than are the calculated ones.

On the other hand, the thermal gradients across the housing are slightly lower on test than those obtained by analysis. The temperature differences between calculated and measured values in the ball bearing outer race appear to be mainly due to the assumption for calculations of a relatively low thermal resistance between the ball bearing outer race retainer and the adjacent housing. As pointed out earlier, the fit between these two parts strongly affects the heat transfer path in this region. A major part of the observed difference is very likely due to a loose fit with its resulting insulating properties.

C. The axial stiffnesses of the ball bearing as calculated through the use of the rolling element computer program available at MTI, agrees very well with the actual measured values throughout the test range. The accurate prediction of the axial ball bearing stiffness is important in the hybrid boost bearing concept inasmuch as it determines the response of the combined hybrid boost bearing system to external loading and by it also the load sharing of the system.

D. The oil flow requirements to keep the fluid film bearing satisfied, in particular at high temperature, high speed, and low load conditions, both measured and calculated, are much too high for practical consideration in a jet engine application. Reduction in flow down to acceptable jet engine levels can, however, be achieved by limiting the oil flow supply. This means that as long as the loading is low (clearance on fluid film component is high) the fluid film component will remain inactive. On the other hand, as soon as the load increases to normal operational levels (the fluid film bearing clearance is low) the fluid film bearing becomes activated and participates in the load sharing.

E. The power losses as measured on test are in reasonable agreement with those predicted by the analysis. The fluid film bearing components power losses are about twice as high as those in the ball bearing. A further reduction in the power losses is possible mainly through reductions in outer diameter as well as through the selection of face geometries with inherently low power loss characteristics, such as those containing large recesses over most of the face area.

F. The thermal deformations are low, and do not affect the performance of the fluid film or ball bearing components to any appreciable degree. This is confirmed by the analysis which is initially based on higher thermal gradients than those obtained on test.

In view of the conclusions reached above, the shrouded-step fluid film thrust bearing theory should be refined. Development of a more exact, nonisothermal film theory should allow better prediction of thrust loads, flow rates, and power losses. Furthermore, configurations other than the Rayleigh shrouded step fluid film bearing should be closely examined for their compatibility with the hybrid boost bearing requirements of low flow and low power loss.

REFERENCES

1. Wachman, C., Wilcock, D.F., and Yampolsky, J., "Design of a Process Fluid Turbulent Film Shrouded Step Thrust Bearing for Circulators for High-Temperature Helium Cooled Reactors," Bearing and Seal Design in Nuclear Power Meeting, ASME, 1967, 11, 354-370.

2. "Technical Design Systems Handbook," edited by Dr. H. Rothbart, McGraw-Hill, 1965, Chapter 13 by A. B. Jones.

3. Nemith, Z.N., Macks, E.F., and Anderson, W.J., "Investigation of 75 mm Bore Deep Grooved Ball Bearing Under Radial Load at High Speeds II — Oil Inlet Temperature Viscosity and Generalized Cooling Correlation," NACA TN30D3, 1952.

4. Winn, L.W., "Development and Test of Long Life Hybrid Boost Thrust Bearings for Small, High Speed Jet Engine Applications," MTI 69TR17, June 1964.

5. Bootsma, J., "The Effect of Viscosity Variation with Temperature on Performance of Spiral Groove Bearings," ASLE Transactions, Vol. 12, No. 4, Oct. 1969.

APPENDIX A

A PROCEDURE FOR THE ANALYSIS OF BEARINGS OPERATING IN THE TRANSITION RANGE BETWEEN LAMINAR AND FULLY DEVELOPED TURBULENT FLOW

by

V.N. Constantinescu
C.H.T. Pan
F.C. Hsing

NOMENCLATURE

B_x = Parameter defined by Eq. (C17), = $\frac{h^2}{\mu V} \frac{\partial p}{\delta x}$

c = Radial clearance

C_f = Friction coefficient = $\frac{8\tau}{\rho V^2}$

f = Correlation function for transition flow

G_x, G_y = Turbulent correction parameter depending on Reynolds number only

h = Film thickness

h_o = Film thickness at the maximum pressure location

k^* = Mixing length constant for transition flow

k_t^* = Mixing length constant for fully developed turbulent flow

l_a = Mixing length

M_x = Mass flux

p = Pressure

Q = Total flux

Q_x, Q_y = Flux Components

r_1, r_i, r_o = Radii

R = Modified Reynolds number = k^{*2} Re

Re = Reynolds number = $\frac{\rho V h}{\mu}$

R_e^+ = Reynolds number defining the upper limit of transition flow

R_e^* = Nominal Reynolds number = $\frac{\rho V C}{\mu}$

Re_c = Reynolds number defining the lower limit of transition flow

Re_e = Equivalent Reynolds number defined by Eq. C33

Re_m = Mean Reynolds number

Re_p = Reynolds number for Poiseuille flow

NOMENCLATURE (Continued)

Re_{c_c} = Critical Reynolds number for Couette flow

t = Time

T = Taylor number

u,v,w = Velocity components

U = Mean velocity due to Poiseuille flow

U_m = Mean relative sliding velocity

V = Relative sliding velocity = $\left|V_1-V_2\right|$

V_1,V_2 = Sliding velocities

V_c = Couette flow velocity

x,y = Cartesian coordinates

y^+ = Dimension coordinate for the universal velocity profile

δ^+ = Constant defines the laminar sublayer

ϵ = Eccentricity ratio, also eddy viscosity

μ = Apparent viscosity

ν = Apparent kinematic viscosity

ρ = Density

τ = Combined shearing stress

$\tau_{xy},\tau_{yy},\tau_{zy}$ = Shearing stress

$\tau^*_{xy},\tau^*_{yy},\tau^*_{zy}$ = Shearing stress

τ_c = Couette frictional stress

$\bar{\tau}_c$ = Normalized Couette frictional stress = $\frac{h}{\mu V}$

$\tau_{o,h}$ = Frictional stress at the two walls

ϖ = Function defined by Eq. (C38)

Ψ = Clearance ratio = h/r_1

INTRODUCTION

Numerous methods at the present time exist for designing various types of bearings in laminar regime. Most of these methods have been also extended to the use of bearings operating in fully developed turbulent flow. However, there is still a lack of information concerning the bearings operation as well as design procedures in the region of transition between laminar and turbulent regimes of flow in the film.

Actually, with the increasing trend toward higher speeds in machinery, more and more bearings are operating in the range of higher Reynolds numbers. It is thus obvious that the transition region is of practical interest and therefore a method for the analysis of bearings operating in this particular region is needed in order to be able to evaluate the operating characteristics of the bearings.

In order to perform such an analysis, it is first necessary to evaluate or to define the limits of the transition region. The lower limit is obviously the so called "critical" Reynolds number Re_c up to which the flow retains a pure laminar character. The upper limit should be another value of the Reynolds number, Re^+, from which one can assume that the flow has a fully developed turbulent pattern.

Once those limits Re_c, R_e^+ are defined, then, a procedure for predicting the flow details must be carried out. Unfortunately, it appears that such a goal is rather difficult to achieve with the present knowledge concerning transition from laminar to turbulent flow. Indeed, the physical mechanism of the transition is not yet well understood [1],[2].* Moreover, depending on the type of flow, the mechanism of transition may be entirely different. Thus for plane Couette flow or Poiseuille flow the transition is a more or less direct one (occurrence of turbulent spots, intermittency). For other flows, such as flow between cylinders, a complex laminar vortex cell pattern first occurs.

However, there are strong reasons to believe that for shear flows in thin

---

* Bracketed numbers identify references listed in the back of this appendix.

layers the detailed physical peculiarities mentioned above have less importance on overall characteristics of a lubricant film. Indeed, if we take the two external cases, i.e. pure laminar and fully developed turbulent flow, both theoretical and experimental results [3] show without any doubt that turbulence does not affect qualitatively the operating characteristics of a bearing of any type. In other words, the influence of the variation of film thickness, the pressure distribution, etc. exhibit qualitatively the same kind of variation. This fact can be explained because for thin films, the equilibrium of an element of the film leads to the relation

$$\frac{\partial \tau_{xy}}{\partial y} = \frac{\partial p}{\partial x} \tag{C1}$$

where τ_{xy} is the tangential stress, p is the pressure and the axis y is directed across the film.

Consequently, for any type of flow (namely both for laminar and turbulent flow), the pressure distribution develops as a consequence of the shear flow. As a result, the pressure differential equation retains a unique form both for laminar and turbulent flows [3],[4].

$$\frac{\partial}{\partial x}\left(\frac{h^3}{\mu} G_x \rho \frac{\partial p}{\partial x}\right) + \frac{\partial}{\partial z}\left(\frac{h^3}{\mu} G_z \rho \frac{\partial p}{\partial z}\right) = \frac{\partial(\rho h)}{\partial t} + \frac{V_1 + V_2}{2} \frac{\partial(\rho h)}{\partial x} . \tag{C2}$$

where, in laminar flow

$$G_x = G_z = \frac{1}{12} \tag{C3}$$

while in fully developed turbulent flow, $G_{x,z}$ depend on the local Reynolds number

$$Re = \frac{\rho \left| V_1 - V_2 \right| h}{\mu} = \frac{\rho V h}{\mu} ; \quad V = \left| V_1 - V_2 \right| \tag{C4}$$

and eventually on the pressure gradients $\partial p/\partial x$, $\partial p/\partial z$ [4]. For most self-act-

ing lubrication problems, parameters $G_{x,z}$ can be assumed as being functions only of the Reynolds number (C4).

Under these conditions, it seems reasonable to expect that within the transition region, the pressure equation (C2) will be still valid but parameters $G_{x,z}$ will have some intermediate values between those corresponding to laminar flow (C3) and to fully developed turbulent flow. Such a conclusion is reinforced by the existing experimental evidence such as pressure distribution for Taylor vortex flow between eccentric cylinders [6]. The problem is how to evaluate the parameters G_x and G_z in the transition region.

EVALUATION OF THE LIMITS OF THE TRANSITION REGION IN BEARINGS

As mentioned before, the limits of the transition region may be defined as the critical Reynolds number Re_c from transition from laminar flow and another Reynolds number Re^+ from which the flow can be regarded approximately as a fully turbulent one.

For simple flows such as plane Couette flow the critical Reynolds number is [1],[7]

$$Re_c = \frac{\rho V_c h}{\mu} \simeq 2000 \qquad (C5)$$

where $V = \left| V_2 - V_1 \right|$ is the relative speed between the two surfaces.

It is to be noticed that the same value (C5) appears to hold true also for the case of two co-axial cylinders (journal bearings), when the outer member rotates. Thus, in Fig. A1 , a diagram reproduced from reference [8] is given, which some of the existing experimental evidence is synthesized. It is seen that when the clearance ratio is small enough ($< 10^{-2}$), the critical Reynolds number tends toward value (C5).

Consequently as a first approximation the critical value (5) may be considered as valid in all cases when the laminar flow breaks down directly into a turbulent one.

However, it is to be pointed out that in most bearings, critical values for the Reynolds number smaller than value (C5) are occurring. Thus, for journal bearings with the inner member rotating, a Taylor vortex pattern is occurring at a critical Reynolds number [9],

$$Re_c = \frac{41.1}{\sqrt{\Psi}} \qquad (C6)$$

where $\Psi = h/r_1$ is the clearance ratio. Formula (C6) should be used in cases

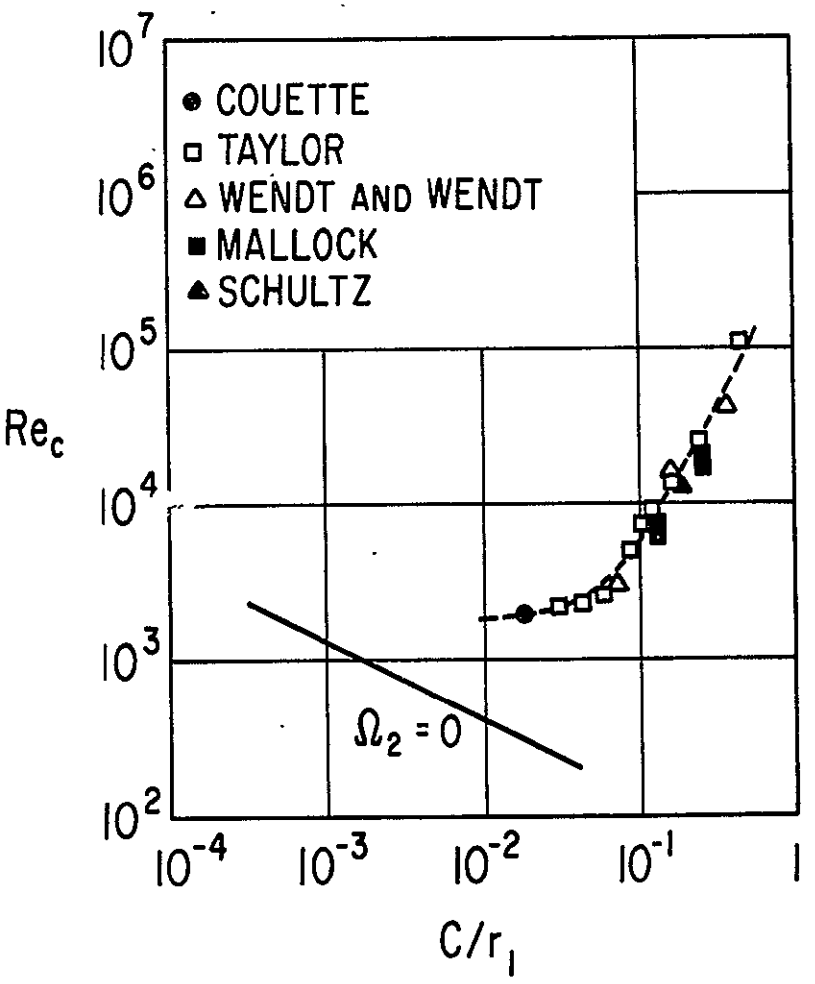

Fig. A-1 Critical Reynolds Number for Flow Between Co-axial Cylinders (Outer Cylinder Rotating, Inner Cylinder at Rest) [8]

when $\Psi > 0.0004$. It gives values Re_c less than the value (C5). This implies that for usual clearance ratios Taylor vortices occur before turbulence.

For thrust bearings, a spiral vortex flow may appear in some cases [10]. Although this problem requires more attention [11] it seems quite possible that critical values for the local Reynolds number, which are smaller than value (C5) can again be obtained.

$$Re_c = \frac{\rho(\omega r)_c h}{\mu} < 2000 \qquad (C7)$$

Some recent experimental evidence [11] shows that critical Reynolds nunber as low as $Re_c = 600$ may occur in flow between rotating disks.

As a conclusion one may emphasize that for simple Couette flows (unloaded bearings), the critical Reynolds number Re_c may be roughly evaluated with the aid of simple formulas as (C5) or (C6). Additional information however is needed, to obtain better estimates in the thrust bearing area.

At the same time, by examining the existing experimental evidence it seems that the transition zone extends over an interval roughly equal to Re_c. In Fig. A-2 the experimental data provided by Smith and Fuller are reproduced [12]. It is seen that the critical Reynolds number is in this case $Re_c = 760$, a value which is consistent with formula (C6), while at a Reynolds number of about 1500 fully turbulent flow appears.

Another extreme example is given in Fig. A-3, reproduced from Reference [1] for a pure Poiseuille flow (pipe flow). In this figure the critical Reynolds number is approximately equal to 2200 while at about $Re_c^+ = 4400$ the flow seems to be a fully turbulent one.

Based upon the values quoted above one may assume that with a reasonable approximation the upper limit of the transition zone is

$$Re_c^+ \tilde{=} 2\, Re_c \qquad (C8)$$

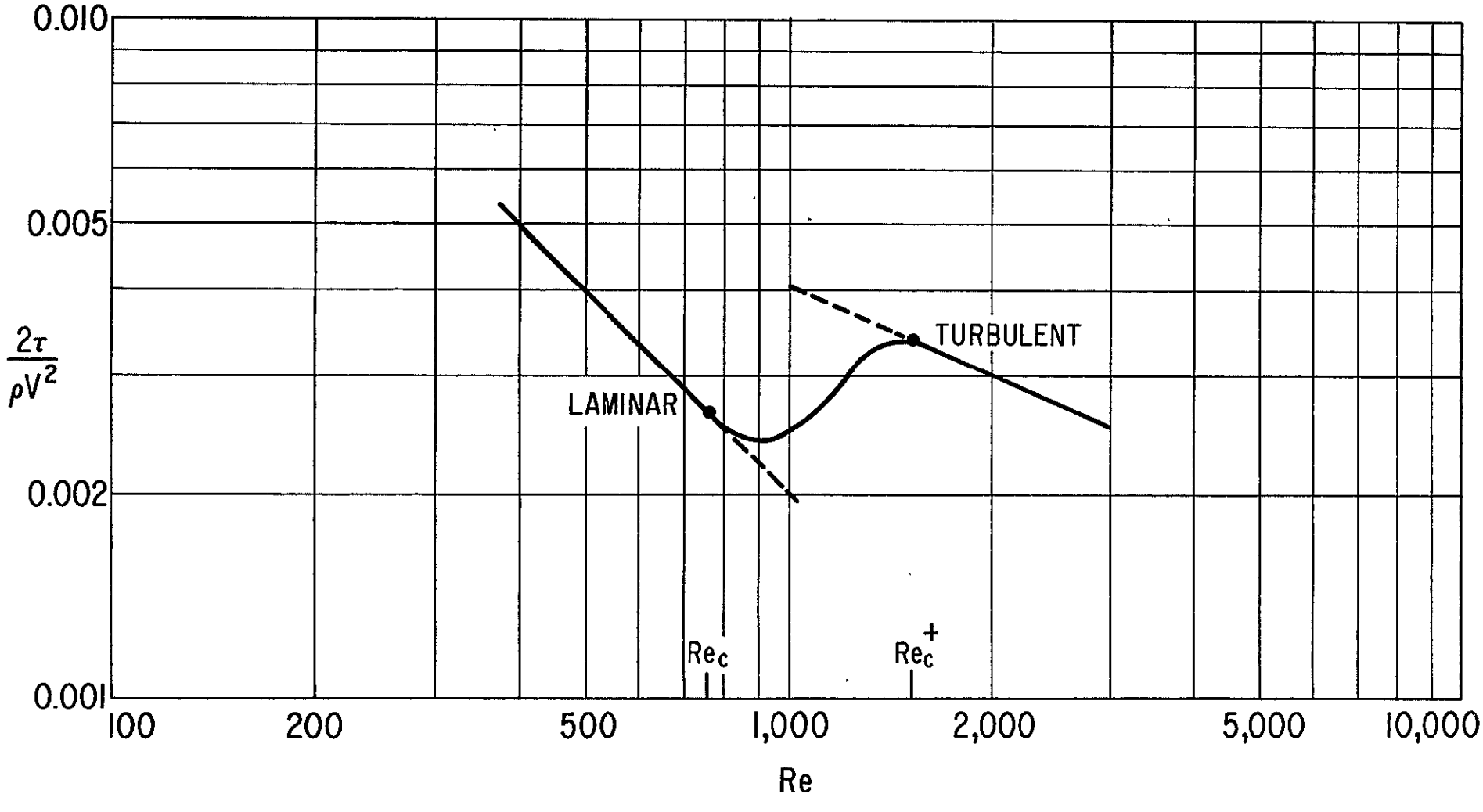

Fig. A-2 Experimental variation of the friction factor in a water lubricated journal bearing (clearance ratio Y = 0.00293, inner member rotating) [12].

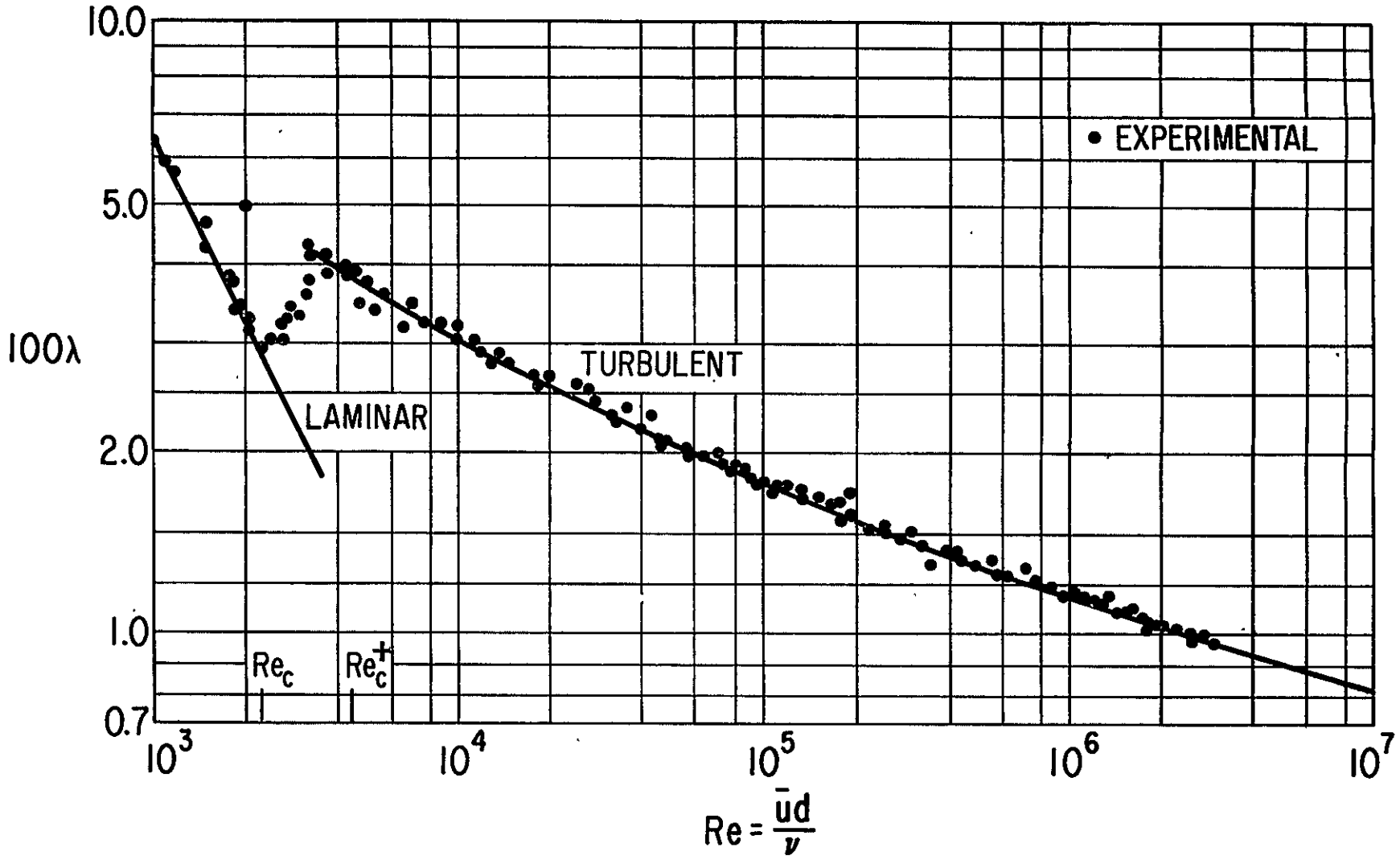

Fig. A-3 Frictional resistance in smooth pipes [1].

In this way the transition zone is determined by the two Reynolds numbers Re_c and Re_c^+ and actually it is necessary to estimate more or less accurately only the critical Reynolds number Re_c.

For pure Couette flow, the critical Reynolds number is given by one of the relationships (C5-C7) according to the type of flow (planar, curved, etc). However, it is more difficult to estimate the critical Reynolds numbers for actual lubricant films in which the flow is a combination of Couette and Poiseuille flows and in addition the viscosity may be variable due to temperature field (the density may also be variable when the lubricant is compressible).

Actually the local critical value of the Reynolds number will depend on several factors, namely

a. Local value of the film thickness
b. Local value of the viscosity
c. Local value of the density
d. Local flow or local mean velocity
e. Influence of the shape of the velocity profile on the stability of the flow as well as of the type of flow (planar or curved flow)

When defined in the usual way (C4), the Reynolds number takes into account only effects (a), (b), (c) mentioned above, and eventually effect (e) partially, as in relation (C6) (the effect of the local clearance ratio for curved flows). If the effect of the shape of velocity profile is neglected, for example for flows not much differing from Couette ones, then effects (a)-(d) can be considered in a rather simple way, by defining a new local Reynolds number [3], [13] as

$$Re_m = \frac{2\rho U_m h}{\mu} = \frac{2Q}{\nu} \qquad (C9)$$

Factor 2 is used in order to make relation (C9) identical to (C4) for pure Couette flow when $U_m = V/2$. Note again that as for relation (C4), U_m represents the total mean relative velocity due to the relative sliding motion.

Indeed in a pure rolling motion, the pressures are generated in the film via the surface velocity components directed along the normal to the surfaces. Therefore, although the sum $V_1 + V_2$ is intervening in the differential equation (C2), the transition phenomena and turbulence are generated in the film only by the tangential shear stresses, i.e. by the sliding motion governed by the relative speed $V = |V_1 - V_2|$. A comparison of the local mean Reynolds number value (C9) with the critical value (C5-C7) will give a more accurate indication concerning the critical condition for the occurrence of some kind of super-laminar flow (vortex flow, turbulent spots, etc).

The mean Reynolds number (C9) can also be evaluated directly in terms of the total flux

$$Q = \sqrt{Q_x^2 + Q_z^2} \simeq Q_x$$

$$Q_x = U_m h = \frac{h^3}{\mu} G_x \frac{\partial p}{\partial x} + \frac{Vh}{2} \qquad \text{(C10)}$$

where $G_x = 1/12$ if the flow is laminar. For compressible flow, the mean Reynolds number will be computed with the aid of mass flux

$$\mu_x = \rho U_m h = -\frac{h^3}{\mu} G_x \rho \frac{\partial p}{\partial x} + \frac{\rho V h}{2} \qquad \text{(C11)}$$

Consequently,

$$Re_m = \frac{2\rho Q_x}{\mu} = \frac{2\mu_x}{\mu} \qquad \text{(C12)}$$

Re_m is thus constant for infinitely long bearings, if μ is constant. Finite bearings will emphasize some diminishing of the Reynolds number, due to the side leakage flow (Q diminishes with x).

In order to verify the error which results from neglecting the influence of the shape of the velocity profile on the critical conditions we will compare the results obtained by using the mean Reynolds number (C9) with the results

obtained by DiPrima [14] by using a theoretical stability analysis. For this purpose, in addition to the usual Couette Reynolds number (C4), let us define a Poiseuille Reynolds number

$$Re_p = \frac{\rho U h}{\mu} ; \quad U = U_m - \frac{V}{2} \tag{C13}$$

where U is the mean velocity due to Poiseuille flow.

In reference [14] a stability chart relating Re and Re_p for critical conditions is given. This chart is reproduced in Fig. A-4.

On the other hand, by taking into account relations (C13) the mean Reynolds number (C9) may be written as

$$Re_m = Re + 2Re_p \tag{C14}$$

and by equating Re_m to the critical value (C7) one obtains

$$Re\sqrt{\frac{h}{r}} + 2Re_p\sqrt{\frac{h}{r}} = 41.2 \tag{C15}$$

which represents a straight line. For $Re < 0$ we obtain a parallel line

$$-Re\sqrt{\frac{h}{r}} + 2Re_p\sqrt{\frac{h}{r}} = 41.2 \tag{C16}$$

Relationships (C15, C16) are presented in Fig. A-4. It is seen that although the agreement with the theoretical stability map is good qualitatively, there are some differences which emphasize the influence of the shape of the velocity profile on the stability. Thus, when for example $Re > 0$, a positive pressure gradient will improve the stability of the basic laminar flow, while a contrary effect occurs when $Re_p < 0$. In one limit, when the Couette Reynolds number is small as compared to R_p (Re = 0), relations (C15, C16) give $Re_{pc} = 20.6\sqrt{h/r}$ while DiPrima's results show $Re_p = 38\sqrt{h/r}$. However, in the vicinity

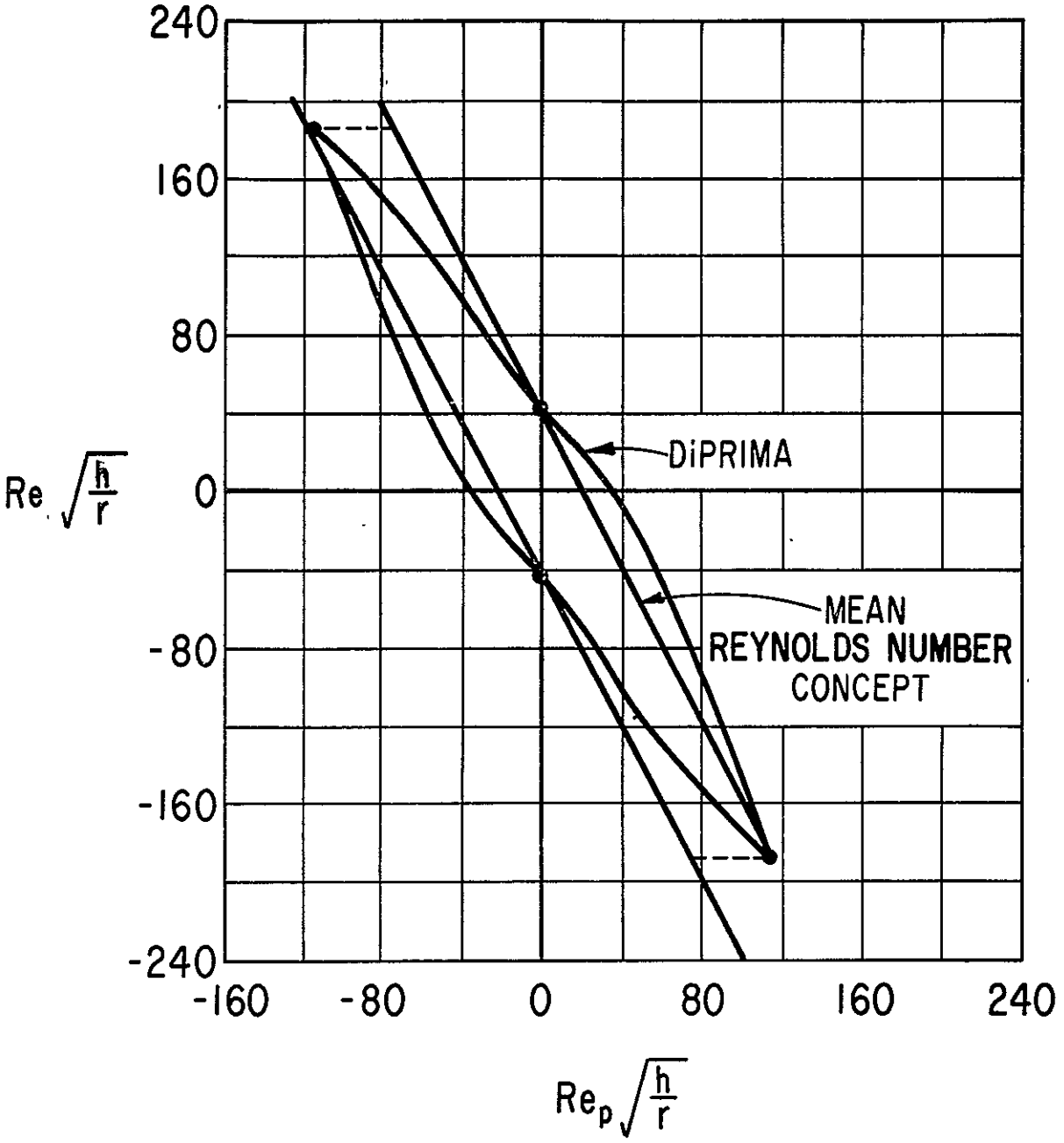

Fig. A-4 Stability chart for coupled Couette-Poiseuille flow between rotating cylinders (inner cylinder rotating) [14].

of $Re_p = 0$, which is the lubrication case, the differences are less important so that the mean Reynolds number concept may be expected to provide a satisfactory estimation of the critical conditions at least for bearings having small and moderate eccentricity ratios.

Moreover, it is to be pointed out that DiPrima's stability map itself is subject to some approximation and probably overestimates the importance of the Poiseuille flow. Indeed, the existing experimental evidence concerning the stability of the flow between eccentric cylinders [6] discloses an interesting fact, namely that the dimension of the vortex cell is effectively that corresponding to the case of coaxial cylinders and remains unaltered when the eccentricity ratio is increased.

This result is not in agreement with the theoretical calculations [14] which show that the wavelength for which the instability first occurs depends on both Re and Re_p and even a jump in wavelength occurs under certain circumstances. Consequently a supplementary effect exists which actually tends to increase the influence of the Couette flow. In other words some restoring effect is produced in the film which tends to keep the wavelength of the unstable perturbation more or less constant. As a consequence, the critical values Re, Re_p may be modified and we may thus expect that in the stability chart of Fig. A-4, the experimental data will lie somewhere between the DiPrima's curve and the straight lines (C14, C15).

Nevertheless, relations (C14, C15) will introduce an error which increases continuously especially for strong adverse pressure gradients. According to the mean Reynolds number concept, the flow is small enough (zero net flow, $U \sim - V/2$). Actually it is probably that, for example if the Couette Reynolds number is large enough, the flow is no more laminar irrespective of the value of the Poiseuille Reynolds number, and a similar conclusion will be also true when the Poiseuille Reynolds number is large enough. In other words, the stability chart should be a closed curve rather than an infinite strip.

The approximations introduced by the mean Reynolds number concept are better

emphasized when the stability chart of Fig. A5 is plotted as critical Couette Reynolds number $(Re)_c$, or critical mean Reynolds number $(Re_m)_c$ as a function or ratio,

$$\frac{Re_p}{Re} = \frac{U}{V} = G_x B_x; \; Bx = -\frac{h^2}{\mu V}\frac{\partial p}{\partial x} \tag{C17}$$

where again $G_x = 1/12$ for laminar flow.

In Fig.A5 the DiPrima chart of Fig. A4 has been presented in terms of $(Re)_c$ and $(Re_m)_c$ versus ratio U/V, together with the values given by the mean Reynolds number concept. In this last case, for relation (C14) one obtains,

$$(Re)_c\sqrt{\frac{h}{r}} = \frac{41.2}{1 + 2U/V}\;; \quad (Re_m)_c\sqrt{\frac{h}{r}} = \pm 41.2 \tag{C18}$$

Again a qualitative agreement with DiPrima's values is emphasized, with the exception of the case U/V = -0.5 (zero net flow). Actually $U/V > -0.5$ in self-acting films since it is not conceivable to obtain a reverse Q_x without external pressurization.

An indirect evaluation of the validity of the mean Reynolds number concept can be done for journal bearings subjected to increasing eccentricity ratios. Thus, by assuming a Sommerfeld solution for the laminar pressure distribution one obtains

$$Re^*\sqrt{\frac{c}{r}} = \frac{20.6\,(2+\varepsilon^2)}{\sqrt{1+\varepsilon}\,(1-\varepsilon^2)}\;; \quad Re^* = \frac{\rho V c}{\mu} \tag{C19}$$

where c is the radial clearance. Relation (C19) is graphically presented in Fig. A-6 together with DiPrima's calculations [14] and some experimental data [6]. It is seen that formula (C19) gives reasonable good results for small and moderate eccentricity ratios, namely when $\varepsilon < 0.5$.

Another indirect indication concerning the validity of the mean Reynolds

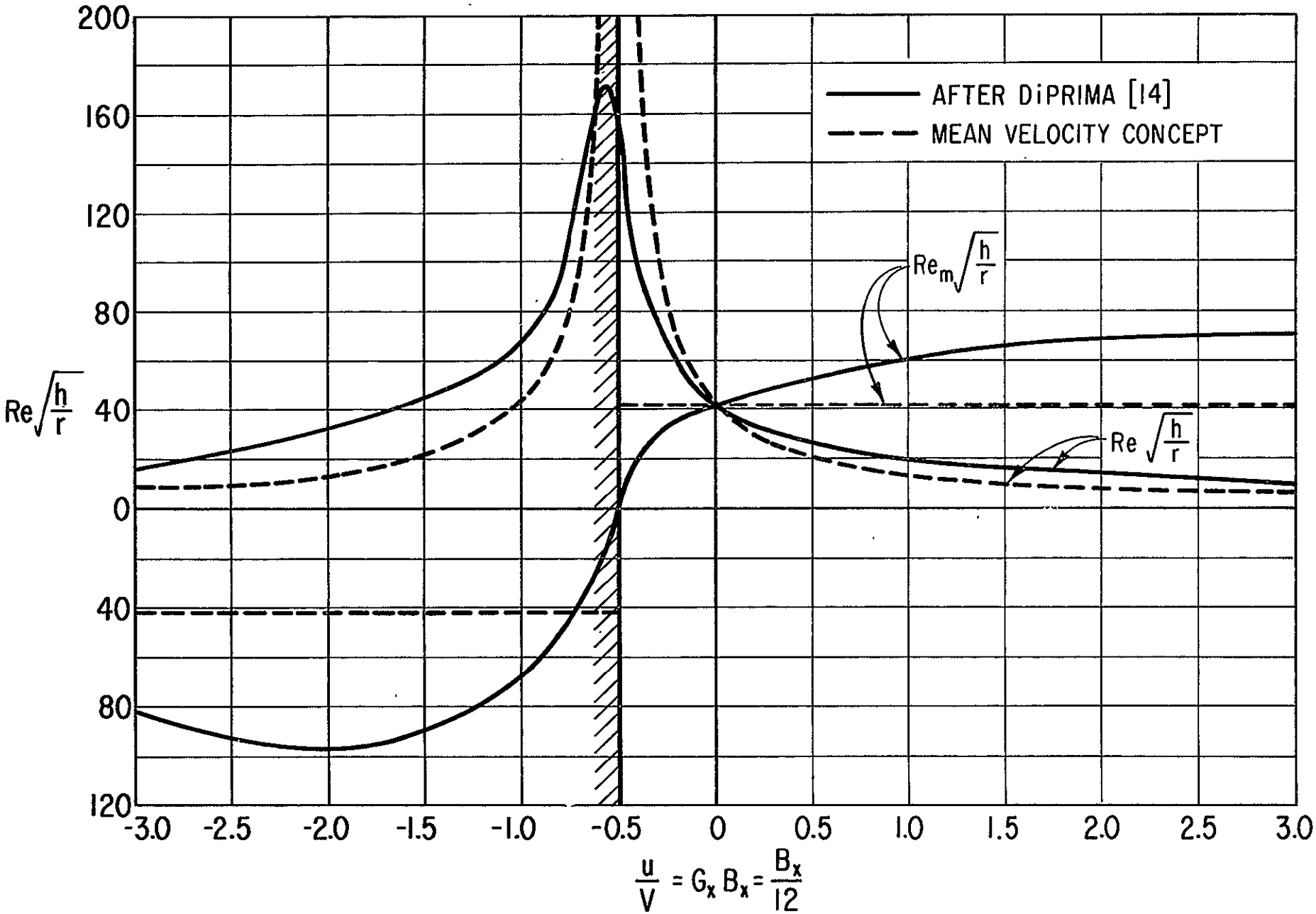

Fig. A-5 Critical values for the Couette Reynolds number Re and for the mean Reynolds number Re_m, versus ratio U/V.

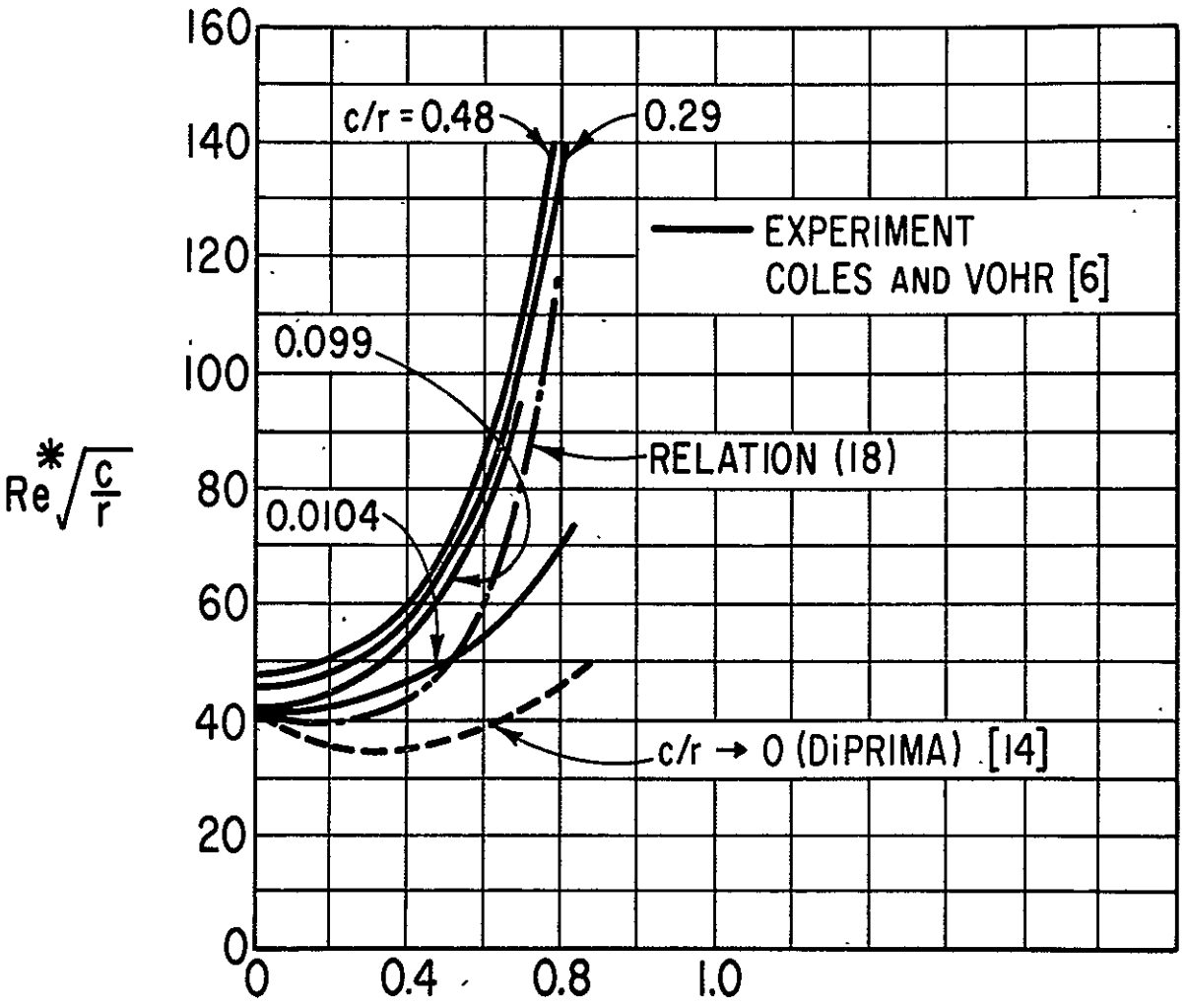

Fig. A-6 Influence of Eccentricity Ratio on the Critical Reynolds Number in Journal Bearings

number concept is the case of pure planar flows. In this case (C14)

$$Re + 2Re_p = 2000 \qquad (C20)$$

(Fig. A-7). Relation (C20) seems to be better confirmed by the existing experimental evidence. Indeed, as mentioned $Re_c \cong 2000$ when $Re_p = 0$ (C5). On the other hand, relation (C20) gives $(Re_p)_c = 1000$ when $Re = 0$ (pure Poiseuille flow). But by starting from the critical value $Re = \rho UD/\mu \cong 2200$ for a circular pipe ([1], Fig.A-3) and introducing the hydraulic diameter $D_h = 2h$ one finds $(Re_p)_c \cong 1100$ which is close to the value given by relation (C20). One may thus expect a better agreement of the mean Reynolds number concept for planar flows, with the exception again of a narrow region close to the case of zero net flow...

As a conclusion, one may assume that for flows differing not much from Couette flows, the local critical conditions may be estimated in a rather simple manner by using the mean Reynolds number (C9) and by comparing its value to the critical one. At the same time (C8) one may consider approximately that fully turbulent conditions are achieved when the mean Reynolds number reaches a value equal to the double of the critical value of the Reynolds number. In this way the limits of the transition region are approximately evaluated.

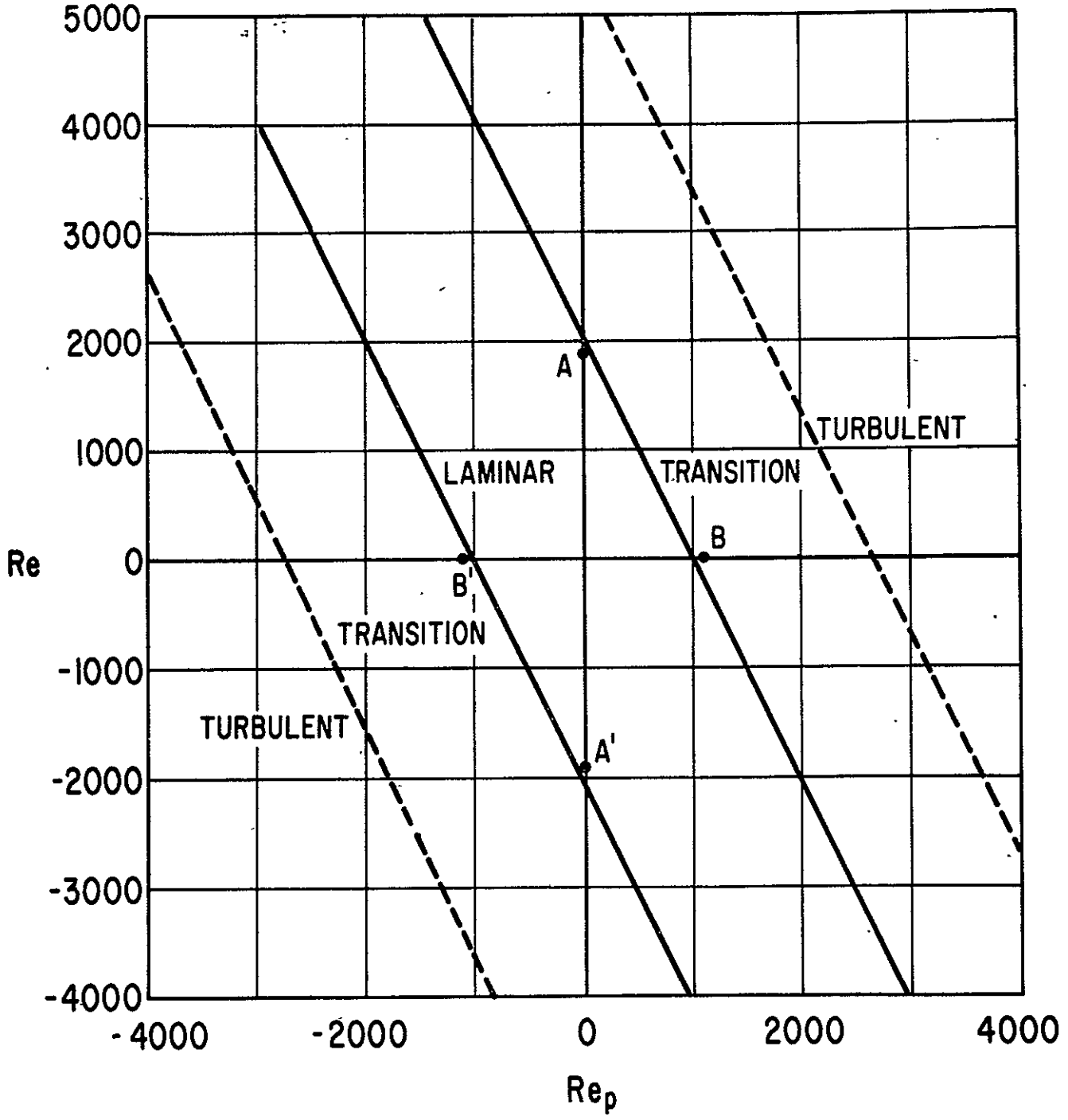

Fig. A-7 Stability chart for pure planar flow (mean Reynolds number concept).

EVALUATION OF THE VELOCITY PROFILES IN THE TRANSITION REGION

As mentioned in the introduction, although the physical mechanism responsible for transition flow may be different in various types of bearings, the overall effect on the pressure distribution is that of increasing the pressure to some intermediate value inbetween that corresponding to pure laminar and that corresponding to fully developed flow. Consequently, for analytical purposes one can interpret the flow as a "quasi-turbulent" one, i.e., having additional apparent stresses similar to the turbulent ones but smaller in absolute magnitude.

Thus, the equations of motion can be written as

$$\left.\begin{aligned} \frac{\partial p}{\partial x} &= \frac{\partial^2 u}{\partial y^2} + \frac{\partial \tau_{xy}}{\partial y} \\ \frac{\partial p}{\partial y} &= \frac{\partial \tau^*_{yy}}{\partial y} \\ \frac{\partial p}{\partial z} &= \mu \frac{\partial^2 w}{\partial y^2} + \frac{\partial \tau^*_{zy}}{\partial y} \end{aligned}\right\} \qquad \text{(C21)}$$

while the continuity equation is

$$\frac{\partial \rho}{\partial t} + \frac{\partial \rho u}{\partial x} + \frac{\partial \rho v}{\partial y} + \frac{\partial \rho w}{\partial z} = 0 \qquad \text{(C22)}$$

where u,v,w are mean values of the velocity components and τ^*_{xy}, τ^*_{yy}, τ^*_{zy}, etc. are additional stresses which behave in a similar way as the turbulent stresses and vanish on the two surfaces. At the same time, as for turbulent flow [15], the pressure variation across the film has a secondary influence on the velocity profiles and on the pressure distribution on the two lubricated surfaces.

Under these circumstances, any of the existing turbulent theories can be used with proper corrections for the additional stresses, as well as some interpola-

tion techniques for evaluating parameters G_x and G_z. As examples, we will illustrate in the following how the existing turbulent lubrication theories might be adapted to the transition region.

Modified Mixing Length Approach

As it is known [3],[13],[15], in the modified mixing length approach method the turbulent stresses along the direction of the relative speed are evaluated according to the formula

$$\tau^*_{xy} = \rho \ell_a^2 \frac{\partial u}{\partial y} \frac{\partial u}{\partial y} \tag{C23}$$

where

$$\left.\begin{aligned} \ell_a &\cong k^* y \quad ; \quad 0 \le y \le h/2 \\ \ell_a &\cong k^* (h-y) \quad ; \quad h/2 \le y \le h \end{aligned}\right\} \tag{C24}$$

Usually, according to Prandtl [1], $k^* = 0.4$. However, in reference [15] additional approximations are introduced in order to simplify the integration of the momentum equation (by dividing the film into two laminar sublayers near the walls and a turbulent core with smooth joining conditions). In order to compensate for these approximations the constant $k^* < 0.4$, and may be presented as a function of the Reynolds number [16]. Actually all the parameters of interest can be deduced as function of a modified Reynolds number,

$$R = k^{*2} \, Re \tag{C25}$$

so that the obtained results are valid for any value k^*. Thus, in the range of interest (small values for the modified Reynolds number), the parameters of interest, i.e. G_x, G_z and Couette friction stress

$$\bar{\tau}_c = \frac{h}{\mu V} \tau_c = \frac{2}{Re} \frac{\tau_c}{\rho/2 \, V^2} \tag{C26}$$

are presented in Figs. A-8 and A-9. At the same time the corrected value k^* for various Reynolds numbers Re is presented in Fig. A-10 for the range of small and moderate Reynolds numbers.

The laminar conditions correspond to $k^* = 0$, while the fully turbulent ones to $k^* = k^*_t$ (Fig. A-10). Thus in the transition range we know that we are able to approximately describe the flow by assuming that constant k^* will be equal to zero when $Re_m \leq Re_c$ and $k^* = k^*_t$ when $Re_m \geq Re_c^+$.

$$k^* = 0 \quad ; \quad Re_m \leq Re_c$$

$$k^* = f\left(\frac{Re_m}{Re_c}\right) \quad ; \quad Re_c \leq Re_m \leq Re^+ = 2Re_c \qquad (C27)$$

$$k^* = k^*_t(Re) \quad ; \quad Re_m \geq Re_c^+ = 2Re_c$$

since $Re_c^* \simeq 2Re_c$ (C8). Here k_t^* should be taken from Fig. A10 for $Re = Re_c^+ = 2Re_c$, and $f(0) = 0$, $f(1) = 1$.

In this way the problem is completely solved if the function f is known: for any pair of values B_x, R one can determine the velocity profile by using the results given in reference [15] while G_x, G_z, $\bar{\tau}_c$ may be taken from Figs. A8-A10. Therefore, the pressure equation (C2) can be integrated. At the same time the friction stresses on the two surfaces τ_o, τ_h are

$$\bar{\tau}_{o,h} = \frac{h}{\mu V}\,\tau_{o,h} = \bar{\tau}_c \pm B_x \qquad (C28)$$

This problem should be solved by iteration, since the mean Reynolds number is not known "a priori". Thus, the first iteration may be either laminar flow or $Re_m = Re$. Once the pressure distribution is known, one can compute Re_m (C12) and thus, k^* (C27) and R (C25). Then new values G_x, G_z, $\bar{\tau}_c$ are obtained, etc. Note that when k^* is taken following relations (C27) one can compute the flow parameters even in bearings having some regions operating in all laminar, transition and turbulent regimes.

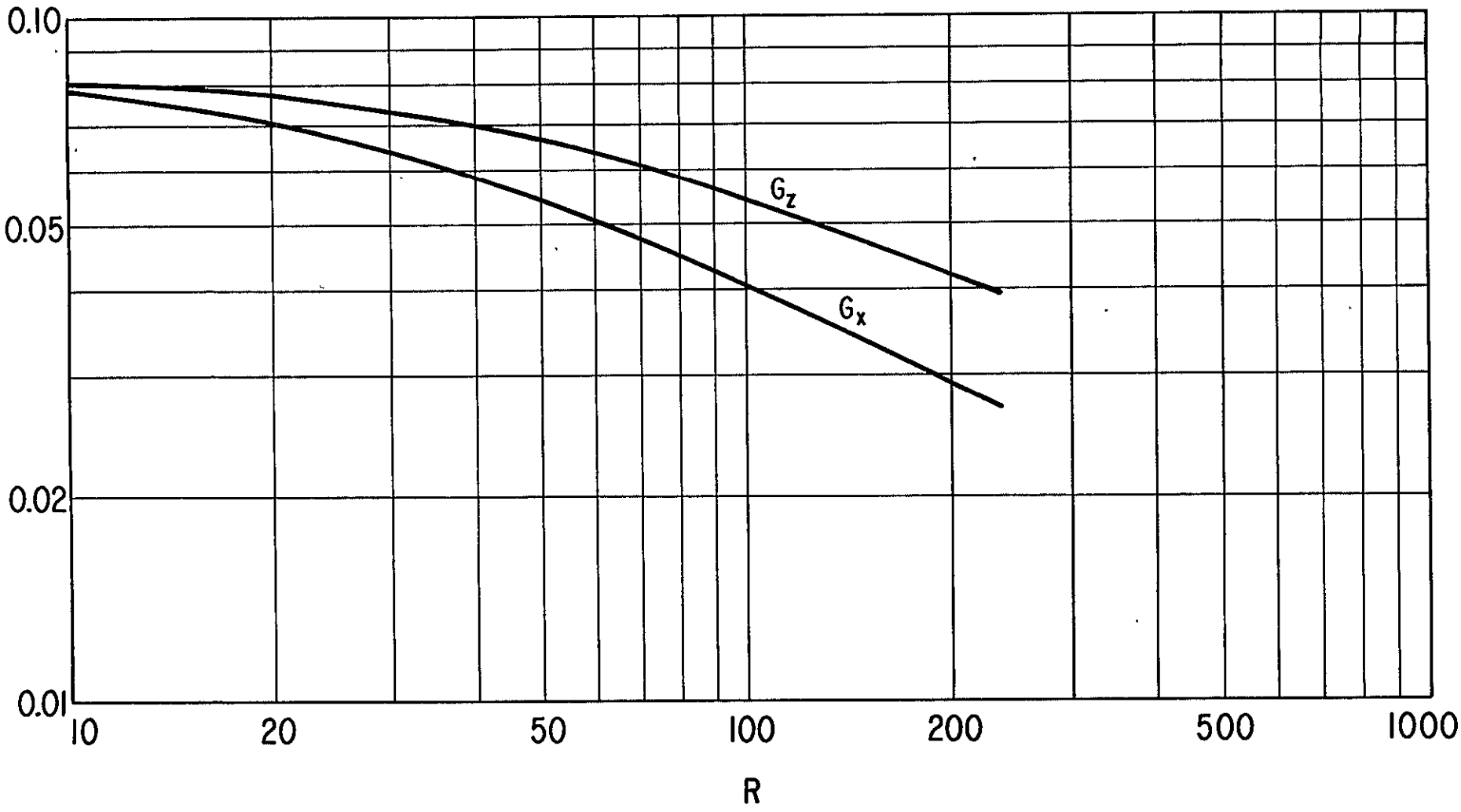

Fig. A-8 Parameters G_x, G_z as functions of the modified Reynolds number R.

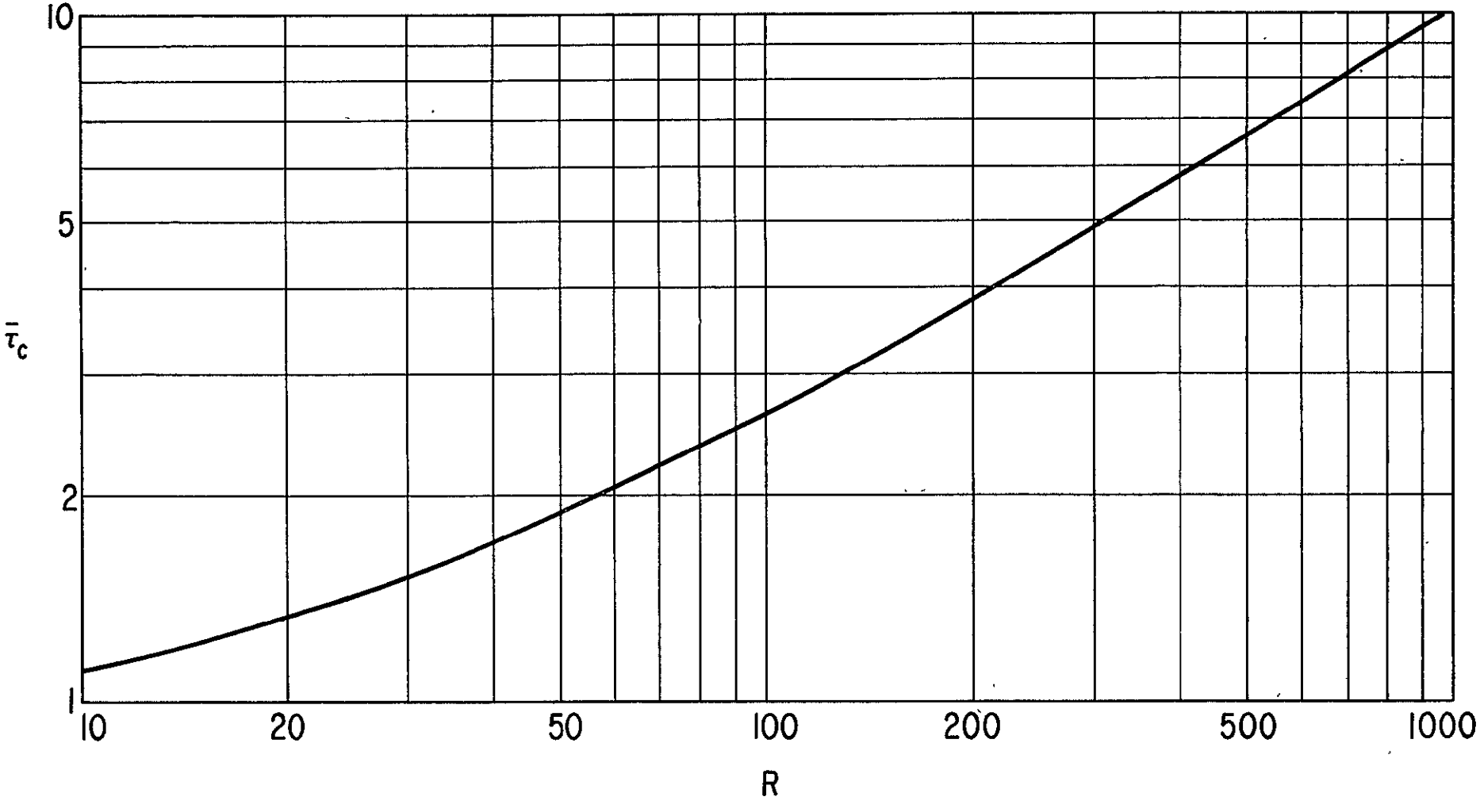

Fig. A-9 Couette friction stress $\bar{\tau}_c = h\,\tau_c/\mu V$ as a function of the modified Reynolds number.

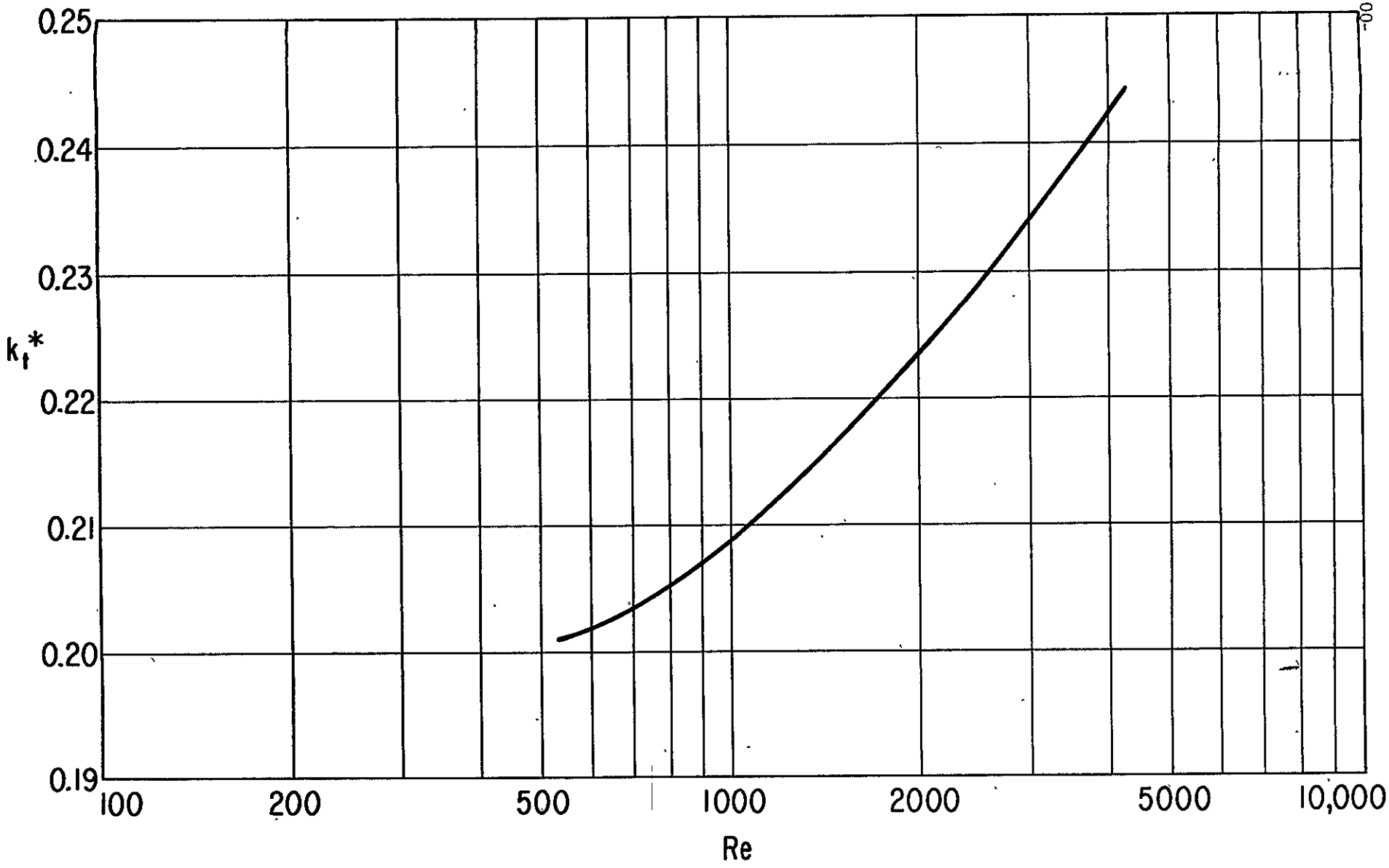

Fig. A-10 Constant k_t^* for fully turbulent flow as a function of the Reynolds number.

In order to obtain an indication concerning the shape of the function f (C27) let us first use Smith and Fuller's experimental curve [12] for co-axial cylinders with a clearance ratio of $\Psi = 0.00293$ (Fig. A-2), which is presented again in Fig. A11 as $\bar{\tau}_c$ vs Re. By starting from the experimental data for $\bar{\tau}_c$ of Fig. A11 and by using relations (C27), (C25) and the diagram of Fig. A-10, the variation of the function f given in Fig. A12 is obtained. It is seen that a reasonable approximation of this dependence is the parabolic variation

$$f = \frac{k^*}{k_t^*} = \sqrt{\frac{Re}{Re_c} - 1} \qquad (C29)$$

The corresponding variation $\bar{\tau}_c(Re)$ in the transition region obtained by using relation (C29) is presented in Fig. A11. As shown, the calculated curve follows fairly well the experimental one.

Another indirect possible check of the validity of relations (C27) and (C29) is to compare these results with the theoretical results obtained by DiPrima for the velocity profile in Couette - Taylor vortex flow. For this purpose in Fig. A13 various Couette velocity profiles obtained for various modified Reynolds numbers are presented by using the method given in references [3], [15]. At the same time in Fig. A14 a velocity profile obtained in reference [14] for a Taylor number

$$T = 2\,Re^2\,\frac{c}{r} \qquad (C30)$$

equal to T = 5000 is presented. Because the critical value of the Taylor number is $T_c = 3389.9$ [14], the result is that $T/T_c = Re^2/Re_c^2 = 1.485$ so that $Re/Re_c = 1.22$.

By using the results of Fig. A10 and relations (C27), (C29) the velocity profiles for two extreme cases are also presented in Fig. A14. The mentioned two extreme cases are $Re_c = 760$ (large clearance ratio $\Psi \simeq 0.003$) and $Re_c = 2000$ (pure planar Couette, or zero clearance ratio). It is seen that both velocity profiles are fairly close to the one obtained in reference [14].

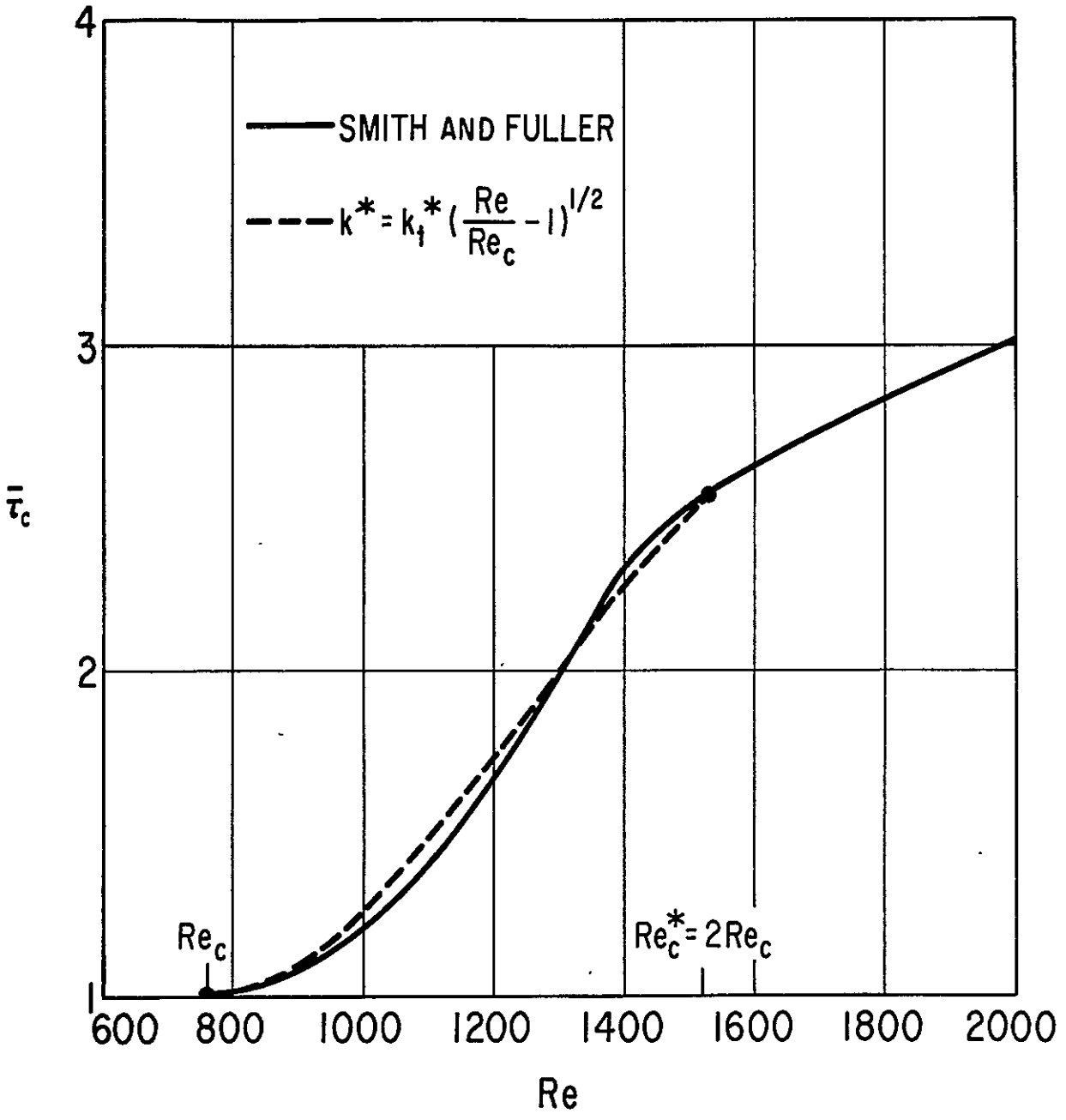

Fig. A-11 Couette friction stress $\bar{\tau}_c$ versus Reynolds number for the experimental curve of Fig. 2.

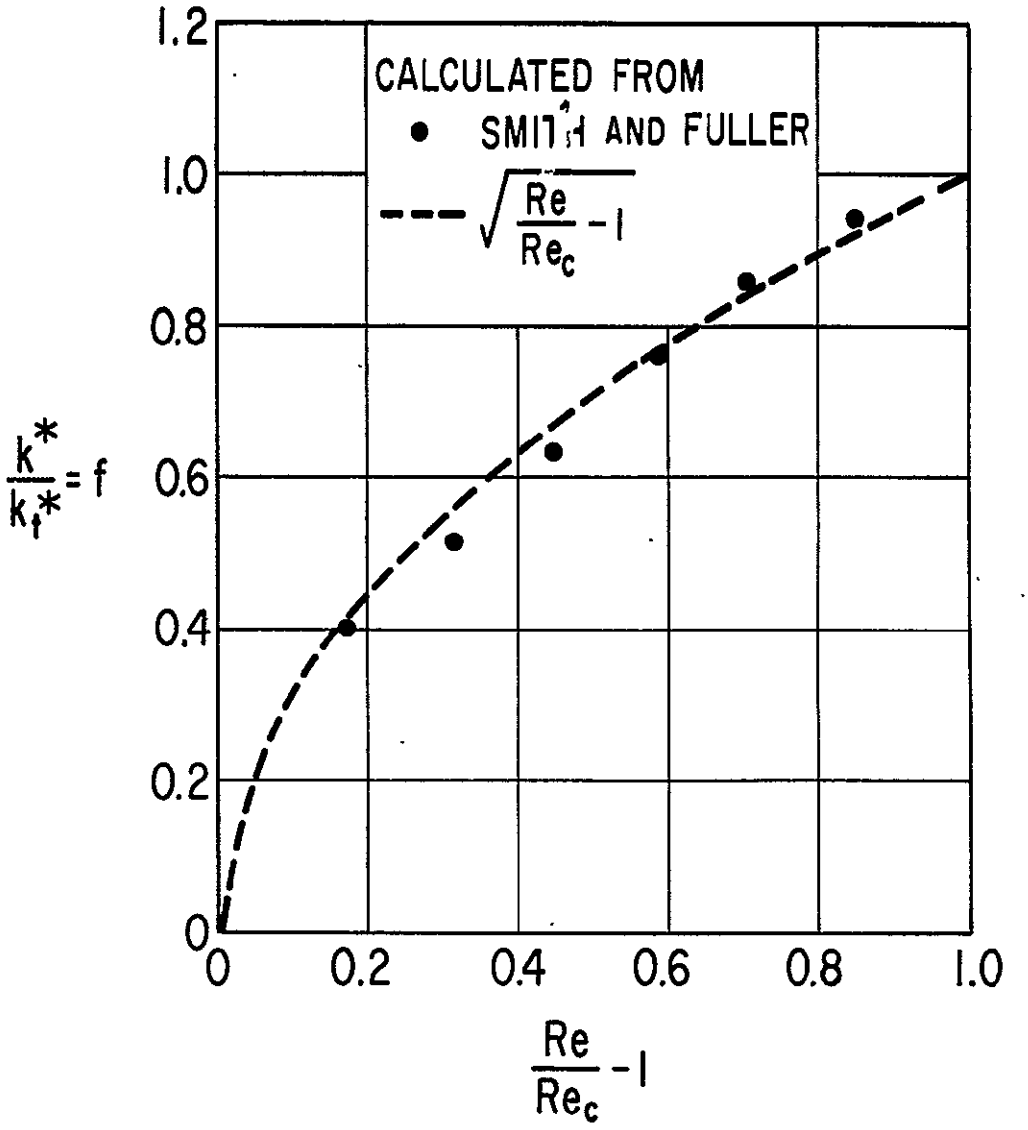

Fig. A-12 Interpolation function $f = k^*/k_t^*$ versus $(Re/Re_c -$ for the experimental case of Fig. 2.

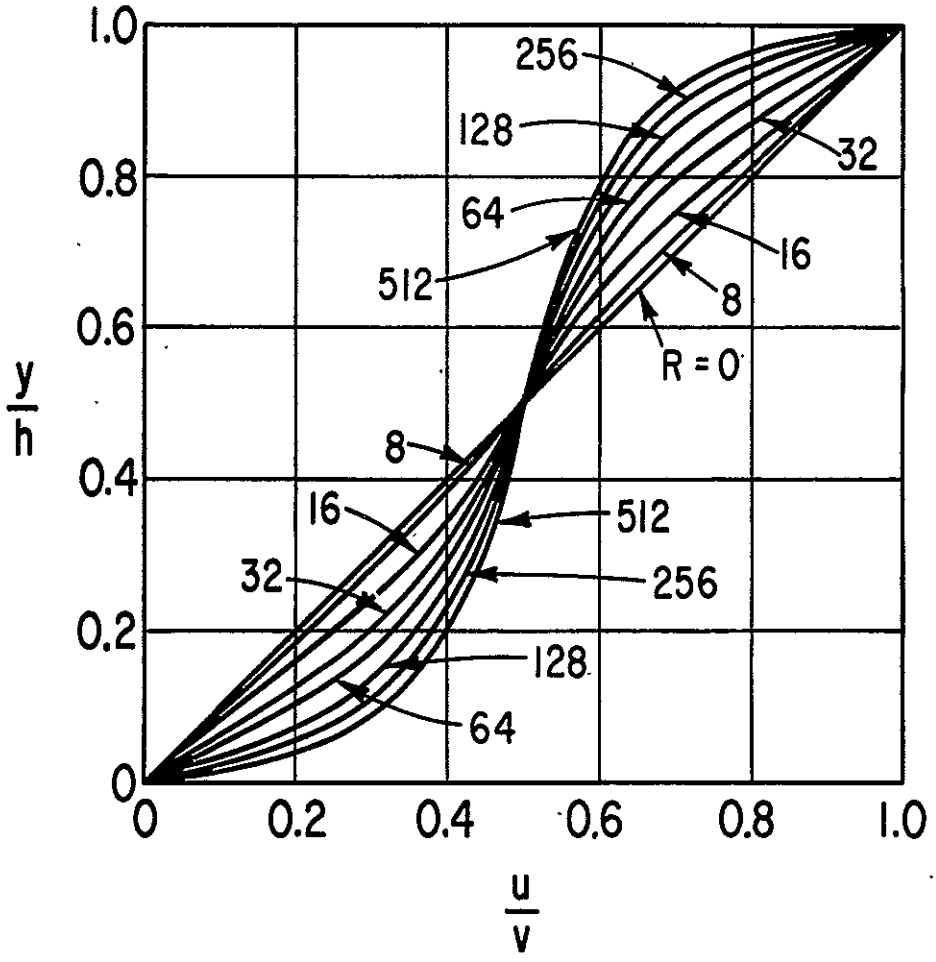

Fig. A-13 Couette velocity profiles for various modified Reynolds numbers $\bar{R}$.

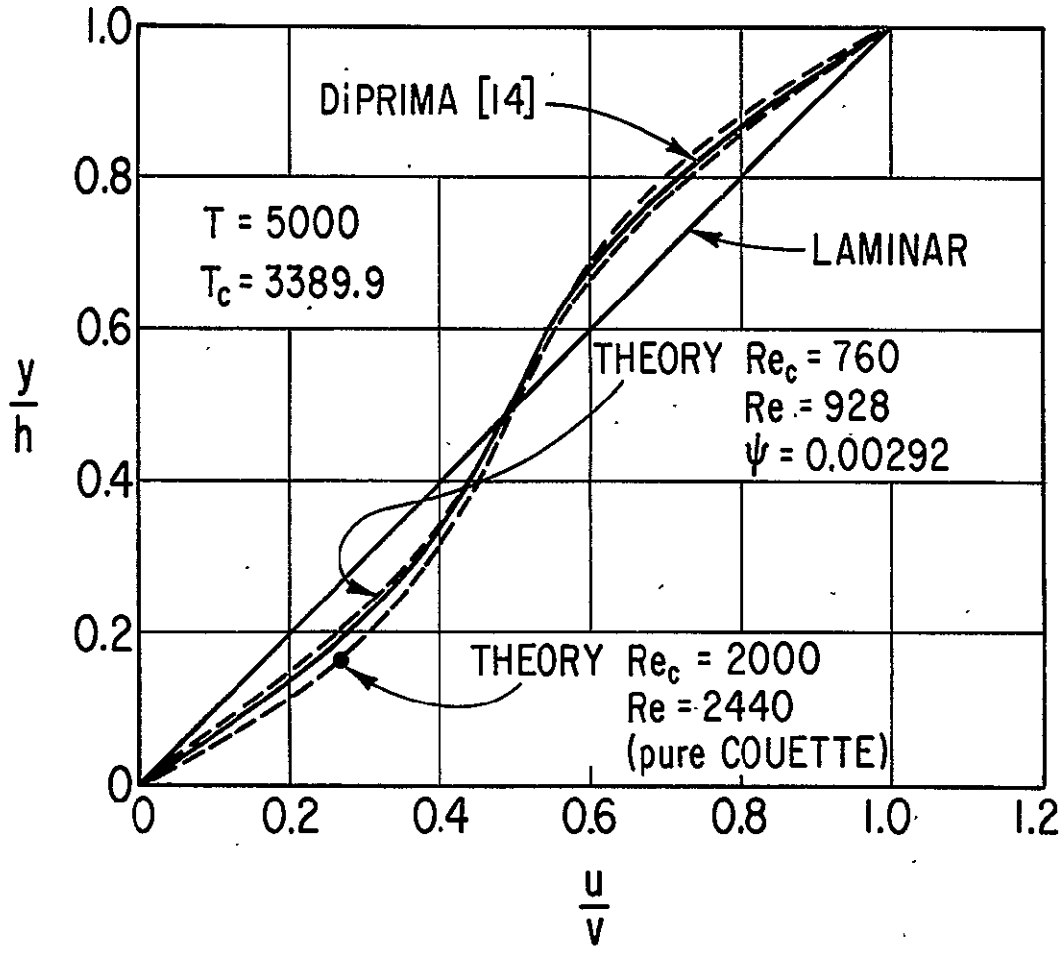

Fig. A-14 Comparison between the results obtained by using the modified mixing length approach and DiPrima's [14] velocity profile for a Taylor vortex flow.

One should, however, be cautious in connection with this check because of two reasons. Firstly, the pure Couette velocity profile does not vary too much even under rather different conditions as seen from Fig. A-14. Secondly, the numerical case studied by DiPrima was taken in the middle of the transition region, where any kind of interpolation is likely to give more or less the same result. Actually, the trend of the operating parameters in the transition region is different from that emphasized in Smith and Fuller experiments. Indeed, the friction coefficient exhibits a smooth variation in the experiments of Smith and Fuller, while DiPrima's calculations give a rapid variation (jump in the friction coefficient where the Reynolds number slightly exceeds the critical value).

The mentioned considerations enable us to assert that if the trend in the friction coefficient given in Smith and Fuller's experiment is correct, then the mentioned modified mixing length approach is most likely to give reasonably good results in the transition region by using the interpolation formula (C27) for the mixing length, where f has the parabolic variation (C29). Then by using the previous mentioned mean Reynolds number concept, it is reasonable to assume that for a coupled Couette - Poiseuille flow, relation (C27) may still be used, but in the function f (C29) the mean Reynolds number Re_m should be introduced instead of the Couette Reynolds number Re, i.e.

$$f = \frac{k^*}{k_t^*} = \sqrt{\frac{Re_m}{Re_c} - 1} \qquad (C31)$$

Finally, it is extremely interesting to note that the interpolation law (C31) enables us to carry out an iterative procedure which is even simpler than that mentioned before. Indeed, by taking into account relations (C25), (C27), (C31), the modified Reynolds number may be written as

$$R = k^{*2} Re = k_t^{*2} \left(\frac{Re_m}{Re_c} - 1\right) Re \qquad (C32)$$

But now, we can define an "equivalent" Reynolds number Re_e as

$$Re_e = \frac{R}{k_t^{*2}} = \left(\frac{Re_m}{Re_c} - 1\right) Re \qquad (C33)$$

Consequently the parabolic interpolation in terms of the constant k^* is equivalent to a linear interpolation in terms of the Reynolds number. It is seen that again $0 \leq Re_c \leq Re_c^*$ in the transition region. Moreover, it is no more necessary to use as an intermediate stage the modified Reynolds number R (C25) as well as the dependences $G_{x,z}(R)$, $\bar{\tau}_c(R)$ given in Figs. A-8 and A-9. Instead one can use directly the existing numerical results [4],[5] for $G_{x,z}(Re)$, $\bar{\tau}_c(Re)$ by simply replacing Re by the equivalent number Re_e. In this way the method of analysis becomes very simple and all the existing numerical procedures for computing operating characteristics for turbulent bearings can easily be adapted to predict the operating characteristics in the transition region by an iterative method.

The Use of the Eddy Viscosity Approach

Similar results can be obtained by using the "law of wall" [4]. Then

$$\tau_{xy}^* = \mu \frac{\varepsilon}{\nu} \frac{\partial u}{\partial y} \qquad (C34)$$

where

$$\frac{\varepsilon}{\nu} = k \left(y^+ - \delta^+ \tanh \frac{y^+}{\delta^+} \right) \qquad (C35)$$

in which

$$y^+ = \frac{u_\tau y}{\nu} \quad ; \quad u_\tau = \sqrt{\frac{|\tau|}{\rho}} \qquad (C36)$$

τ being the total shear stress. In turbulent flow $k = 0.4$ and δ^+ in a similar way as done in (C27) for the mixing length, namely

$$\frac{1}{\delta^+} = 0 \qquad ; \quad Re_m \leq Re_c$$

$$\frac{1}{\delta^+} = \varphi\left(\frac{Re_m}{Re_c}\right) \qquad ; \quad Re_c \leq Re_m \leq Re^+ \simeq 2Re_c \tag{C37}$$

$$\frac{1}{\delta^+} = 1/10.7 \qquad ; \quad Re_m \geq Re^+$$

Therefore, the function φ should vary in the transition region from 0 to 1/10.7.

Fig. A-15 shows some of the results which can be obtained in this way. As in the case of the function f, the function φ can be determined by starting from some experimental data, for example, the friction coefficient C_f. Thus, if Smith and Fuller's data are considered, then a reasonable approximation is found to be

$$\varphi = \frac{1}{10.7}\left(\frac{Re_m}{Re_c} - 1\right) \tag{C38}$$

Again, as for the function f (C27), other expressions may be found when other variations of $C_f(Re)$ are considered in the transition region.

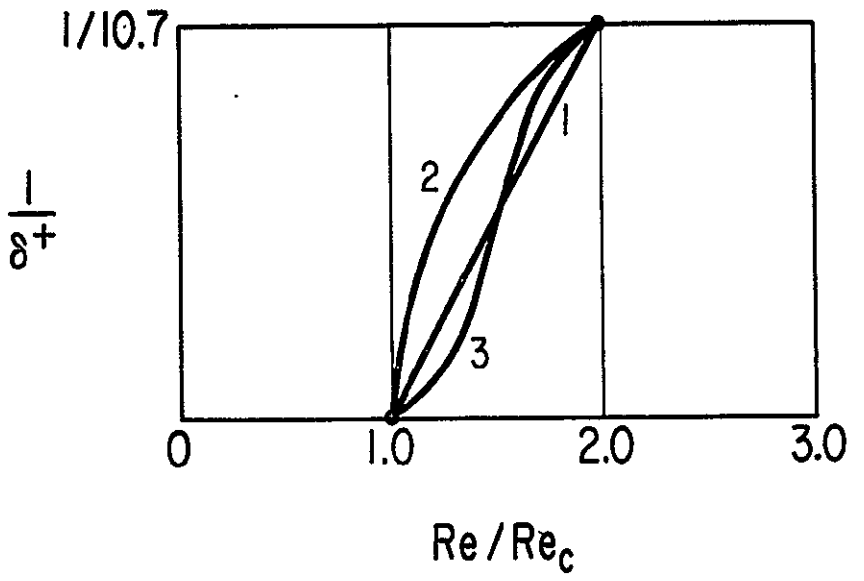

$$1 \quad \frac{1}{\delta^+} = \frac{1}{10.7}\left(\frac{Re_m}{Re_c} - 1\right)$$

$$2 \quad \frac{1}{\delta^+} = \frac{2}{10.7}\left(\frac{Re_m}{Re_c} - 1\right)\left[1 - \frac{1}{2}\left(\frac{Re_m}{Re_c} - 1\right)\right]$$

$$3 \quad \frac{1}{\delta^+} = \frac{3}{10.7}\left(\frac{Re_m}{Re_c} - 1\right)^2\left[1 - \frac{2}{3}\left(\frac{Re_m}{Re_c} - 1\right)\right]$$

a) Corrected δ^+

Fig. A-15 Evaluation of the transition data by using the eddy viscosity law with corrected values δ^+.

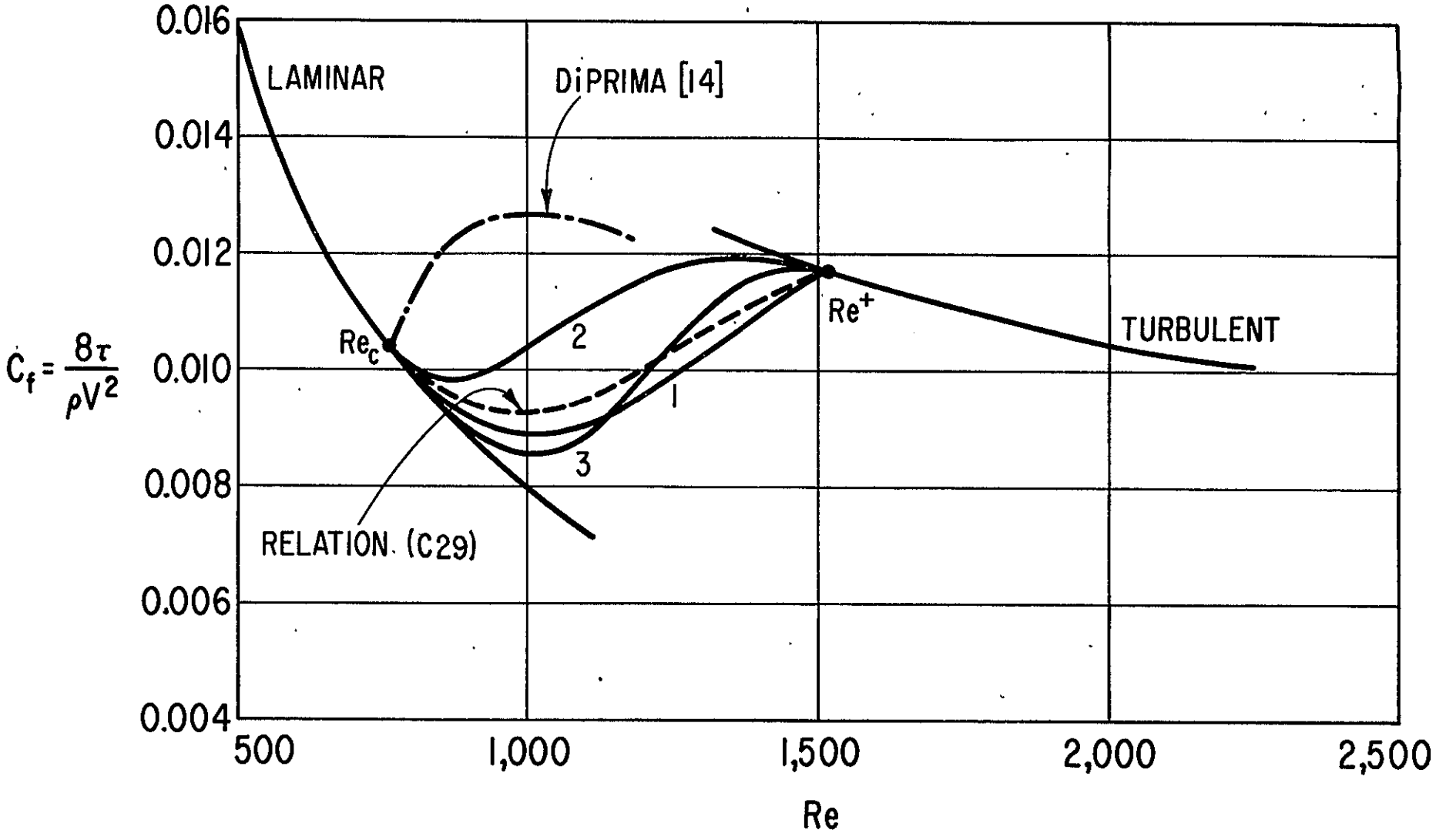

b) C_f

Fig. A-15 (continued) Evaluation of the transition data by using the eddy viscosity law with corrected values δ^+.

A PROCEDURE FOR THE ANALYSIS OF BEARINGS IN THE TRANSITION REGION

It has been shown that by considering the flow as having a pseudo-turbulent character, the additional apparent stresses can be determined in a half-empirical way by starting from some experimental data concerning the variation of friction stresses in the transition region. Thus, if Smith and Fuller's data are considered as valid (Fig. A-11), then the interpolation function F (C29) can be used together with the mixing length theory, or alternately, the interpolation function φ (C38) can be used together with the eddy viscosity approach.

At the same time, another, even simpler approach appears to be equivalent to the mentioned two approaches, namely that of defining an "effective" or "equivalent" Reynolds number (33) so that,

$$\left.\begin{aligned} Re_e &= 0 && ; \quad Re_m \leq Re_c \\ Re_e &= F\left(\frac{Re_m}{Re_c}\right) Re && ; \quad Re_c \leq Re_m \leq Re^+ \\ Re_e &= Re && ; \quad Re_m \geq Re^+ \end{aligned}\right\} \qquad (C39)$$

Then the pressure differential equation (C2) is still valid, but parameters G_x, G_z are evaluated according to the existing turbulent data, using the effective Reynolds number Re_e instead of the local Reynolds number Re.

The only problem is how to evaluate the interpolation function F. In this respect some more careful experimental data are needed. However, by properly using the already existing information it is possible to limit the uncertainty of such an evaluation to a reasonable low level ($\sim$ 20%). Thus, Smith and Fuller's experimental data can be considered as a lower limit giving a rather smooth variation of the function coefficient (Fig. A-16 - Curve I). In this case (C33)

$$F = \frac{Re_m}{Re_c} - 1 \qquad (C40)$$

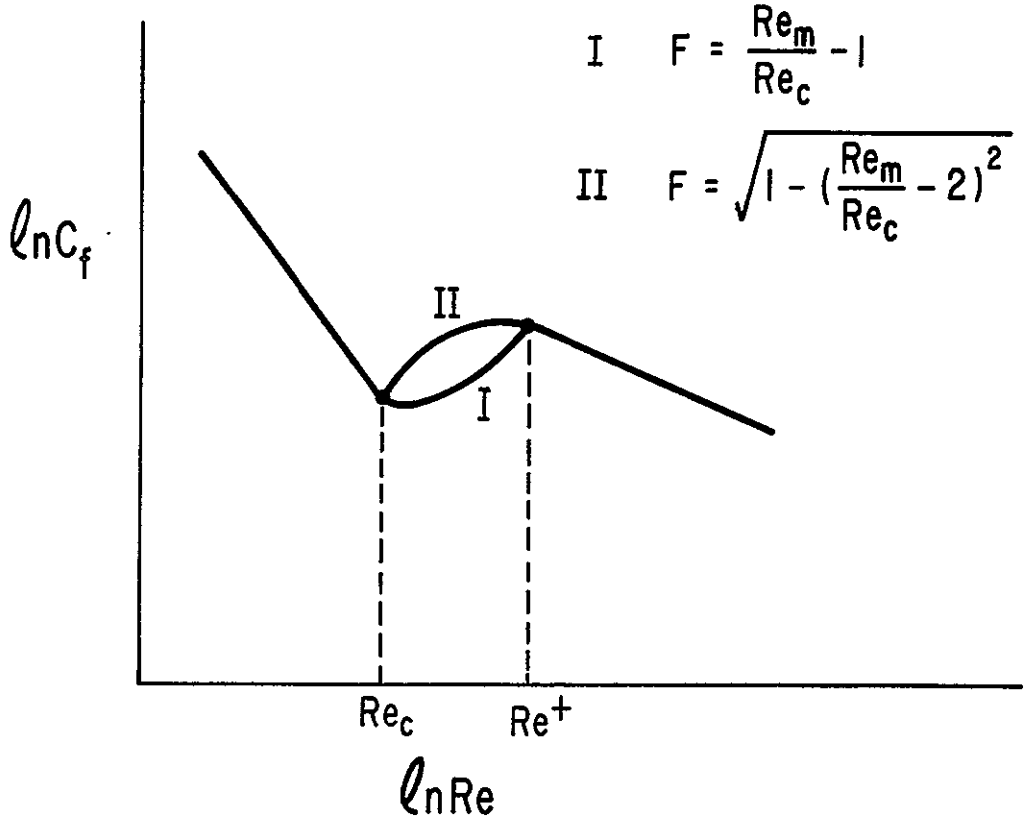

Fig. A-16 Limiting transition curve for pure Couette flow.

i.e., a linear variation of the interpolation of function F.

The upper limit (Fig. A-16 Curve II) is suggested by DiPrima's analysis [14] as well as by the existing experimental evidence for boundary layers. Basically the coefficient C_f exhibits a rather rapid increase when the critical Reynolds number is exceeded and then tends smoothly toward the turbulent value. In such a case the interpolation curve may be approximated by

$$F = \sqrt{1 - \left(\frac{Re_m}{Re_c} - 2 \right)^2} \qquad \text{(C41)}$$

The actual values will be in between the two interpolation laws (C40), (C41).

In order to illustrate the method, as well as the differences between the laws (C40) and (C41) let us consider a numerical example.

Numerical Example: Let us consider an infinitely long journal bearing having a clearance ratio of 3 mils/in (mm/meter) and let us calculate the operating characteristics for various Reynolds numbers and eccentricity ratios in two situations:

(a) Inner member rotating, i.e., a critical Reynolds number (C6), $Re_c \simeq 750$, $Re^+ = 1500$

(b) Outer member rotating, i.e., (C5) $Re_c = 2000$, $Re^+ = 4000$

The calculations are performed by an iterative method. For each case, one starts by assuming either that the flow is laminar (small Reynolds number), or turbulent (large Reynolds number). Then, the pressure differential equation (C2) is integrated. Thus, the flow at each point can be calculated as well as the mean Reynolds number (C9) (for one dimensional film, both flow and Re_m are constant, because of the continuity requirement). Then the local Reynolds number Re_e is calculated by using relations (C39) and new values G_x are obtained. The pressure differential equation (C2) is again solved with the new values G_x and the procedure is repeated until the convergence is achieved.

The obtained results are plotted in Figs. A17-A25. Figs. A17-A19 show the variation of the friction coefficient (on the moving member) as a function of the Reynolds number for $\varepsilon = 0$; 0.3; 0.5. The features emphasized by the case when the inner member rotates are particularly interesting. Thus, due to the local variation of the critical Reynolds number with the ratio h/r_1, the transition zone is broadened when the eccentricity ratio increases. At the same time, the variation of the friction coefficient becomes smooth. Such a behavior was already found experimentally in reference [6]. For a qualitative comparison, Fig. A20 is reproduced from reference [6]. A comparison of Figs. A20 and A19 clearly shows a similar trend. Figs. A21-A23 give the same data as Figs. A17-A19, but in terms of variation of the dimensionless torque against the Reynolds number.

The load capacity is presented in Figs. A24-A25 against the Reynolds number, for $\varepsilon = 0.3$ and $\varepsilon = 0.5$ respectively. Again, the peculiar behavior, especially when the inner member is rotating, may be seen, due to the local variation of the critical Reynolds number. Moreover, the mean Reynolds number is

$$Re_m = \frac{h_o}{c} Re^* \quad ; \quad Re^* = \frac{V c}{\nu} \tag{C42}$$

where h_o is the film thickness at the location where the pressure distribution reaches a maximum ($\partial p/\partial x = 0$). Therefore, h_o retains a value very close to the laminar one. When the Reynolds number increases, the turbulent zone extends itself over the film so that at a certain Reynolds number the parameter h_o will also be influenced, i.e., will be decreased. But according to (C42) the mean Reynolds number increase will be slowed down and the transition curve will take another shape.

For the same reason, the transition region, when the outer member is rotating, is diminished. Thus at $\varepsilon = 0$, $Re_c^* = 750$ and $Re^{*+} = 2Re_c = 1500$ while at $\varepsilon = 0.5$, $Re_c^* = 3000$ and $Re^{*+} = 5700 = 1.9\ Re_c^*$. However, there is no special influence on the shape of the transition curves, because the value Re_c is constant, so that transition and turbulence occur under equal conditions over the whole film.

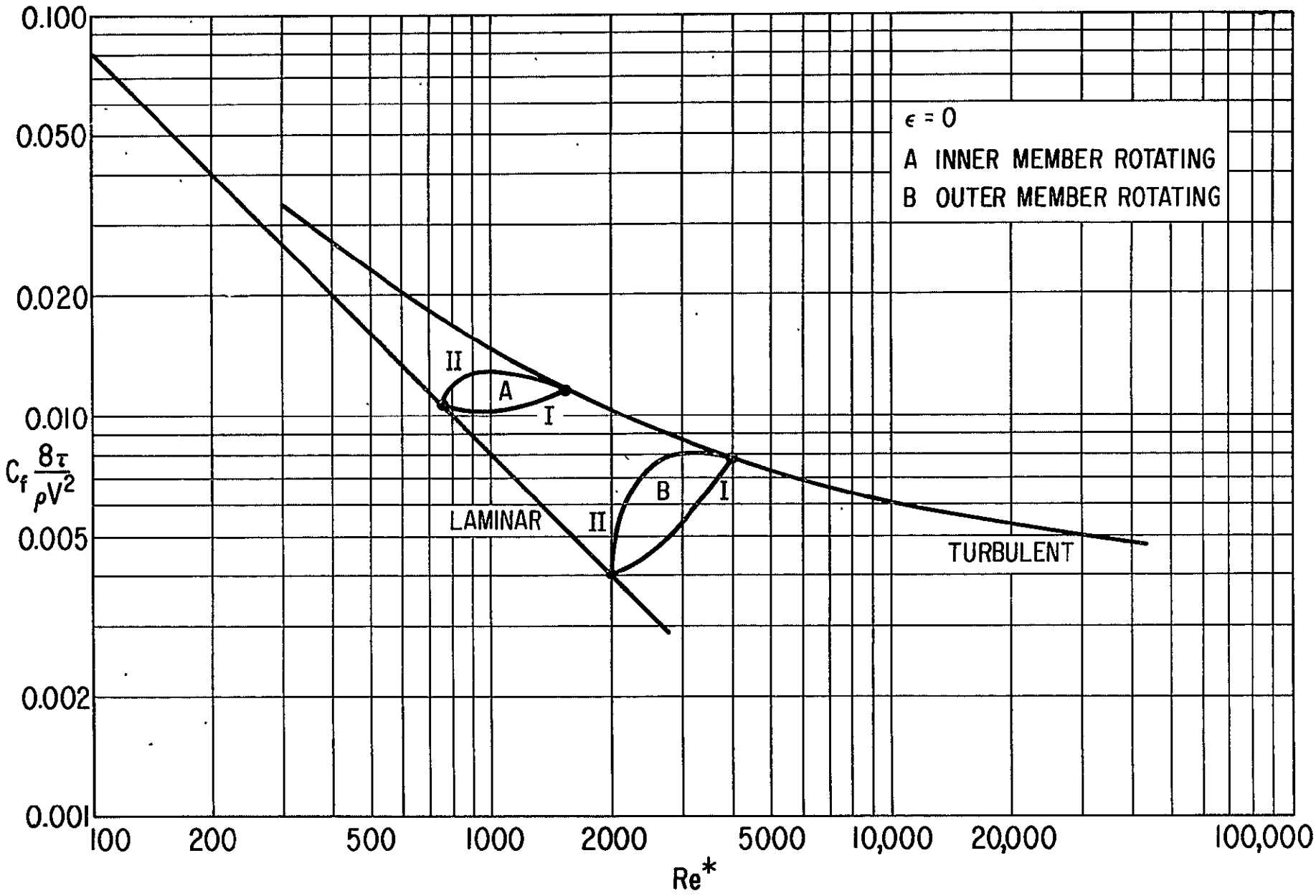

Fig. A-17 Friction factor against the Reynolds number Re = V c/ν for a journal bearing (ϵ = 0; c/r_1 = 0.003).

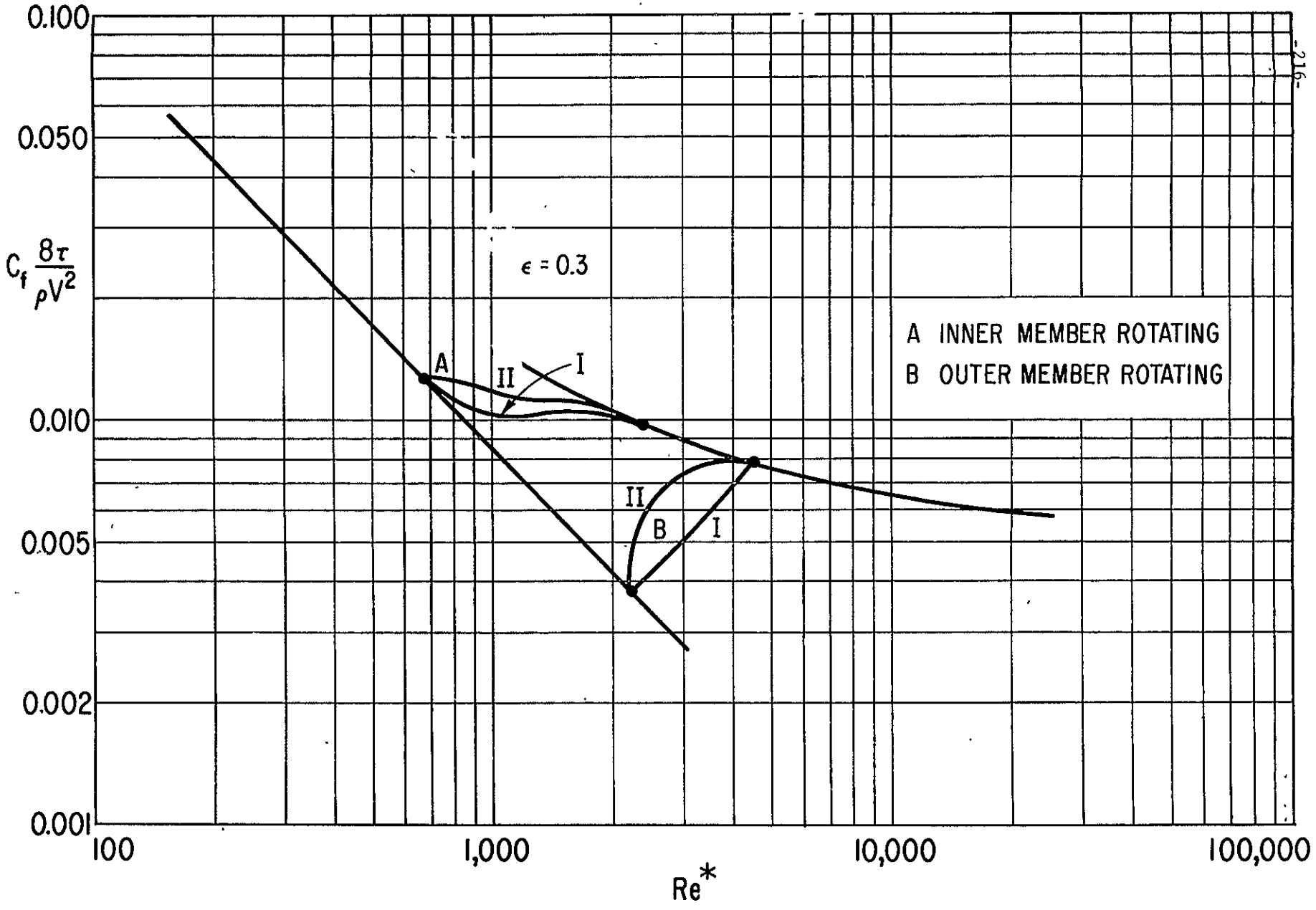

Fig. A-18 Friction factor against the Reynolds number Re for an infinitely-long journal bearing ($\epsilon = 0.3$; $c/r_1 = 0.003$).

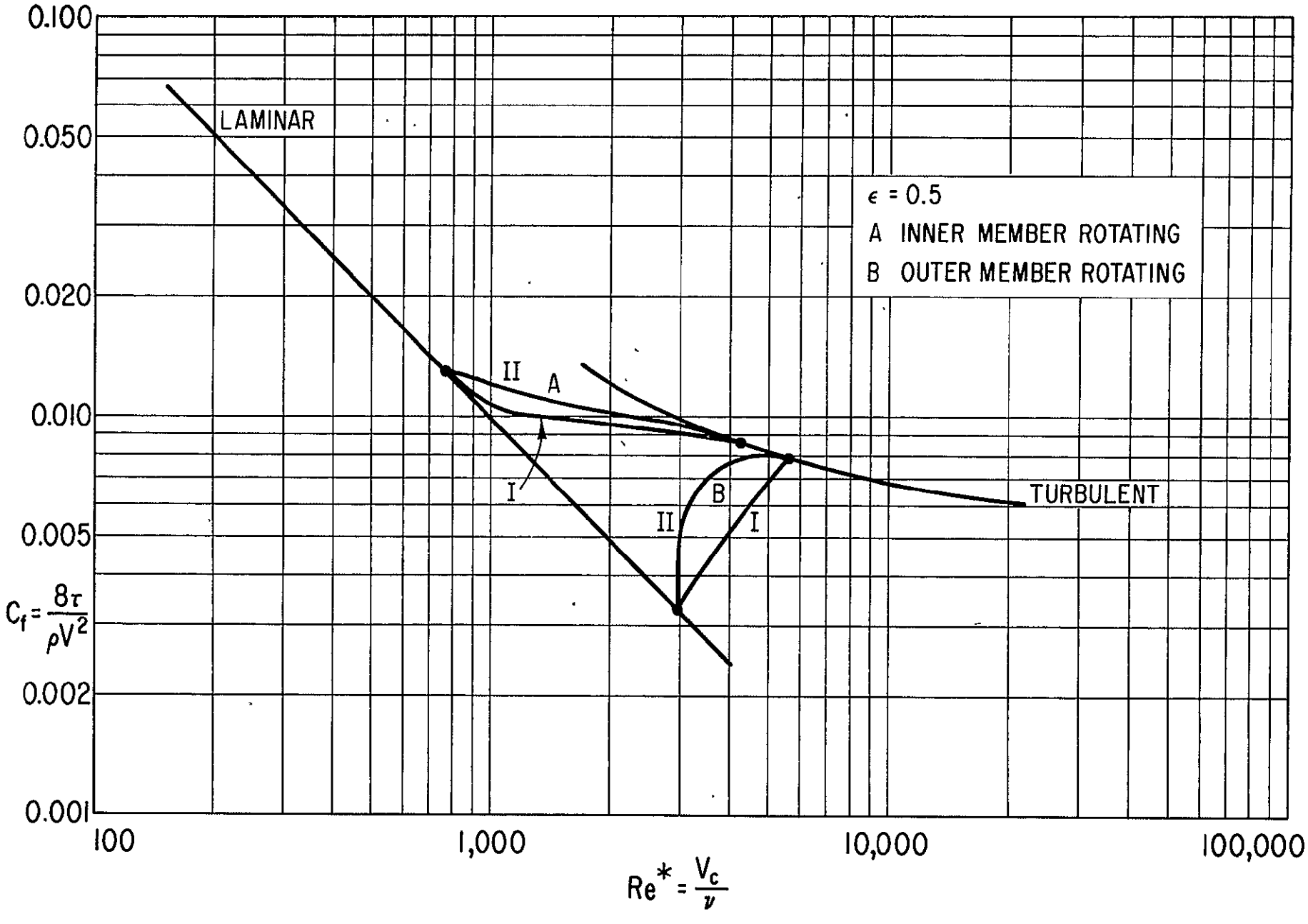

Fig. A-19 Friction factor against the Reynolds number for an infinitely-long journal bearing ($\epsilon = 0.5$: $c/r_1 = 0.003$)

MIT-9134

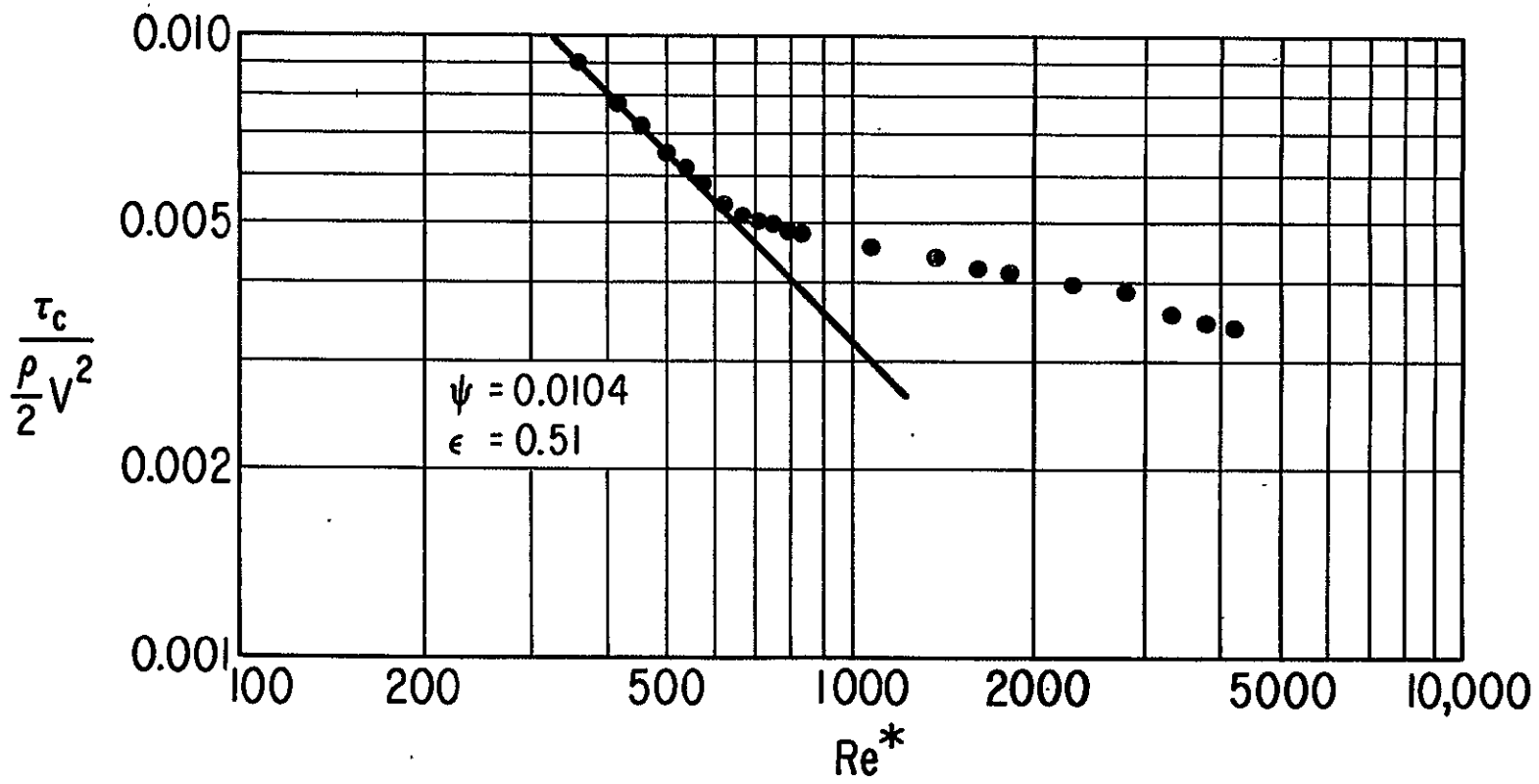

Fig. A-20 Experimental results concerning the variation of the friction factor vs. Reynolds number for two non-concentric cylinders (inner member rotating, $c/r_1 = 0.0104$; $\varepsilon = 0.51$) [6].

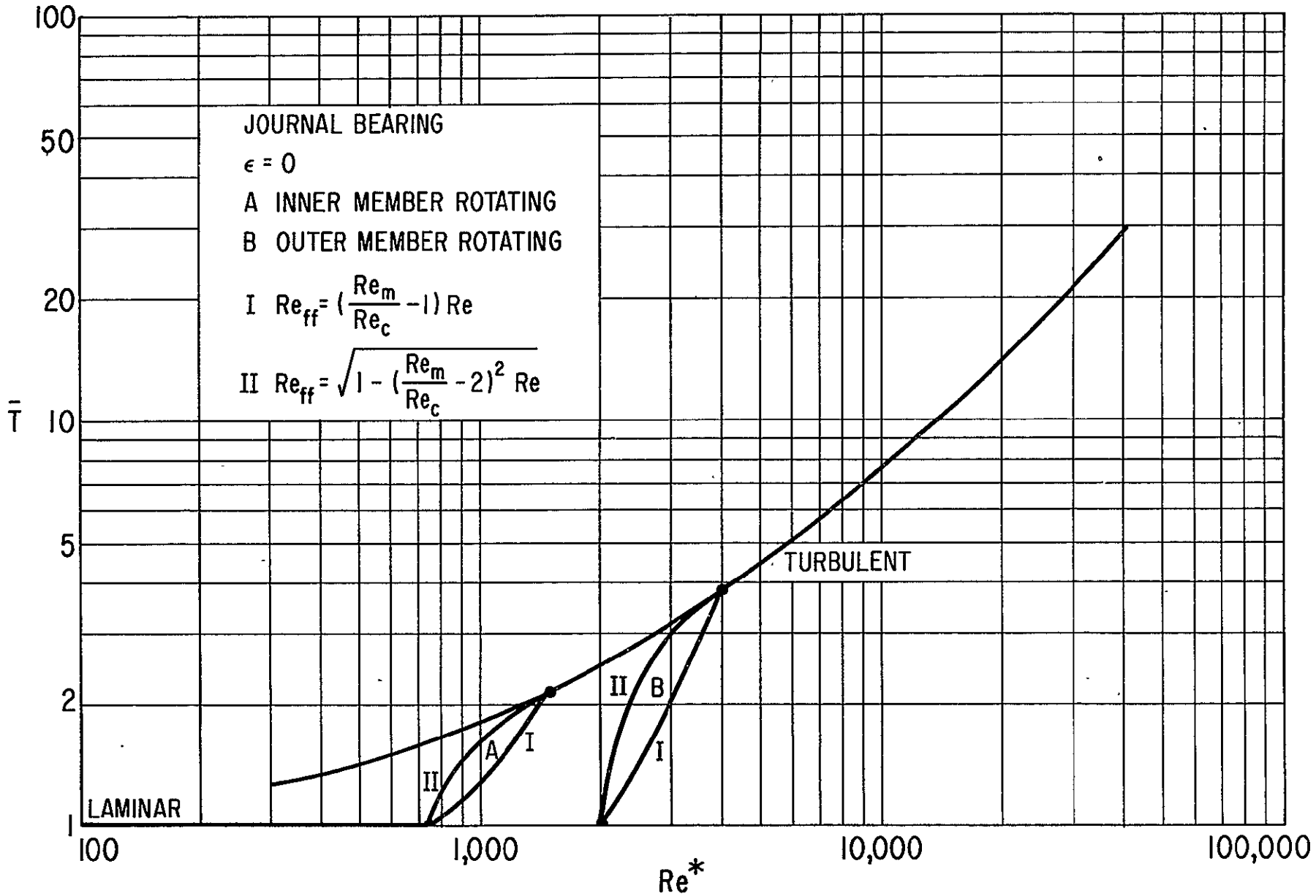

Fig. A-21 Dimensionless torque versus Reynolds number for a journal bearing ($\epsilon = 0$; $c/r_1 = 0.003$).

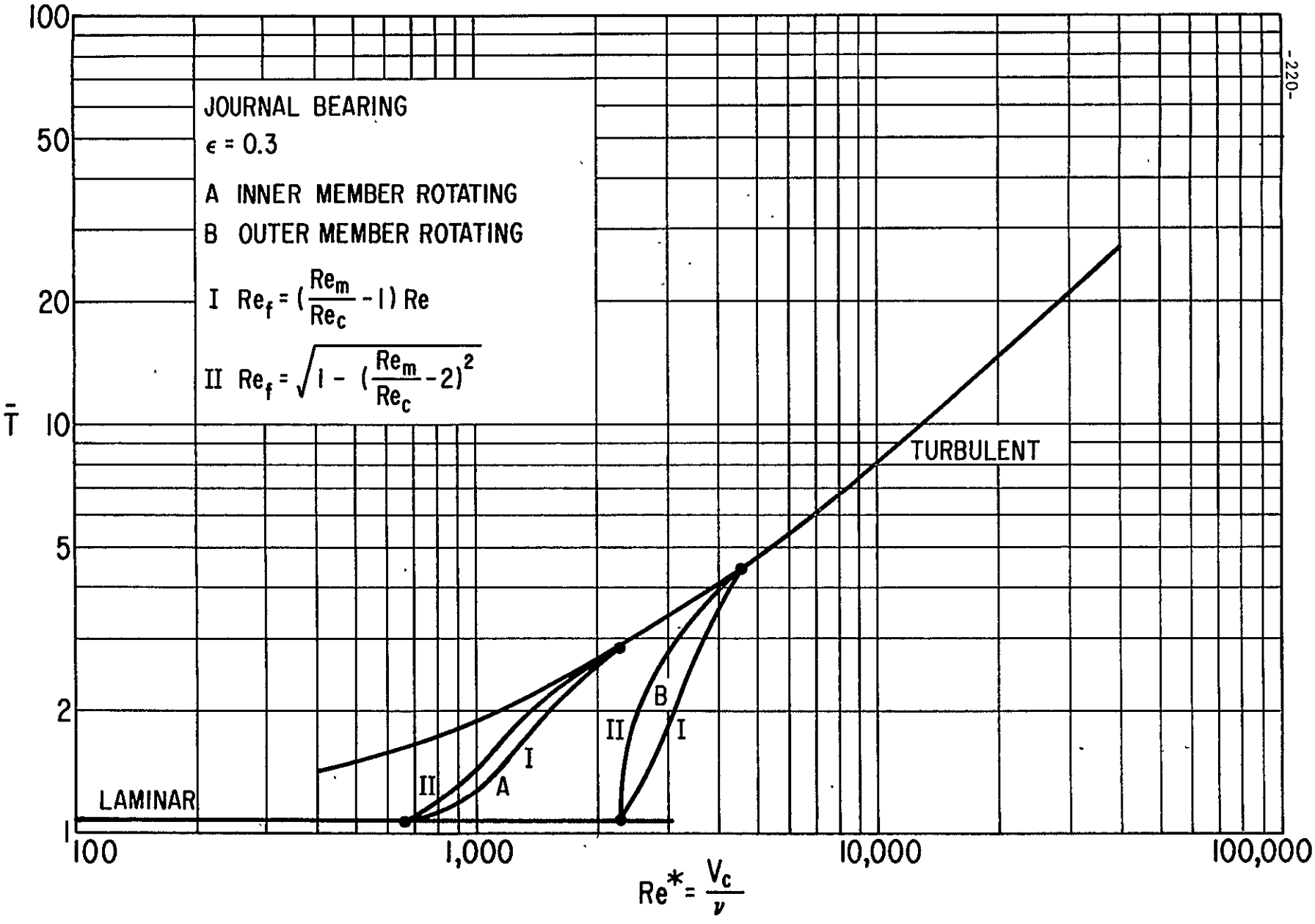

Fig. A-22 Dimensionless torque versus Reynolds number for an infinitely-long journal bearing ($\epsilon = 0.3$; $c/r_1 = 0.003$).

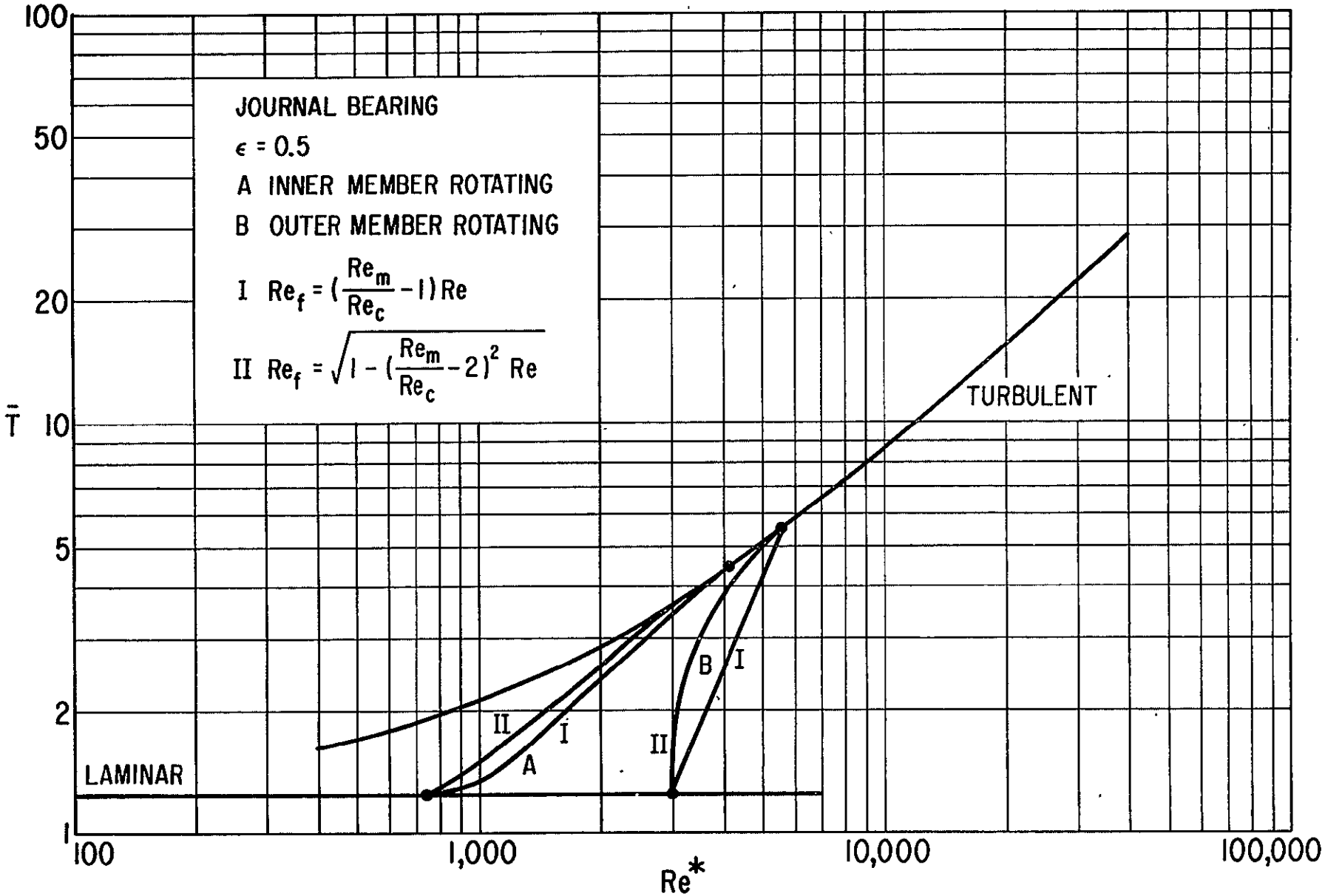

Fig. A-23 Dimensionless torque versus Reynolds number for an infinitely-long journal bearing ($\epsilon = 0.3$; $c/r_1 = 0.003$).

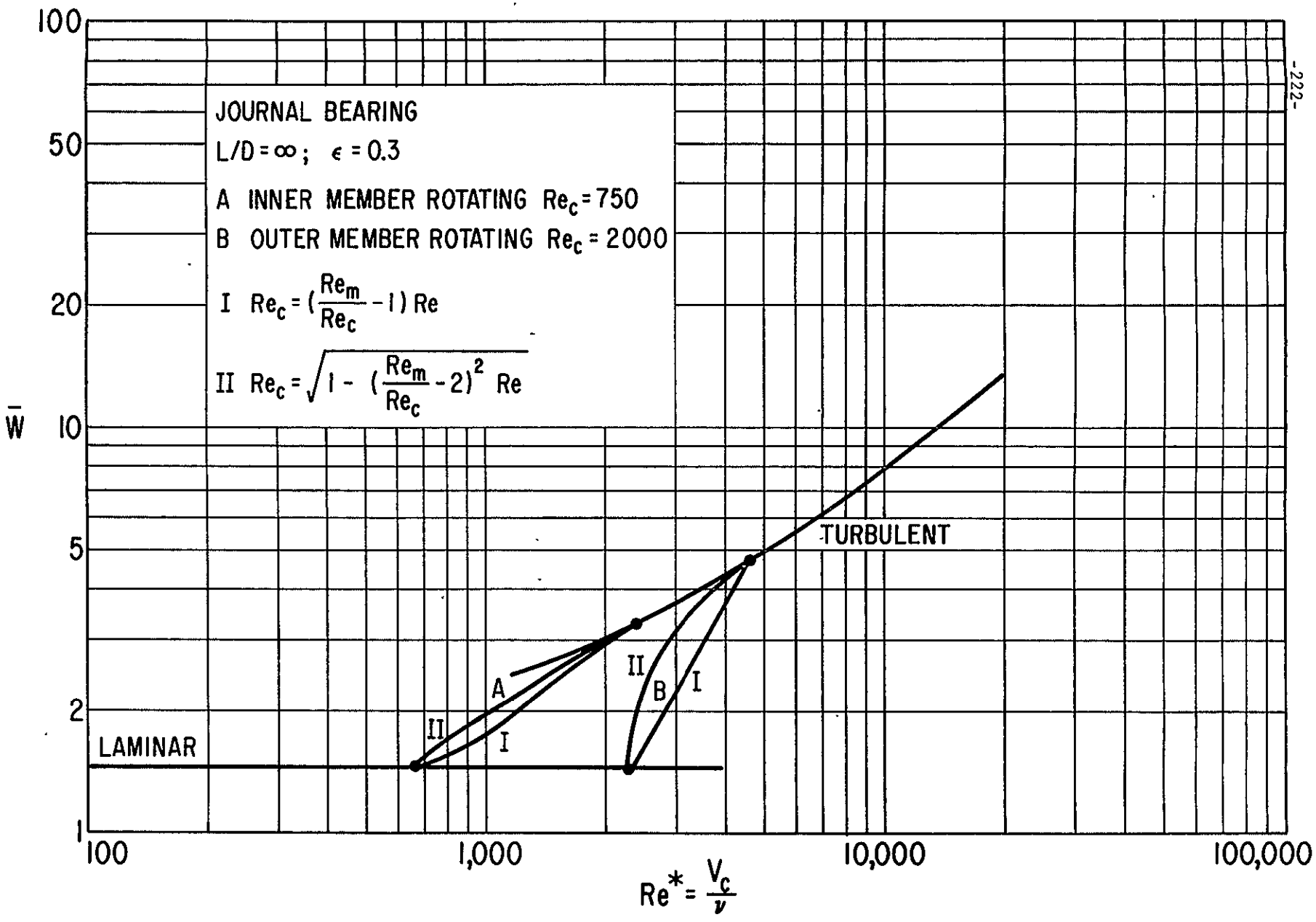

Fig. A-24 Dimensionless load versus Reynolds number for an infinitely-long journal bearing ($\epsilon = 0.3$; $c/r_1 = 0.003$).

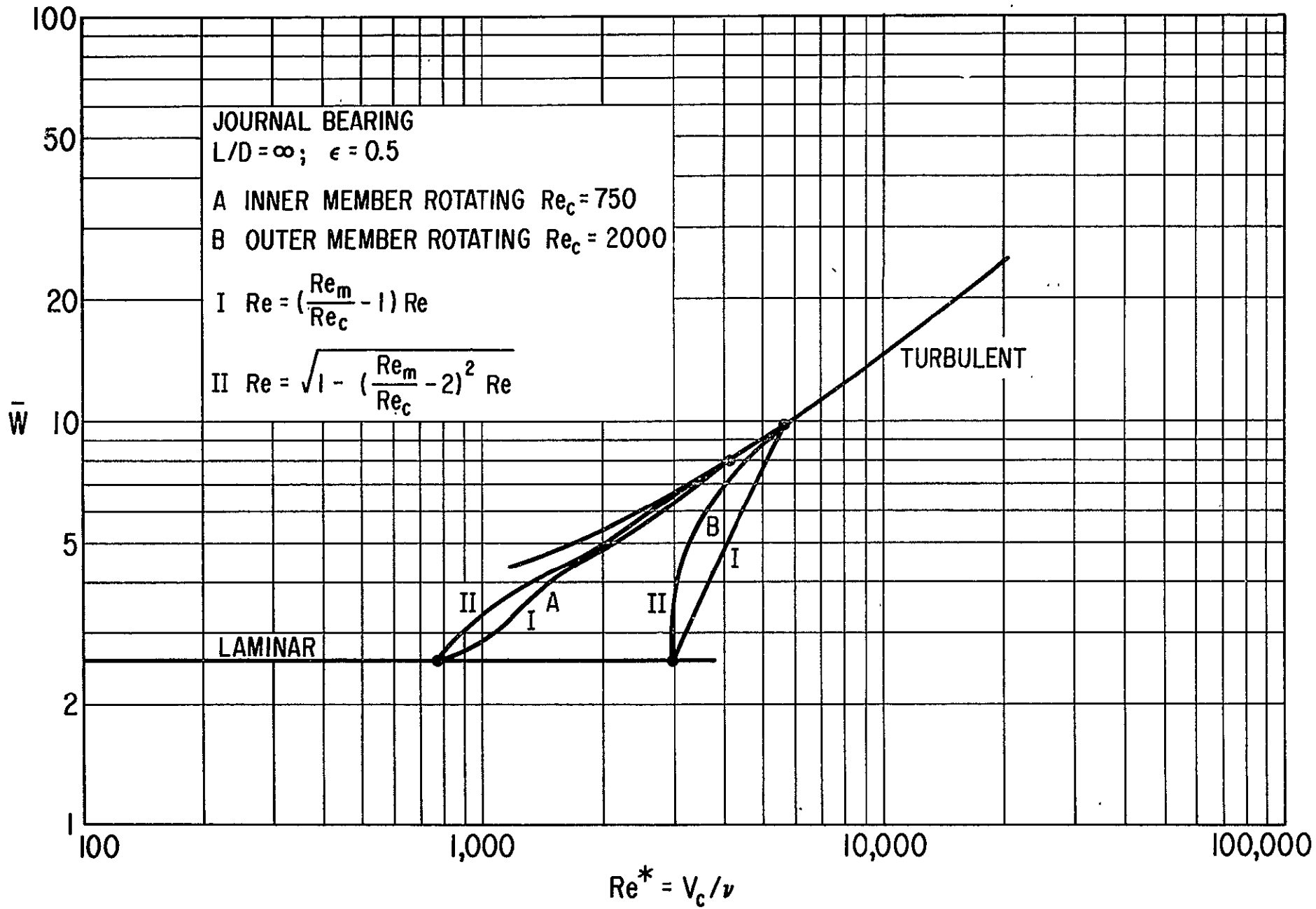

Fig. A-25 Dimensionless load versus Reynolds number for an infinitely-long journal bearing ($\epsilon = 0.5$; $c/r_1 = 0.003$).

MTI-9101

Numerical Example: Circular Disks Some peculiarities similar to those encountered in journal bearings are expected to occur also in thrust bearings. Thus even when the local critical Reynolds number is constant, the transition does not occur at the same time all over the bearing, since the speed and thus the Reynolds number is varying with the local radius.

As an example, Figs. A26 and A27 show the friction coefficient C_f and dimensionless torque, for two parallel disks (ratio between internal radius r_i and external one r_e, $r_i/r_e = 0.5$), by considering a critical value for the Reynolds number $Re_c = 700$. It is seen that because of the radius variation the transition region is rather wide (for the mentioned example it extends from $Re_o = 700$ to $Re_o = 2800$). The general trend of the transition curve is in a qualitative agreement with the experimental data obtained at NASA Lewis Center [11].

Numerical example: Step slider Let us consider an infinitely-long step slider having the step located at 0.7 of the total length and the ratio of film thicknesses be $h_1/h_2 = 6$. Then, because of the strong adverse pressure flow, the Couette Reynolds number in the pocket must reach large values (~5000) in order to obtain transition and turbulence, even when $Re_c = 750$. Obviously, the analysis overestimates the stability of the laminar flow in such an extreme case. An improvement can be done by assuming that when the Couette Reynolds number exceeds a certain value Re_{cc}, the transition occurs irrespective of the value of the pressure gradient. From Fig. A4 it is seen that $Re_{cc} \cong 4.2\ Re_c$. By using such an approach, the results concerning the load capacity are plotted in Fig. A28.

Numerical example: Shrouded step bearing Finally, the shrouded step thrust bearing analyzed in Reference [17] was considered, with the numerical values given in Fig. A29. The criterion for transition is again Re_{cc}, since the film thickness ratio is again large. The load capacity versus speed is plotted in Fig. A30.

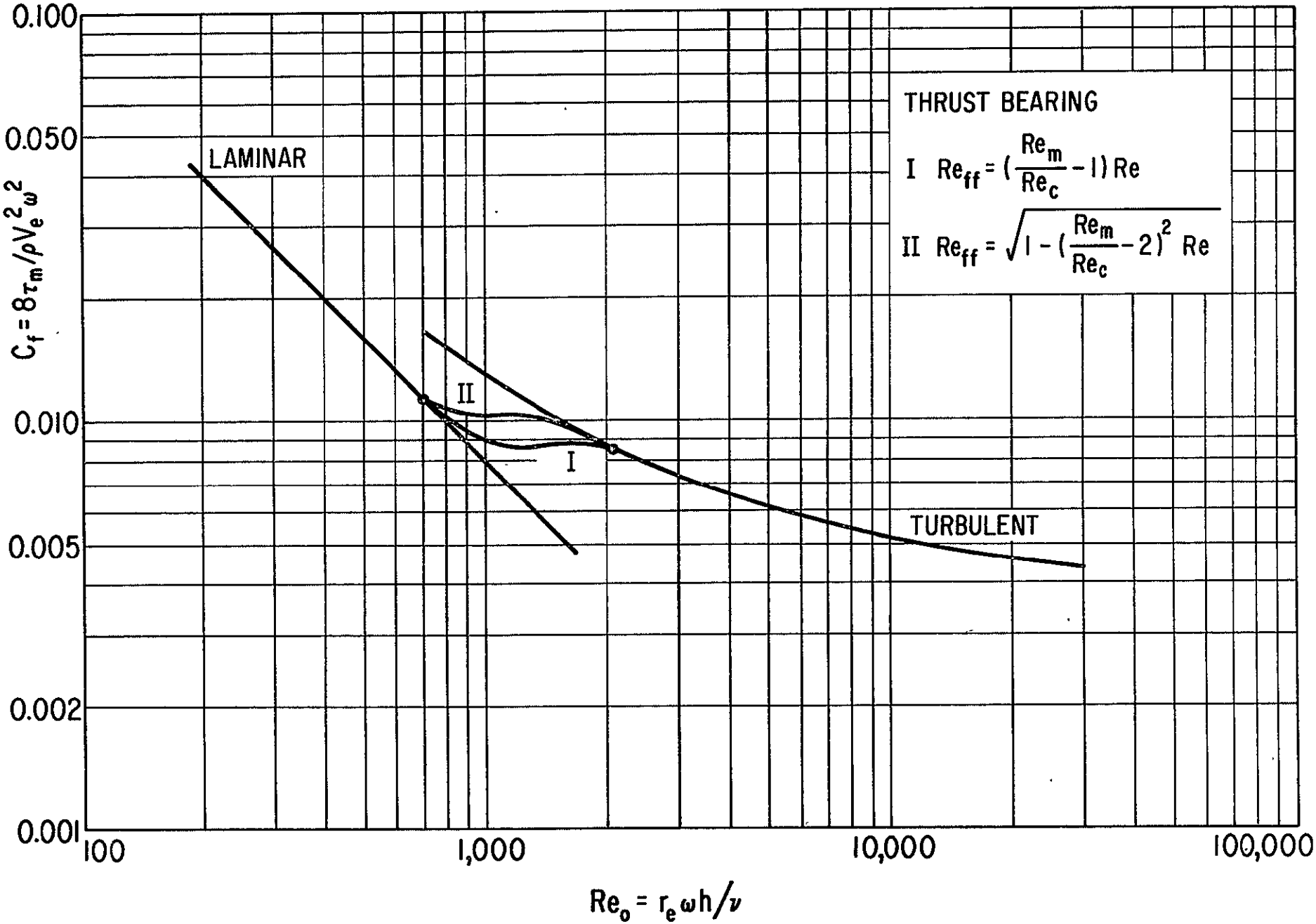

Fig. A-26 Friction factor versus Reynolds number for flow between rotating disks (r_i/r_e = 0.5; Re_c = 700).

MTI-9063

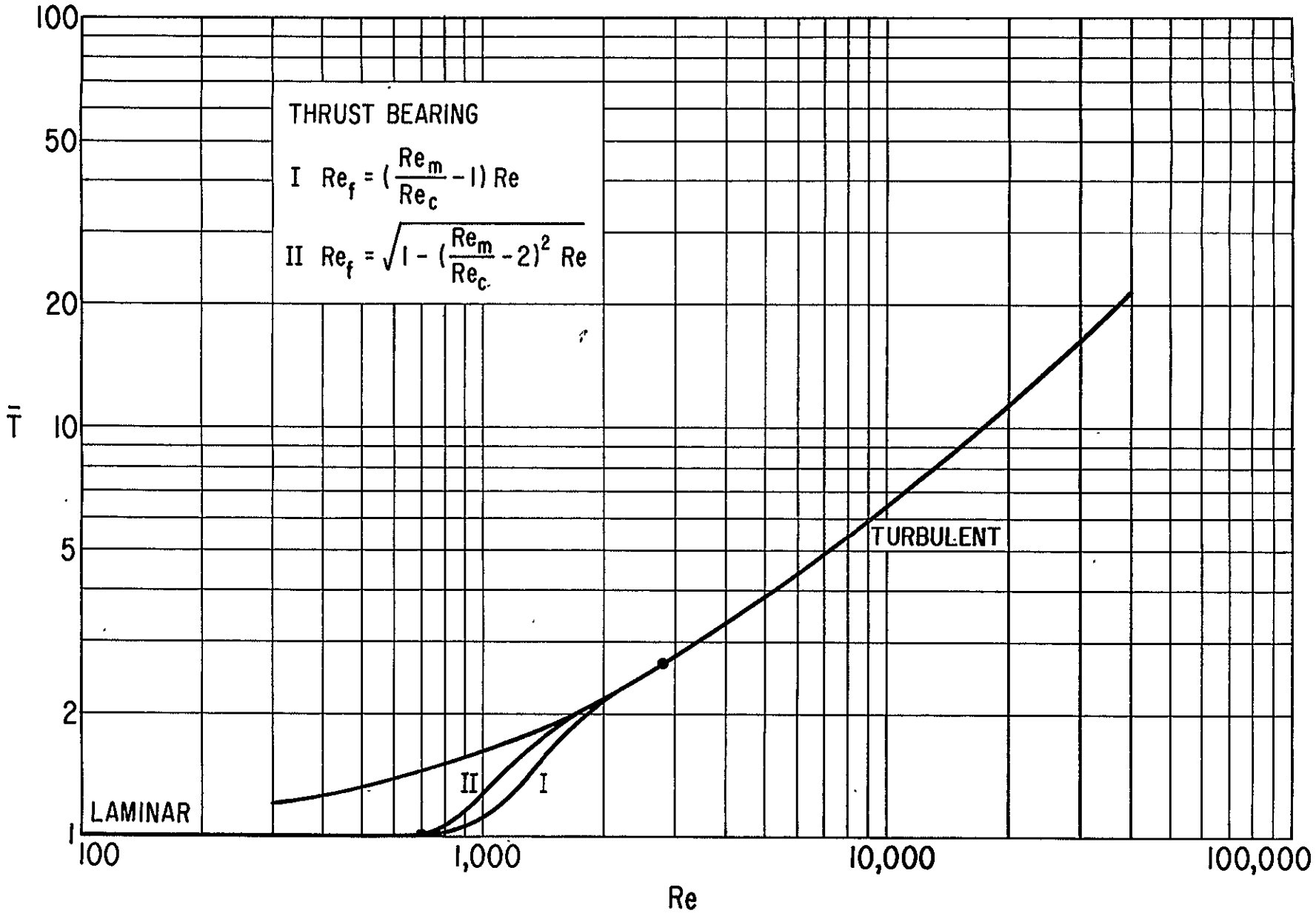

Fig. A-27 Dimensionless torque versus Reynolds number for flow between rotating disks (r_i/r_e = 0.5: Re_c = 700).

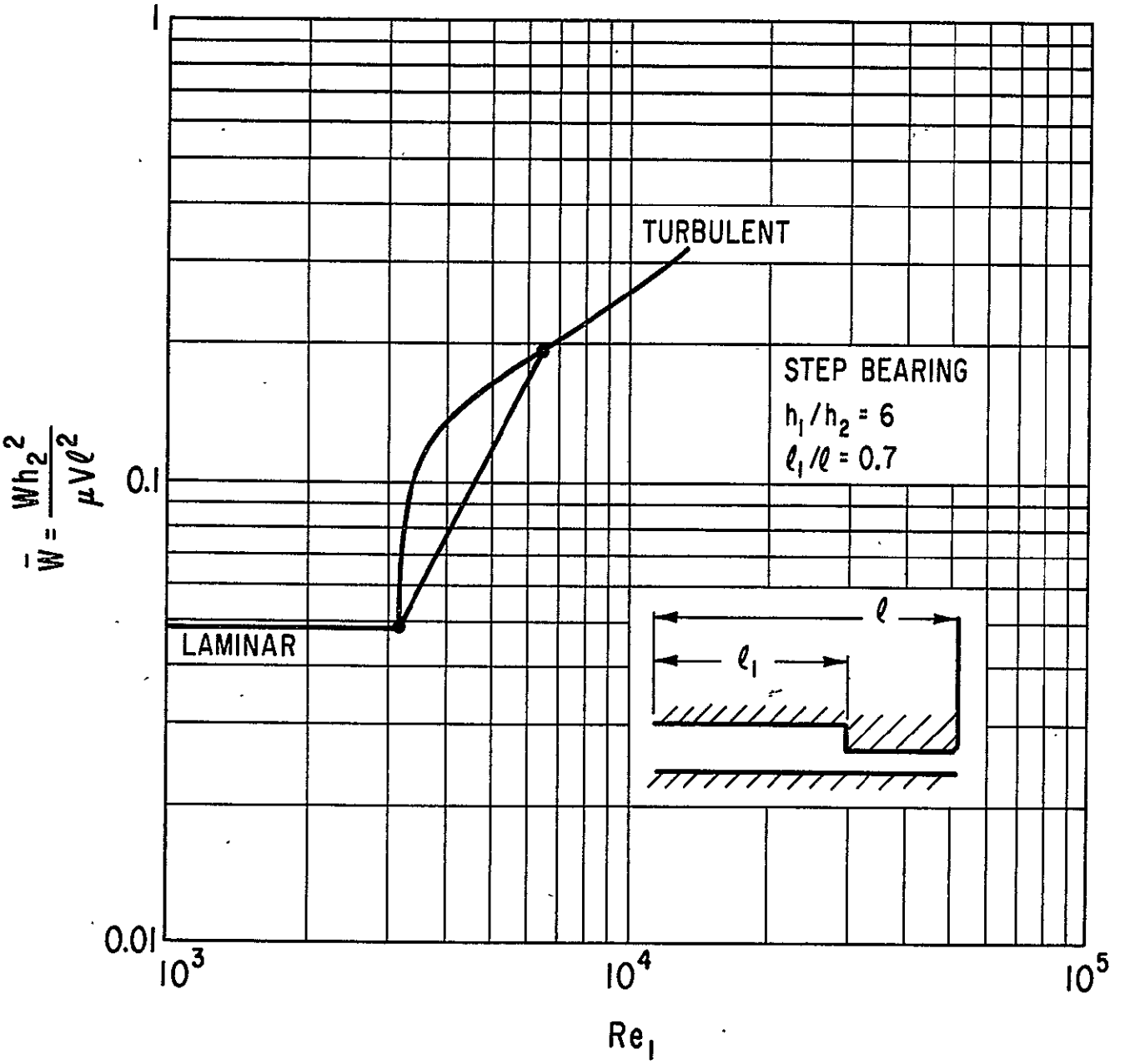

Fig. A-28 Load capacity versus pocket Reynolds number for a step bearing.

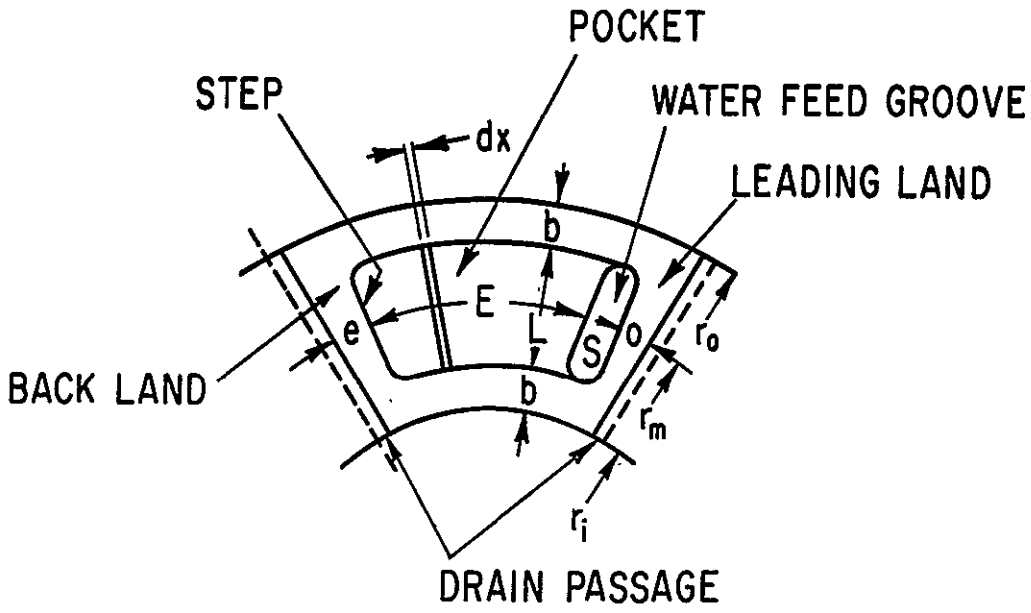

Fig. A-29 Diagrammatical representation of one pad of the shrouded step thrust bearing.

Numerical data used in the example of Fig. 30:

Re_c = 750; Re_{cc} = 3150; p_i = 64.7 psi; L = 0.425 in.;

r_m = 2.1625 in.; E = 1.91 in.; e = 0.81 in.; b = 0.125 in.;

μ = 3.97×10^{-6} Reyns; S = 0.188 in.; a = 0.372 in.;

h_1 = 0.0033 in.; δ = 0.015 in.

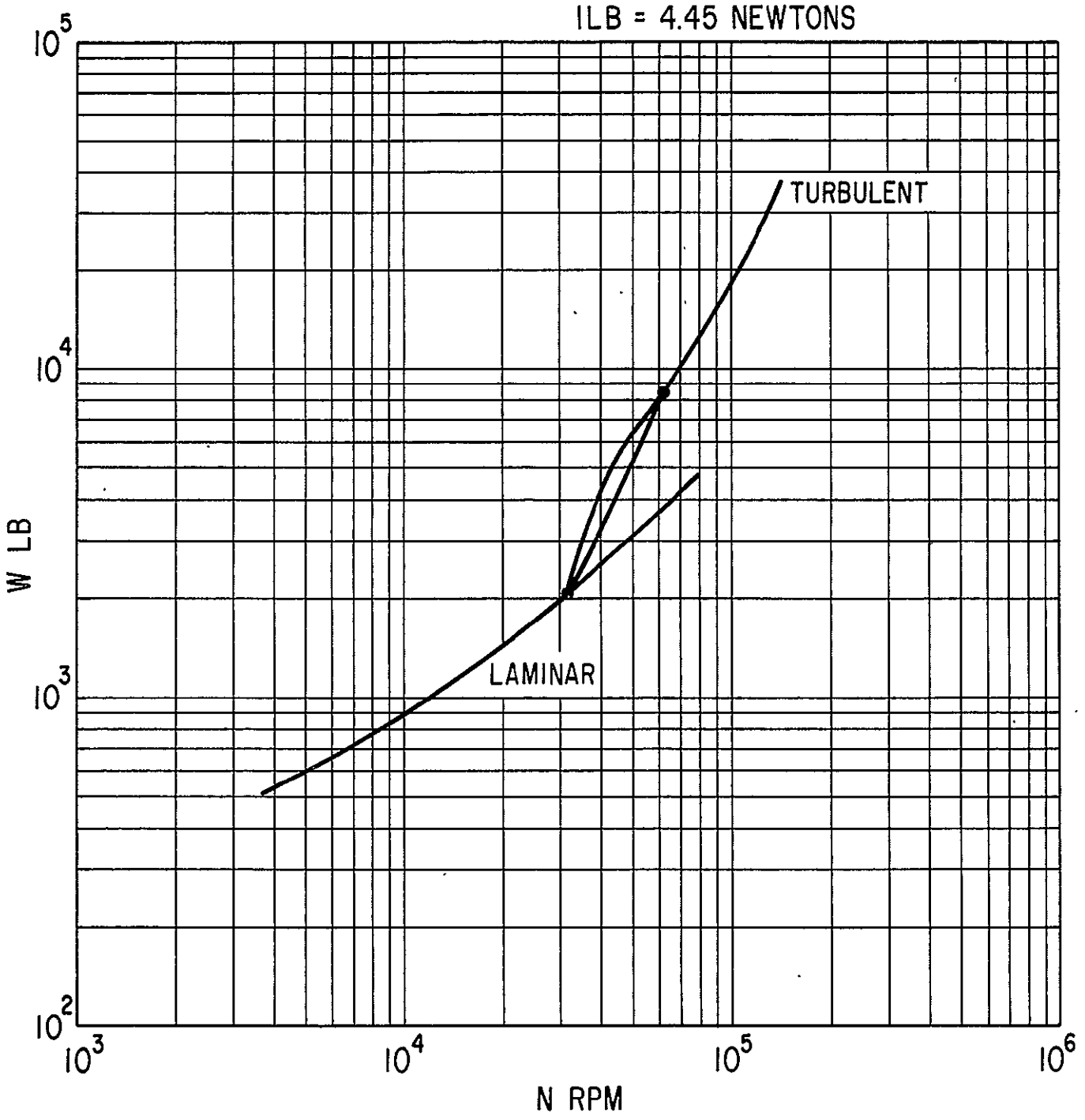

Fig. A-30 Load capacity versus speed for a shrouded step thrust bearing

CONCLUSIONS

The main results obtained in the present study are:

- A method for determining the limits of the transition region in actual bearings was developed. The method basically uses as criteria the limits for the transition region known experimentally for pure Couette or pure Poiseuille flow and for constant film thickness which are compared with a local mean Reynolds number (C9), based on local film thickness, viscosity and mean speed. The method gives good agreement with existing experimental evidence for low and moderate film thickness variations (eccentricity ratios). Therefore, until more exact theories are performed, the mentioned method may constitute a practical engineering tool in evaluating the limits of the transition region.

- A method for evaluating the operating characteristics of loaded bearings in the transition zone, consistent with and similar to the existing methods utilized for laminar flow and for turbulent flow. This method is originated by treating the transition flow as a pseudo-turbulent one, i.e., by considering that some additional apparent stresses occur due to the eventual vortex pattern or turbulent spots. The additional apparent stresses may be evaluated by quasi-empirical means starting from experimental data (velocity distribution or some global quantities such as friction stresses), and using one of the standard methods already employed in the turbulent lubrication theory such as mixing length, eddy viscosity, etc. The obtained results show that for practical purposes one can use the standard pressure differential equation (C2) where the coefficients G_x, G_z take some intermediate values between the laminar ($G_{x,z} = 1/12$) and the turbulent ones. An equivalent simple approach is to consider the turbulent values $G_{x,z}$ but for an "equivalent" Reynolds number Re_e, which is zero in laminar flow, $Re_e = Re$ in fully developed turbulent flow and takes intermediate values in the transition region (C39). A required interpolation function F can be determined by starting from transition data for

pure Couette Flow. Because the existing experimental data are subject to interpretation, it is rather difficult to obtain an exact interpolation function. However, the examination of the existing experimental data can be included between two interpolation curves (C40), (C41) which give a lower and a upper limit. An examination of the numerical examples given in the paper shows that the uncertainty in evaluating the operating characteristics in loaded bearings is less than 20% in most cases.

The proposed method is simple and can be used in connection with any existing numerical program for calculating turbulent bearings. Moreover, it includes also the laminar case, so that the procedure is valid for the entire range of Reynolds numbers.

The present study has pointed out that in the present state-of-art of the transition problem in bearings there are still a number of topics which require further, more careful, experimental investigation. The problems which need more experimental information are:

- Information concerning the critical value of the Reynolds number in thrust bearings. Until now there is almost a complete lack of information concerning this problem.

- Information concerning the value of Reynolds numbers from which the flow in lubricating films (both journal and thrust) may be considered as being already fully turbulent.

- Careful experiment to obtain information concerning the variation of the operating characteristics in the transition region. This must be done to obtain a confident interpolation law for this peculiar regime.

REFERENCES

[1] H. Schlichting - "Boundary Layer Theory", Fourth Edition, McGraw Hill Book Co., New York, 1960.

[2] J.O. Hinze - "Turbulence", McGraw Hill Book Co., New York, 1959.

[3] V.N. Constantinescu - "Lubrication in Turbulent Regime" (English Translation), U.S. Atomic Energy Commission / Division of Technical Information, AEC-TR-6959, 1968.

[4] C.W. Ng and C.H.T. Pan - "A Linearized Turbulent Lubrication Theory" ASME Trans., Series D, Journal of Basic Eng., Vol. 87, No. 3, 1965, pp. 675-688.

[5] H.G. Elrod and C.W. Ng - "A Theory for Turbulent Films and its Application to Bearings" ASME Trans., Series F, Journal of Lubrication Technology.

[6] J.H. Vohr - "An Experimental Study of Taylor Vortices and Turbulence in Flow Between Eccentric Rotating Cylinders", ASME Trans., Series F, Journal of Lubrication Technology, Vol. 1, 1968, pp. 285-296.

[7] J.M. Robertson - "On Turbulent Plane Couette Flow", Proc. 6th Midwestern Conference on Fluid Mechanics, University of Texas, 1959.

[8] F. Schultz-Grunow - "Zur Stabilitat der Couette-Stromung", ZAMM, Vol. 39, Heft 3/4, 1959, pp. 101-110.

[9] G.I. Taylor - "Stability of a Viscous Liquid Contained Between Two Rotating Cylinders", Phil. Trans., Series A, Vol. 223, 1923, p. 289.

[10] N. Gregory, J.T. Stuart and W.S. Walker - "On the Stability of Three-Dimensional Boundary Layers with Application to the Flow Due to a Rotating Disk", Proc. Roy. Soc. (London) Series A, Vol. 248, 1955, p. 155-199.

[11] J. Zuk - private communication

[12] M.I. Smith and D.D. Fuller - "Journal Bearings Operation at Superlaminar Speeds", ASME Trans., Vol. 78, 1956, pp. 469-474.

[13] V.N. Constantinescu - "Analysis of Bearings Operating in Turbulent Regime", ASME Trans., Series D, Journal of Basic Engineering, Vol. 84, 1962, pp. 139-151.

[14] R.C. DiPrima - "Viscous Flow Between Rotating Concentric Cylinders with a Circumferential Pressure Gradient at Speeds above Critical", ASLE Trans., Vol. 7, No. 4, 1964, pp. 333-341.

[15] V.N. Constantinescu - "On Turbulent Lubrication", Proc. of the Institution of Mechanical Engineers, London, Vol. 173, No. 38, 1959, pp. 881-900.

[16] V.N. Constantinescu - "The Pressure Equation for Turbulent Lubrication", Proc. of the International Conference on Lubrication and Wear, I.M.E., London, 1967.

[17] C. Wachmann, D.F. Wilcock and J. Yampolsky - "Design of a Process Fluid Turbulent Film Shrouded Step Thrust Bearing for Circulators for High Temperature Helium Cooled Reactors", Bearing and Seal Design in Nuclear Power Machinery ASME Symposium, June 5-7, Miami Beach, Florida, ASME Publications, 1967, pp. 354-370.

APPENDIX B

NOMENCLATURE

a = Upstream (front) land width, inches

b = Outer and inner land width

b = Preload spring width, inches

d = Drain groove width at mean radius

d = Ball bearing bore size, mm

d = Preload spring thickness, inch

D_i = Fluid film bearing inner diameter, inches

D_o = Fluid film bearing outer diameter, inches

D_m = Fluid film bearing mean diameter, inches

e = Downstream (back) land width, inches

e = Fluid film bearing eccentricity, inch

E = Step area length, inches

F_a = Axial load

F_z = Radial load

h_1 = Land to runner clearance, inches

h_2 = Runner to pocket bottom clearance, inch

h_F = Axial fluid film bearing film thickness, inches

HP = Power loss

K_{1-4} = Spindle bearing radial stiffnesses, lb/in

K_B = Axial stiffness of ball bearing ("x" direction) lb/in

K'_B = Radial stiffness of test ball bearing lb/in

K_e = Equivalent axial ball bearing stiffness, lb/in

K'_e = Equivalent axial hybrid boost bearing stiffness, lb/in

K_F = Fluid film bearing axial stiffness, lb/in

K_s = Preload spring stiffness, lb/in

K_z = Radial stiffness of ball bearing (z direction) lb/in

L = Step area width, inches

L = Preload spring length, inches

N = Speed, rpm

P_i = Inlet pressure at housing, psig

P_s = Pocket pressure at oil inlet, psi

q = Ball bearing heat rejection, btu/in

Q = Hybrid boost bearing oil flow, gpm

Q_B = Ball bearing oil flow, gpm

r_i = Inner radius, inches

r_o = Outer radius, inches

r_m = Mean radius, inches

s = Oil groove width, inches

T_B = Temperature at back face of fluid film bearing stator, ^oF

T_{IL} = Inner land temperature, ^oF

T_{in} = Oil inlet temperature, ^oF

T_{OL} = Outer land temperature, ^oF

T_{OR} = Ball bearing outer race temperature, ^oF

T_p = Temperature at pocket center

W = Land on preload spring, lb

W_H = Weight of bearing,

δ = Pocket depth, inch

δ_s = Preload spring deflection, inches

δ_x = Deflection between ball bearing inner and outer races, inches

ϵ = Fluid film bearing eccentricity ratio

μ = Viscosity, lb-sec/in^2

UNCLASSIFIED
Security Classification

DOCUMENT CONTROL DATA - R & D

(Security classification of title, body of abstract and indexing annotation must be entered when the overall report is classified)

1 ORIGINATING ACTIVITY (Corporate author)	2a. REPORT SECURITY CLASSIFICATION
Mechanical Technology Incorporated 968 Albany-Shaker Road Latham, New York 12110	UNCLASSIFIED
	2b. GROUP None

3 REPORT TITLE

Development of Long Life Jet Engine Thrust Bearings

4 DESCRIPTIVE NOTES *(Type of report and inclusive dates)*

Final Report

5. AUTHOR(S) *(First name, middle initial, last name)*

Leo W. Winn

Robert H. Badgley

6. REPORT DATE	7a. TOTAL NO. OF PAGES	7b. NO. OF REFS
August 1970	245	5

8a. CONTRACT OR GRANT NO.	9a. ORIGINATOR'S REPORT NUMBER(S)
NAS3-11163 b. PROJECT NO.	MTI 70TR44
c.	9b. OTHER REPORT NO(S) *(Any other numbers that may be assigned this report)*
d.	NASA CR-72744

10 DISTRIBUTION STATEMENT

Distribution of this Document is Unlimited.

11. SUPPLEMENTARY NOTES	12 SPONSORING MILITARY ACTIVITY
	The National Aeronautics and Space Administration

13. ABSTRACT

This report describes the analyses, design and testing of a Hybrid Boost Bearing. The hybrid boost bearing makes use of the inherent advantages of both the fluid film and rolling contact element bearings, and at the same time minimizing their disadvantages and limitations. The net result is a bearing with extended life and low wear characteristics. The life extension is mainly achieved via a load sharing process.

DD FORM 1 NOV 65 1473 (PAGE 1)

S/N 0101-807-6801

UNCLASSIFIED
Security Classification

14 KEY WORDS	LINK A		LINK B		LINK C	
	ROLE	WT	ROLE	WT	ROLE	WT
Jet Engine Thrust Bearings						
Thrust Bearings						
Hybrid Boost Bearings						
Fluid Film Bearing Tests						
Ball Bearing Tests						